UNIVERSITY OF LIVERPOOL

Electrochemical testing of alkali metal-oxygen batteries

Thesis submitted in accordance with the requirements of the University of Liverpool for the Degree of Doctor in Philosophy

Filipe Braga

November 2017

Supervisor: Laurence J. Hardwick

STEPHENSON INSTITUTE FOR RENEWABLE ENERGY

Battery and Electrified Interfaces Group

CAPES

Valeu a pena? Tudo vale a pena se a alma não é pequena. **(Fernando Pessoa)**

Abstract

The main focus of this thesis is the development of high specific energy alkali metal-oxygen batteries. Chapter 1 provides a general point of view of the energy storage field and the specific background knowledge of each alkali metal-oxygen system. Chapter 2 discusses the experimental methods and techniques applied for the investigation of these battery devices.

Chapter 3 investigates specific approaches for the development of the non-aqueous lithium-oxygen battery. An attempt to fabricate more suitable positive electrodes is made by utilising hypercrosslinked polymer carbons. The effect of nitrogen heteroatom doping and pore volume on the performance of lithium-oxygen cell is discussed. The effect of integrating a tertiary amine acting as a singlet oxygen quencher on the performance of the cell is evaluated. Analysis of the chemical nature and morphology of discharge products helped elucidate the processes occurring during galvanostatic cycling.

Chapter 4 sets out an investigation into several aspects of the non-aqueous sodium-oxygen battery. The stability of various cells components, such as carbon, polymeric binder and electrolyte solvent, against superoxide radical attack is evaluated. The conditions in which the discharge of the cell undergoes different solution or surface mechanisms is determined as well as the conditions in which different reaction products are obtained. The stability of sodium superoxide, the desired discharge product, in the battery environment is discussed.

Chapter 5 presents a comprehensive study into the non-aqueous potassium-oxygen battery. In ether based electrolytes, faster kinetics for the formation and

decomposition of potassium superoxide are obtained. Electrolyte degradation products are detected to a lesser extent compared to other alkali metal-oxygen cells. The main factor hindering long cycling are instabilities associated with the metal anode. The condition in which a protective surface layer or a passivating surface layer are formed on the metal anode are determined. Attempts to enhance the stability of the protective surface layer are performed by utilising highly concentrated electrolytes and ionic liquid based electrolytes. An alternative antimony based anode material is investigated and stable cycling with capacities close to the theoretical value are obtained. Finally, the oxygen reduction/evolution reactions occurring at the positive electrode are analysed by looking into the stability of polymer binders, the performance of carbon cathodes and the stability of potassium superoxide in the cell environment.

Acknowledgments

I would like to thank **Prof. Laurence Hardwick** for accepting me in his research group, providing me with all the tools to develop my PhD research and for continuous support and guidance over the past four years.

I would like to thank *Coordenação de Aperfeiçoamento de Pessoal de Nível Superior* (CAPES) and the Science without borders program for funding my project.

I would like to thank all present and former members of the Hardwick research group for making it the best working place one could hope for. I am very fortunate to have worked with and learned from such talented and hardworking people during my PhD. Particularly, I am extremely grateful to **Dr. Nick Drewett** for helping me develop the electrochemical test rig and training me in most of the techniques which I am know familiar with. I am thankful to **Dr. Iain Aldous** for the development of the oxygen line, AFM experiments and singlet oxygen research. I am thankful to **Dr. Laura Cabo-Fernandez** for continual help with Raman spectroscopy.

I would like to thank **Jose A. C. Clemente** for the XPS measurements and **Jet-Sing M. Lee** for the hypercrosslinked polymers.

I would like to thank **Dr. Tobias Heil** and **Dr. Karl Dawson** for SEM and EDS training.

I am thankful to **Vince Vasey** and **Paul Cross** for the time and effort spent on the mechanical and glassware work necessary for this research.

A special thanks to **Dr. Caroline Uchoa**, who five years ago revised the grant proposal for this PhD and supported me to be where I am today.

Finally, I would like to dedicate this thesis to my family, whom I love the most.

Table of Content

List of Abbreviations

ACN	Acetonitrile
AFM	Atomic force microscopy
AN	Acceptor number
CMC	Carboxymethylcellulose sodium
CV	Cyclic voltammetry
DABCO	1, 4-diazabicyclo [2.2.2] octane
DEGDME	Diethylene glycol dimethyl ether
DFT	Density functional theory
DME	1,2 dimethoxyethane
DMSO	Dimethylsulfoxide
DN	Donor number
EDS	Energy dispersive X-ray spectroscopy
FTIR	Fourier transform infrared spectroscopy
GDL	Gas diffusion layer
HSAB	Hard soft acid base theory
IA	Ionic association strength
K_2O_2	Potassium peroxide
KO_2	Potassium superoxide
K-O_2	Non-aqueous potassium oxygen battery
Li_2O_2	Lithium peroxide
LiO_2	Lithium superoxide
Li-O_2	Non-aqueous lithium oxygen battery

Na_2O_2	Sodium peroxide
$Na_2O_2 \cdot 2H_2O$	Sodium peroxide dihydrate
NaO_2	Sodium superoxide
$Na\text{-}O_2$	Non-aqueous sodium oxygen battery
$O_2^{\bullet-}$	Superoxide radical anion
OER	Oxygen evolution reaction
ORR	Oxygen reduction reaction
PC	Propylene carbonate
PTFE	Poly(tetrafluoroethylene)
PVDF	Poly(vinylidene fluoride)
PXRD	Powder X-ray diffraction
SEI	Solid electrolyte interphase
SEM	Scanning electron microscopy
TEGDME	Tetraethylene glycol dimethyl ether
XPS	X-ray photoelectron spectroscopy

Chapter 1. Introduction

1.1 Initial considerations

It is commonly recognised that securing energy demand in a sustainable environmentally benign manner is one of the biggest challenges of contemporary society. The digital revolution that took place in the 20th century and the steady growth of global population are two of the main reasons. In 2001, 13 TW were reported as required to "power the planet" and 85% of this amount was obtained by burning finite fossil fuels[1], which poses serious global warming concerns. A two-fold increase in the annual global energy production by 2050 has been predicted[1, 2], therefore the dependency on fossil fuels needs to be reduced. In order to achieve that, thinking more efficiently and finding better ways to store energy is crucial.

Batteries are devices that convert the energy stored in chemical bonds into electric energy (i.e. direct current). A battery is composed of two, or more, electrochemical cells put together in parallel or in series. An electrochemical cell consists of two, or more, electrodes with different chemical potential separated by an ionically conducting electrolytic solution called the electrolyte[3]. A lot has changed since the first battery was reported by Alessandro Volta in 1800[4], known as the voltaic column, which consisted zinc and silver electrodes piled up between cardboard papers soaked in brine. However, this configuration is still similar to the alkali metal-air batteries which are the scope of this thesis.

Volta's invention also opened a new research field in science: electrochemistry. Electrochemistry as a science field is mainly concerned with the

chemical changes produced by electricity and vice versa. Among many practical applications with real impact in everyday life, such as electroplating, electrophoresis, corrosion science, electrochemical desalination, electrochemical production of raw materials; energy storage is most economically significant branch of electrochemistry with billions of battery units currently produced per year[3]. The great outreach of this industry also makes the point of prolonging battery lifetime aiming to reduce environmental impacts.

Lithium-ion (Li-ion) technology celebrates 26 years since it was first commercialised by Sony Corporation in 1991 achieving a status of "the most impressive success of modern electrochemistry"[5]. Delivering a surprising, for the time, 80 Wh kg^{-1} which doubled the specific energy of nickel-cadmium batteries, Sony's original battery quickly dominated the market for cameras, computers and communications[6]. Undoubtedly, Li-ion energy storage played a key role in the evolution of smartphones and other portable electronic devices that certainly shaped modern society's lifestyle.

Apart from portable electronic devices, lithium battery systems are also a centre issue in the electrification of transportation. The development of better energy storage devices is the current bottleneck for a wider spread of electric and hybrid electric vehicles; problems like range anxiety, high costs and long charging hours need to be addressed in order to achieve mass-market commercialisation. Realising full electrification of ground transportation would have a significant environmental impact, aiming to reduce greenhouse-gas emission related to the burning of petroleum derived fuels in internal combustion engines.

The mass production and utilisation of electric and hybrid cars is only environmentally worthwhile if CO_2–free primary electricity is produced to eventually charge the batteries which power these vehicles. In this direction, a lot of effort has been put into harvesting energy from renewable sources, such as wind, solar, biomass, geothermal and tidal. The intermittent nature of green energy sources creates the need for energy storage devices that could balance their fluctuating generation and integration into the electrical grid. Combining electricity generation from non-polluting renewable sources and low emission electrified road transportation would be of great interest for a more sustainable society.

For application in stand-alone renewable power plants, durability and cost efficiency are more relevant parameters than volumetric energy density, which is more significant in an automotive vehicle[7]. This highlights the necessity to identify and prioritise the main requirements of the storage device for a given system, as one battery system is unlikely to be suitable for a diverse range of applications.

Despite the current success of Li-ion batteries as energy storage devices, there is still considerable demand for improvement in order to satisfy current and future markets. Consequently, research into this area is still of great interest from both academic and industrial perspectives.

1.2 The lithium-ion battery

The Li-ion battery was launched in 1991, but the notion of a "rocking chair" type lithium ion intercalation cell was studied since the 1970s[8, 9]. A lithium-ion battery is composed of a negative electrode (anode), a lithium ion conducting non-aqueous electrolyte and a positive electrode (cathode), as shown in Figure 1.1. Both electrode materials are capable of lithium intercalation/deintercalation. The cell composition is not fixed, and multiple materials can be used to assemble a device with different characteristics (Figure 1.2).

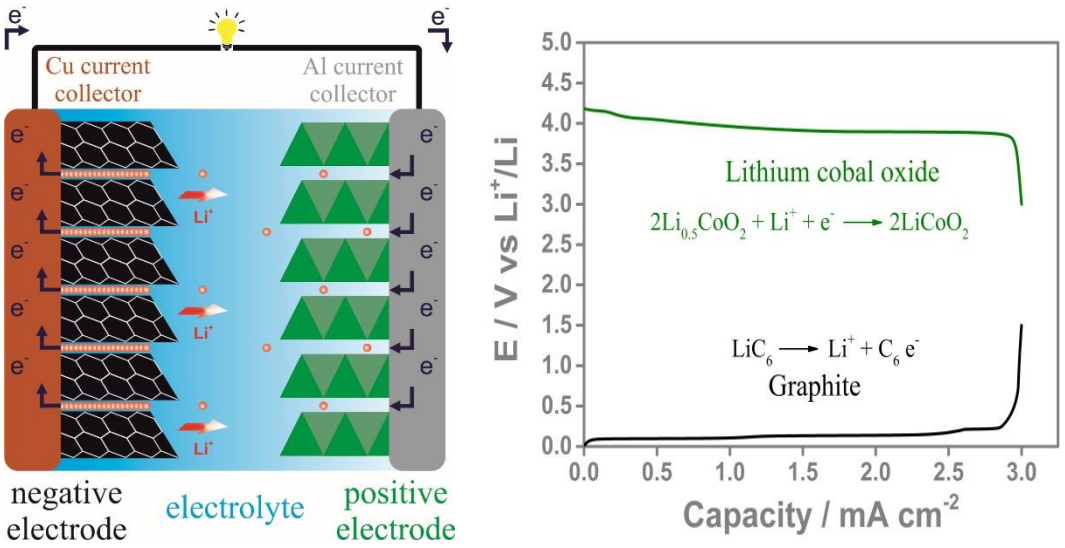

Figure 1.1: Representative scheme of a lithium-ion cell during discharge (left) and a typical potential vs capacity profile for both electrodes in the cell (right).

Typically, graphitic carbons are used as anodes for being safer than metallic lithium whilst having similar lithiation redox potential, it is also low cost and environmentally benign. Different metallic compounds are employed as cathodes, such layered metal oxides ($LiCoO_2$ – LCO), olivines ($LiFePO_4$ – LFP) and spinels ($LiMn_2O_4$ – LMO)[10]. A part from the active material, both electrodes make use of

polymeric binders for mechanical strength (e.g. polyvinylidene fluoride) and conductive carbon black additives due to low conductivity. A common electrolyte composition is a solution of lithium hexafluorophosphate in ethylene carbonate-diethylcarbonate ($LiPF_6$ in EC/DEC) for its ability of forming a stable solid electrolyte interphase with the carbonaceous anode[11].

Upon discharging the device, lithium ions leave the negative host electrode, are transported through the electrolyte and are inserted on the positive intercalation host electrode. Electrons move through the outer circuit as a result of a change in the metallic centre oxidation state (e.g. $Co^{+3/+4}$) maintaining net charge neutrality. The inverse process is observed when a voltage is applied in the opposite direction to charge the device with charge carriers "rocking" back and forth between two insertion electrodes (equations 1.1-1.2).

$$LiMO_2 \leftrightharpoons Li_{1-x}MO_2 + xLi^+ + xe^- \quad 1.1$$

$$C_6 + xLi^+ + xe^- \leftrightharpoons Li_xC_6 \quad 1.2$$

When combining a material that deintercaltates/intercalates lithium ions at low potential, such as graphite (0.1 V vs Li^+/Li), with a material that intercalates/deintercalates lithium ions at high potential such as lithium cobalt oxide (3.5-4.3 V vs Li^+/Li), a high power device is obtained. Figure 1.1 shows a typical discharge profile of a full Li-ion cell exhibiting large potential difference. Figure 1.2 illustrates how different active material components in lithium-ion batteries can render high capacity, high voltage devices. High power along with high energy density, improved safety and long cycle life explain the rapid success of Li-ion

compared to other energy storage systems, such as nickel-cadmium and lead-acid batteries.

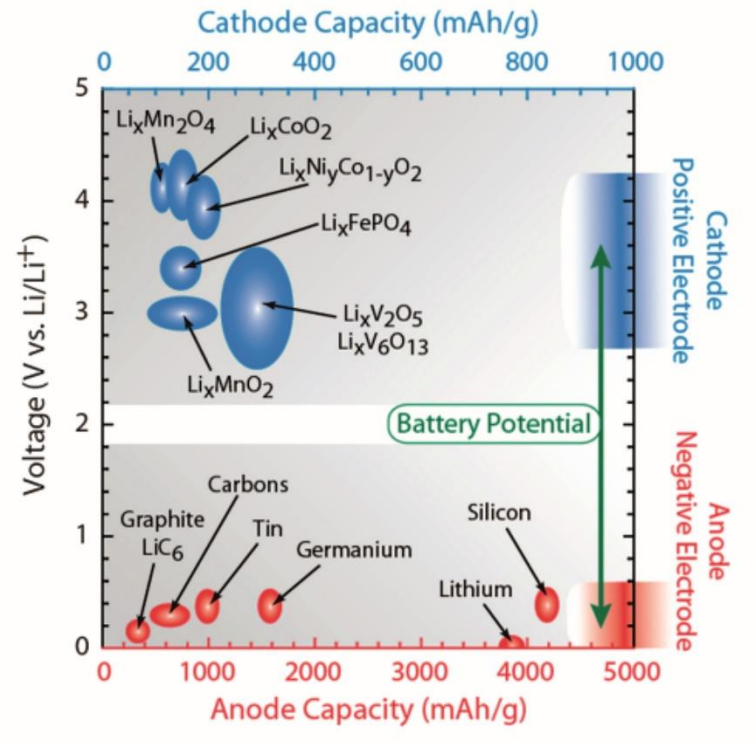

Figure 1.2: Voltage versus capacity diagram for various positive and negative electrodes in lithium-ion batteries. Taken from Brian J. Landi *et al.*[12]

The Li-ion technology has seen a significant and steady increase in the energy density of commercial devices over the past 26 years, from an initial 80 Wh kg^{-1} - 250 Wh L^{-1} to 260 Wh kg^{-1} - 770 Wh l^{-1} nowadays[6, 10, 13]. Extensive investigation on the cell components (cathode, electrolyte and anode) is responsible for this impressive advance.

Several research strategies are able to improve the electrochemical activity of the positive electrode material. The development of lithium rich mixed metal oxides[14, 15] and multi-electron redox couple materials[16, 17] are examples of approaches which can yield higher specific capacities. Cathode materials with

polyanionic groups are able to intercalate Li^+ at higher potentials, hence improving power density[18]. Nanoarchitectured electrodes promote a reduction in charge carriers path length which enables faster charge/discharge rates (i.e. rate capability)[19, 20].

At the anode side, research onto titanium based compounds, such as lithium titanate oxide, and intermetallic lithium metal alloys, such as tin, aluminium and silicon, would significantly improve the performance of lithium ion batteries. Lithium titanate oxide has the advantage of being compatible with aluminium current collectors, which are cheaper than copper, commonly used with traditional graphite anodes, and exhibits enhanced thermal stability due to lower operating voltage[21]. Lithium metal alloys are interesting for their natural resource abundance and higher theoretical specific capacity (tin - 990 mAh g^{-1}, aluminium – 2235 mAh g^{-1} and silicon – 4200 mAh g^{-1}) when compared to conventional graphite (370 mAh g^{-1})[3, 22].

The search for more stable electrolytes than present combustible organic carbonates would improve the safety of lithium-ion batteries. Two particularly promising approaches are the use of solid electrolytes and ionic liquid (room temperature molten salts) based electrolytes. The large electrochemical window stability of these electrolyte systems enables the use of high voltage and high capacity cathode materials which are incompatible with liquid organic solvents[3, 13].

Li-ion technology will continue to show incremental enhancements in its performance over the years to come. However, intrinsic characteristics hinder the practical energy density of these devices; a physicochemical limit in energy density

has been predicted on the literature, which the exact value depends on the cell design[13, 23]. Such characteristics include the low diffusion coefficient of lithium ions in the solid state, which ultimately relates to the rate capability of the battery, the depth of intercalation in cathode materials has to be limited to avoid irreversible structural changes (e.g. $0.5 < x < 1$ mol of Li^+ per equivalent host material for Li_xCoO_2), transition metal oxides are heavy elements and thus have inherent low gravimetric energy density.

New energy storage systems must be developed to meet the ever increasing energy demands of modern society. This is specifically true for the electric vehicle market, where Li-ion batteries fails to reach gasoline's much higher tank-to-wheel efficiency. Electric and hybrid electric vehicles are currently a high-end market due to the large size of the battery pack which significantly increases the final price of the car. To achieve a major change in energy density new approaches must be considered, such as moving from intercalation chemistry to electrochemical conversion devices.

1.3 Beyond lithium-ion batteries

Lithium-sulphur is concrete example of a step-change battery technology which can outperform traditional intercalation batteries with companies already developing commercial prototypes used in aerospace applications, where the size of the device is of prime importance[24, 25]. The cell concept, known since 1968[26, 27], is based on a lithium metal negative electrode and a solid sulphur positive electrode. Upon discharge, elemental sulphur is reduced and reacts with alkali metal ions to form lithium sulphide (Li_2S) as a final product (Equation 1.3). Each sulphur atom releases two electrons per reduction, which is an improvement over lithium ion intercalation systems. Some of the advantages in these systems arise from the natural abundance, multiple valency, non-toxicity and low cost of elemental sulphur and the theoretical specific energy of the cell reaction which exceeds lithium-ion batteries by a factor of 5 (2615 Wh kg^{-1})[28].

$$2Li^+ + 2e^- + \frac{1}{8}S_8 \leftrightharpoons Li_2S \qquad 1.3$$

Despite considerable advantages, fundamental challenges hinder a mass commercialisation of lithium-sulphur batteries including the insulating nature of sulphur and lithium sulphide (5.10^{-30} S/cm at room temperature) which reduced the exploitation of carbon active sites and causes poor rechargeability. A paramount issue for the operation of lithium-sulphur cells is the diffusion of soluble polysulphide intermediates into solution which can diffuse to the metal anode and undergo chemical reduction reaction resulting in self-discharge and forming

solid/insulating precipitates. Significant volume expansion and clogging of the lithium ions diffusion pathway due to high sulphur loading is also a critical issue[29, 30].

Polysulphides intermediates are intrinsically highly polar molecules due electronegative terminal sulphur elements and this characteristic can be used to architecture novel cathode host materials which can entrap the intermediates generated mitigating the shuttling problem. Several approaches have been investigated for this purpose, such as: utilising meso and microporous carbon electrodes, carbon nanotubes and graphene based electrodes (aiming to physically confine the polysulphides)[30, 31], polar functionalised conductive polymers, mixed metal oxides, transition metal and doped carbonaceous materials (aiming to confine polysulphides via strong polar-polar interactions)[29, 32]. However, these methods fail to entirely control polysulphide shuttling and significantly increase the cost of a final device. These are some of the matters that need to be addressed for the realisation of the full potential of lithium-sulphur systems.

Elemental oxygen is in principle an even more exciting active material for conversion chemistry batteries in comparison to sulphur; it is lighter, readily available, liable of multiple electrochemical redox reactions and it can render higher energy density devices.

Alkali metal-oxygen batteries (AM-O_2) can be divided in four groups based on the electrolyte employed: non-aqueous[33], aqueous[34], dual electrolyte[35] and solid-state cells[36]. Each battery group has their own scientific appeal and particular challenges, however, only non-aqueous systems will be discussed in details as they are the main scope of this thesis.

Both alkali metal-oxygen and alkali metal-air are promising energy storage devices, the only difference being the gas supplied to the system. When atmospheric air is employed, moisture and carbon dioxide contaminations have been proved to be harmful for the electrochemical performance of the battery[37]. For the development of practical metal-oxygen batteries, O_2 selective membranes must be developed or pure O_2 must be supplied to the system. Again, only metal-oxygen systems are part of the scope of this thesis and will discussed in the next sections. Therefore, the non-aqueous room-temperature alkali metal-oxygen battery will be henceforth referred as simply lithium/sodium/potassium-oxygen battery.

Among the energy storage systems that go beyond the Li-ion system, metal-oxygen batteries really stand out due to their unparalleled theoretical specific energy (Figure 1.3), which, in the case of lithium-oxygen (Li-O_2), compares to the usable energy density of gasoline in automotive applications[38]. However, this affirmation needs to be looked carefully, as practical devices will surely have energies far below its theoretical value. Metal-oxygen batteries gain weight as they are discharged due to the precipitation of solid reaction products, which reduces gravimetric energy densities. Furthermore, other cell components will add "dead weight" to the final device – binder, electrolyte/separator, oxygen supply and excess of metal anode. Whilst reliable practical cell energies are surely difficult to estimate, a target of 500 Wh kg^{-1} is believed to be achievable by alkali metal-oxygen cells[23, 38, 39].

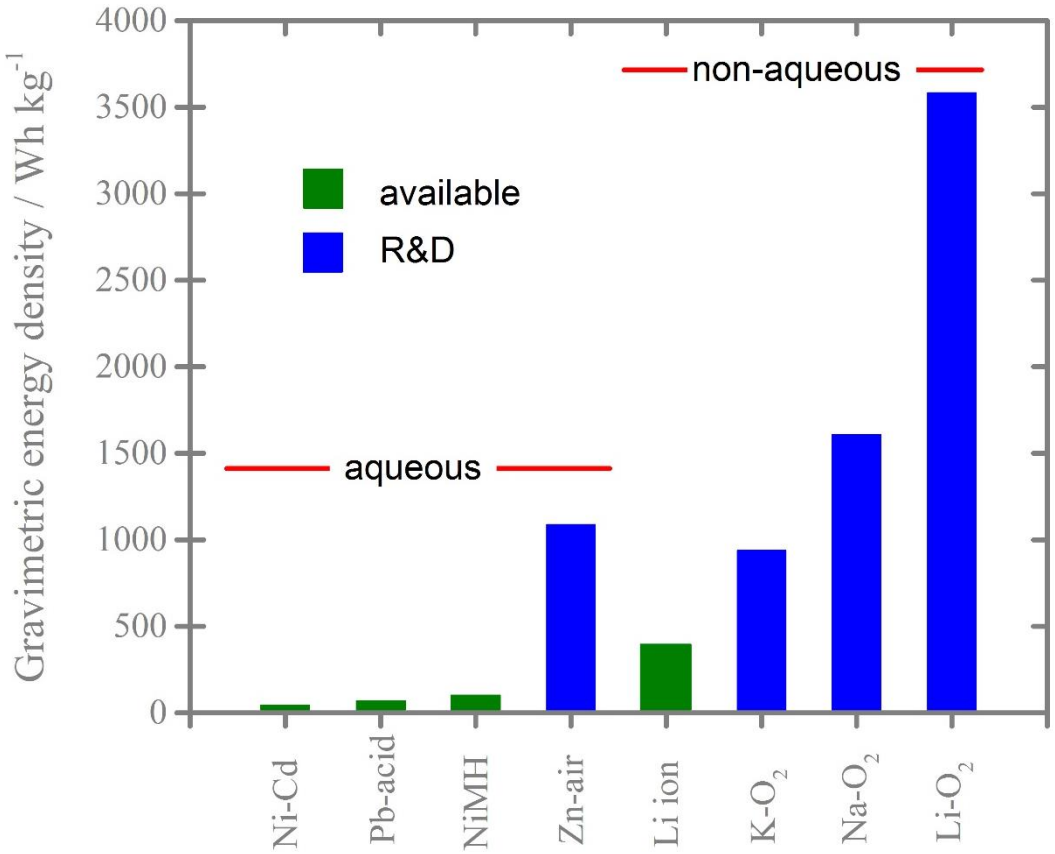

Figure 1.3: Gravimetric energy density of various rechargeable battery chemistries currently commercially available and under development.

AM-O_2 batteries use molecular oxygen as the electroactive redox material in the positive terminal of the cell. The cell is composed of an alkali metal anode, which undergo striping and plating reactions and a carbon cathode, often referred as the air-cathode, which serves as a substrate for the oxygen reduction/evolution reaction. The air-cathode is generally composed of a porous carbon, a polymeric binder and a metal catalyst if needed. Both electrodes are separated by organic aprotic electrolytes containing alkali metal (AM) ions as support salts. Figure 1.4 depicts the working principle of AM-O_2 batteries and an overall reaction is shown in equation 1.4.

$$xAM^{+} + xe^{-} + O_2 \leftrightharpoons AM_xO_2 \qquad 1.4$$

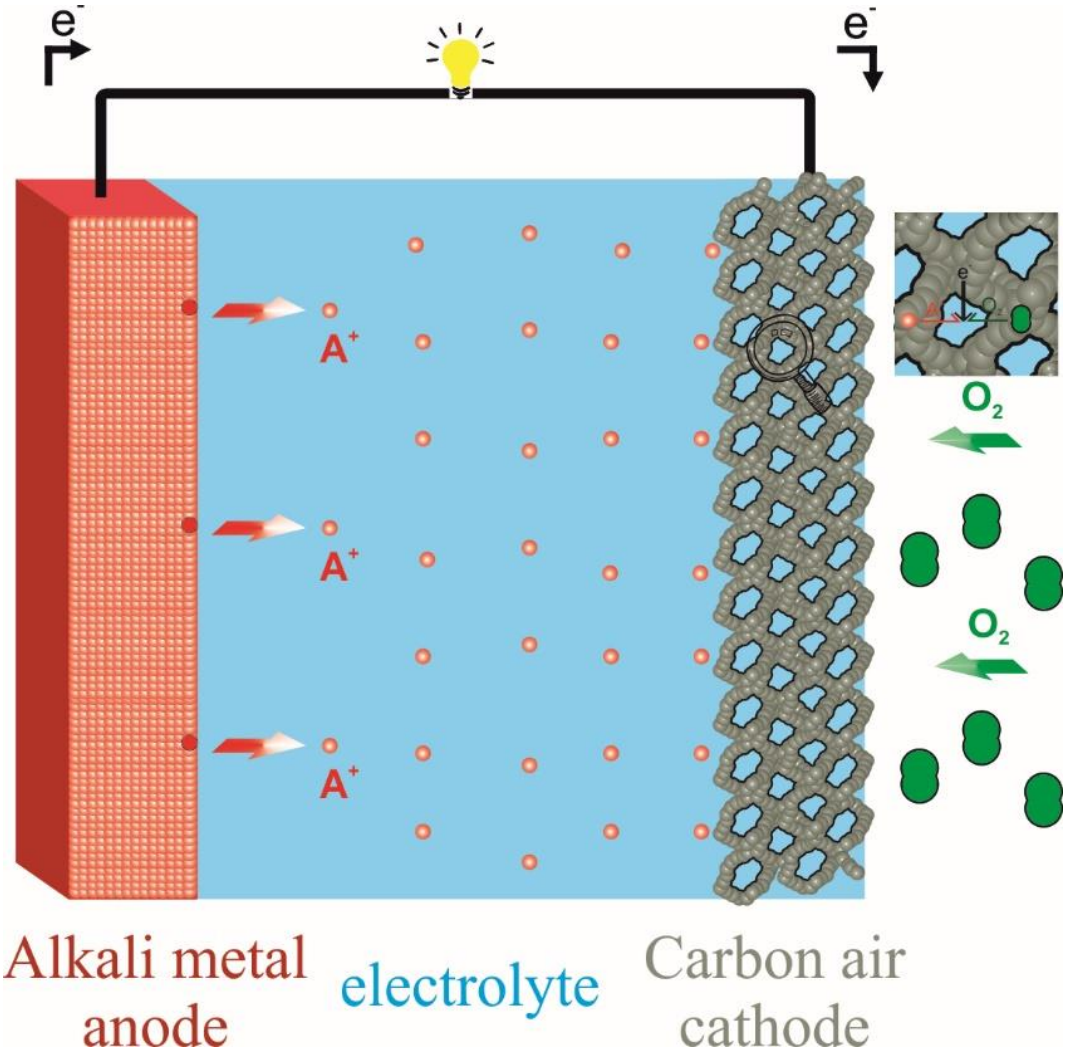

Figure 1.4: Representative scheme of alkali metal-oxygen batteries during the discharge process. The reversible chemical reaction is observed upon charge.

1.4 Lithium-oxygen batteries

The Li-O_2 battery has been investigated since 1960s, when significant research was devoted to evaluating several metal-air chemistries (zinc, iron, aluminium, lithium and magnesium) already aiming for transportation applications. Back then, mostly aqueous alkaline electrolytes were investigated, and zinc-air seemed a more viable candidate since lithium anodes are unstable in this electrolyte medium[40].

The concept was revisited in 1996 when Abraham and Jiang reported a pioneering battery design[41]. The cell comprised a thin film polymer electrolyte, an acetylene black cathode containing cobalt catalyst and a lithium metal anode. By exposing the cell to atmospheric air, capacities far superior to Li-ion cells were obtained (1400 mAh g^{-1}). Lower cell capacities were reported for a microcrystalline graphite electrode, and a first indication was made on the relevance of the carbon cathode surface area. Raman spectroscopy analysis of the discharged carbon electrode detected a weak band at 795 cm^{-1}, which suggested to the authors that lithium peroxide (Li_2O_2) was the main reaction products of the cell[41].

In 2002, Read *et al.*[42] reported the first Li-O_2 battery using liquid electrolytes. Several organic solvents were investigated, including: alkyl carbonates, linear and cyclic ethers and ketones. The specific capacity obtained for the cells was highly dependent on the current rates and oxygen solubility/diffusivity, which was linked to the electrolyte formulation. Both Li_2O_2 and lithium oxide (Li_2O) were assumed as discharge products based on gas consumption measurements. The formation of Li_2O was also deemed possible

during battery discharge by Abraham *et al.*[41] based on very similar standard Gibbs free energy of formation for both chemical compounds (ΔG = -134 kcal mol^{-1} for Li_2O_2 and ΔG = - 145 kcal mol^{-1} for Li_2O)[41].

The interest in Li-O_2 batteries by the scientific community sparked after a publication by Ogasawara *et al.*[43], where rechargeability and multiple cycling were reported for the first time. In a propylene carbonate based electrolyte, the decomposition of Li_2O_2 rendering lithium ions and oxygen gas was proven via *in situ* mass spectroscopy (MS) and *ex situ* powder x-ray diffraction (PXRD). Manganese oxide catalysts were used to lower the oxidation potential of Li_2O_2.

These initial reports created significant excitement around Li-O_2 batteries, heralded as the energy storage system of the future, leading to extensive research on fundamental aspects of the battery and towards practical devices. A comprehensive understanding of the O_2/Li_2O_2 couple eventually tempered the initial optimism as the main hurdles of the battery were identified, namely: electrolyte and cathode stability, anode reactivity and large voltage polarisation, which will be explored in the following sections.

1.4.1 O_2 reduction and evolution mechanism in lithium-oxygen batteries

Significant progress was made on elucidating the processes that occur upon discharging aprotic Li-O_2 batteries. The reaction pathway was found to be heavily dependent on the current density applied, overpotential and the solvent-solute combination, which relates to the lithium superoxide (LiO_2) intermediate solubility[44-46]. The first step when discharging the cell is the formation of the

superoxide radical anion via a one-electron reduction at the carbon cathode (Eq. 1.4). In a Li^+ containing environment, the reactive superoxide species rapidly forms lithium superoxide (Eq. 1.5), which can either be adsorbed (LiO_2*) to the electrode surface or be solvated into solution ($LiO_{2\ (sol)}$). After that, the LiO_2 intermediate can undergo chemical disproportionation reaction[47] (Eq. 1.6) or follow a consecutive electron reduction[48] (Eq. 1.7), resulting in lithium peroxide as the main discharge product of the battery. The formation of Li_2O_2 happens at a thermodynamic potential of 2.96 V vs Li^+/Li.

$$O_2 + e^- \rightarrow O_2^- \quad 1.4$$

$$O_2^- + Li^+ \rightarrow LiO_2 \quad 1.5$$

$$2LiO_2 \rightarrow Li_2O_2 + O_2 \quad 1.6$$

$$LiO_2 + Li^+ + e^- \rightarrow Li_2O_2 \quad 1.7$$

$$Li_2O_2 \rightarrow 2Li^+ + 2e^- + O_2 \quad 1.8$$

The charging process (Eq. 1.8) of the Li-O_2 cell does not follow the reverse discharge reactions in Eq. 1.6-1.7, and the oxidation of Li_2O_2 follows a direct two-electron step[47]. Hummelshoj *et al.*[49] reported very low theoretical charge overpotential for the oxidation of Li_2O_2 (less than 0.2 V) and in fact oxygen evolution is detected at early stages of the charge step (around 3.0 V *vs* Li^+/Li)[50]. However, much larger overpotentials are observed experimentally (around 1.3 V), which are ultimately linked to the morphology of Li_2O_2 and the collateral formation of parasitic products.

Two possible mechanisms for the oxygen reduction reaction (ORR) were proposed by Johnson *et al.*[46] based on the solubility of the LiO_2 intermediate. A solution route takes place when the LiO_2 is soluble in the electrolyte, while a surface route takes place in a comparatively low solubility case.

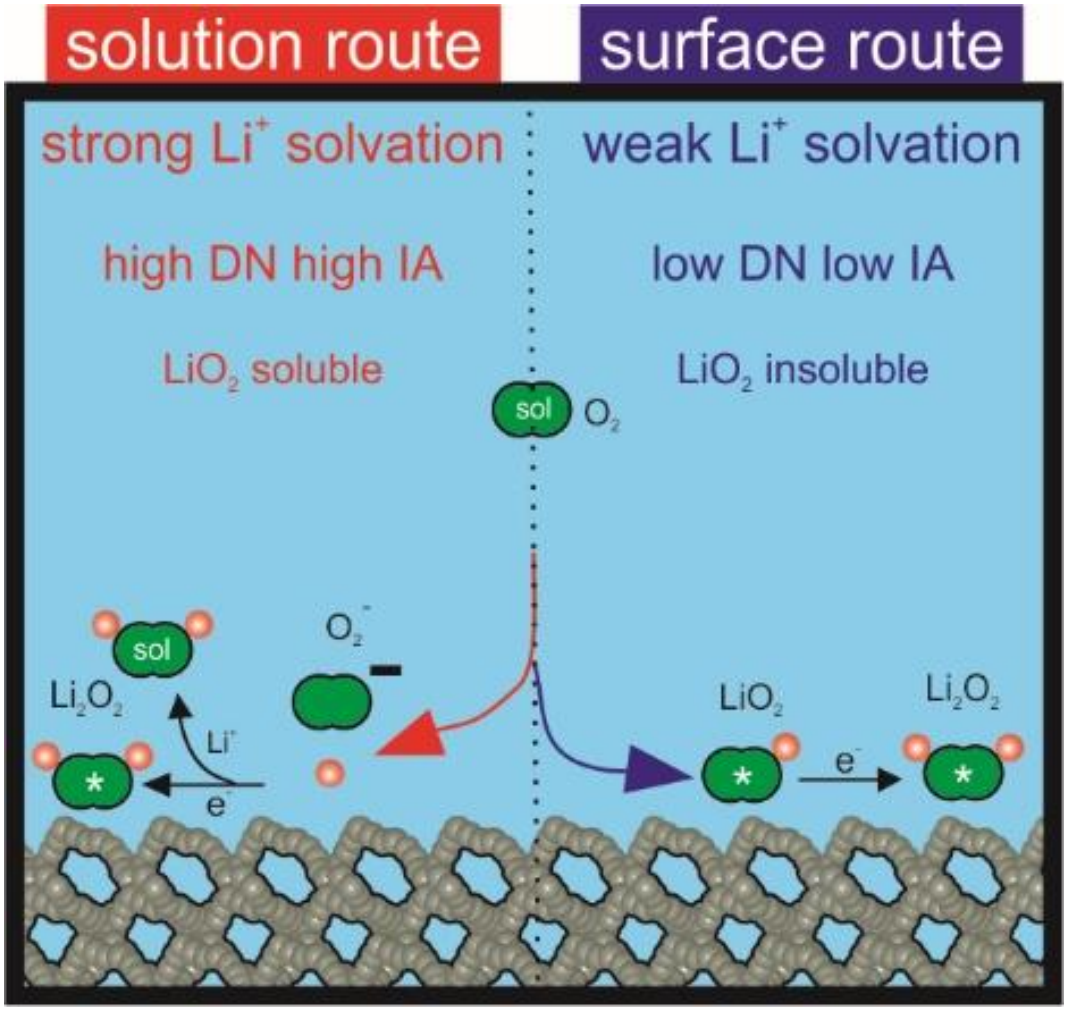

Figure 1.5: Representation of solution and surface mechanism routes in a Li-O_2 cell. *denotes a chemical species adsorbed to the carbon surface.

Three aspects directly affect the solubility of lithium superoxide in non-aqueous electrolytes: the solvent's Guttmann donor number (DN), the ionic association strength (IA) of the supporting salt and final water content[33, 46]. The

later, however, should be kept at a minimum, since water impurities can shift the main electroactive reaction from the formation of Li_2O_2 to LiOH, and whether or not this is beneficial to the development of Li-O_2 batteries is still debatable. Most Li-O_2 investigations will use dry electrolytes also to avoid instability with the metal anode, therefore, the solubility of the LiO_2 intermediate is more associated to the other two factors.

The Guttmann DN is a scale of the nucleophilicity/basicity of solvents while the electrophilicity/acidity is characterised by the acceptor number (AN)[51]. The ionic association strength is a property of the counter ion and is related to how the overall negative charge of the ion is distributed by its volume[52]. Highly associated salts can strongly solvate lithium ions in solution in a similar effect to high donor number solvents.

The practical outcome for Li-O_2 batteries of these characteristics of the solvent and support salt are shown in Figure 1.5. In a low donor number and low ionic association regime, the LiO_2 formed after a first electron reduction reaction predominantly stays attached to the carbon surface, where it forms Li_2O_2 via Eq. 1.7 or 1.8. This surface route results in the growth of a film-like peroxide deposit with thickness around 5 nm[33]. The insulating nature of Li_2O_2 results in electrode passivation which limits the specific capacity achieved. In a high donor number high ionic association situation, the LiO_2 intermediate is strongly solvated by the electrolyte. If the solvation energy is larger than the adsorption free energy, the equilibrium between $LiO_2^* \leftrightarrow LiO_{2\,(sol)}$ is shifted to the right. This allows the growth of large Li_2O_2 toroid shaped particles and higher specific capacities are achieved[33, 46].

1.4.2 Electrolyte stability

The identification of suitable electrolytes is a principal requirement for the development of Li-O_2 batteries. High ionic conductivity, large electrochemical window and chemical compatibility with the metal anode are expected characteristics from the electrolyte media. On top of these basic demands, the solvent and solute must be stable against oxygen reduced species that are formed during the discharge process as well as the final discharge product Li_xO_y which can also act as a nucleophile inducing degradation reactions[53]. The solubility and diffusivity of O_2 will allow fast discharge/charge rates and is linked to the maximum capacity achieved[37]. Since the reaction takes place in a three phase boundary (Figure 1.4) wetting of the cathode by the electrolyte is essential to maximise reaction sites. Finally, due to the open configuration of the cell, a low volatile electrolyte is necessary to avoid evaporation.

It seems a natural conclusion to explore similar electrolytes used in Li-ion systems in Li-O_2 cells. Initial studies employed organic carbonates electrolytes, e.g lithium hexafluorophosphate dissolved in propylene carbonate (PC) or a blend of ethylene carbonate/dimethylcarbonate (EC/DMC)[42, 43]. However, the instability of these solvents was reported by Mizuno *et al.*[54], showing that the main electrochemical reaction taking place was the formation of lithium carbonate (Li_2CO_3). This implies that the initial cycling of Li-O_2 cells reported by Ogasawara *et al.*[43] was in fact due to electrolyte consumption instead of the desired peroxide formation/oxidation.

A comprehensive study on the performance of organic carbonates electrolytes reported by Freunberger *et al.*[55] identified several side reaction products, namely $C_3H_6(OCO_2Li)_2$, Li_2CO_3, HCO_2Li, CH_3CO_2Li, CO_2 and H_2O. A discharge mechanism was proposed in which the superoxide radical anion induces ring opening of the PC molecule via a nucleophilic attack on the less sterically hindered carbon. Ultimately, the accumulation of parasitic side products causes large charge overpotentials, rapid capacity fade and cell failure.

Following the observation of carbonates instability, ether molecules were proposed as a suitable electrolyte. Density functional theory calculations reported by Bryantsev *et al.*[56] predicted that a nucleophilic attack on ether molecules is extremely unfavourable due to the high activation energy barrier. Using potassium superoxide (KO_2) as a source for superoxide radical anion ($O_2^{\bullet -}$), Uta Schwenke *et al.*[57] reported no degradation of ether solvents via nucleophilic attack.

In fact, ether-based electrolytes have been the main solvent media investigated in alkali metal-oxygen cells. Key advantages for their use include: compatibility with alkali metal anodes (Li, Na and K), large electrochemical window (no redox processes on cell's operation range), thermally stable, low cost, low volatility (for high molecular weight ethers), low viscosity (which improves oxygen solubility and facilitates mass transport) and high dielectric constant (which improves the supporting salt solubility)[58, 59].

Numerous studies reported glyme-based electrolytes in Li-O_2 batteries. Glymes are a family of linear polyethers varying the chain length. Their relative non-polar structure, in comparison to PC and dimethyl sulfoxide (DMSO) for instance, makes them less susceptible to nucleophilic attack. However, solvent

decomposition via hydrogen abstraction reaction has been predicted on literature[56] and was later demonstrated in practical Li-O_2 cells by Freunberger *et al.*[58]. The H-abstraction in ether molecules results in similar side reactions products such as carbonates, carboxylates, polyesters, CO_2 and H_2O. However, the electrolyte degradation seems to happen to a less extent for ether-based cells, as Li_2O_2 is observed as the main discharge product[50] and higher cyclability (up to 100 cycles) has been reported[60].

A simple approach to reduce degradation reactions in linear glymes was proposed by Adams *et al.*[61] where the acid hydrogens in ethylene groups were substituted via methylation reaction. The methyl substituted ether electrolyte showed considerable reduction of CO_2 evolution during charge, associated with the oxidation of electrolyte decomposition products. This result shows that glymes are not final electrolytes for Li-O_2 batteries and their structure can be modulated and improved for this specific application.

Various organic solvents have been tested as electrolytes for Li-O_2 batteries, dimethylformamide (DMF)[62], N-methyl-2-pyrrolidone (NMP)[63], dimethyl sulfoxide (DMSO)[64-67], acetonitrile (ACN)[44, 48], N,N-dimethylacetamide (DMA)[68], and ionic liquids[69-71]. The formation of lithium peroxide as the main discharge product of the battery was confirmed in all systems.

DMSO based electrolytes are particularly attractive due to its high basicity (DN = 30 kcal mol^{-1}) which induces the desired solution route as previously discussed. Long cycling with high capacity retention has been reported using DMSO combined with nanoporous gold[66] and titanium carbide[67] cathodes. In contrast, when using conventional carbon electrodes, other research group have

reported extensive electrolyte degradation upon discharge[64] and upon long exposure to lithium peroxide[65, 72].

As is to be expected, the stability of an electrolyte combination cannot be evaluated on its own, but taking into consideration other chemicals present in the cell. It is important, and challenging, to isolate the contributions – negative or positive, of all the cell components.

1.4.3 Cathode stability

A typical cathode for Li-O_2 battery application is composed of a conductive substrate, a catalyst and a binder. Initial studies used a combination of carbon black, Poly(vinylidene fluoride) (PVDF) and manganese oxide catalyst to cast free standing electrodes. The stability of these three components during the cycling of Li-O_2 cells has been extensively investigated.

Carbon materials are the basis of the positive electrode in Li-O_2 batteries, for being low cost, low weight, highly conductive and has the ability to produce hierarchic porous structures. However, the instability of carbon in the Li-O_2 cell environment during charge was unquestionably proven by McCloskey *et al.*[73] Ottakam Thotiyl *et al.*[74] using ^{13}C carbon cathodes. The detection of $^{13}CO_2$ via mass spectroscopy during cell operation implies oxidative decomposition of the carbon itself and enabled the isolation of different contributions from the electrolyte and cathode. However, carbon degradation products were detected only at voltages above 3.5 V vs Li^+/Li, indicating that if Li_2O_2 was charged bellow these voltages multiple cycling could be obtained.

Lithium carbonate is more stable than lithium peroxide and its formation, from both electrolyte and carbon cathode, creates a layer of insulating products between the carbon electrode and the lithium peroxide deposit, which explains the high overpotentials necessary to charge the cell (Figure 1.6).

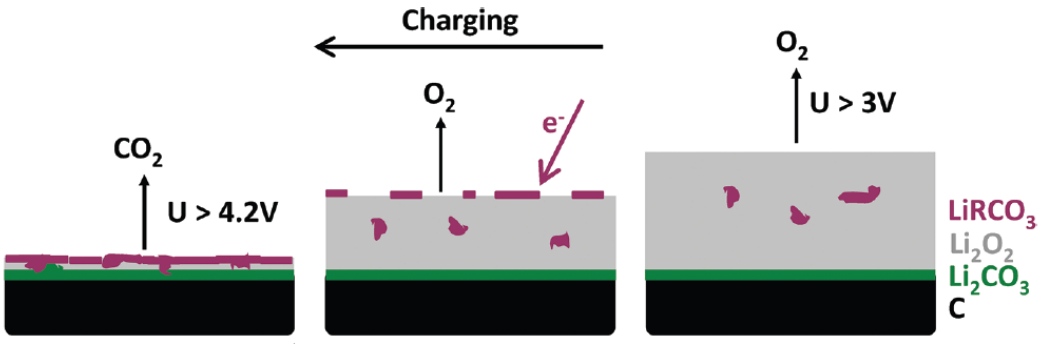

Figure 1.6: Scheme for the relation between electrolyte degradation and rising charging overpotential in a typical carbon cathode-glyme electrolyte Li-O_2 cell. Taken from Bryan D. McCloskey *et al.*[73].

McCloskey *et al.*[75] evaluated the efficiency of several electrocatalysts, such as noble metals and transition metal oxides, and found similar CO_2 evolution during charge for the different catalyst analysed compared to pure carbon. It was suggested that undesired electrolyte degradation reaction could also be electrocalalysed together with the oxygen evolution reaction, which was especially true for Pt (the best known catalyst for the OER). The use of heterogeneous catalyst was concluded to be unnecessary.

Similar to the cathode fabrication in intercalation batteries, the polymeric binder serves the purpose of providing mechanical stability to the active material. Ideally, the binder should only make up a small fraction of the electrode composition, to maximise energy density while maintain chemical/electrochemical

stability with cycling. However, even as a small fraction, all the components of the battery must be stable towards reactive intermediates for the successful implementation of Li-O_2 batteries.

Poly(vinylidene fluoride) is the most widely utilised polymeric binder for metal-oxygen batteries application. This is explained by its superior binding capability and electrochemical stability, which is transferred knowledge from Li-ion know-how. However, for Li-O_2 systems, Black *et al.*[76] identified a dehydroflurionation reaction (Eq. 1.6) when reacting PVDF with chemically generated superoxide anion radical (KO_2 + crown ether). The parasitic reaction of the binder did not inhibit the formation of lithium peroxide the final discharge product of the battery, which was identified via PXRD. The same dehydroflurionation was observed by Younesi *et al.*[77], who detected lithium fluoride as a binder degradation residue upon cycling.

$$LiO_2 + (CH_2\text{-}CF_2) \rightarrow (CH{=}CF) + 2LiF + HO_2 \qquad 1.9$$

Nasybulyn *et al.*[78] extended these investigation to eleven different polymers and reported only poly(tetrafluoroethylene) (PTFE), polyethylene (PE) and polypropylene (PP) to be stable against oxidative reactions by chemically generated superoxide anion radical.

1.4.4 Cathode design

Significant research has been developed looking into designing better architectures for the positive electrode. The air-cathode works as a substrate for the ORR and the OER during cell operation, and should be constructed aiming to maximise overall capacity while minimising voltage polarisation and side reactions. Therefore, the electrode active material must be sufficiently electronic conductive to ensure a large reaction site area throughout its extension. The electrode structure must be so as to allow oxygen diffusion to reaction sites, and also be able to accommodate a large volume of lithium peroxide deposit which is a wide band gap insulator and insoluble in non-aqueous electrolytes[23, 37].

To date, the high theoretical specific energy of Li-O_2 batteries has not been converted to high energies in practical cells and a potential cause is the poor performance of the porous cathode, especially related to the available pore volume. During the discharge process, the deposition of solid Li_2O_2 causes pore clogging that limits the transport of active material (O_2, Li^+) to reaction sites. Another important factor is the increase in charge transfer resistance reported by Viswanathan *et al.*[79] in a flat (non-porous) glassy carbon electrode, where pore clogging is not possible. A phenomenon coined as "sudden death" of the cell, characterised by a drop of cell voltage at limited capacities, was predicted to happen at a critical thickness of 10 nm of Li_2O_2 deposit. When the conformal film reaches this thickness, the charge transfer resistance no longer supports electron tunnelling effects through the film.

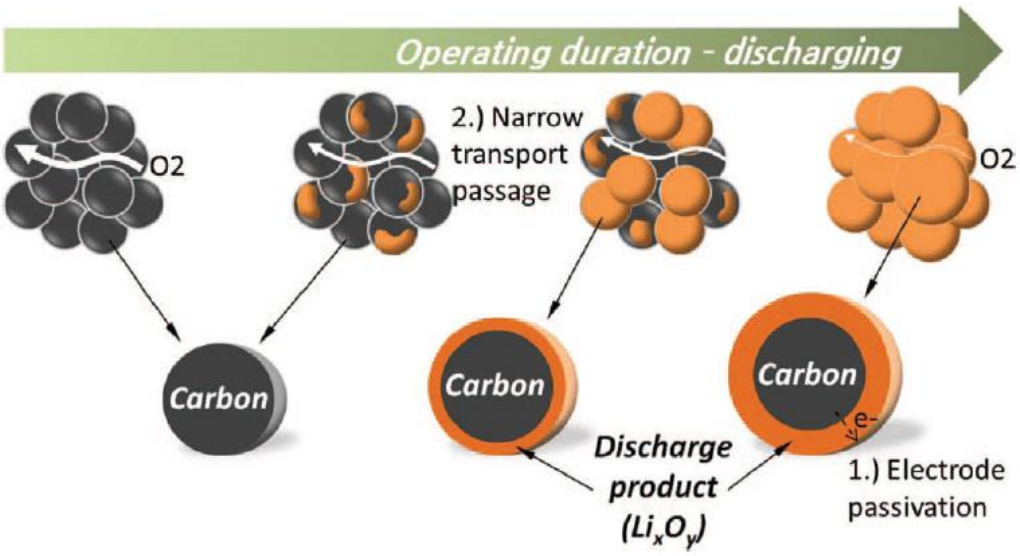

Figure 1.7: Representation of issues rising from deposition of insoluble/insulating discharge products. Taken from Yun Wang and Sung C. Cho[80].

Meini *et al.*[81] reported a linear relation between the carbon cathode surface area and specific capacity. For the electrochemical conditions employed, dry ether electrolytes and low current density, a conformal film Li_2O_2 morphology was obtained, for which a larger surface area indicates more space for the film deposition. Ding *et al.*[82] reached similar conclusions looking into different pore sizes in carbonaceous materials, where larger pores yielded higher capacities up to a certain pore size. The deposition of a few nanometre Li_2O_2 monolayer was the main discharge mechanism.

Microporous electrodes (≤ 2 nm) undergo rapid passivation by solid discharge products, resulting in poor utilisation of active sites inside the porous structure. In this case, large surface area does not relate to high capacities[83]. An ideal electrode design should have low surface area and a mesoporous ($2 <$ pore size $50 \geq$ nm) structure[33].

The positive electrode can be designed in order to reduce unwanted parasitic reactions. Hydrophilic carbons are more catalytic toward electrolyte decomposition[74] and defect sites and oxygen functional groups promote the formation of lithium carbonate side product[84, 85]. Practical approaches including atomic layer deposition of a layer of alumina on defect sites[86] and carbon doping with more stable nitrogen functionalities[87] have successfully lowered the voltage gap, increased capacities and improved cycle life.

1.4.6 Soluble redox mediators

As previously discussed, one of the main challenges faced by Li-O_2 systems is the oxidation of lithium peroxide, whether it forms as a thin conformal film (surface route) or as large toroidal particles (solution route). Even though the latter is the most favourable route for the achievement of higher capacities, the oxidation of large Li_2O_2 particles is more challenging. One of the reasons is that relatively large deposits have particles without direct contact to the conductive substrate. One relatively new approach to face this issue is the addition of soluble redox mediators to the electrolyte.

Mediators differ from electrocatalysts, as the latter is normally dispersed within the positive electrode and act by lowering the activation energy barrier for the OER. Redox mediators (RM) are molecules in the electrolyte solution which can undergo reduction/oxidation reactions within tunnelling distance from the electrode surface. By doing so, the redox molecule is electrochemically reduced and chemically oxidises lithium peroxide finally returning to its initial oxidation

state (Figure 1.8). As a basic requirement, the soluble RM molecule must possess a thermodynamic standard potential above that of lithium peroxide – $E^0_{RM} > E^0_{Li_2O_2}$.

Figure 1.8: Working principle of a redox mediator for the oxidation of lithium peroxide.

Promising results were initially reported using a tetrathiafulvalene (TTF) mediator, which allowed up to 100 cycles based on lithium peroxide formation/decomposition[88]. Several other RM molecules were studied based on standard reduction potentials closer to that of lithium peroxide, such as 2,2,6,6-tetramethyl-1-piperidinyloxy (TEMPO)[89], lithium iodide (LiI)[90, 91] and organic viologens[92]. A reduction of the charge overpotential was observed in all cases.

A recent approach reported by Gao *et al.*[93] used a redox mediator molecule to promote a solution route discharge mechanism in an electrolyte combination which otherwise promoted a surface confined mechanism. The use of 2,5-di-tert-butyl-1,4-benzoquinone (DBBQ) allowed the growth of large toroidal Li_2O_2 particles and higher capacities were achieved. The same research group developed a dual RM configuration in which TEMPO and DBBQ facilitated both ORR and OER[94]. The use of redox mediators however requires the protection of the lithium metal anode to avoid chemical reduction that would incapacitate the mediator.

1.4.6 Lithium metal anode reactivity

Lithium metal is the most desirable anode for energy storage application. It is the most electropositive metal of the periodic table (E^0 = -3.04 V vs SHE) and its very low density (σ = 0.53 g cm^{-3}) relates to extremely high gravimetric capacity (3,860 mAh g^{-1})[95]. The exploration of elemental lithium negative electrodes, however, was abandoned in early stages of the Li-ion development due to safety issues. During cell operation, the plating of lithium metal occurs via dendrite ("tree-like" in Greek) and mossy formation, causing internal short-circuits and thermal runaway[96].

In Li-O_2 batteries, added to the already extremely challenging dendrite problem, oxygen crossover must be suppressed. The separators used in Li-O_2 configuration does not block oxygen diffusion, which can react at the metal anode causing reductive decomposition of the electrolyte. The formation of degradation product on the anode surface will increase the charge transfer resistance across the interface[97].

Unless the aforementioned issues are resolved, lithium metal cannot be a suitable electrode in a safe battery. Possible alternatives include additives which can stabilise the solid electrolyte interphase, like 2-bromoethanesulfonate lithium salt[98] and caesium iodide[99], and the substitution for more stable lithium metal alloys, like tin, aluminium and silicon.

1.5 Sodium-oxygen batteries

The replacement of lithium for sodium and potassium batteries have the appeal of producing low cost energy storage systems. That is based on the higher natural abundancy of these elements (Figure 1.9) and the chemical compatibility with aluminium current collectors, also more abundant in the earth's crust than copper (used in lithium batteries).

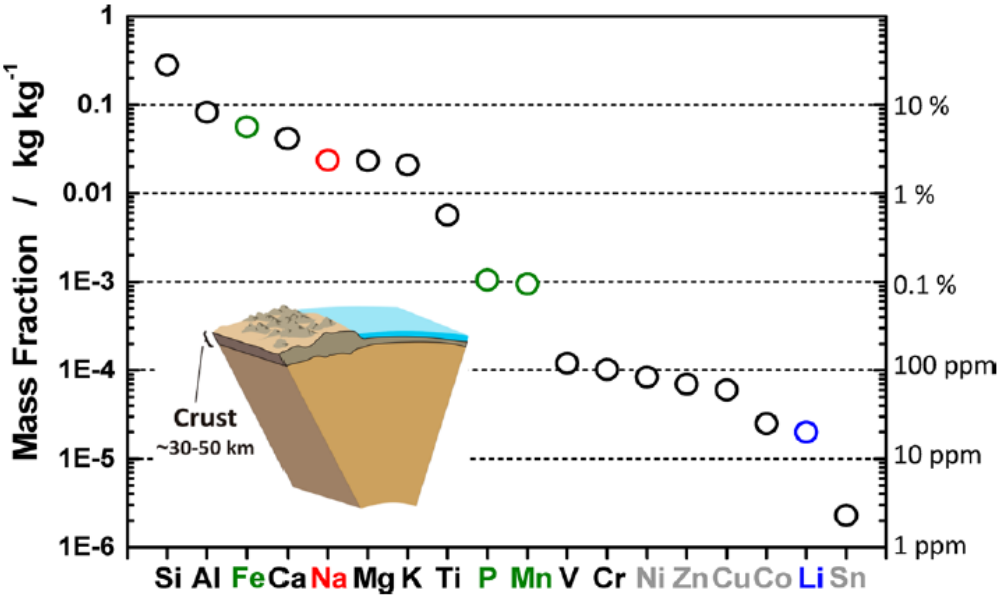

Figure 1.9: Natural abundance of different elements in the earth's crust. Taken from Naoaki Yabuuchi *et al.*[100].

In the first ever reported sodium-oxygen (Na-O_2) battery, Peled *et al.*[101] proposed liquid sodium metal as an alternative to the aforementioned issues with lithium metal reactivity. The cell operated with a molten sodium anode based on its lower melting point compared to lithium (98 °C). A mixture of polyethylene glycol dimethyl ether/propylene carbonate (90:10) was used as a solid-polymer-

electrolyte. The anodic reaction was not completely reversible and limited cyclability was reported. Sodium peroxide was the proposed discharge product, without however, any further investigation on the nature of the reaction products formed. Nonetheless, the work by Peled *et al.* opened a large field of research which pointed toward Na-O_2 systems as an alternative to the many challenges faced by Li-O_2.

The first ever reported room-temperature Na-O_2 cell used a mixture of alky carbonates (1M sodium hexafluorophosphate in 1:1 v/v EC:DMC) as the non-aqueous electrolyte[102]. Sodium peroxide was observed via selected area electron diffraction (SAED) as the main discharge product upon discharge to 1.5 V. Upon charge to 4.0 V, SAED analysis showed no diffraction peaks from sodium peroxide, indicating that the cell could be successfully recharged. Infra-red analysis showed evidence of sodium carbonate as an electrolyte degradation side reaction. This report by Sun *et al.*[102] already points towards fundamental differences between Na-O_2 batteries and analogous Li-O_2 systems whereas no evidence of an oxygen reduction to peroxide was observed for similar organic carbonate solutions.

In 2012, Hartman *et al.*[103] reported a rechargeable Na-O_2 battery that increased the interest in these systems. Intriguingly, the Na-O_2 battery performed in stark contrast to analogous Li-O_2 batteries, even though lithium and sodium are neighbour elements in the periodic table. The cell reported by Hartmann achieved much higher practical capacities and presented much lower charging overpotential. A reversible one-electron per oxygen process (Eq. 1.10 and 1.11) was the main cell reaction, instead of a two-electron reaction, differing from Li-O_2 cells, in which the peroxide phase is the most widely reported, as LiO_2 is an unstable intermediate.

$$Na^+ + O_2 + e^- \rightarrow NaO_2 \quad 1.10$$

$$NaO_2 \rightarrow Na^+ + O_2 + e^- \quad 1.11$$

Following these investigations, a variety of different discharge products have been reported using similar, or in fact the same, ether based electrolyte in Na-O_2 cells. Most common reaction products are: sodium superoxide (NaO_2)[103-106], sodium peroxide (Na_2O_2)[87, 107-110], dihydrated sodium peroxide ($Na_2O_2 \cdot 2H_2O$)[106, 111-113], sodium carbonate (Na_2CO_3)[107, 111, 114] and sodium hydroxide (NaOH)[111]. Different experimental conditions (oxygen pressure, water content in the electrolyte, among others), a lack of standardisation (different electrochemical cells, different drying procedure for carbon cathodes, electrolyte and oxygen gas, among others) and possible misidentification of the products are certainly the cause of this different reports. Therefore, a completely confident determination of the discharge product chemistry is a key point of metal-oxygen research.

The factors that can steer the reaction towards a one-electron or a two-electron process are not yet completely understood. From a thermodynamic point of view, Na_2O_2 ($\Delta_rG° = -449.7$ kJ mol^{-1}) and NaO_2 ($\Delta_rG° = -437.15$ kJ mol^{-1}) can both compete between each other based on similar standard Gibbs reaction energy. Sodium peroxide is actually the preferential phase and is expected to form at higher potentials, whilst sodium superoxide is obtained at extreme conditions (high O_2 pressures and high temperatures, or in liquid ammonia)[115].

The equilibrium between different sodium and oxygen phases is affected by the oxygen activity (i.e. partial pressure). Kang *et al.*[116] reported that NaO_2 is the favoured product at standard conditions, while Na_2O_2 would be preferable at low

oxygen pressure. Electrolytes such as ionic liquids, that have low oxygen solubility, could favour the two electron reaction. It was also reported a lower surface energy for nano-sized NaO_2, while Na_2O_2 would be more stable in the bulk (Figure 1.10). A transition between the two oxide phases was reported by Aldous *et al.*[117] by varying the donicity of the solvent. Low donor number solvents would induce a consecutive reduction of surface bound superoxide, while high donor number would increase the solubility of NaO_2 and favour a solution route one electron process.

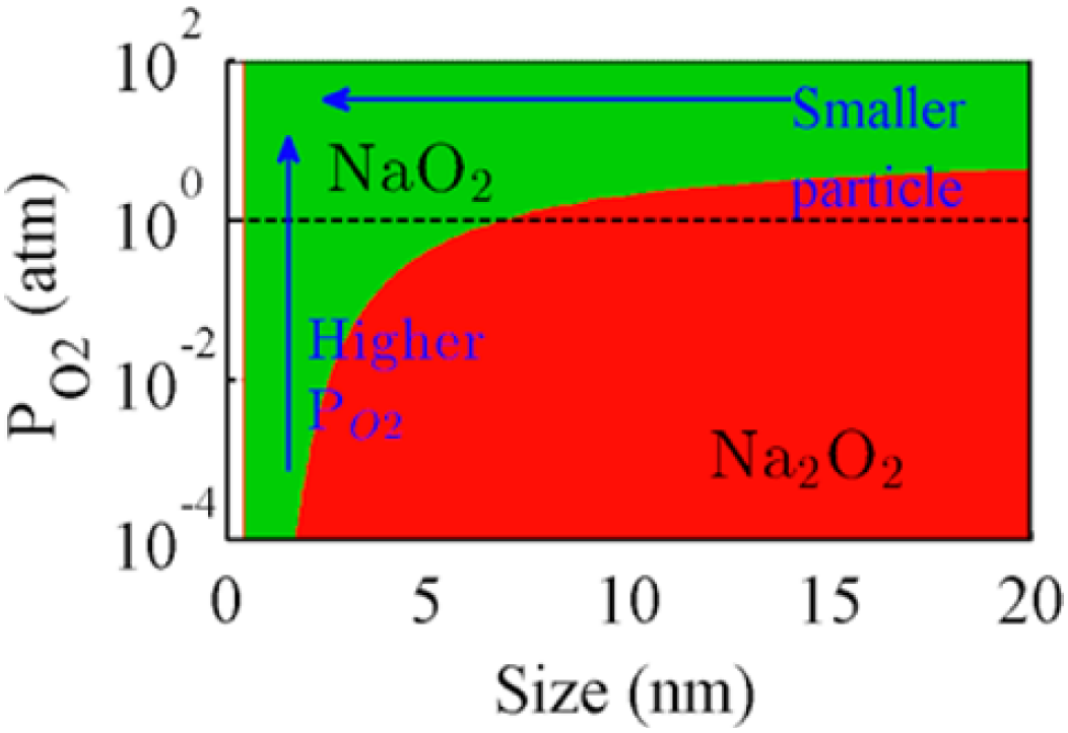

Figure 1.10: Stability phase diagram of sodium oxides based on O_2 partial pressure and particle size. Taken from Shin Y. Kang *et al.*[116].

Aiming for high power devices, a Na-O_2 battery based on peroxide formation and decomposition is actually more desirable since higher theoretical energy densities are expected for this system (4482 Wh l^{-1} for Na_2O_2 in comparison

to 2438 Wh l^{-1} for NaO_2). However, the advantages of Na-O_2 over Li-O_2 cells have only been reported when the cell chemistry favours the formation/decomposition of sodium superoxide. Sodium peroxide based cells suffer from similar shortcomings as do Li-O_2 cells, mainly high overpotentials and sluggish kinetics. The use of electrocatalysts have been proposed to aid the peroxide oxidation[118].

Although initial promising results were reported for the Na-O_2 battery, many challenges still remain to be solved. The low polarisation and high coulombic efficiency does not translate into good cyclability. Poor cycle life can be related to instability of cell components (electrolyte, binder, and carbon), moisture contamination or accumulation of insulating reaction products. Most reported practical capacities are much below desired values to compete with existing technologies, such as Li-ion. The reasons for the low capacity reported related to early death of the cell are not yet fully understood as well as the growth mechanism of NaO_2 precipitates. Optimised cathode designs in terms surface area and porosity need to be developed to enhance cell performance.

1.6 Potassium-oxygen batteries

Concomitant to the report by Hartmann *et al.*[103] of a rechargeable sodium-oxygen battery, Ren *et al.*[119] developed a similar potassium system. The K-O_2 cell presented a similar electrochemical behaviour to sodium and differing from lithium cells. Galvanostatic cycling followed the formation and decomposition of KO_2 (Eq. 1.12 and 1.13) with even lower charge overpotential ($\leq$ 50 mV) and higher coulombic efficiency than other AM-O_2 cells. The superior performance is explained by the higher stability of KO_2, which is both thermodynamic and kinetically stable in contrast to LiO_2 and NaO_2 (the latter is only thermodynamically stable and the former is neither). For this reason, KO_2 is commonly used as a source of $O_2^{\bullet-}$ in solution for the investigation of the stability of cell components, such as electrolyte binder and carbon cathode[76,78].

$$K^+ + O_2 + e^- \rightarrow KO_2 \qquad 1.12$$

$$KO_2 \rightarrow K^+ + O_2 + e^- \qquad 1.13$$

Different from the reaction products in lithium and sodium oxygen batteries, potassium superoxide is a semiconductor at room temperature (>10 S cm^{-1})[120], which also explains the lower voltage hysteresis of the cell. Another advantage is the larger radius (r = 2.2 Å) and Lewis acidity of potassium ions, which permits the stabilisation of the [K^+--$O_2^{\bullet-}$] ion pair in solution based on the hard soft acid base theory (HSAB)[48]. In fact, the addition of potassium salts has been proposed as an

alternative to promote the desired solution route in Li-O_2 batteries and facilitating the ORR[121].

As can be expected, the reactivity of potassium metal anode and safety issues are the major hurdles for the progress of K-O_2 batteries. The higher electropositivity of potassium can induce reductive instabilities with the electrolyte and the large radius complicates the plating of the metal anode upon charge.

Ren *et al.*[122] reported a high degree of oxygen crossover during cell operation, forming an insulating layer composed of potassium superoxide, potassium carbonate and potassium hydroxide. The increase in charge transfer resistance across the electrode/electrolyte interface limited the cycle life of the battery.

Investigating the formation of more stable solid electrolyte interphases or developing safer and reliable anode alternatives to elemental potassium are necessary to develop potassium energy storage systems.

1.7 Aims

The overall aim of this thesis was the development of next generation non-aqueous room-temperature alkali-metal oxygen batteries, which are attractive energy storage devices based on unsurpassed specific energy density. In the lithium-oxygen system, extensive literature investigation identified electrolyte instabilities and cathode oxidative decomposition as the main hurdles to overcome. Therefore, the specific aim for this systems is mitigating the large voltage polarisation originating from the aforementioned parasitic reactions.

Rechargeable sodium-oxygen and potassium-oxygen batteries offer a promising alternative for the issues associated with the lithium system since much lower overpotentials are obtained upon cycling. However, much less is known about the cell chemistry resulting in different discharge products, the capacity limiting parameters and the stability of the cell components. Therefore, the specific aim for these superoxide based batteries is to investigate the aforementioned questions, as well as the stability of the metal anode against reactive oxygen reduced species, which is a more relevant matter in sodium and potassium batteries.

1.8 References

1. N. S. Lewis, *MRS Bull.*, 2007, **32**, 808-820.
2. D. Larcher and J.-M. Tarascon, *Nat. Chem.*, 2015, **7**, 19-29.
3. B. Scrosati, J. Hassoun and Y.-K. Sun, *Energ. Environ. Sci.*, 2011, **4**, 3287-3295.
4. A. Volta, *Philos. Trans. R. Soc. London*, 1800, 403-431.
5. D. Aurbach, *J. Electrochem. Soc.*, 2017, **164**, Y1-Y1.
6. Y. Nishi, *Chem. Rec.*, 2001, **1**, 406-413.
7. K. Abraham, *J. Phys. Chem. Lett*, 2015, **6**, 830-844.
8. B. Scrosati, *J. Electrochem. Soc.*, 1992, **139**, 2776-2781.
9. M. S. Whittingham, *J. Electrochem. Soc.*, 1976, **123**, 315-320.
10. M. S. Whittingham, *Chem. rev.*, 2004, **104**, 4271-4302.
11. K. Xu, *Chem. Rev.*, 2004, **104**, 4303-4418.
12. B. J. Landi, M. J. Ganter, C. D. Cress, R. A. DiLeo and R. P. Raffaelle, *Energ. Environ. Sci.*, 2009, **2**, 638-654.
13. J. Janek and W. G. Zeier, *Nat. Energy*, 2016, **1**, 16141.
14. M. M. Thackeray, S.-H. Kang, C. S. Johnson, J. T. Vaughey, R. Benedek and S. Hackney, *J. Mater. Chem.*, 2007, **17**, 3112-3125.
15. M. Iftekhar, N. Drewett, A. Armstrong, D. Hesp, F. Braga, S. Ahmed and L. Hardwick, *J. Electrochem. Soc.*, 2014, **161**, A2109-A2116.
16. M. Yoshio, T. Konishi, Y. Todorov and H. Noguchi, *Electrochemistry*, 2000, **68**, 412-414.
17. J. Cho, Y. Kim and M. G. Kim, *J. Phys. Chem. C*, 2007, **111**, 3192-3196.
18. C. Liu, Z. G. Neale and G. Cao, *Mater. Today*, 2016, **19**, 109-123.
19. A. S. Aricò, P. Bruce, B. Scrosati, J.-M. Tarascon and W. Van Schalkwijk, *Nat. Mat.*, 2005, **4**, 366-377.
20. P. G. Bruce, B. Scrosati and J. M. Tarascon, *Angew. Chem. -Int. Edit.*, 2008, **47**, 2930-2946.
21. Z. Chen, I. Belharouak, Y. K. Sun and K. Amine, *Adv. Funct. Mater.*, 2013, **23**, 959-969.

22. Z. Sun, Z. Chen, Q. Fu and X. Jiang, IOP Conference Series: Materials Science and Engineering, 2017.
23. L. Grande, E. Paillard, J. Hassoun, J. B. Park, Y. J. Lee, Y. K. Sun, S. Passerini and B. Scrosati, *Adv. Mater.*, 2015, **27**, 784-800.
24. O. Energy, *Next Generation Battery Technology. Lithium sulfur: an energy revolution*, https://oxisenergy.com/, Accessed 12/10/2017, 2017.
25. S. Power, *Drive farther. Enabling a new era of electrified trasnportation solutions*, http://www.sionpower.com/, Accessed 12/10/2017, 2017.
26. R. Rauh, K. Abraham, G. Pearson, J. Surprenant and S. Brummer, *J. Electrochem. Soc.*, 1979, **126**, 523-527.
27. Bhaskara, R. M. L.; Patent, U. S., Ed. 1968; Vol. US3413154 A.
28. W. Kang, N. Deng, J. Ju, Q. Li, D. Wu, X. Ma, L. Li, M. Naebe and B. Cheng, *Nanoscale*, 2016, **8**, 16541-16588.
29. Y. Jiao, W. Chen, T. Lei, L. Dai, B. Chen, C. Wu and J. Xiong, *Nanoscale Res. Lett.*, 2017, **12**, 195.
30. Q. Pang, X. Liang, C. Y. Kwok and L. F. Nazar, *Nat. Energy*, 2016, **1**, 16132.
31. S. Evers and L. F. Nazar, *Accounts Chem. Res.*, 2012, **46**, 1135-1143.
32. J. Song, M. L. Gordin, T. Xu, S. Chen, Z. Yu, H. Sohn, J. Lu, Y. Ren, Y. Duan and D. Wang, *Angew. Chem. -Int. Edit.*, 2015, **54**, 4325-4329.
33. D. Aurbach, B. D. McCloskey, L. F. Nazar and P. G. Bruce, *Nat. Energy*, 2016, **1**, 16128.
34. T. Zhang, N. Imanishi, Y. Takeda and O. Yamamoto, *Chem. Lett.*, 2011, **40**, 668-673.
35. Y. Wang and H. Zhou, *J. Power Sources*, 2010, **195**, 358-361.
36. J. Kumar and B. Kumar, *J. Power Sources*, 2009, **194**, 1113-1119.
37. L. J. Hardwick and P. G. Bruce, *Curr. Opin. Solid State Mater. Sci.*, 2012, **16**, 178-185.
38. G. Girishkumar, B. McCloskey, A. Luntz, S. Swanson and W. Wilcke, *J. Phys. Chem. Lett.*, 2010, **1**, 2193-2203.
39. N. Imanishi, A. C. Luntz and P. Bruce, *The lithium air battery: fundamentals*, Springer Science & Business Media, 2014.

40. K. F. Blurton and A. F. Sammells, *J. Power Sources*, 1979, **4**, 263-279.
41. K. Abraham and Z. Jiang, *J. Electrochem. Soc.*, 1996, **143**, 1-5.
42. J. Read, *J. Electrochem. Soc.*, 2002, **149**, A1190-A1195.
43. T. Ogasawara, A. Débart, M. Holzapfel, P. Novák and P. G. Bruce, *J. Am. Chem. Soc*, 2006, **128**, 1390-1393.
44. C. O. Laoire, S. Mukerjee, K. Abraham, E. J. Plichta and M. A. Hendrickson, *J. Phys. Chem. C*, 2010, **114**, 9178-9186.
45. B. D. Adams, C. Radtke, R. Black, M. L. Trudeau, K. Zaghib and L. F. Nazar, *Energy Environ. Sci.*, 2013, **6**, 1772-1778.
46. L. Johnson, C. Li, Z. Liu, Y. Chen, S. A. Freunberger, P. C. Ashok, B. B. Praveen, K. Dholakia, J.-M. Tarascon and P. G. Bruce, *Nat. Chem.*, 2014, **6**, 1091-1099.
47. Z. Peng, S. A. Freunberger, L. J. Hardwick, Y. Chen, V. Giordani, F. Bardé, P. Novák, D. Graham, J. M. Tarascon and P. G. Bruce, *Angew Chem.*, 2011, **123**, 6475-6479.
48. C. O. Laoire, S. Mukerjee, K. Abraham, E. J. Plichta and M. A. Hendrickson, *J. Phys. Chem. C*, 2009, **113**, 20127-20134.
49. J. Hummelshøj, A. Luntz and J. Nørskov, *J. Chem. Phys.*, 2013, **138**, 034703.
50. B. D. McCloskey, A. Valery, A. C. Luntz, S. R. Gowda, G. M. Wallraff, J. M. Garcia, T. Mori and L. E. Krupp, *J. Phys. Chem. Lett.*, 2013, **4**, 2989-2993.
51. V. Gutmann, *Electrochim. Acta*, 1976, **21**, 661-670.
52. W. A. Henderson, *J. Phys. Chem. B*, 2006, **110**, 13177-13183.
53. R. Younesi, M. Hahlin, F. Björefors, P. Johansson and K. Edström, *Chem. Mater.*, 2012, **25**, 77-84.
54. F. Mizuno, S. Nakanishi, Y. Kotani, S. Yokoishi and H. Iba, *Electrochemistry*, 2010, **78**, 403-405.
55. S. A. Freunberger, Y. Chen, Z. Peng, J. M. Griffin, L. J. Hardwick, F. Bardé, P. Novák and P. G. Bruce, *J. Am. Chem. Soc*, 2011, **133**, 8040-8047.

56. V. S. Bryantsev, V. Giordani, W. Walker, M. Blanco, S. Zecevic, K. Sasaki, J. Uddin, D. Addison and G. V. Chase, *J. Phys. Chem. A*, 2011, **115**, 12399-12409.
57. K. U. Schwenke, S. Meini, X. Wu, H. A. Gasteiger and M. Piana, *Phys. Chem. Chem. Phys.*, 2013, **15**, 11830-11839.
58. S. A. Freunberger, Y. Chen, N. E. Drewett, L. J. Hardwick, F. Bardé and P. G. Bruce, *Angew. Chem. -Int. Edit.*, 2011, **50**, 8609-8613.
59. J. Read, *J. Electrochem. Soc.*, 2006, **153**, A96-A100.
60. H.-G. Jung, J. Hassoun, J.-B. Park, Y.-K. Sun and B. Scrosati, *Nat. Chem.*, 2012, **4**, 579-585.
61. B. D. Adams, R. Black, Z. Williams, R. Fernandes, M. Cuisinier, E. J. Berg, P. Novak, G. K. Murphy and L. F. Nazar, *Adv. Energy Mater.*, 2015, **5**.
62. Y. Chen, S. A. Freunberger, Z. Peng, F. Bardé and P. G. Bruce, *J. Am. Chem. Soc*, 2012, **134**, 7952-7957.
63. H. Wang, K. Xie, L. Wang and Y. Han, *J. Power Sources*, 2012, **219**, 263-271.
64. D. Sharon, M. Afri, M. Noked, A. Garsuch, A. A. Frimer and D. Aurbach, *J. Phys. Chem. Lett.*, 2013, **4**, 3115-3119.
65. D. G. Kwabi, T. P. Batcho, C. V. Amanchukwu, N. Ortiz-Vitoriano, P. Hammond, C. V. Thompson and Y. Shao-Horn, *J. Phys. Chem. Lett.*, 2014, **5**, 2850-2856.
66. Z. Peng, S. A. Freunberger, Y. Chen and P. G. Bruce, *Science*, 2012, **337**, 563-566.
67. M. M. O. Thotiyl, S. A. Freunberger, Z. Peng, Y. Chen, Z. Liu and P. G. Bruce, *Nat. Mater.*, 2013, **12**, 1050.
68. W. Walker, V. Giordani, J. Uddin, V. S. Bryantsev, G. V. Chase and D. Addison, *J. Am. Chem. Soc*, 2013, **135**, 2076-2079.
69. L. Cecchetto, M. Salomon, B. Scrosati and F. Croce, *J. Power Sources*, 2012, **213**, 233-238.
70. H. Nakamoto, Y. Suzuki, T. Shiotsuki, F. Mizuno, S. Higashi, K. Takechi, T. Asaoka, H. Nishikoori and H. Iba, *J. Power Sources*, 2013, **243**, 19-23.
71. T. Zhang and H. Zhou, *Angew. Chem.*, 2012, **124**, 11224-11229.

72. R. Younesi, P. Norby and T. Vegge, *ECS Electrochem. Lett.*, 2014, **3**, A15-A18.
73. B. McCloskey, A. Speidel, R. Scheffler, D. Miller, V. Viswanathan, J. Hummelshøj, J. Nørskov and A. Luntz, *J. Phys. Chem. Lett.*, 2012, **3**, 997-1001.
74. M. M. O. Thotiyl, S. A. Freunberger, Z. Peng and P. G. Bruce, *J. Am. Chem. Soc*, 2013, **135**, 494-500.
75. B. D. McCloskey, R. Scheffler, A. Speidel, D. S. Bethune, R. M. Shelby and A. Luntz, *J. Am. Chem. Soc*, 2011, **133**, 18038-18041.
76. R. Black, S. H. Oh, J.-H. Lee, T. Yim, B. Adams and L. F. Nazar, *J. Am. Chem. Soc*, 2012, **134**, 2902-2905.
77. R. Younesi, M. Hahlin, M. Treskow, J. Scheers, P. Johansson and K. Edström, *J. Phys. Chem. C*, 2012, **116**, 18597-18604.
78. E. Nasybulin, W. Xu, M. H. Engelhard, Z. Nie, X. S. Li and J.-G. Zhang, *J. Power Sources*, 2013, **243**, 899-907.
79. V. Viswanathan, K. S. Thygesen, J. Hummelshøj, J. K. Nørskov, G. Girishkumar, B. McCloskey and A. Luntz, *J. Chem. Phys.*, 2011, **135**, 214704.
80. Y. Wang and S. C. Cho, *J. Electrochem. Soc.*, 2013, **160**, A1847-A1855.
81. S. Meini, M. Piana, H. Beyer, J. Schwämmlein and H. A. Gasteiger, *J. Electrochem. Soc.*, 2012, **159**, A2135-A2142.
82. N. Ding, S. W. Chien, T. A. Hor, R. Lum, Y. Zong and Z. Liu, *J. Mater. Chem.*, 2014, **2**, 12433-12441.
83. X.-h. Yang, P. He and Y.-y. Xia, *Electrochem. Commun.*, 2009, **11**, 1127-1130.
84. D. M. Itkis, D. A. Semenenko, E. Y. Kataev, A. I. Belova, V. S. Neudachina, A. P. Sirotina, M. Hävecker, D. Teschner, A. Knop-Gericke and P. Dudin, *Nano Lett.*, 2013, **13**, 4697-4701.
85. A. I. Belova, D. G. Kwabi, L. V. Yashina, Y. Shao-Horn and D. M. Itkis, *J. Phys. Chem. C*, 2017, **121**, 1569-1577.
86. J. Lu, Y. Lei, K. C. Lau, X. Luo, P. Du, J. Wen, R. S. Assary, U. Das, D. J. Miller and J. W. Elam, *Nat. Commun.*, 2013, **4**, ncomms3383.

87. Y. Li, H. Yadegari, X. Li, M. N. Banis, R. Li and X. Sun, *Chem. Commun.*, 2013, **49**, 11731-11733.
88. Y. Chen, S. A. Freunberger, Z. Peng, O. Fontaine and P. G. Bruce, *Nat. Chem.*, 2013, **5**, 489-494.
89. B. J. Bergner, A. Schürmann, K. Peppler, A. Garsuch and J. r. Janek, *J. Am. Chem. Soc*, 2014, **136**, 15054-15064.
90. H. D. Lim, H. Song, J. Kim, H. Gwon, Y. Bae, K. Y. Park, J. Hong, H. Kim, T. Kim and Y. H. Kim, *Angew. Chem. -Int. Edit.*, 2014, **53**, 3926-3931.
91. W.-J. Kwak, D. Hirshberg, D. Sharon, H.-J. Shin, M. Afri, J.-B. Park, A. Garsuch, F. F. Chesneau, A. A. Frimer and D. Aurbach, *J. Mater. Chem.*, 2015, **3**, 8855-8864.
92. M. J. Lacey, J. T. Frith and J. R. Owen, *Electrochem. Commun.*, 2013, **26**, 74-76.
93. X. Gao, Y. Chen, L. Johnson and P. G. Bruce, *Nat. Mater.*, 2016, **15**, 882-888.
94. X. Gao, Y. Chen, L. R. Johnson, Z. P. Jovanov and P. G. Bruce, *Nat. Energy*, 2017, **2**, 17118.
95. K. Zhang, G. H. Lee, M. Park, W. Li and Y. M. Kang, *Adv. Energy Mater.*, 2016.
96. D. Lin, Y. Liu and Y. Cui, *Nat. Nanotechnol.*, 2017, **12**, 194-206.
97. R. S. Assary, J. Lu, P. Du, X. Luo, X. Zhang, Y. Ren, L. A. Curtiss and K. Amine, *ChemSusChem*, 2013, **6**, 51-55.
98. S. Choudhury, C. T.-C. Wan, W. I. Al Sadat, Z. Tu, S. Lau, M. J. Zachman, L. F. Kourkoutis and L. A. Archer, *Sci. Adv.*, 2017, **3**, e1602809.
99. F. Ding, W. Xu, G. L. Graff, J. Zhang, M. L. Sushko, X. Chen, Y. Shao, M. H. Engelhard, Z. Nie and J. Xiao, *J. Am. Chem. Soc*, 2013, **135**, 4450-4456.
100. N. Yabuuchi, K. Kubota, M. Dahbi and S. Komaba, *Chem. Rev.*, 2014, **114**, 11636-11682.
101. E. Peled, D. Golodnitsky, H. Mazor, M. Goor and S. Avshalomov, *J. Power Sources*, 2011, **196**, 6835-6840.
102. Q. Sun, Y. Yang and Z.-W. Fu, *Electrochem. Commun.*, 2012, **16**, 22-25.

103. P. Hartmann, C. L. Bender, M. Vračar, A. K. Dürr, A. Garsuch, J. Janek and P. Adelhelm, *Nat. Mater.*, 2013, **12**, 228-232.
104. P. Hartmann, C. L. Bender, J. Sann, A. K. Dürr, M. Jansen, J. Janek and P. Adelhelm, *Phys. Chem. Chem. Phys.*, 2013, **15**, 11661-11672.
105. B. D. McCloskey, J. M. Garcia and A. C. Luntz, *J. Phys. Chem. Lett.*, 2014, **5**, 1230-1235.
106. N. Zhao, C. Li and X. Guo, *Phys. Chem. Chem. Phys.*, 2014, **16**, 15646-15652.
107. S. K. Das, S. Xu and L. A. Archer, *Electrochem. Commun.*, 2013, **27**, 59-62.
108. W. Liu, Q. Sun, Y. Yang, J.-Y. Xie and Z.-W. Fu, *Chem. Commun.*, 2013, **49**, 1951-1953.
109. W.-M. Liu, W.-W. Yin, F. Ding, L. Sang and Z.-W. Fu, *Electrochem. Commun.*, 2014, **45**, 87-90.
110. W.-W. Yin and Z.-W. Fu, *Chem. Commun.*, 2017, **53**, 1522-1525.
111. J. Kim, H.-D. Lim, H. Gwon and K. Kang, *Phys. Chem. Chem. Phys.*, 2013, **15**, 3623-3629.
112. Z. Jian, Y. Chen, F. Li, T. Zhang, C. Liu and H. Zhou, *J. Power Sources*, 2014, **251**, 466-469.
113. H. Yadegari, Y. Li, M. N. Banis, X. Li, B. Wang, Q. Sun, R. Li, T.-K. Sham, X. Cui and X. Sun, *Energy Environ. Sci.*, 2014, **7**, 3747-3757.
114. N. Zhao and X. Guo, *J. Phys. Chem. C*, 2015, **119**, 25319-25326.
115. C. L. Bender, P. Hartmann, M. Vračar, P. Adelhelm and J. Janek, *Adv. Energy Mater.*, 2014, **4**.
116. S. Kang, Y. Mo, S. P. Ong and G. Ceder, *Nano Lett.*, 2014, **14**, 1016-1020.
117. I. M. Aldous and L. J. Hardwick, *Angew. Chem. -Int Edit.*, 2016, **55**, 8254-8257.
118. W.-W. Yin, Z. Shadike, Y. Yang, F. Ding, L. Sang, H. Li and Z.-W. Fu, *Chem. Commun.*, 2015, **51**, 2324-2327.
119. X. Ren and Y. Wu, *J. Am. Chem. Soc*, 2013, **135**, 2923-2926.
120. A. U. Khan and S. Mahanti, *J. Chem. Phys.*, 1975, **63**, 2271-2278.

121. I. Landa-Medrano, M. Olivares-Marín, B. Bergner, R. Pinedo, A. Sorrentino, E. Pereiro, I. Ruiz de Larramendi, J. r. Janek, T. Rojo and D. Tonti, *J. Phys. Chem. C*, 2017, **121**, 3822-3829.
122. X. Ren, K. C. Lau, M. Yu, X. Bi, E. Kreidler, L. A. Curtiss and Y. Wu, *ACS Appl. Mater. Inter.*, 2014, **6**, 19299-19307.

Chapter 2.
Experimental Procedures and Techniques

2.1 Experimental procedures

2.1.1 Chemicals and materials

Following is a list of all chemicals and materials utilised throughout this thesis: diethylene glycol dimethyl ether (anhydrous 99.5% Sigma-Aldrich), molecular sieves (4 Å, Sigma-Aldrich), Lithium bis (trifluoromethanesulfonyl)imide (99.95%, Sigma-Aldrich), 1, 4-diazabicyclo [2.2.2] octane (> 99%, Sigma-Aldrich), carbon black Super C65 (Imerys), poly(tetrafluoroethylene) (60 wt% dispersion in H_2O, Sigma-Aldrich), carbon fibre paper P50 (Avcarb), glass fibre separators GF-G grade (Whatmann), Lithium (ribbon 99.9%, Aldrich), LiSICON (Ohara glass), oxygen (N5 purity, 99.999%, BOC), phosphorous pentoxide (99.99% Sigma-Aldrich), propylene carbonate (99%, Sigma-Aldrich), 1,2 dimethoxyethane (99.5%, Sigma-Aldrich), tetraethylene glycol dimethyl ether (99.5%, Sigma-Aldrich), calcium hydride (99.9%, Sigma-Aldrich), sodium hexafluorophosphate (99%, Sigma-Aldrich), sodium trifluoromethanesulfonate (98%, Sigma-Aldrich), gas diffusion layer H24 (Freudenberg & Co.), graphite felt GFD 2.5EA (SGL Group), single wall carbon nanotube (Elicarb), conductive carbon black Ketjenblack EC 600 JD (AkzoNobel), Kynarflex (Arkema), carboxymethylcellulose sodium salt (Sigma-Aldrich), Sodium (ACS reagent dry, Sigma-Aldrich), sodium peroxide (ACS reagent, >93%,

Sigma-Aldrich), 1-butyl-1-methylpyrrolidinium bis(trifluoromethylsulfonyl)imide (99%, ion-li-tec), potassium hexafluorophosphate (>99.5%, Aldrich), potassium trifluoromethanesulfonate (98%, Sigma-Aldrich), potassium bis (fluorosulfonyl)imide (95%, Combi-Blocks) and potassium bis (trifluoromethanesulfonyl)imide (99.5%, Solvionics), potassium (chunks in mineral oil, 98%, Sigma-Aldrich), potassium hydroxide (Sigma-Aldrich), antimony (~100 mesh, Sigma-Aldrich), ethylene carbonate (anhydrous 99%, Sigma-Aldrich), diethyl carbonate (anhydrous >99.5%, Sigma-Aldrich).

2.1.2 Purification and drying techniques

Water contamination significantly affects the performance of AM-O_2 cells, not only by reacting vigorously with the metal anode, but also changing the discharge mechanism of the cell. Unless it is the purpose of the investigation, water concentration in the electrolyte should be kept to a minimum. In AM-O_2 cells, main sources of water contamination will be the organic solvent, the supporting salt and oxygen gas.

Diethylene glycol dimethyl ether and tetraethylene glycol dimethyl ether were refluxed with calcium hydride and distilled under reduced pressure[1]. All solvents were dried for at least one week over freshly activated molecular sieves (4 Å). The sieves were activated by heating under vacuum at 300°C for at least 12 hours. The support salts were dried by heating at 120°C under vacuum for at least 12 hours prior to electrolyte preparation. Both solvents and salts were stored inside an argon filled glovebox. The glovebox was kept at water content < 0.1 ppm and

O_2 content < 0.1 ppm throughout the experiments. High purity oxygen (99.999%) was used for the study of alkali metal-oxygen batteries and dried using a packed column of phosphorous pentoxide connected to the gas line.

The final water content was determined by Karl Fischer titration (Mettler-Toledo). Typically, the titration was performed using 1 ml of solvent of known density. The water content of solvents was found to be <1 ppm. The electrolyte titration was performed by weight/volume and was found to be <10 ppm. The water content of ionic liquid electrolytes, used in Chapter 5 – section 5.44, was found to be <30 ppm.

2.1.3 Electrode preparation

Two types of carbon electrodes were employed as cathodes in AM-O_2 cells: binder free gas diffusion layer (GDL) and composite electrodes. GDL electrodes are composed of carbon fibres pressed together into a paper, typically employed in fuel cells. Owing to their light well defined morphology and high gas permeability, GDLs are being utilised in fundamental studies in AM-O_2 cells. The GDL electrodes were cut into 10 mm diameter discs and washed with acetone and ethanol to remove any carbon powder. Finally the electrodes were dried under vacuum at 120°C and transferred to the glovebox without atmosphere exposure.

The composite electrodes were prepared by mixing different carbon materials with PTFE binder (mass ratio 70/30% or 80/20%) mixed into a slurry by adding acetone. The result putty like mixture was put in a calender and pressed to a thickness of 100 μm to obtain self-supporting films. The electrodes were punched

into 10 mm discs, then dried at 120 °C under vacuum for at least 12 hours and transferred to the glovebox without atmosphere exposure. Figure 2.1 shows a photograph and an SEM image of a typical carbon black composite electrode. For the investigation of the stability of different polymeric binders, the same casting procedure was utilised substituting PTFE for PVDF and CMC.

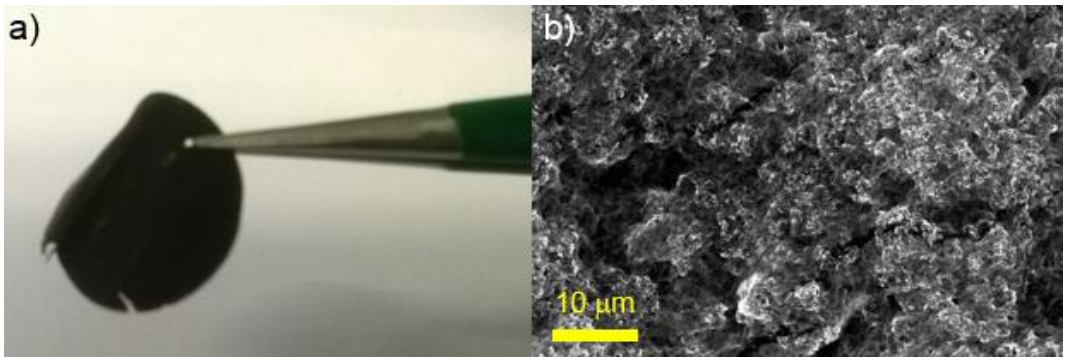

Figure 2.1: a) photograph and b) SEM image of a self-supported carbon black electrode.

Specifically for the discussion in Chapter 3 – section 3.4.1, hypercrosslinked polymer carbons (HCPC) were utilised to fabricate porous electrodes. The synthesis of HCPCs was performed by Jet-Sing M. Lee at the University of Liverpool. Hypercrosslinked polymers were obtained via a one-step Friedel Crafts alkylation of benzene and pyrrole monomers. HCPCs was prepared by heat treatment of the polymers at 900°C (for the compound labelled as HCPC-75) and at 800°C (for the compound labelled as HCPC-54). Nitrogen heteroatom doping was performed by pyrolysation using ammonia as activator (HCPC-54)[2]. The same casting and drying procedure was utilised to fabricate HCPC electrodes.

2.1.4 Swagelok cell assembly

A standardised electrochemical cell has not yet been stablished for AM-O_2 application and most research groups will develop their own setup. The electrochemical testing of Li-O_2, Na-O_2 and K-O_2 systems was performed in a home-built battery-type Swagelok cell, described in Figure 2.2.

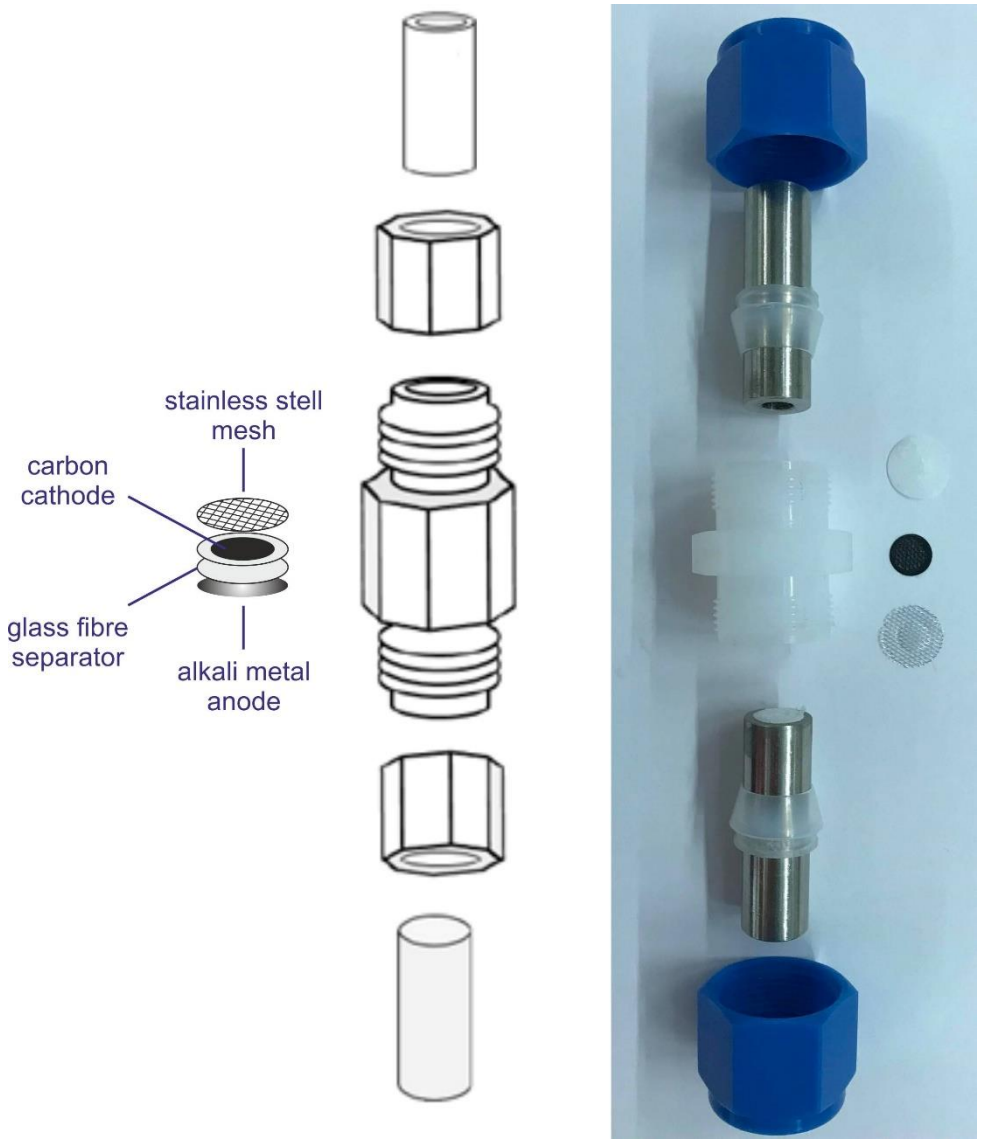

Figure 2.2: Schematics of PFA Swagelok cells used for AM-O_2 electrochemical testing (left). Photograph of cell parts (right).

Swagelok cells were assembled by stacking the metal anode (lithium, sodium or potassium), roll pressed and cut into 0.785 cm^2 discs, two Whatman glass fibre separators (GF-G grade, 470 μm) impregnated with the appropriate electrolyte and the carbon cathode between two stainless steel current collectors. A stainless steel mesh was employed to ensure electric contact through the carbon cathode. The top stainless steel current collector was hollow to expose the cathode to oxygen atmosphere.

Specifically for the investigation of 1, 4-diazabicyclo [2.2.2] octane as an electrolyte additive, discussed in Chapter 3 – section 3.4.2, a LiSICON membrane (Ohara glass) was stacked between the two glass fibre separators. The electrolyte in contact with the metal anode only consisted of solvent and support salt, while 1, 4-diazabicyclo [2.2.2] octane was added to the electrolyte in contact with the cathode.

The Swagelok cells were assembled inside an argon filled glovebox, sealed in an air-tight glass vessel containing two Young's valves (Figure 2.3) and transferred to the gas line for oxygenation. While the cell was under argon atmosphere, the gas line was evacuated for five minutes to remove any residual water contamination. The valves were opened to the gas line and oxygen was allowed into the vessel at 1 atm. Oxygen was flown through the cell for ten minutes and the cell went through an equilibration period until the open circuit potential was stabilised. The electrochemical measurements were performed inside a Memmert oven set to 25°C using a Bio-Logic MPG-2 battery cycler.

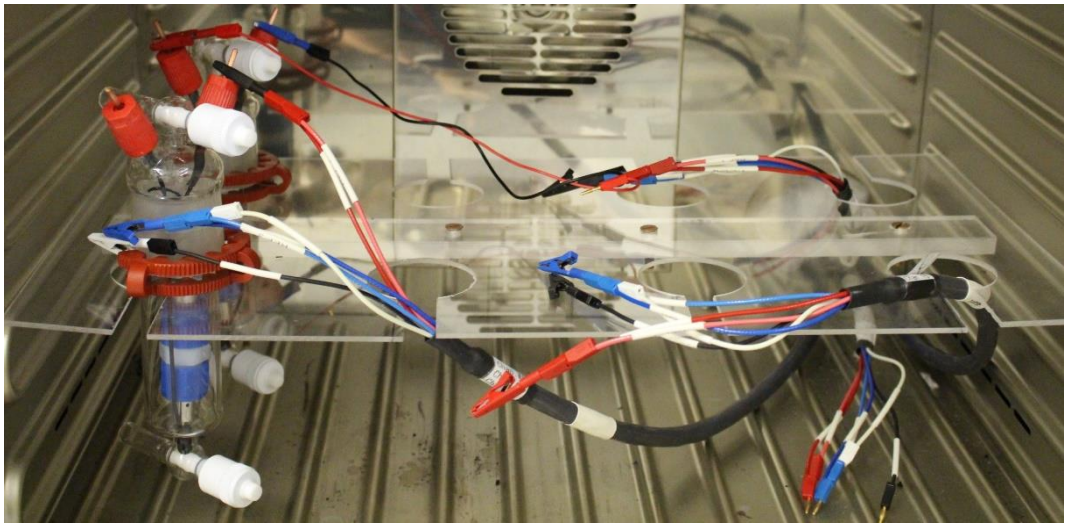

Figure 2.3: Photograph of experimental rig for testing of AM-O_2 cells at controlled temperature (25°C).

2.1.4 Swagelok cell disassembly and analysis

After undergoing galvanostatic cycling, the Swagelok cells were brought inside an argon filled glovebox and disassembled without exposure to the atmosphere. Both cathode and anode were washed with the electrolyte solvent to remove the support salt from the electrode surface. The remaining solvent was removed by drying the electrode under vacuum for at least two hours.

Specifically for the investigation of the stability of NaO_2 in DEGDME electrolyte, discussed in Chapter 4 – section 4.4.7, the cell rested assembled for a period up to 15 hours before being brought to the glovebox. Unless otherwise stated, the disassembly and characterisation of the reaction products was performed immediately after the electrochemical measurements.

Characterisation of the reaction products formed on the cathode was performed by Raman spectroscopy, Fourier transform infrared spectroscopy,

powder X-ray diffraction, scanning electron microscopy, energy dispersive X-ray spectroscopy and atomic force microscopy. Characterisation of the surface layer formed on the metal anode was performed by Raman spectroscopy, Fourier transform infrared spectroscopy and X-ray photo electron spectroscopy.

2.1.5 Sb-C nanocomposite preparation and electrochemical testing

Specifically for the investigation of an antimony-carbon nanocomposite as an anode material for potassium-oxygen batteries, discussed in Chapter 5 – section 5.4.5, galvanostatic cycling was performed using CR2025 type coin cells. The cells were assembled inside an argon filled glovebox (water content < 0.1 ppm and O_2 content < 0.1 ppm) by stacking a potassium metal counter electrode, a Whatman glass fibre separator (GF-G grade, 470 μm) impregnated with the appropriate electrolyte and the antimony working electrode between the stainless steel coin cell cases. Galvanostatic cycling was performed inside a Memmert oven set to 25°C using a Maccor Series 4200 battery cycler.

The antimony-carbon nanocomposite was synthesised via mechanical milling following a procedure described by Qian *et al.*[3]. Commercial antimony (~100 mesh) and conductive carbon black (Super C65, Imerys) were directly ball milled at a 7:3 ratio in a Fritsch Premium Line 7 planetary mill for 22 h at 1000 rpm under ambient atmosphere with zirconia grinding balls (5 mm diameter).

The working electrodes for the coin cell cycling was cast by mixing Sb-C, carbon black and CMC binder in a 64:21:15 ratio in water and casting on a copper current collector. The electrodes were punched into 12 mm diameter discs, then

dried at 80 °C under vacuum for at least 12 hours and transferred to the glovebox without atmosphere exposure. A commercial antimony electrode was cast for comparison using the same procedure.

In situ Raman studies were carried out to gain further insight on the electrochemical processes between Sb-C and potassium. To allow the Raman laser to hit the working electrode through the cell aperture, self-supporting (without current collector) electrodes were cast using 35% CMC and 22% carbon black. The electrodes were punched into 6 mm diameter discs, then dried at 80°C under vacuum for at least 12 hours.

Galvanostatic cycling was performed using a Bio-Logic MPG-2 battery cycler. Raman data was collected using an ECC-Opto-STD, El-Cell GmBH cell which was positioned on top of a motorised stage (Figure 2.4). Data was recorded using a Renishaw in via microscope with a 633 nm laser (2 mW cm^{-2}) focussed through a microscope (Leica) via a 50x objective lens (Leica).

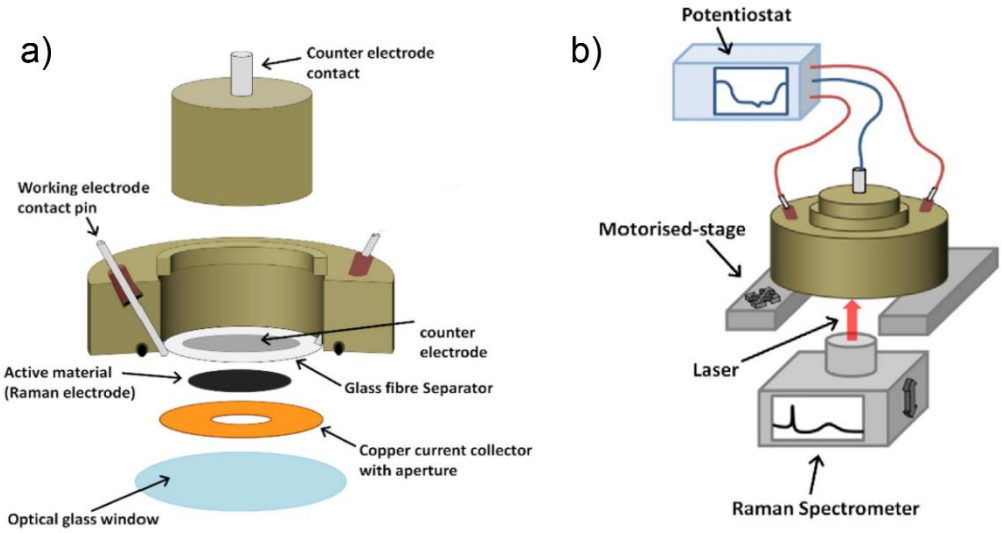

Figure 2.4: a) Schematics of *in situ* Raman apparatus and b) cell positioning during cycling[4].

2.2 Techniques

2.2.1 Cyclic voltammetry

Electrochemistry as a research field is mainly concerned with the correlation of electricity and chemical processes. A central part of electrochemical phenomena is the chemical changes resulting from charge transfer across interfaces and through solution. Cyclic voltammetry is an important tool to probe such phenomena in which the current response of a system is recorded over a cyclic potential ramp (Figure 2.5). The scan rate (ν / V s^{-1}) at which the potential steps are applied is simply defined by the ratio of potential step size (E / V) over time (t / s).

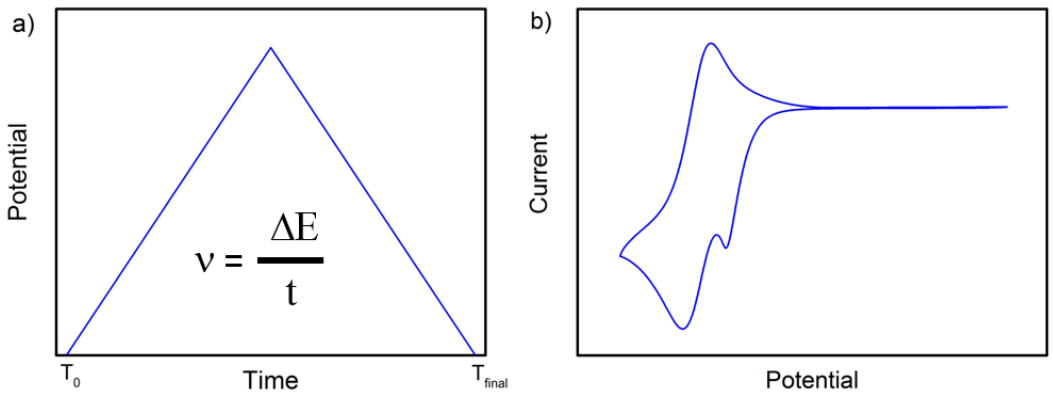

Figure 2.5: a) Example of the applied potential-time signal in a cyclic voltammetry and b) example of a current-potential plot.

The potential applied by an external power source (e.g. potentiostat) will modulate the energy of electrons within the solid electrode, typically a semiconductor material, such as gold, platinum and glassy carbon. When a cathodic sweep is scanned, from high potentials to low potentials, an electroactive species

(O) in solution can be reduced. Charge transfer across the interface will occur when the electrons in the solid phase are in a higher energy level than the LUMO (lowest unoccupied molecular orbital) of O. The oxidation reaction takes place when the scan direction is reversed ($O + ne^- \leftrightarrow R$)[5].

2.2.2 Chronopotentiometry

Chronopotentiometry is an electrochemical technique commonly employed in the evaluation active materials which compose of energy storage devices. A constant current pulse is applied between the working and reference electrodes of the cell, driving electron transfer reactions through the solid/liquid interface causing electroactive species to be reduced/oxidised.

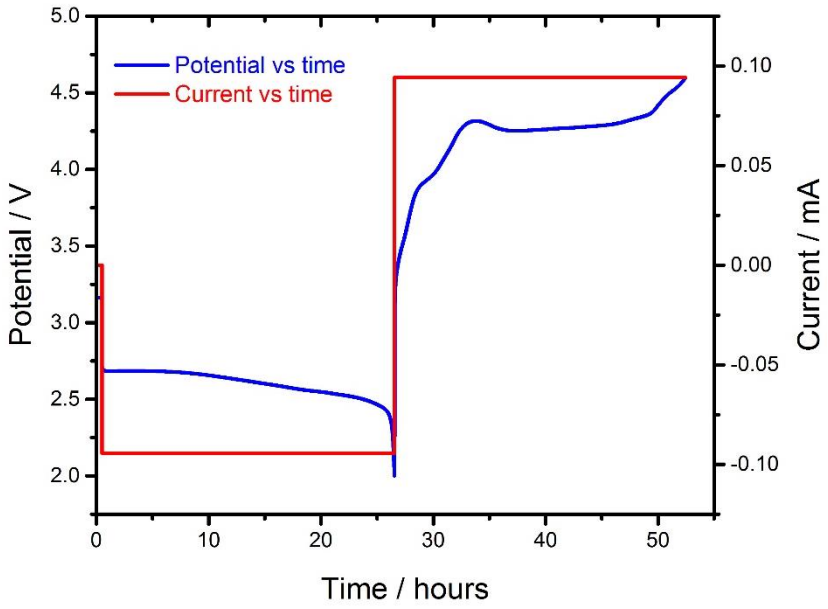

Figure 2.6: Variation of potential and current as a function of time during a chronopotentiometry experiment.

The redox reaction will result in a potential change, which is recorded by the potentiostat. Discharge/charge experiments are performed by cycling the constant current between opposite values after each transition. The potential will change according to the electrochemical reactions taking place on the working electrode interface. When a certain reaction is depleted, the potential will change

until it reaches the thermodynamic potential for the following available reaction. Therefore, it is important to select the potential window in order to include the redox reactions being investigated, but excluding the unwanted oxidation/reduction of the electrolyte components[6].

2.2.3 Relevant principles of electrochemical energy storage

Faraday's law of electrolysis

Faraday's law of electrolysis states that the mass (m) of a material undergoing electrochemical reaction is directly proportional to the electric charge (Q) passed through the cell. Where F is the Faraday's constant (96485 A s mol^{-1}) and n is the number of electrons transferred per mole of a substance with molar mass (M)[7].

$$Q = nF\frac{m}{M} \qquad \text{Eq. 2.1}$$

This relation was relevant for the calculation of the maximum achievable capacity obtained upon discharging sodium-oxygen cells with different carbon cathodes discussed in Chapter 4.

Cell potential

A secondary battery consists of more than one electrochemical cells connected in series. The potential of the cell is determined by the Gibbs free energy of the chemical reactions occurring at the solid/liquid interface. The chemical energy associated with this reaction will be reversibly converted into electrical energy in a secondary battery. A potential difference across solid/liquid interface will arise as a result of the arrangement of ion in solution to compensate the charge in the electrode surface.

The equilibrium cell potential (ΔE) can be calculated by the following equation, in which ΔG_f is the variation of Gibbs free energy.

$$\Delta G_f = -nFE^0 \qquad \text{Eq. 2.2}$$

This relation was relevant for the calculation of the thermodynamic potential for the formation of the desired products in AM-O_2 cells. The formation of Li_2O_2 can be calculated using Eq. 2.2.

ΔG_f (Li_2O_2) = -570.82 kJ mol^{-1} ; n = 2 ; F = 96485 A s mol^{-1} ; E^0 = 2.96 V.

Gravimetric energy density and energy density

The theoretical gravimetric energy density (or specific energy) is the maximum amount of energy a battery can store normalised per unit mass. The theoretical energy density is the maximum amount of energy a battery can store normalised by unit volume. The gravimetric energy density (W_g) is calculated by Eq. 2.3.

$$W_g = \frac{(nF)}{M} E^0 \qquad \text{Eq. 2.3}$$

For a Li-O_2 cells based on the formation of Li_2O_2, W_g is calculated as follows:

W_g = ((2 x 96485 A s mol^{-1})/45.88 g mol^{-1})x 2.96 V) = 3458 Wh kg^{-1}

2.2.4 Fourier transform infrared spectroscopy (FTIR)

Infrared spectroscopy (IR) is an important analytical technique to investigate vibrational properties of chemical species. It involves the absorption of radiation in the infrared frequency range (2 - 12 x 10^{13}Hz) by a sample molecule inducing an excitation between two vibrational energy levels. The result of quantum mechanics formalism indicates that only a limited number of discrete energy levels are allowed (Eq. 2.4)

$$E = (\nu + ½) \cdot h\nu_\nu \qquad \text{Eq. 2.4}$$

in which ν is the vibrational quantum number, h is Plank's constant and ν_ν is the molecular vibrational frequency. Since the selection rule for a harmonic oscillator indicates that only transitions with $\Delta\nu = \pm 1$ are allowed, and most molecular vibrations exclusively occupy the ground state at ambient temperature, the experimentally observed IR absorption results from the $\nu = 0 \rightarrow \nu = 1$ transition, known as the fundamental vibration (Figure 2.7)[8].

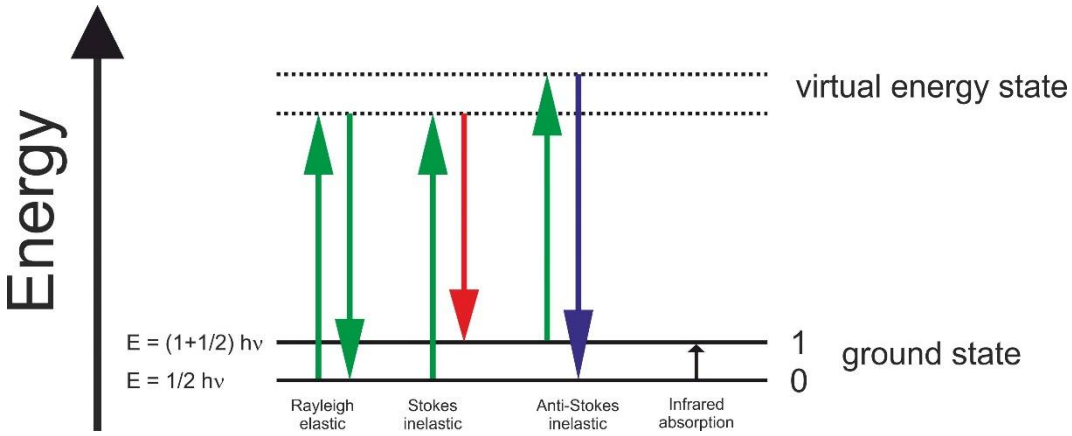

Figure 2.7: Energy level diagram showing Raman scattering and IR absorption.

A typical Infrared spectra is presented as a function of the wavenumber, which is the number of waves in one centimetre, hence the unit of cm^{-1}. IR spectroscopy is extremely useful to identify and differentiate functional groups, because the position of the wavenumber of absorbance is related to the strength of the chemical bond according to Eq. 2.5 derived from the harmonic oscillator model

$$\nu_\nu = \frac{1}{2\pi c}\sqrt{\frac{f}{\mu}} \qquad \text{Eq. 2.5}$$

in which *f* is the force constant, *c* is the velocity of light in vacuum and μ is the reduced mass. A vibrational transition is IR active (observable in the IR spectrum) if it induces a change in the electric dipole moment of a sample molecule[8].

In a Fourier-transform infrared spectrometer, the most common configuration is the Michelson interferometer, an interferogram is obtained as a result of the change in path length between two radiation beams. The IR source emits radiation which is bisected by a beam splitter allowing half of the light to a fixed mirror and half of the light to a moving mirror. This results in a modulated (polychromatic) radiation beam interacting with the sample molecule before reaching the detector[9].

FTIR analysis was utilised to characterise the reaction products formed upon cycling of AM-O_2 cells. FTIR experiments reported henceforth were performed inside a nitrogen filled glovebox using a Nicolet 6700 spectrometer (Thermo Fisher Scientific). Samples were prepared by grinding portions of the cathode or anode into CsI pellets in order to detect vibration modes in the far-infrared region (400 – 10 cm^{-1}). Data was collected in the transmission mode.

2.2.5 Raman spectroscopy

Raman spectroscopy is a vibrational spectroscopy technique which involves the excitation of a sample molecule with monochromatic light (typically in the visible, near-infrared, and near-ultraviolet range), rather than absorption as in IR. A vibrational mode is Raman active (observable in the Raman spectrum) if it prompts a change in the induced dipole moment (polarisability) of the sample molecule. Polarisability indicates a degree in which the electron cloud of the sample molecule rearranges in the presence of an electric field[10].

Therefore, Raman spectroscopy can provide complementary information to IR investigation. For instance, vibration modes symmetrical with respect to an inversion centre are IR inactive, but Raman active[8]. An example is the superoxide radical anion ($O_2^{\bullet -}$), a molecule of interest in the study of alkali metal-oxygen batteries, for which the symmetric stretching mode (ν_s) is detectable via Raman spectroscopy.

A Raman response is obtained when light is scattered after colliding with a sample molecule. Most of the incident light will pass directly though the sample, resulting in a Rayleigh signal which is obtained if after collision the scattered light has the same frequency (energy) as the incident radiation. When the incident light loses energy (higher frequencies) after the scattering event, part of the photon energy will cause a transition to a higher energy state and a Stokes shift is obtained. If the vibrational transition starts from an excited state ($\nu = 1$), the molecule will relax to a lower energy ground state, and the scattered light will have higher energy (lower frequency). This process, known as anti-Stokes scattering, occurs at lower

intensity, since most of the molecules will occupy the ground state at ambient temperature. Therefore, Stoke shifts are generally more useful. The three scattering processes are depicted in Figure 2.7.

The obtention of Raman spectra is relatively more straightforward in comparison to FTIR. The sample molecule is illuminated by a stable monochromatic beam producing different scattering events. After interacting with the sample, the scattered light will pass through a notch filter, which blocks same frequency radiation (Rayleigh) and allows lower frequency radiation (Stokes) collected onto a detector. The experiments reported henceforth were performed on a Renishaw inVia confocal Raman microscope. Either 633 or 532 nm wavelength lasers were utilised.

2.2.6 Powder X-ray diffraction (PXRD)

X-ray diffraction is a powerful tool for materials characterisation. It relies on the phenomenon of diffraction by X-rays to determine the crystal structure of the sample. A crystalline solid is described as an ensemble of crystallographic lattice planes with long range order. X-ray radiation is generated by bombarding a metal target (anode), such as copper and molybdenum, with a beam of high-energy charged particles (such as electrons) under vacuum. For the diffraction phenomenon to occur, the wavelength of the X-ray radiation must be of the same order of magnitude as the distance between crystallographic lattice planes[11]. Bragg's law (Eq. 2.6) describes the appearance of diffraction patterns when the incident radiation hits the sample and the resulting interference is constructive. In Eq. 2.6, n is an integer number, λ is the radiation wavelength and d is the interplanar spacing.

$$n\lambda = 2d \sin\theta \qquad \text{Eq. 2.6}$$

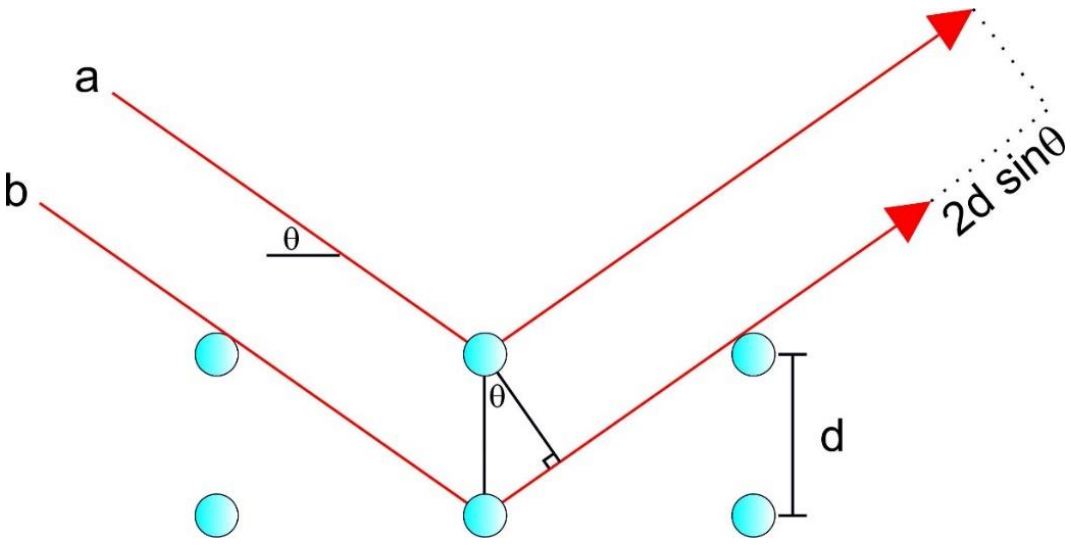

Figure 2.8: Schematic representation of the X-ray radiation diffraction.

XRD patterns are characteristics of the crystalline solid and can be utilised for phase identification of the sample. The position of Bragg peaks depends on the incident radiation wavelength (λ) and contains information about the structure, identity and lattice parameters of the sample. The intensity of Bragg peaks is related to the count of X-rays for a given diffraction angle (θ) and contains information about the chemical elements present in the sample. The width of Bragg peaks is proportional to the crystallite size[9].

XRD data reported henceforth was obtained using a PANalytical X'Pert Pro diffractometer (Cu or Mo $K\alpha_1$) in Bragg-Brentano geometry. The sample preparation was executed inside an argon filled glovebox. Portions of the discharged carbon cathodes were sealed in borosilicate glass capillary tubes using silicon rubber to seal. After removing the capillary from the glove box they were heat sealed with a blowtorch. Data was collected without exposure to the atmosphere.

2.2.7 X-ray photoelectron spectroscopy (XPS)

X-ray photoelectron spectroscopy is a surface sensitive analytical technique capable of probing the electronic structure of atoms and molecules. In XPS, the sample is bombarded with low energy X-rays (~1.5 keV) to excite the emission electrons from the core-level of a sample atom. The velocities of the ejected electrons (photoelectrons) are measured by the spectrometer and are characteristic of the sample atom being described as a function of the binding energy (Eq. 2.7).

$$E_K = h\nu - E_B - \phi \qquad \text{Eq. 2.7}$$

in which E_K is the kinetic energy (measured) of the ejected electron, $h\nu$ is the energy of the incident X-ray photon (known), E_B is the binding energy of the electron in the sample and ϕ is the spectrometer work function (calibrated) [9]. Therefore, Eq. 2.7 can be solved for the binding energy of the dislodged electron providing information on its electronic structure. The binding energy increases with atomic number and is sensitive to the chemical environment (electronegativity shifts) of the atom.

XPS experiments reported henceforth were performed in a standard ultrahigh vacuum surface science chamber consisting of a PSP Vacuum Technology electron energy analyser (angle integrating ± 10^o) and a dual anode Mg Kα (1253.6 eV) X-ray source. The base pressure of the system was 2×10^{-10} mbar, with hydrogen as the main residual gas in the chamber. The spectrometer was calibrated using Au 4f7/2 at 83.9 eV. XPS spectra were fitted using Voigt functions after Shirley background removal. The overall resolution is 0.2 eV.

2.2.8 Scanning electron microscopy (SEM)

Scanning electron microscopy is an important technique to investigate the morphology and topography of samples down to nanometre the scale. Electrons can be thermoionically generated by the electron gun or striped from a sharp metal tip by an electric field. The latter is known as field emission SEM (or cold cathode SEM) and has the advantage of generating brighter (higher resolution) electron beams. The generated electrons are accelerated by a second anode and irradiate the sample with a kinetic energy relative to the acceleration voltage.

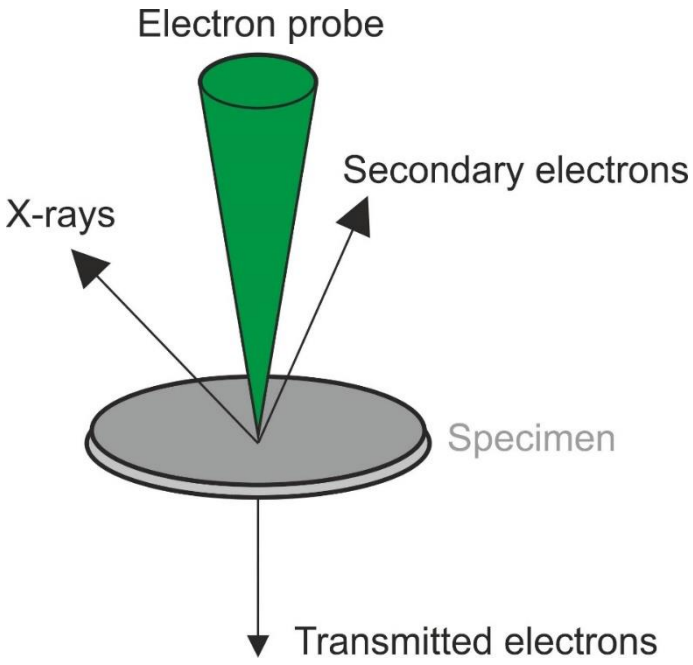

Figure 2.9: Simplified schematics of the electron-solid interactions.

When the incident electron beam hits the sample, X-rays and secondary electrons (but not only) are emitted and detected by the equipment (Figure 2.9). Secondary electrons (SE) are low energy electrons ejected from the interaction of

the primary beam with the valence shell of the sample. SE are produced typically from the surface of the sample (5-50 nm) and are collected to generate topographic imaging. The X-ray photons are produced by the primary beam ejecting core shell electrons leaving holes which are filled by the relaxation of outer shell electrons. The X-ray photons are generated at the total complete interaction volume and have characteristic energies for each element. The interaction volume of the primary electrons will depend on the acceleration voltage of the beam and the atomic number of the sample. Information regarding the chemical composition of the sample is obtained via energy dispersive X-ray spectroscopy (EDS)[12].

SEM images reported henceforth were recorded with a JEOL JSM-7001F field emission electron microscope fitted with energy dispersive X-ray spectroscopy analysis equipment (Oxford Instruments INCAx-act X-ray detector).

2.2.9 Atomic force microscopy (AFM)

Atomic force microscopy is a type of scanning probe microscopy (SPM), with resolution under fractions of a nanometre. Two advantages of AFM for the investigation of AM-O_2 systems, in which the desired reaction products are typically insulating solids, are that it does not require a conducting sample since is does not rely on tunnelling phenomenon (in the case of scanning tunnelling microscopy) and it does not suffer from primary electron beam build up on insulating samples (in the case of SEM). Information on the topography of the sample is acquired by measuring the force between sample and tip, which is obtained by collecting the deflection of a laser beam hitting the AFM tip[13].

AFM experiments reported henceforth were executed using scanasyst air tips (spring constant 0.7 Nm^{-1}, resonant frequency 150 KHz) using quantitive nanomechanical mapping (QNM) techniques. In QNM imaging, the tip periodically taps the sample and the forces between tip and sample are measured directly by the deflection of the cantilever. Image analysis was performed upon nanoscaleanalysis as provided by Bruker.

2.5 References

1. W. L. Armarego, *Purification of laboratory chemicals*, Butterworth-Heinemann, 2017.
2. J. S. M. Lee, M. E. Briggs, T. Hasell and A. I. Cooper, *Adv. Mater.*, 2016, **28**, 9804-9810.
3. J. Qian, Y. Chen, L. Wu, Y. Cao, X. Ai and H. Yang, *Chem. Commun.*, 2012, **48**, 7070-7072.
4. N. E. Drewett, I. M. Aldous, J. Zou and L. J. Hardwick, *Electrochim. Acta*, 2017, **247**, 296-305.
5. N. m. Elgrishi, K. J. Rountree, B. D. McCarthy, E. S. Rountree, T. T. Eisenhart and J. L. Dempsey, *J. Chem. Educ.*, 2017.
6. S.-I. Pyun, H.-C. Shin, J.-W. Lee and J.-Y. Go, *Electrochemistry of insertion materials for hydrogen and lithium*, Springer Science & Business Media, 2012.
7. F. C. Walsh, *Transactions of the IMF*, 1991, **69**, 155-157.
8. M. Reichenbächer and J. Popp, *Challenges in molecular structure determination*, Springer Science & Business Media, 2012.
9. C. P. Poole Jr and F. J. Owens, *Introduction to nanotechnology*, John Wiley & Sons, 2003.
10. P. Vandenabeele, *Practical Raman spectroscopy: an introduction*, John Wiley & Sons, 2013.
11. B. E. Warren, *X-ray Diffraction*, Courier Corporation, 1969.
12. J. Goldstein, *Practical scanning electron microscopy: electron and ion microprobe analysis*, Springer Science & Business Media, 2012.
13. S. Morita, F. J. Giessibl, E. Meyer and R. Wiesendanger, *Noncontact atomic force microscopy*, Springer, 2015.

Chapter 3.
Aprotic Lithium-Oxygen Battery Systems

3.1 Abstract

This chapter discusses two practical strategies to confront the large (> 1V) voltage polarisation between discharge and charge faced by aprotic lithium-oxygen systems using ether-based electrolytes. In the first approach, the suitability of hypercrosslinked polymer based carbon cathodes in lithium-oxygen cells was investigated. Different synthetic routes allowed the evaluation of the effect of pore volume, surface area and nitrogen heteroatom doping in the cell performance. Secondly, the effect of adding a tertiary amine to the electrolyte (1, 4-diazabicyclo [2.2.2] octane) acting as a physical singlet oxygen quencher was studied. The additive concentration and its influence on the cell chemistry of lithium-oxygen cells were evaluated.

3.2 Introduction

Non-aqueous aprotic lithium-oxygen (Li-O_2) batteries offers a real step change energy storage alternative to current state-of-the-art lithium-ion batteries based on theoretical specific energy approaching that of gasoline[1]. This lead to extensive research on the fundamental electrochemistry taking place during discharge/charge cycling of Li-O_2 cells over the past decade which identified several shortcoming hindering the development of long lasting practical devices. Perhaps the most significant challenge is to circumvent electrolyte and cathode degradation particularly taking place at oxidative potentials, in which a deviation from the stoichiometric 2 electron per O_2 process has been reported for a variety of electrolyte/cathode combinations[2].

Most Li-O_2 studies employed carbon based materials to fabricate positive electrodes with attractive properties, such as high conductivity, high surface area, low cost, and low mass. However, employing ^{13}C-labeled cathodes, different authors reported the evolution of $^{13}CO_2$ during the OER, indicating unwanted reactions between lithium peroxide (Li_2O_2) and the carbon electrode[3, 4]. Thotiyl *et al.*[4] reported the onset of this carbon corrosion at 3.5 V vs Li^+/Li, imposing a stringent electrochemical window for the operation of carbon-based Li-O_2 cells.

However, the detection of carbon corrosion upon charging of Li-O_2 cells does not necessarily rule out the utilisation of carbon-based cathodes. Itikis *et al*[5], reported that more resilient can be obtained via modification of the carbon structure and electrolyte additives have been reported to bring down the oxidation plateau of Li_2O_2 within the stability of carbon towards oxidative decomposition.

Regarding both electrolyte and cathode instabilities, an important breakthrough was reported by Wandt *et al.*[6], which provided experimental confirmation of the formation of singlet oxygen as a reaction intermediate for the Li_2O_2 oxidation reaction in Li-O_2 cells.

On the ground state configuration (Figure 3.1), molecular oxygen assumes a triplet electronic state $^3\Sigma_g^-$ (commonly abbreviated $^3O_2$) composed of two excited singlet states: $^1\Delta_g$ (commonly abbreviated $^1O_2$) is the lowest excited energy state and $^1\Sigma_g^+$ is the highest excited state, which is unstable and rapidly decays to $^1\Delta_g$. A triplet state refers to the three possible orientation that can be adopted by two parallel electron spins (↑↑). A single state refers to only one possible orientation in space of a paired electron spin (↑↓)[7].

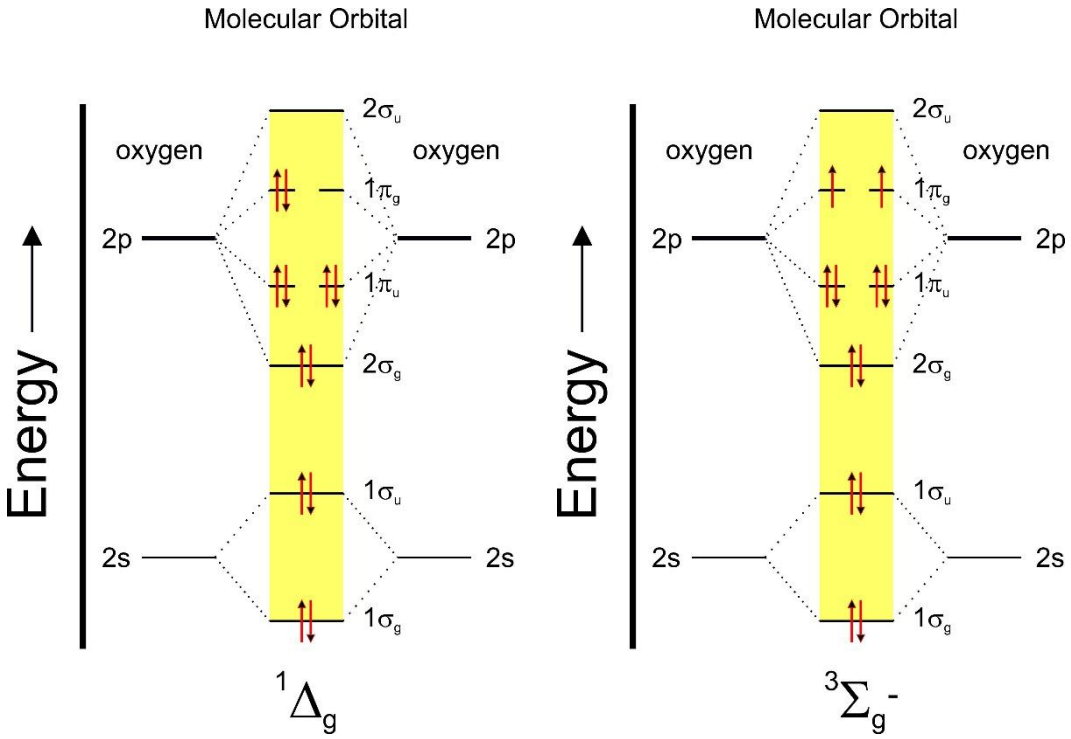

Figure 3.1: Molecular orbital diagrams of $^1\Delta_g$ and $^3\Sigma_g^-$ states of molecular oxygen.

The report by Wandt *et al.*[6] unveiled the importance of singlet oxygen for the development of Li-O_2 batteries. The onset of singlet oxygen evolution was detected at 3.55 V vs Li^+/Li, close to threshold of carbon instabilities reported by Thotiyl *et al.*[4]. Thus indicating that these two phenomena can be correlated. Later, Mahne *et al.*[8] demonstrated that singlet oxygen is already evolved at the onset of charge (~ 3 V vs Li^+/Li) and is also produced at lower amounts during discharge of Li-O_2 cells. Furthermore, singlet oxygen is a strong oxidising agent[9], highly reactive with organic compounds, and hypothesised as a possible origin for the rechargeability limitations common in Li-O_2 cells[2].

This chapter will examine two practical approaches to lower the oxidation overpotential of ether-based Li-O_2 cells using carbon cathodes. The performance of hypercrosslinked polymers carbons (HCPCs) yielding highly porous, hydrophobic, carbon electrodes is investigated. The effect of introducing nitrogen heteroatom doping is also evaluated. Finally, the influence of introducing a tertiary amine to the electrolyte acting as a singlet oxygen quencher is discussed.

3.3 Experimental Methods

This section provides specific experimental conditions for the results discussed in this chapter. For more detailed information see: Chapter 2. Experimental procedures and techniques.

3.3.1 Synthesis of hypercrosslinked polymer carbons

The synthesis of hypercrosslinked polymer carbon materials was developed and performed by Jet-Sing M. Lee at the University of Liverpool. A complete description of the procedure is described elsewhere[10].

In summary, hypercrosslinked polymers (HCP) were obtained via a one-step Friedel Crafts alkylation reaction previously described in the literature[11]. The selected monomer: benzene (HCPC-75) or pyrrole (HCPC-54) was added to 1,2-dichloroethane under nitrogen atmosphere in a sealed flask. Then reacted with dimethoxymethane and iron (III) chloride for 24 hours. The precipitate obtained was filtered and purified with ethanol.

Carbonised HCPC materials were obtained by mixing the HCP precursor with potassium hydroxide at a 1:4 ratio and heating under nitrogen flow to a specific temperature at a 5 C min^{-1} rate. For the obtention of nitrogen doped HCPC, ammonia was used as activator. A pyrolysation temperature of 800 °C was used for the nitrogen doped HCPC-54 and a temperature of 900 °C was used for the non-nitrogen doped HCPC-75. The temperature was held for 2 hours and finally cooled

to room-temperature. Detailed information on relevant physical properties of HCPC materials is provided in table 3.1.

The characterisation of HCPCs was performed by Raman spectroscopy and X-ray photoelectron spectroscopy (XPS).

Raman data was recorded on a Renishaw in via microscope with a 633 nm laser (2 mW cm^{-2}) in a gas-tight cell (ECC-Opto-STD, El-Cell GmBH) focussed through a microscope (Leica) via a 50x objective lens (Leica).

XPS experiments were performed in a standard ultrahigh vacuum surface science chamber consisting of a PSP Vacuum Technology electron energy analyser (angle integrating ± 10^{o}) and a dual anode Mg Kα (1253.6 eV) X-ray source. The base pressure of the system was 2×10^{-10} mbar, with hydrogen as the main residual gas in the chamber. The spectrometer was calibrated using Au 4f7/2 at 83.9 eV. XPS spectra were fitted using Voigt functions after Shirley background removal. The overall resolution is 0.2 eV.

3.3.2 Electrolyte preparation

The selected solvent diethylene glycol dimethyl ether (DEGDME) was distilled and dried over freshly activated molecular sieves (4 Å). The solvent was stored in an argon-filled glovebox (<0.1 ppm H_2O and <0.1 ppm O_2). Lithium bis (trifluoromethanesulfonyl)imide (LiTFSI) was used as supporting salt and dried under vacuum at 80°C for at least 12 hours. The tertiary amine used as an electrolyte additive 1, 4-diazabicyclo [2.2.2] octane (DABCO) was dried in the glovebox vacuum chamber for at least 12 hours. The electrolyte solutions were prepared

inside an argon-filled glovebox and H_2O content measured with a Karl Fischer Coulometer. Final electrolytes were found to have <10 ppm water.

3.3.3 Carbon cathode preparation

The air-cathodes consisted of HCPC or conductive carbon black (Super C65, Imerys). The composite electrodes were prepared using poly(tetrafluoroethylene) (PTFE) binder (70% active carbon material, 30% binder) by mixing into a slurry with ethanol. The putty like mixture was put in a calender and pressed to a thickness of 100 μm to obtain self-supporting films. The electrodes were punched into 10 mm disk then dried at 120 °C under vacuum for at least 12 hours. The binder-free carbon fibre electrodes (P50, Avcarb) were dried in a similar manner.

3.3.4 Swagelok cell assembly

Li-O_2 cells were assembled using a custom built Swagelok set-up. Lithium metal was used as an anode, roll pressed and cut into a 0.785 cm^2 discs. Two Whatman glass fibre separators (GF-G grade, 470 μm) were impregnated with 0.12 mL of the chosen electrolyte. The separators went through the same cleaning and drying process as the cathodes. In the cells using the DABCO electrolyte additive, a LiSICON (Ohara glass) membrane was used to separate the catholyte (containing DABCO) and anolyte.

Different carbon materials were used as cathodes as 10 mm diameter discs. The cathodes were held by a stainless steel current collector containing holes to allow O_2 access. The assembled Swagelok cells were transferred in a sealed glass chamber to the O_2 line station. The chamber was purged with dry O_2 for 10 minutes, and the cell rested for 3 hours at the open-circuit potential (OCP) prior to discharge. The galvanostatic discharge was performed using a Bio-Logic MPG-2 battery cycler. The discharge rate was based on the geometric cross-sectional area of the cathodes. All potentials are referenced against Li^+/Li.

3.3.5 Cell disassembly and cathode characterisation

After electrochemical measurements, the Swagelok cells were disassembled inside the glovebox without atmosphere exposure. The positive electrodes were washed twice with dry DEGDME, 10 minutes each time. Finally the electrodes were dried in the glovebox vacuum chamber for at least 12 hours.

Fourier-transform infrared (FTIR) data was collected on a Nicolet 6700 spectrometer (Thermo Fisher Scientific) by grinding portions of the discharged cathode into CsI pellets. Data was collected in transmission mode inside a nitrogen-filled glove box.

Scanning electron microscopic (SEM) images were recorded with a JEOL JSM-7001F field emission electron microscope.

3.4 Results and Discussion

3.4.1 Investigation of hypercrosslinked polymer carbon cathodes in Li-O_2 cells

The carbonisation of HCPCs varying synthesis parameters such as monomer, pyrolysation temperature and activator molecule, allowed the fabrication of carbon electrodes with different properties summarised in Table 3.1. The chemical structures of the precursor HCPs are depicted in Figure 3.2.

Table 3.1: Surface area and pore characteristics of synthesised HCPCs and a commercial carbon black.

Carbon	BET ($m^2 g^{-1}$)	Pore volume ($cm^3 g^{-1}$)	Micropore volume ($cm^3 g^{-1}$)	Pore size (Å)	Nitrogen (%)
Super C65	62	0.04	0.002	79	0
HCPC-75	422	0.42	0.2	36-55	0
HCPC-54	418	0.29	0.2	12/14/23-48	11.5

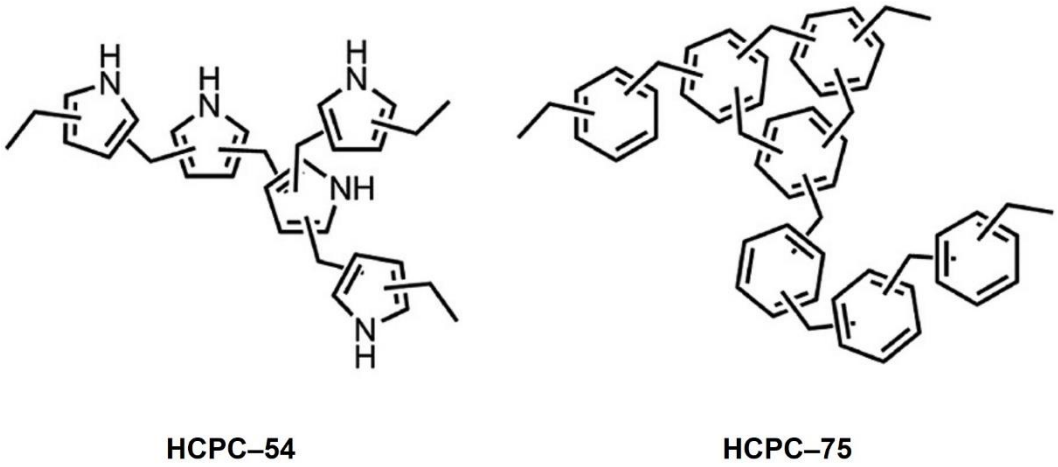

Figure 3.2: Chemical structure of the HCP precursors used for the carbonisation process. Taken from Jet-Sing M. Lee *et al.*[10].

To evaluate the performance of the synthesised compounds, Li-O_2 cells were prepared by assembling both HCPC-75 and HCPC-54 with a lithium metal anode and a 1.0 LiTFSI in DEGDME electrolyte. Figure 3.3 shows the first galvanostatic discharge/charge cycle of the HCPC cathodes with an electrochemical window of 2-4.15 V vs Li^+/Li at 0.12 mA cm^{-2} current rate. A commercial carbon black, commonly employed in Li-O_2 cell cathodes is used for comparison.

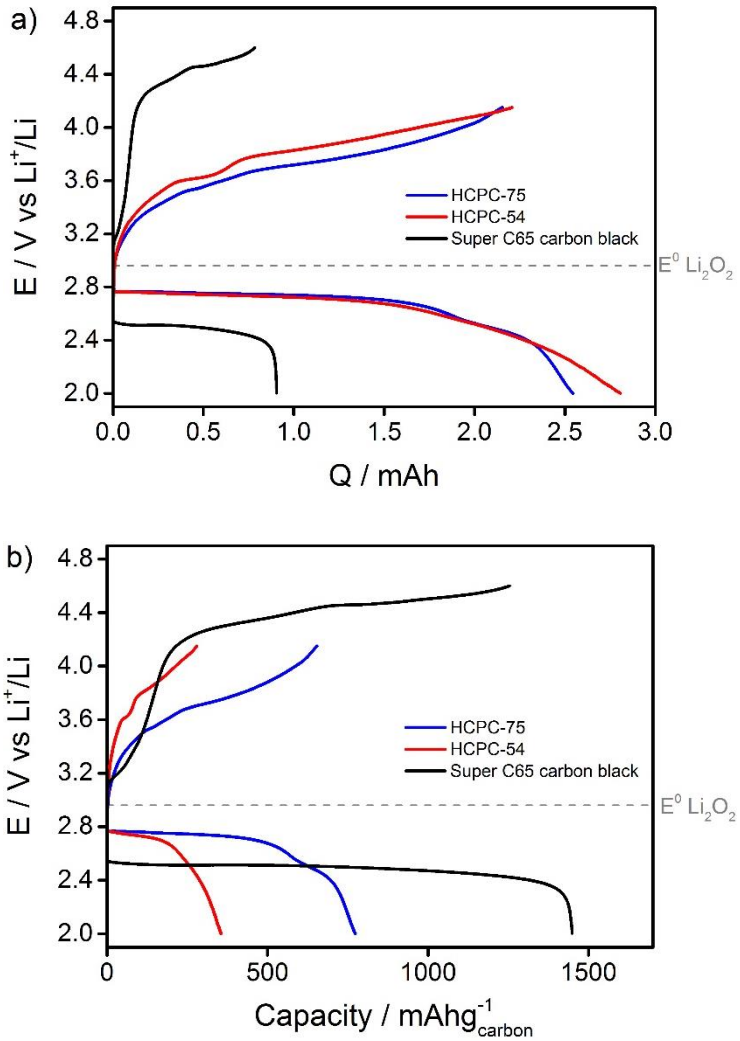

Figure 3.3: First galvanostatic discharge/charge cycle of Li-O_2 cells using HCPC75, HCPC54 and Super C65 carbon black cathodes showing a) absolute capacity and b) specific capacity plots. Electrolyte: 1.0 M LiTFSI in DEGDME electrolyte. Current rate: 0.12 mA cm^{-2}.

The voltage profile of the HCPC cathode cells shows important differences from typical behaviour of carbon based Li-O_2 cells. The discharge potential plateaus were similar for both cells, HCPC-75 (2.74 V vs Li^+/Li) and HCPC-54 (2.72 V vs Li^+/Li), at lower overpotential in comparison to the carbon black cell (2.51 V vs Li^+/Li), indicating higher electrocatalytic activity towards the ORR in the HCPC cells.

The charge curve using HCPC cathodes show considerably lower voltage gap in comparison to the carbon black cell, with two distinguishable plateaus at low and high overpotentials. The charge mechanism of electrochemically formed Li_2O_2 was proposed by Ganapathy *et al.*[12] to be a two-step process. The first step at low overpotential would be the removal of non-crystalline peroxide in agreement to theoretical calculations indicate a low overpotential for Li_2O_2 oxidation (<0.2 V[13]). The charge process follows a transition from crystalline Li_2O_2 to a lithium-deficient peroxide ($Li_{2-x}O_2$) component which causes the overpotential to increase as the transition reaches the bulk of electrochemically formed Li_2O_2.

The Raman characterisation of the different carbon materials (Figure 3.4) shows a higher concentration of defect sites on the HCPCs, measured by the intensity ratio of the D (~ 1348 cm^{-1}) and G (~ 1593 cm^{-1}) bands, in comparison to the carbon black material. The nitrogen doped HCPC-54 shows lower concentration of defect sites in comparison to the HCPC-75, which is counter intuitive as the introduction of N functional groups is accompanied by the formation of defects in the carbon backbone structure[14].

Further characterisation of the HCPCs by XPS (Figures 3.5 and 3.6) shows similar oxygen containing functional groups in both carbon materials (C=O, C-O

and O-C=O). Both defect sites and oxygen containing functionalities have been reported to result in a higher electrocatalytic activity for oxygen reduction[15, 16], thus explaining the higher discharge plateau obtained for the HCPC cells. Theoretical calculations reported by Xiao *et al.*[17] explained the higher electrocatalytic activity based on stronger interactions with oxygen functionalised lattice resulting in a preferential nucleation of Li_2O_2.

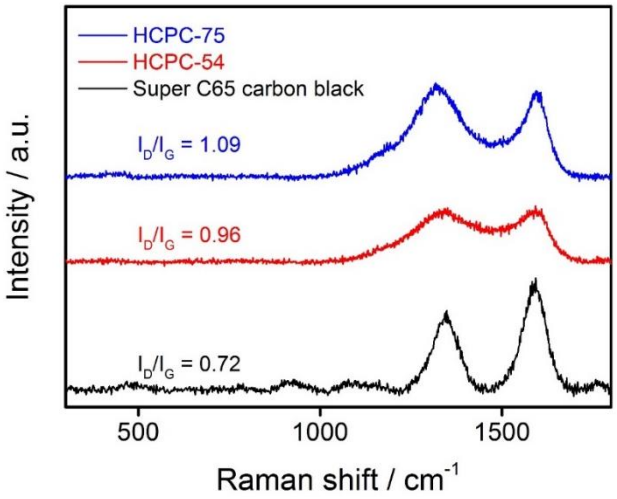

Figure 3.4: Raman spectra of HCPC-75 and HCPC-54 and Super C65 carbon black.

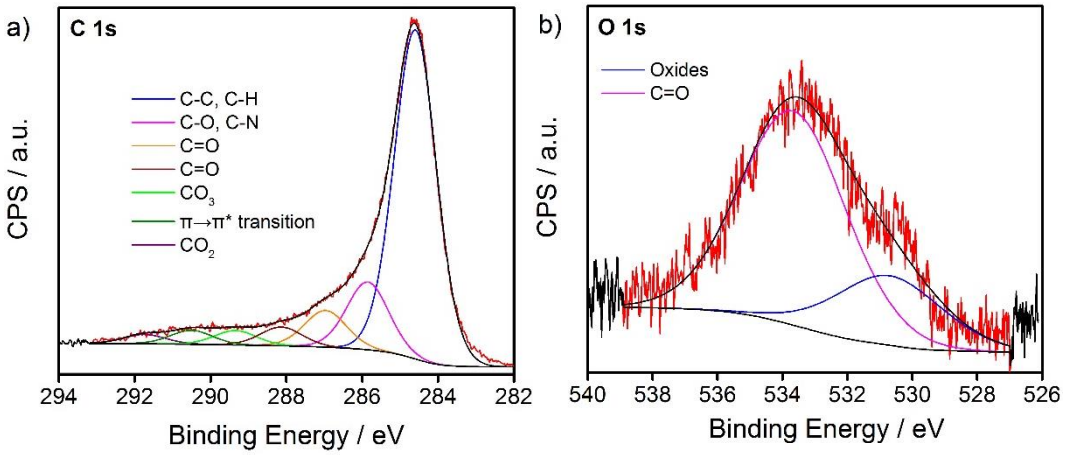

Figure 3.5: XPS a) C 1s and b) O 1s spectra of HCPC-75. (XPS analysis performed by Jose A. C. Clemente).

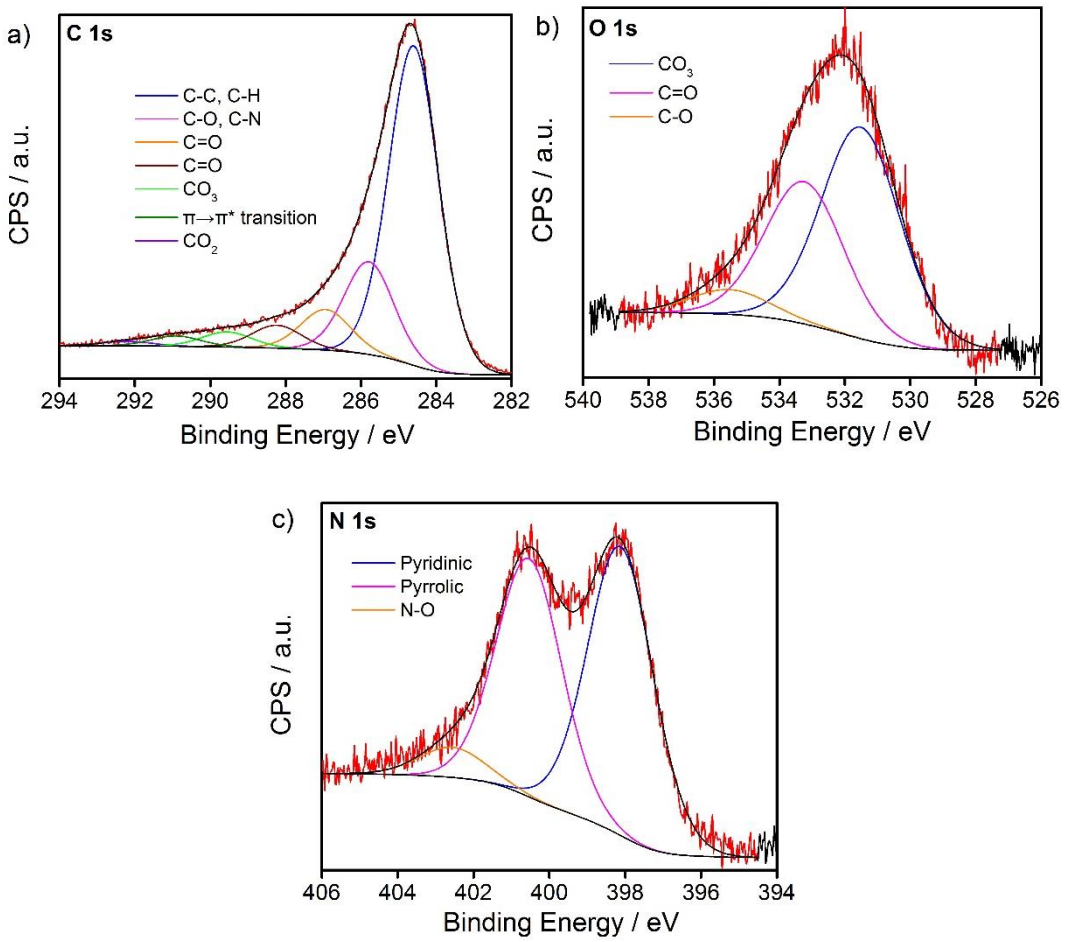

Figure 3.6: XPS a) C 1s, b) O 1s and c) N 1s spectra of HCPC-54. (XPS analysis performed by Jose A. C. Clemente).

The N 1s spectrum shows that the NH_3 heat treatment mainly introduced pyridinic and pyrolic functionalities, which are common for NH_3 heat treated nitrogen doping procedure[18]. The introduction of these N-functionalities has been reported to induce a charge deficiency in the adjacent carbon which is beneficial to dioxygen and oxygen reduced intermediates adsorption, resulting in higher electrocatalytic activity for the ORR and OER[19].

In contrast, HCPC-75 and HCPC-54 Li-O_2 cells exhibited similar voltage plateaus on the first galvanostatic discharge/charge cycle and comparable absolute

capacities. This is in line with a report by Li *et al.*[20], in which the heat treatment of carbon black with NH_3 had no influence on the capacity and voltage polarisation of ether-based Li-O_2 cells, and in divergence with reports of N-doped carbon nanotubes and graphene nanosheets cathodes which showed enhanced electroactivity and improved capacities[16, 19, 21].

The HCPC-75 and HCPC-54 cathodes delivered significant improvement in the absolute capacity compared to the carbon black cathode. The specific capacity (normalised by the carbon mass) is larger for the carbon black cathode as a result of the low carbon loading of the electrode. The higher absolute capacities obtained for the HCPC cells are related to the superior pore volume and surface area of the carbon substrates, as both parameters have been reported to be directly linked to first discharge capacity[22, 23].

Higher mesoporosity (2-50 nm) in the cathode substrate is associated with the formation of more three phase boundaries (carbon-electrolyte-oxygen) where the ORR process takes place, thus resulting in higher capacities. Macroporosity and microporosity can be associated with electrode flooding and pore clogging, respectively[24].

Table 3.2: Mass loading, average discharge capacities for the five carbon cathodes tested in Li-O_2 cells.

Carbon	m (mg)	Q (mAh)	Q (mAh g^{-1})	Q (mAh cm^{-2})
Super C65	0.5	0.9	1450	1.15
HCPC-75	3.2	2.5	773	4.98
HCPC-54	7.8	2.8	355	5.57

The chemical identification of the discharge products formed during discharge of Li-O_2 cells using HCPC-75 and HCPC-54 electrodes was performed by FTIR analysis of the discharged cathodes (Figure 3.7). Lithium peroxide (vLi-O at 532, 420 and 337 cm^{-1}) along with typical electrolyte decomposition products (lithium carbonate and lithium carboxylates) were identified as reaction products. For glyme-based electrolytes, the discharge process is expected to be dominated by the 2 electron per oxygen reduction resulting in the formation of Li_2O_2[25]. The formation of carbonates and carboxylates as result of electrolyte degradation has been reported to happen via a superoxide radical anion or Li_2O_2 induced hydrogen abstraction on the ether molecule[26]. The structure of the carbon electrode, defect sites and chemical functionalities, is expected to influence the oxidative stability of the carbon electrode (OER)[4], but not the nature of electrolyte degradation products during ORR[2, 26].

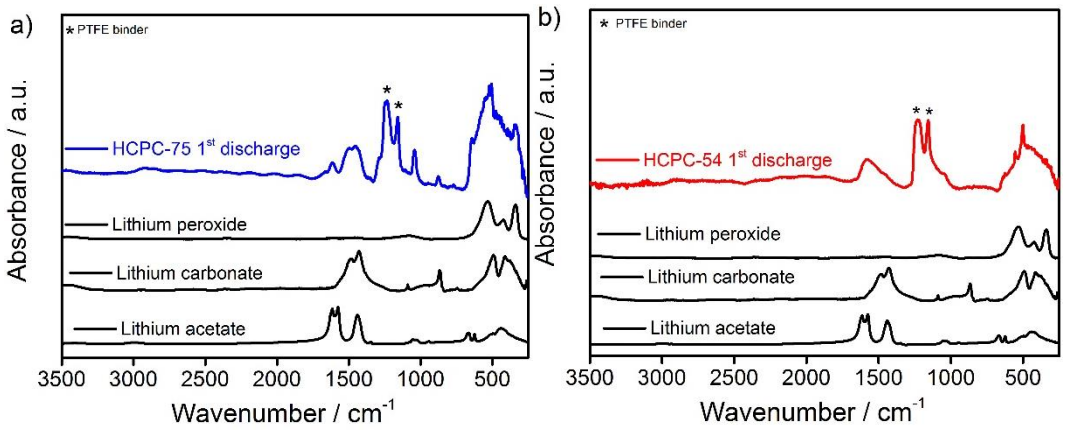

Figure 3.7: FTIR analysis of the HCPC-75 and HCPC-54 cathodes after one discharge process in Li-O_2 cells using a 1.0 M LiTFSI in DEGDME electrolyte at 0.12 mA cm^{-2} current rate.

The cycling data for the Li-O_2 cells using HCPC-75, HCPC-54 and Super C65 carbon black cathodes in 1 M LiTFSI in DEGDME is shown in Figure 3.8.

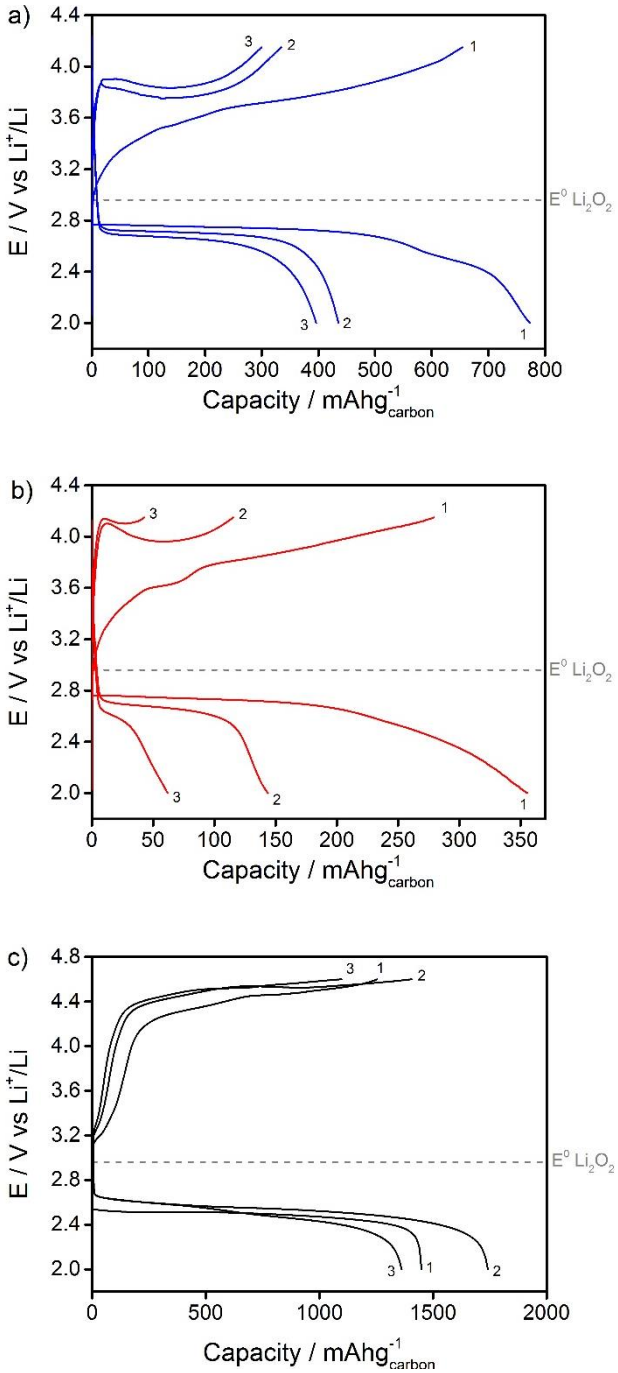

Figure 3.8: First 3 galvanostatic discharge/charge cycles of Li-O_2 cells using a) HCPC75, b) HCPC54 and c) Super C65 carbon black cathodes. Electrolyte: 1.0 M LiTFSI in DEGDME electrolyte. Current rate: 0.12 mA cm^{-2}.

The superior electrocatalytic effect of the HCPCs is lost after the first cycle as the subsequent cycles show continuous increase of voltage overpotentials. Oxidative decomposition reactions occurring at potentials above 3.5 V vs Li^+/Li cause the build-up of electrolyte/cathode degradation products on the carbon surface which limit the rechargeability of the cells causing early cell death.

3.4.2 Li-O_2 cells using a singlet oxygen quencher (DABCO)

The evolution of $^1O_2$ during the charging of Li-O_2 cells could be the underlying reason for the high instability of cathode and electrolyte components during cell operation[6,8]. Therefore, the integration of efficient and stable $^1O_2$ quenchers might be a practical strategy to avoid parasitic reactions and increase cell rechargeability. Aliphatic amines are known to cause the relaxation of the lowest excited energy state of molecular oxygen while maintaining its chemical structure[27] and can be used to increase the stability of Li-O_2 cell components. 1, 4-diazabicyclo [2.2.2] octane (DABCO) has been reported as one of the most efficient physical quenchers of $^1O_2$ in comparison to other tertiary amines and quinones effectively mitigating the photodegradation of different polymers[28].

To investigate the effect of adding DABCO to ether-based electrolytes, Li-O_2 cells were prepared by assembling P50 Avcarb carbon fibre paper cathode with a lithium metal anode and a 1.0 LiTFSI in DEGDME electrolyte with different concentrations 0.01 M, 0.05 M and 0.1 M of the quencher molecule. The cells were cycled with an electrochemical window of 2-4.6 V vs Li^+/Li at 0.12 mA cm^{-2} current rate.

The first galvanostatic discharge/charge cycle is shown in Figure 3.9. Considering the cell without the quencher additive, a typical voltage profile for carbon cathodes in Li-O_2 cells is obtained characterised by large voltage overpotential as a result of cathode and electrolyte components (carbon, binder, salt and solvent) instabilities[4]. When DABCO is added to the electrolyte, a significant reduction of the onset charge plateau is observed followed by a second process at

higher overpotential. Increasing the quencher concentration results in an enhancement of the charge evolved at the lower overpotential plateau and lower overall voltage gap.

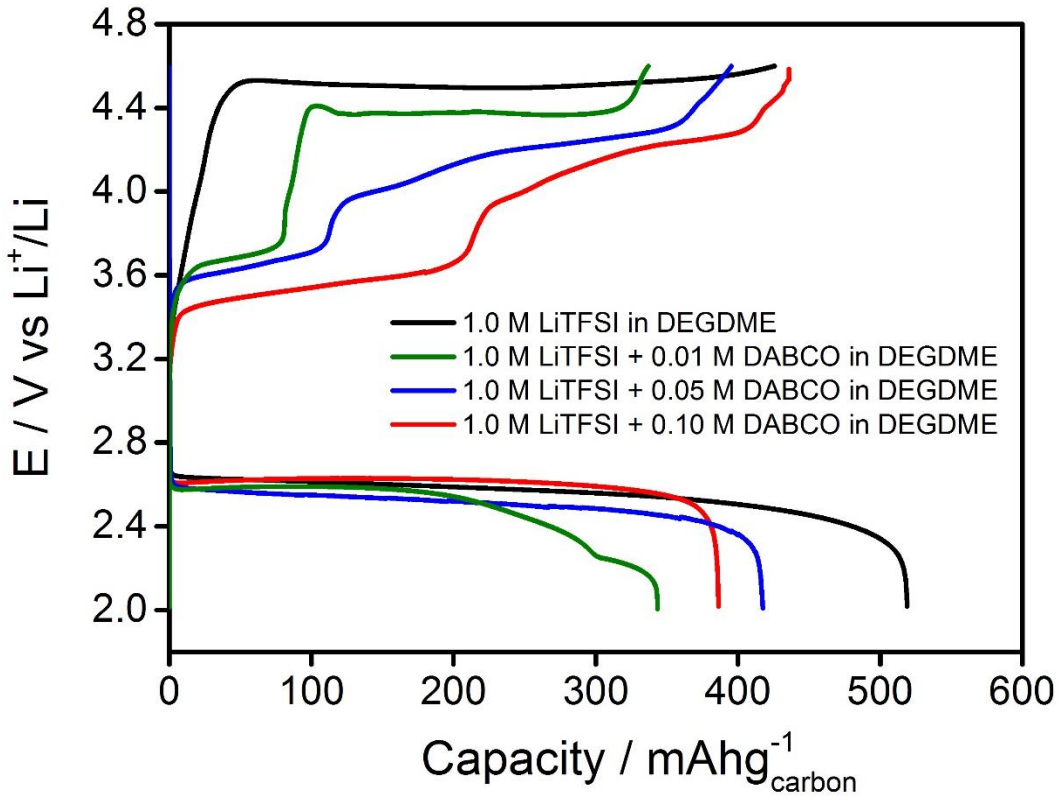

Figure 3.9: First galvanostatic discharge/charge cycle of Li-O_2 cells using P50 Avcarb carbon fibre paper cathode with 1.0 M LiTFSI in DEGDME electrolyte and different concentration of DABCO. Current rate: 0.12 mA cm^{-2}.

The oxidation of Li_2O_2 generates $^1O_2$ in solution at the initiation of the charge process, which is deactivated by the quencher molecule delaying parasitic carbon corrosion processes. The charge potential eventually increases at ~ 3.7 V vs Li^+/Li independent of the quencher additive concentration. The high overpotential plateau can be a result of DABCO electrochemical instability, DABCO complete depletion by $^1O_2$ evolution or as a result of unwanted reaction between DABCO

and lithium metal anode. Mahne *et al.*[8], reported an electrochemical instability of DABCO at potentials above 3.5 V vs Li^+/Li, however, this was not observed for the present cell configuration as shown in Figure 3.10.

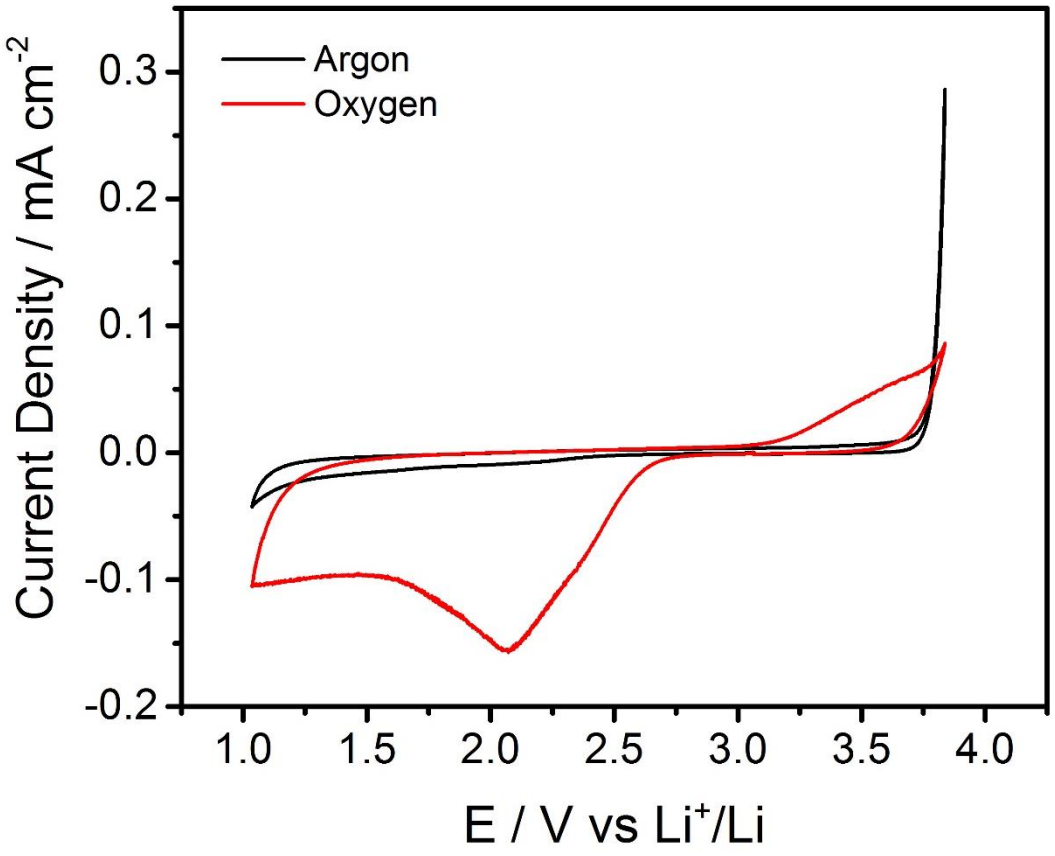

Figure 3.10: Cyclic voltammetry of O_2 enriched (red) 1.0 M LiTFSI + 0.1 M DABCO in DEGDME on a glassy carbon electrode, 25 °C, 0.1 V s^{-1}. Black curve shows the cyclic voltammetry on the same system under argon.

The cyclic voltammetry experiment confirms a stability window of DABCO in this particular electrolyte from 1.0 to 3.8 V vs Li^+/Li. The result indicates that the reduction in overpotential observed when DABCO is added to the electrolyte is a result of purely physical quenching of $^1O_2$ and not a redox mediator effect. A cathodic peak at ~2.6 V vs Li^+/Li indicates the reduction of dioxygen at the glassy

carbon and the formation of Li_2O_2, which irreversibly oxidises at ~3.2 V vs Li^+/Li. The irreversibility observed in the cyclic voltammetry is a result of the Li_2O_2 formed during the cathodic sweep being diffused into solution causing less charge to be oxidised in the anodic sweep. Furthermore, this behaviour is characteristic of Li-O_2 electrochemistry in ether based electrolytes, in which the moderately low donor number induces a surface confined mechanism due to limited solubility of the LiO_2 intermediate[29].

To exclude the possibility of degradation of the quencher additive by the metal anode, Li-O_2 cells were constructed using a lithium conducting solid electrolyte membrane (LiSICON, Ohara). The anolyte was composed of 1.0 M LiTFSI in DEGDME and the catholyte was composed of 1.0 M LiTFSI + 0.1 M DABCO in DEGDME.

Figure 3.11 shows the cycling data for such cell. When the metal anode is isolated, the charge process shows a single potential plateau at 3.55 V vs Li^+/Li. Thus indicating that the high overpotential plateau observed in Figure 3.9 is a result of chemical reaction with the metal anode deactivating the quencher.

The cell constructed with the quencher additive in combination with a LiSICON membrane could be fully recharged at potentials considerably lower than the typical behaviour of carbon based cells[4, 20]. This is an indication that the high voltage polarisation largely reported during the charge of Li-O_2 cells originates from electrolyte degradation (Li_2CO_3 being the dominant degradation product) rather than with sluggish kinetic of Li_2O_2 oxidation. McCloskey *et al.*[3] proposed a model in which the formation of approximately one monolayer of electrolyte degradation products at the carbon/Li_2O_2 interface during galvanostatic charging

increases the charge transport resistance causing the potential to rise and limiting rechargeability.

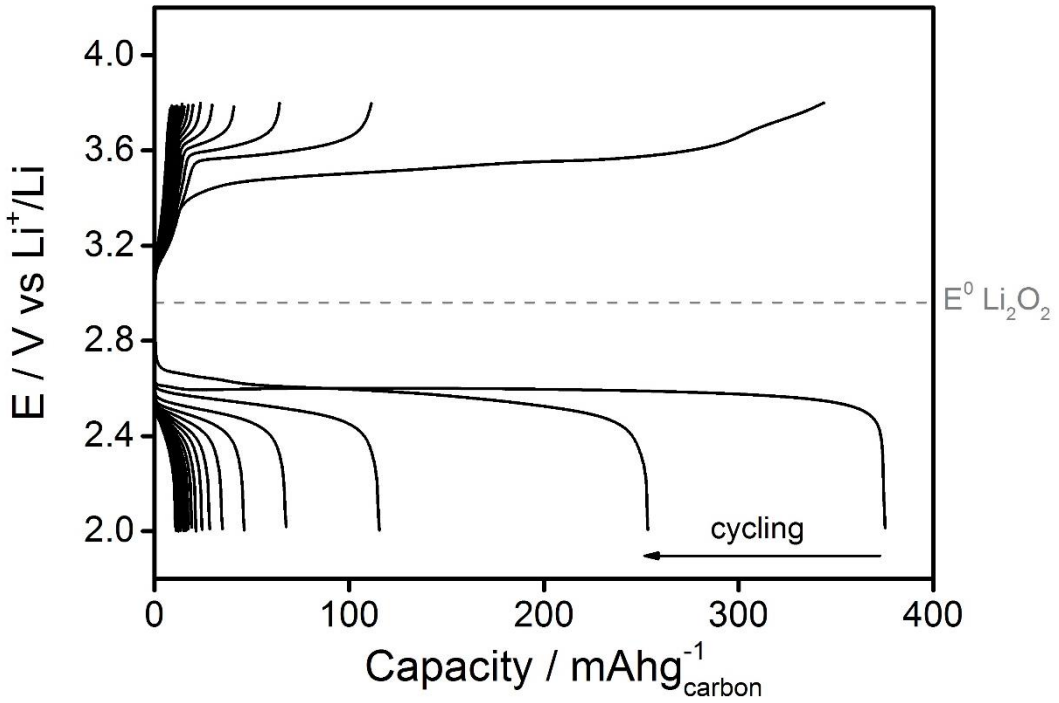

Figure 3.11: Galvanostatic discharge/charge cycling of Li-O_2 cells using P50 Avcarb carbon fibre paper cathode with 1.0 M LiTFSI + 0.1 M DABCO in DEGDME electrolyte. Current rate: 0.12 mA cm^{-2}.

The overall voltage gap monotonically increases with cycling after the first galvanostatic discharge/charge and the cell exhibits rapid capacity fade. It is not clear whether the charge overpotential increases upon cycling as a result of the DABCO additive not being able to divert all the $^1O_2$ formation during peroxide oxidation, if the rate of $^1O_2$ evolution is faster than the rate in which it is converted to $^3O_2$ by DABCO or if the chemical deactivation of $^1O_2$ is not reversible and the quencher is consumed upon cycling. All these possibilities would result in electrolyte stability issues causing poor cyclability. The later however seems a less

likely scenario, based on extensive literature of DABCO application as a reversible $^1O_2$ quencher, DABCO + $^1O_2 \rightarrow {}^3O_2$ + DABCO, in which neither the tertiary amine nor oxygen is depleted[28, 30, 31].

The chemical identification of the discharge products formed during discharge of Li-O_2 cells using DABCO as a quencher was performed by FTIR (Figure 3.12) and SEM (Figure 3.13) analysis of the P50 carbon fibre cathode.

The FTIR analysis confirms that Li_2O_2 is present on the first discharge process, which is corroborated by the morphology observed on the SEM images. Electrochemically formed Li_2O_2 grows as stacked crystalline platelets forming toroidal or disc shapes[32]. The formation of Li_2O_2 is accompanied by peaks associated with Li_2CO_3 in the discharged carbon spectrum.

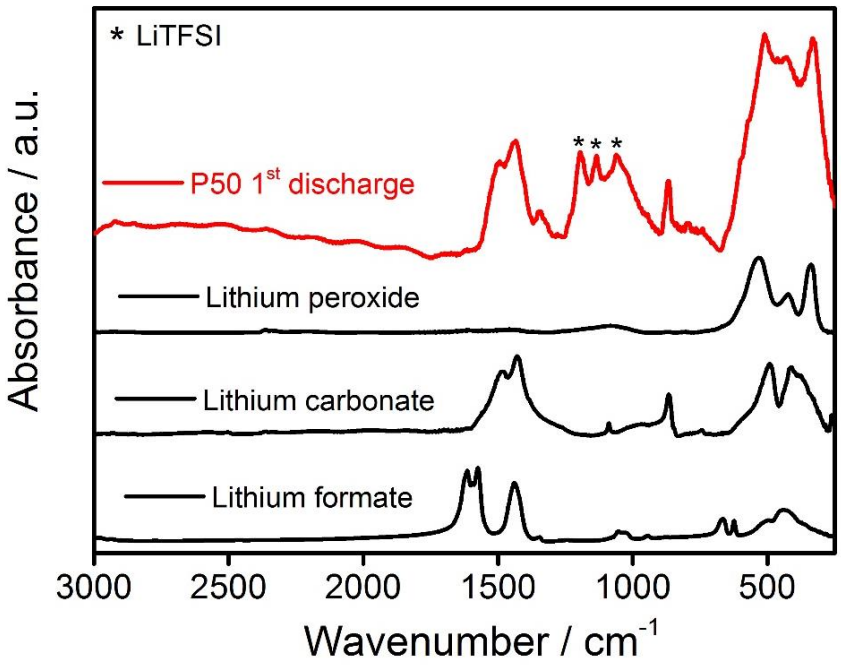

Figure 3.12: FTIR analysis of the P50 Avcarb carbon fibre paper cathode after one discharge process in Li-O_2 cells using a 1.0 M LiTFSI + 0.1 M DABCO in DEGDME electrolyte at 0.12 mA cm^{-2} current rate.

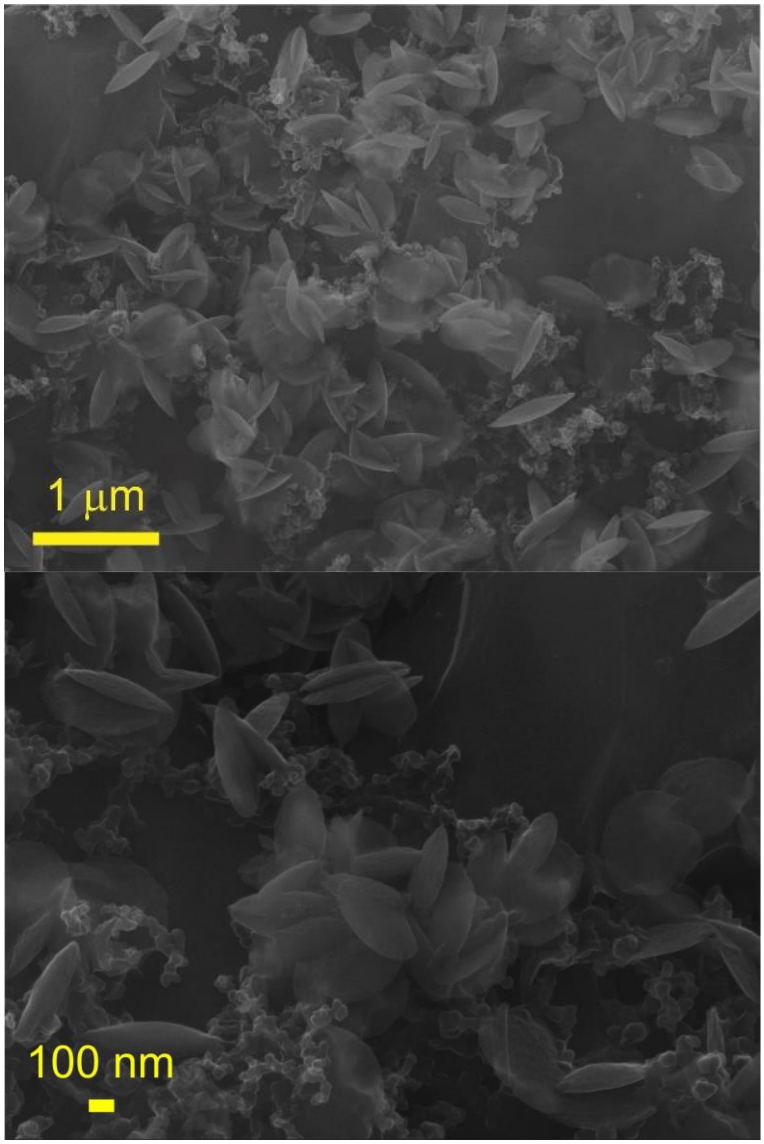

Figure 3.13: SEM images at different magnifications of the P50 Avcarb carbon fibre paper cathode after one discharge process in Li-O_2 cells using a 1.0 M LiTFSI + 0.1 M DABCO in DEGDME electrolyte at 0.12 mA cm^{-2} current rate.

The detection electrolyte degradation products during the discharge of a Li-O_2 cell using DABCO as a quencher, similar to cells discharged without the additive, indicates that the discharge process is less affected by the formation of $^1O_2$. This can be a result of the less amount of $^1O_2$ evolved during the discharge process as reported by Mahne *et al.*[8], or an indication that the underlying reaction

causing electrolyte degradation during discharge, hydrogen abstraction of the ether solvent, occurs despite of $^1O_2$ evolution. The underlying parasitic reactions during charge, carbon oxidative degradation and ether auto oxidation, seem to originate from $^1O_2$ evolution as the successful quenching by DABCO additive reduces the oxidation of Li_2O_2 plateau at approximately 1 V for the present cell configuration, as summarised in Figure 3.14.

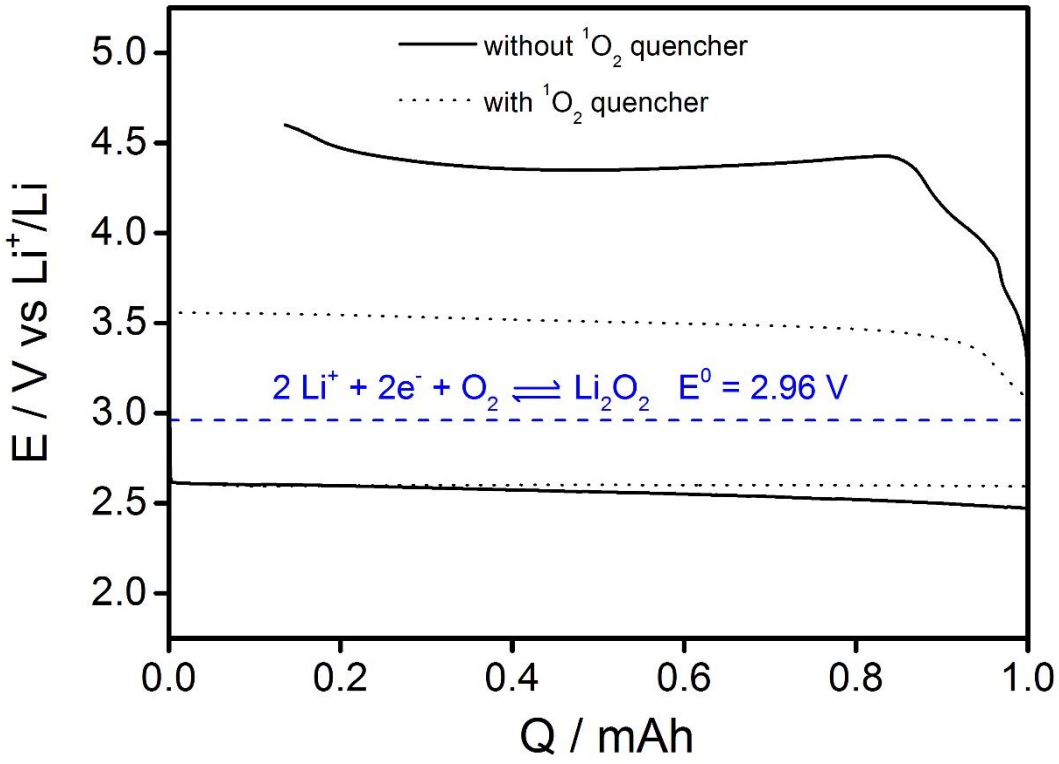

Figure 3.14: First galvanostatic discharge/charge cycle of Li-O_2 cell using a P50 Avcarb carbon fibre paper cathode in combination with a 1.0 M LiTFSI in DEGDME electrolyte with and without the addition of DABCO as a $^1O_2$ quencher.

3.5 Conclusions and future work

Hypercrosslinked polymers carbons were employed as cathode substrates delivering significant improvements in the first cycle performance of ether-based Li-O_2 cells in comparison to a conventional carbon black cathode. The HCPC cells exhibited enhanced absolute capacities and increased electrocatalytic activity towards ORR and OER, evidenced by the lower cathodic and anodic overpotentials obtained. The introduction of nitrogen heteroatom doping by the NH_3 heat treatment of HCP was found to have little influence on the Li-O_2 cell performance, comparable absolute capacities were achieved and the cell presented similar voltage polarisation. The superior electrochemical performance of HCPCs is related to its larger microporosity volume, increasing the number of three phase boundary regions for the oxygen reduction, and larger pore volume facilitating the oxidation process. The Li-O_2 cells using HCPC cathodes presented rapid capacity fade, associated with cathode and electrolyte instabilities characteristic of this system, however, these finding stipulates sensible direction towards designing better carbon materials for application in Li-O_2 cells.

The integration of 1, 4-diazabicyclo [2.2.2] octane (DABCO) to an ether-base electrolyte confirms the link between $^1O_2$ evolution and parasitic reactions characteristic of carbon-based non aqueous Li-O_2 cells. Increasing the concentration of DABCO in the electrolyte was found to be directly linked with a reduction of the voltage polarisation upon charging Li-O_2 cells. DABCO acts as physical quencher, and not as a redox mediator, causing the relaxation of $^1O_2$ as it is generated by the oxidation of Li_2O_2 thus mitigating the degradation of cell

components (carbon, binder, solvent and salt) by the reactive $^1O_2$. The tertiary amine additive was found to reduce the Li_2O_2 oxidation plateau by 1 V and to have little effect on the Li_2O_2 formation plateau. During discharge, Li_2CO_3 was detected along with Li_2O_2 similar to Li-O_2 cells using electrolytes without the quencher molecule. The Li-O_2 cells using DABCO additives also presented rapid capacity fade, possibly indicating that DABCO was not able to completely restrain the side product accumulation by the formation of $^1O_2$. Further research is necessary to provide insights into the mechanism of singlet oxygen quenchers in Li-O_2 cell. Nonetheless, it seems clear that DABCO can be integrated in the cell configuration to decrease the amount of parasitical side reactions.

3.6 References

1. P. G. Bruce, S. A. Freunberger, L. J. Hardwick and J.-M. Tarascon, *Nat. Mater.*, 2012, **11**, 19-29.
2. B. McCloskey, D. Bethune, R. Shelby, T. Mori, R. Scheffler, A. Speidel, M. Sherwood and A. Luntz, *J. Phys. Chem. Lett.*, 2012, **3**, 3043-3047.
3. B. McCloskey, A. Speidel, R. Scheffler, D. Miller, V. Viswanathan, J. Hummelshøj, J. Nørskov and A. Luntz, *J. Phys. Chem. Lett.*, 2012, **3**, 997-1001.
4. M. M. Ottakam Thotiyl, S. A. Freunberger, Z. Peng and P. G. Bruce, *J. Am. Chem. Soc*, 2012, **135**, 494-500.
5. D. M. Itkis, D. A. Semenenko, E. Y. Kataev, A. I. Belova, V. S. Neudachina, A. P. Sirotina, M. Hävecker, D. Teschner, A. Knop-Gericke and P. Dudin, *Nano Lett.*, 2013, **13**, 4697-4701.
6. J. Wandt, P. Jakes, J. Granwehr, H. A. Gasteiger and R. A. Eichel, *Angew. Chem. -Int. Edit.*, 2016, **128**, 7006-7009.
7. P. Atkins and J. De Paula, *Elements of physical chemistry*, Oxford University Press, USA, 2013.
8. N. Mahne, B. Schafzahl, C. Leypold, M. Leypold, S. Grumm, A. Leitgeb, G. A. Strohmeier, M. Wilkening, O. Fontaine and D. Kramer, *Nat. Energy*, 2017, **2**, 17036.
9. P. R. Ogilby, *Chem. Soc. Rev.*, 2010, **39**, 3181-3209.
10. J. S. M. Lee, M. E. Briggs, T. Hasell and A. I. Cooper, *Adv. Mater.*, 2016, **28**, 9804-9810.
11. B. Li, R. Gong, W. Wang, X. Huang, W. Zhang, H. Li, C. Hu and B. Tan, *Macromolecules*, 2011, **44**, 2410-2414.
12. S. Ganapathy, B. D. Adams, G. Stenou, M. S. Anastasaki, K. Goubitz, X.-F. Miao, L. F. Nazar and M. Wagemaker, *J. Am. Chem. Soc*, 2014, **136**, 16335-16344.
13. J. Hummelshøj, A. Luntz and J. Nørskov, *J. Chem. Phys.*, 2013, **138**, 034703.

14. D. Deng, X. Pan, L. Yu, Y. Cui, Y. Jiang, J. Qi, W.-X. Li, Q. Fu, X. Ma and Q. Xue, *Chem. Mater.*, 2011, **23**, 1188-1193.
15. Y. Wang, Y. Shao, D. W. Matson, J. Li and Y. Lin, *ACS Nano*, 2010, **4**, 1790-1798.
16. Y. Li, J. Wang, X. Li, D. Geng, M. N. Banis, R. Li and X. Sun, *Electrochem. Commun.*, 2012, **18**, 12-15.
17. J. Xiao, D. Mei, X. Li, W. Xu, D. Wang, G. L. Graff, W. D. Bennett, Z. Nie, L. V. Saraf and I. A. Aksay, *Nano Lett.*, 2011, **11**, 5071-5078.
18. X.-F. Li, K.-Y. Lian, L. Liu, Y. Wu, Q. Qiu, J. Jiang, M. Deng and Y. Luo, *Sci. Rep.*, 2016, **6**, 23495.
19. C. V. Rao, C. R. Cabrera and Y. Ishikawa, *J. Phys. Chem. Lett.*, 2010, **1**, 2622-2627.
20. Y. Li, X. Li, D. Geng, Y. Tang, R. Li, J.-P. Dodelet, M. Lefèvre and X. Sun, *Carbon*, 2013, **64**, 170-177.
21. Y. Li, J. Wang, X. Li, J. Liu, D. Geng, J. Yang, R. Li and X. Sun, *Electrochem. Commun.*, 2011, **13**, 668-672.
22. S. Meini, M. Piana, H. Beyer, J. Schwämmlein and H. A. Gasteiger, *J. Electrochem. Soc.*, 2012, **159**, A2135-A2142.
23. N. Ding, S. W. Chien, T. A. Hor, R. Lum, Y. Zong and Z. Liu, *J. Mater. Chem.*, 2014, **2**, 12433-12441.
24. H. Cheng and K. Scott, in *Rechargeable Lithium Batteries*, Elsevier, Editon edn., 2015, pp. 41-71.
25. B. D. McCloskey, A. Valery, A. C. Luntz, S. R. Gowda, G. M. Wallraff, J. M. Garcia, T. Mori and L. E. Krupp, *J. Phys. Chem. Lett.*, 2013, **4**, 2989-2993.
26. S. A. Freunberger, Y. Chen, N. E. Drewett, L. J. Hardwick, F. Bardé and P. G. Bruce, *Angew. Chem. -Int. Edit.*, 2011, **50**, 8609-8613.
27. E. A. Ogryzlo and C. W. Tang, *J. Am. Chem. Soc*, 1970, **92**, 5034-5036.
28. B. Enko, S. M. Borisov, J. Regensburger, W. Bäumler, G. Gescheidt and I. Klimant, *J. Phys. Chem. A*, 2013, **117**, 8873-8882.

29. L. Johnson, C. Li, Z. Liu, Y. Chen, S. A. Freunberger, P. C. Ashok, B. B. Praveen, K. Dholakia, J.-M. Tarascon and P. G. Bruce, *Nat. Chem.*, 2014, **6**, 1091-1099.
30. C. Ouannes and T. Wilson, *J. Am. Chem. Soc*, 1968, **90**, 6527-6528.
31. R. H. Young and R. L. Martin, *J. Am. Chem. Soc*, 1972, **94**, 5183-5185.
32. R. R. Mitchell, B. M. Gallant, Y. Shao-Horn and C. V. Thompson, *J. Phys. Chem. Lett.*, 2013, **4**, 1060-1064.

Chapter 4.
Aprotic Sodium-Oxygen Battery Systems

4.1 Abstract

This chapter reports a comprehensive investigation on the different aspects of the chemistry involved in the aprotic room-temperature sodium-oxygen battery (Na-O_2). Initially, the higher stability of ether-based electrolytes towards superoxide attack was demonstrated, in comparison to classic battery electrolyte solvents such as propylene carbonate, and the main reaction product (NaO_2) and side reaction products (Na_2CO_3, CH_3COONa and NaOH) identified via different techniques: Raman, FTIR, PXRD, SEM and EDS. The effect of increasing the ether chain length, and thus the Gutmann donor number of the solvent, was probed for different glyme-based electrolytes and the conditions in which different discharge mechanisms takes place, a surface confined route or a solution route, were evaluated. The nucleation and growth of NaO_2 crystals was investigated during the course of discharge via SEM and AFM for a single current density. The effect of varying current density on the crystals morphology, as well as the electrochemical performance, is also discussed. The stability of NaO_2, the main reaction product for the present cell configuration, is studied, and whether or not it can undergo chemical disproportionation reaction or further electrochemical reduction to other sodium oxide phases previously reported in Na-O_2 batteries. Finally, the chemical stability and electrochemical performance of different polymeric binders and various carbon materials used in the positive electrode of Na-O_2 cells is discussed.

4.2 Introduction

As previously outlined, the main advantage of alkali metal-oxygen batteries over state-of-the-art rechargeable battery systems is their theoretical specific energy (energy per unit mass), which motivated extensive research over the past two decades on fundamental aspects and development of practical cells for the implementation of these systems[1].

The lithium-oxygen (Li-O_2) battery, which has the highest specific energy, suffers from a variety of shortcomings that hinder its realisation. Among practical challenges, the desired discharge product lithium peroxide (Li_2O_2) of the battery can induce electrolyte and cathode instabilities, which have a deleterious effect on capacity retention and limit long cyclability[2]. Thus, this makes the case for investigating alternative alkali metal battery systems such as the analogous Na-O_2 battery.

Intriguingly, different reaction pathways have been reported for the Na-O_2 system, ultimately resulting in the formation of both sodium superoxide (E^0 (NaO_2) = 2.33 V vs Na^+/Na) and sodium peroxide (E^0 (Na_2O_2) = 2.27 V vs Na^+/Na) during the discharge process[3]. Most research papers have reported a single reaction product, instead of a mixture of both. The underlying factors which contribute to the final reaction product are not yet fully understood. However, it seems clear from different reports that the cell chemistry of NaO_2 based cells present certain advantages over Na_2O_2 based cells. Namely, larger capacities, higher coulombic efficiencies, lower voltage gaps and extended cycle life[3].

While initial reports showed promising results[4], there is still many fundamental and practical challenges to be addressed. There is a lack of understanding on how parasitic degradation reactions, from both electrode components (carbon and binder) and electrolyte components (solvent and salts), affect charge retention. Theoretical calculations have predicted the conditions in which NaO_2 or Na_2O_2 is the stable phase[5], however in actual cells it is still not clear how to steer the reaction product. Capacities much lower than the expected theoretical values are reported[6], calling for better cathode optimisation. The early cell "death" and the growth mechanism of NaO_2 precipitates need to be investigated in order to enhance energy density. Rate capabilities need to be improved and better understood, as controversial findings on the effect of current density have been reported[7].

This chapter will examine the aforementioned issues using practical two-electrode electrochemical cell set up and look into different aspects of the Na-O_2 battery system using ether-based electrolytes and carbon cathodes.

4.3 Experimental methods

This section provides specific experimental conditions for the results discussed in this chapter. For more detailed information see: Chapter 2. Experimental procedures and techniques.

4.3.1 Electrolyte preparation

The selected solvents propylene carbonate (PC), 1,2 dimethoxyethane (DME), diethylene glycol dimethyl ether (DEGDME) and tetraethylene glycol dimethyl ether (TEGDME) were distilled and dried over freshly activated molecular sieves (4 Å). Finally they were stored in an argon glove box (<0.1 ppm H_2O and <0.1 ppm O_2). Sodium hexafluorophosphate ($NaPF_6$) and sodium trifluoromethanesulfonate (NaOTf) were used as supporting salts and dried under vacuum at 80°C overnight. The electrolyte solutions: 1.0 M $NaPF_6$ in PC and 0.5 M NaOTf in DME, DEGDME or TEGDME were prepared inside an Ar glove box and H_2O content measured with a Karl Fischer Coulometer. Solvents were found to have <10 ppm water.

4.3.2 Carbon cathode preparation

The air-cathodes consisted of different carbon materials: gas diffusion layer (H24, Freudenberg & Co.), carbon paper (P50, Avcarb), graphite felt (GFD 2.5EA, SGL Group), single wall carbon nanotube (Elicarb), and conductive carbon black (Ketjenblack EC 600 JD, AkzoNobel and Super C65, Imerys). The composite electrodes were prepared using poly(tetrafluoroethylene) (PTFE) binder (80%

active carbon material, 20% binder) by mixing into a slurry with ethanol. The putty like mixture was put in a calender and pressed to a thickness of 100 μm to obtain self-supporting films. The electrodes were punched into 10 mm disc then dried at 120 °C under vacuum overnight. For the investigation into the influence of the polymeric (binder section 4.4.6), carbon black electrodes were cast using the same procedure, but using poly(vinylidene fluoride) (PVDF) and carboxymethylcellulose sodium salt (CMC) instead. The binder-free carbon fibre electrodes were dried in a similar manner.

4.3.3 Cell assembly

Na-O_2 cells were assembled using a custom built Swagelok set-up. Sodium metal was used as an anode, roll pressed and cut into a 0.785 cm^2 disc. Two Whatman glass fibre separators (GF-G grade, 470 μm) were impregnated with 0.12 mL of the chosen electrolyte. The separators went through the same cleaning process as the cathodes. Different carbon materials were used as cathodes as 10 mm diameter discs. The cathodes were held by a stainless steel current collector containing holes to allow O_2 access. The assembled Swagelok cells were transferred in a sealed glass chamber to the O_2 line station. The chamber was purged with dry O_2 for 10 minutes, and the cell rested for 3 hours at the open-circuit potential (OCP) prior to discharge. The galvanostatic discharge was performed using a Bio-Logic MPG-2 battery cycler. The discharge rate was based on the geometric cross-sectional area of the cathodes. All potentials are referenced against Na^+/Na.

4.3.4 Cell disassembly and cathode characterisation

After electrochemical measurements, the Swagelok cells were disassembled inside the glove box without atmosphere exposure. The positive electrodes were washed twice with dry DEGDME, 10 minutes each time. Finally the electrodes were dried in the glove box vacuum chamber overnight.

Fourier-transform infrared (FTIR) data was collected on a Nicolet 6700 spectrometer (Thermo Fisher Scientific) by grinding portions of the discharged cathode into CsI pellets. Data was collected in transmission mode inside a nitrogen-filled glove box.

Raman data was taken on a Renishaw in via microscope with a 532 nm laser (2 mW cm^{-2}) in a gas-tight cell (ECC-Opto-STD, El-Cell GmBH) focussed through a microscope (Leica) via a 50x objective lens (Leica). The cathodes placed behind a quartz window to allow viewing of the electrode.

Powder X-ray diffraction data was obtained using a PANalytical X'Pert Pro diffractometer (Cu Kα1) in Bragg-Brentano geometry. The carbon cathodes were sealed in borosilicate glass capillary tubes under an inert atmosphere (argon-filled glove box) using silicon rubber to seal. After removing the capillary from the glove box they were heat sealed with a blowtorch.

For atomic force microscope (AFM) analysis all carbon paper cathodes were discharged in the same electrolyte. They were cut in half so as to provide clarity between the SEM images and AFM images. The cathodes were scanned using scanasyst air tips (spring constant 0.7 Nm^{-1}, resonant frequency 150 KHz)

using quantitive nanomechanical mapping (QNM) techniques. Image analysis was performed upon nanoscaleanalysis as provided by Bruker.

Scanning electron microscopic (SEM) images were recorded with a JEOL JSM-7001F field emission electron microscope fitted with energy dispersive X-ray spectroscopy (EDS) analysis equipment (Oxford Instruments INCAx-act X-ray detector).

4.4 Results and Discussion

4.4.1 Stability of organic carbonate based electrolytes

To investigate the electrochemical behaviour of alkyl carbonate electrolytes, Na-O_2 cells were assembled using a 1.0 M $NaPF_6$ in PC electrolyte together with a binder free gas diffusion layer (GDL) carbon cathode (H24, Freudenberg & Co., $1 m^2 g^{-1}$). The cell was cycled with a potential window of 1.8 V to 4.4 V vs Na^+/Na at a current density of 0.12 mA cm^{-2}.

The potentiodynamic E vs capacity profile (Figure 4.1a) presents a specific capacity of 112 mAh g^{-1} based on the carbon electrode mass and a discharge plateau of 2.09 V vs Na^+/Na close to thermodynamic potential for NaO_2 formation (E^0 = 2.27 V vs Na^+/Na) and Na_2O_2 formation (E^0 = 2.33 V vs Na^+/Na). The charge curve, however, reached a plateau at 4.3 V similar to the behaviour of alkyl carbonates in Li-O_2 cells[8], characterised by large polarisation, which can be related to sluggish oxidation kinetics or the formation of more stable electrolyte degradation products.

The recharge curve does not show a definitive end point, a sharp increase in voltage when all the products formed during discharge are oxidised. Instead, it steadily increases and only stops when it reaches the voltage cut off. This behaviour is indicative of oxidative decomposition. The carbon electrode is known to be unstable at voltages higher than 3.5 V vs Li^+/Li (3.83 V vs Na^+/Na) in the presence of strong nucleophiles[9], such as NaO_2. The concomitant formation of new side products, while the discharge reaction products are still being oxidised explains the larger charge capacity obtained.

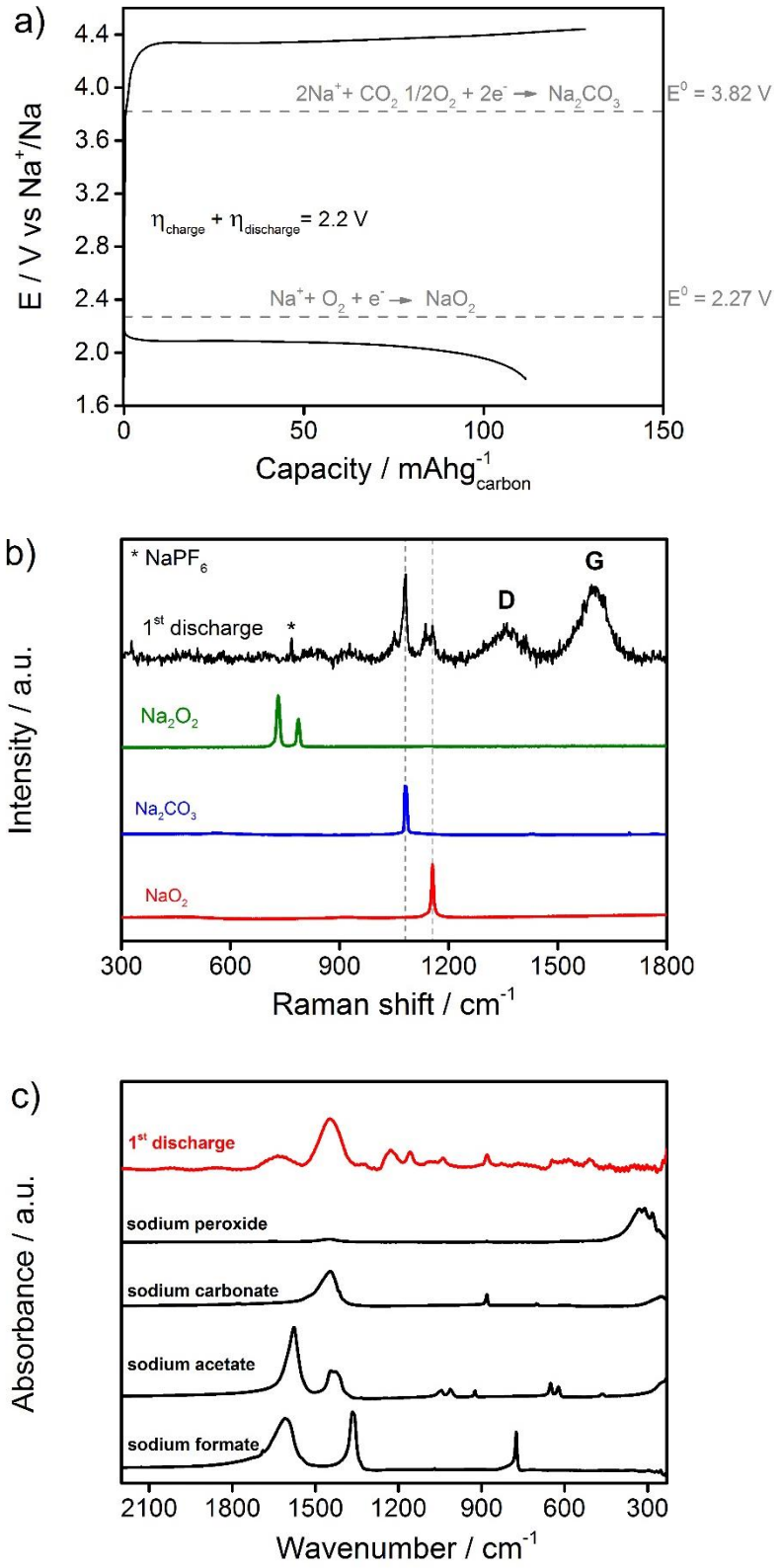

Figure 4.1: a) First galvanostatic discharge/charge cycle; b) FTIR and c) Raman analysis of the GDL H24, Freudenberg carbon cathode after one discharge process in a 1.0 M $NaPF_6$ in PC electrolyte at 0.12 mA cm^{-2} current rate.

The Raman analysis of the discharged cathode (Figure 4.1b) indicates a mixture of NaO_2 at 1156 cm^{-1} and sodium carbonate (Na_2CO_3) at 1080 cm^{-1} as main discharge products, similar to other reports on the literature[10]. The Raman signal at 1060 cm^{-1} is assign to longer chain carbonate species. The Raman signal visible at 1136 cm^{-1} related to the dissolution of NaO_2 and will be discussed in further detail in section 4.4.7. No vibration modes associated with Na_2O_2 were observed via Raman or infrared. FTIR analysis (Figure 4.1c) shows other moieties, such as O–C=O, C=O and C–O–C, indicating further electrolyte decomposition due to the formation of carboxylates and esters.

The morphology of the discharge products observed under the scanning electron microscope further corroborates electrolyte degradation as the main cell process. Images in Figure 4.2 show that the GDL carbon fibres are covered with nano-sized granular shaped particles, similar to the morphology of other reports of Na_2CO_3 as main discharge product in Na-O_2 cells[10]. No micron-sized cubic shaped particles were observed – expected morphology of NaO_2 – indicating that the main reaction pathway using propylene carbonate is electrolyte decomposition. A degradation mechanism for the PC electrolyte during the discharge process is proposed in Scheme 4.1.

The superoxide radical anion ($O_2^{\bullet -}$) that is initially formed upon reduction of molecular oxygen at the carbon cathode induces ring opening in the PC molecule by nucleophilic attack on the ethereal carbon which is less sterically hindered. This reaction is exothermic and has been reported to have a negligible activation energy barrier[11].

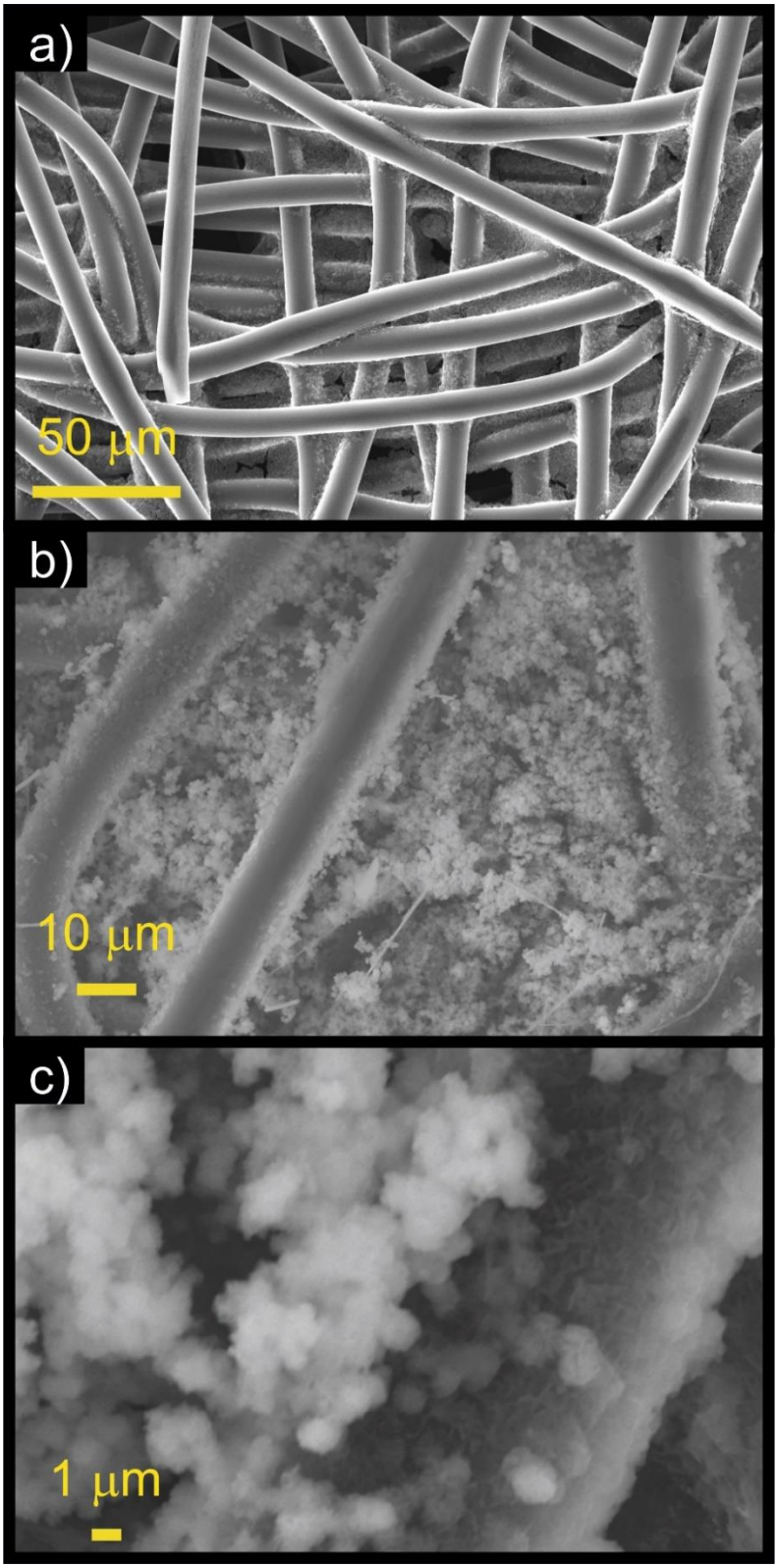

Figure 4.2: SEM images of a) the pristine cathode, b) and c) solid precipitates on the GDL H24, Freudenberg carbon cathode after one discharge process in a 1.0 M $NaPF_6$ in PC electrolyte at 0.12 mA cm^{-2} current rate.

The nucleophilic attack results in the formation of an unstable peroxyalkyl carbonate intermediate which can, through oxidative decomposition, generate carbon dioxide and other by-products. Carbon dioxide further reacts with the superoxide radical anion to form a peroxydicarbonate anion which binds with sodium ions resulting in sodium carboxylates and Na_2CO_3. Evidence of the reaction of superoxide and carbon dioxide has been reported by Compton *et al.*[12] using microelectrode cyclic voltammetry.

Scheme 4.1: Degradation mechanism in propylene carbonate electrolytes.

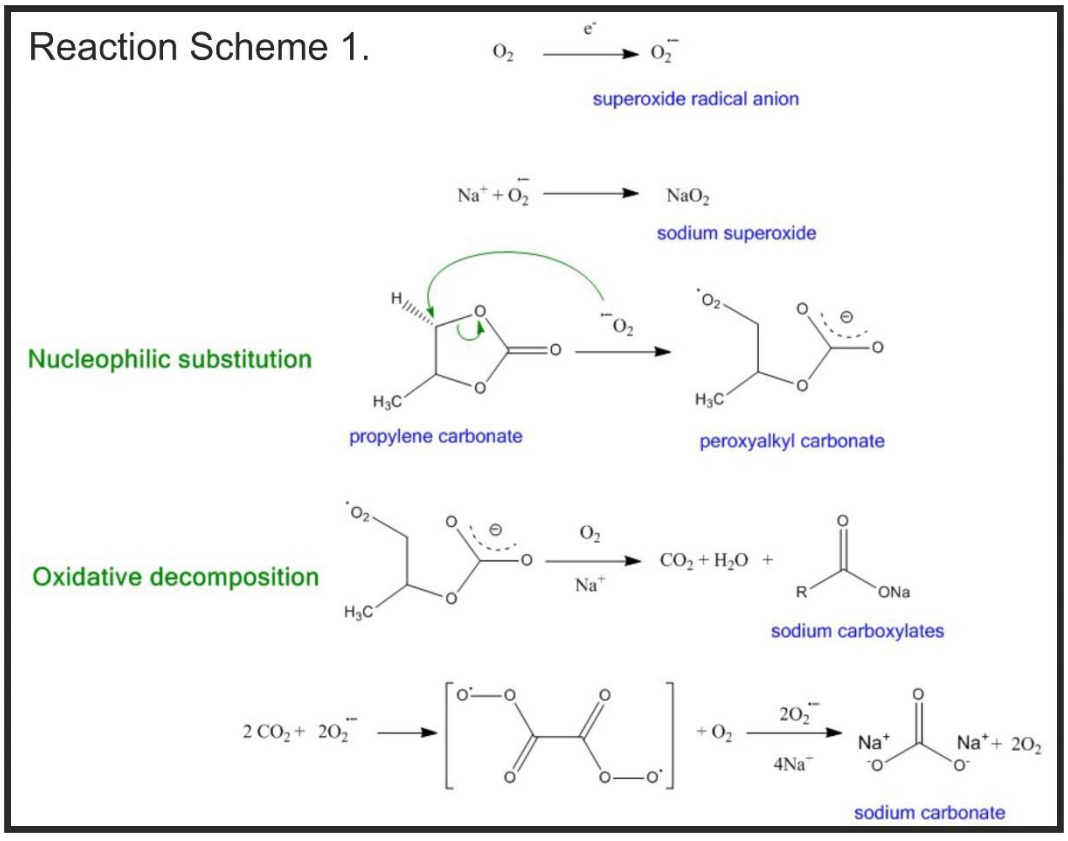

Similar potential vs capacity profiles with large charge overpotential and increasing charge potential plateau were found for a propylene carbonate cell using

a high surface area porous carbon black cathode (see Appendix A, Figure A1). The same mix of NaO_2, Na_2CO_3 and carboxylates was detected as the discharge products with comparable morphology. Thus indicating that the behaviour of the cell is characteristic of the electrolyte and not influenced by the carbon substrate.

In Na-O_2 cells, PC electrolyte undergoes similar degradation processes analogous to lithium systems. Since the one-electron reduction reaction to form NaO_2 is more kinetically favoured compared to the two-electron reduction to form Li_2O_2[13], NaO_2 is still found as a discharge product in alkyl carbonate electrolytes, which differs from the Li-O_2 reports[8]. However, NaO_2 can also act as a nucleophile and react undesirably with the electrolyte.

4.4.2 Stability of ether based electrolytes

To evaluate the performance and stability of ether-based electrolytes, Na-O_2 cells were assembled using a 0.5 M NaOTf in DEGDME electrolyte together with the same GDL carbon cathode (H24, Freudenberg, $1 m^2 g^{-1}$). The cell was cycled with a potential window of 1.8 V to 3.1 V vs Na^+/Na at a current density of 0.12 mA cm^{-2}.

The potentiodynamic E vs capacity profile (Figure 4.3a) presented a specific capacity of 212 mAh g^{-1} based on the carbon mass and 91% capacity retention. The galvanostatic profile differs from Na-O_2 cells using alkyl carbonate electrolytes and Li-O_2 cells using ether-based electrolytes[14] on the larger capacities obtained and much lower oxidation overpotential (η_{charge}) around 150 mV, within the stability of carbon towards oxidative decomposition and minimising electrolyte degradation.

In analogous Li-O_2 cells, using the same GDL cathode and DEGDME electrolyte, the charge curve reaches a plateau at 1.53 V overpotential and, in fact, lower maximum capacities are achieved (See Appendix A, Figure A2). Since both Li_2O_2 and NaO_2 has been reported to be wide band gap insulators[15], the observed lower charge overpotential in Na-O_2 cells must arise from other characteristics of the system such as less extent of electrolyte degradation reactions, which is in fact confirmed by FTIR and Raman analysis.

The Raman spectrum of the discharge cathode (Figure 4.2b) is characterised by a single, intense peak at 1156 cm^{-1} which can be related to the ν_{O-O} stretching mode in NaO_2 and indicates a one-electron reduction of dioxygen (Eq. 4.1). The disappearance of the oxygen vibration indicates that NaO_2 was reversibly oxidised upon charge (Eq. 4.2). The two broad bands observed in the spectrum at 1353 cm^{-1} and 1581 cm^{-1} are assigned to the D and G bands of the carbon substrate.

Discharge	$Na^+ + O_2 + e^- \rightarrow NaO_2$	4.1
Charge	$NaO_2 \rightarrow Na^+ + O_2 + e^-$	4.2

Figure 4.2c shows the FTIR spectra of the discharged carbon cathode together with known standards of possible discharge products. Na_2O_2 stretching modes (ν_{Na-O} ~ 330 cm^{-1}) were not detected as a discharge product and NaO_2 is not expected to appear on the infrared region due to the homopolarity of the superoxide anion. Vibrations associated with Na_2CO_3 and sodium acetate (CH_3COONa) are detected on the carbon electrode due to electrolyte degradation. Other side products such as polyethers/esters reported for Li-O_2 cells[14] were not detected, indicating less extent of parasitic reactions in Na-O_2 systems in comparison to lithium systems.

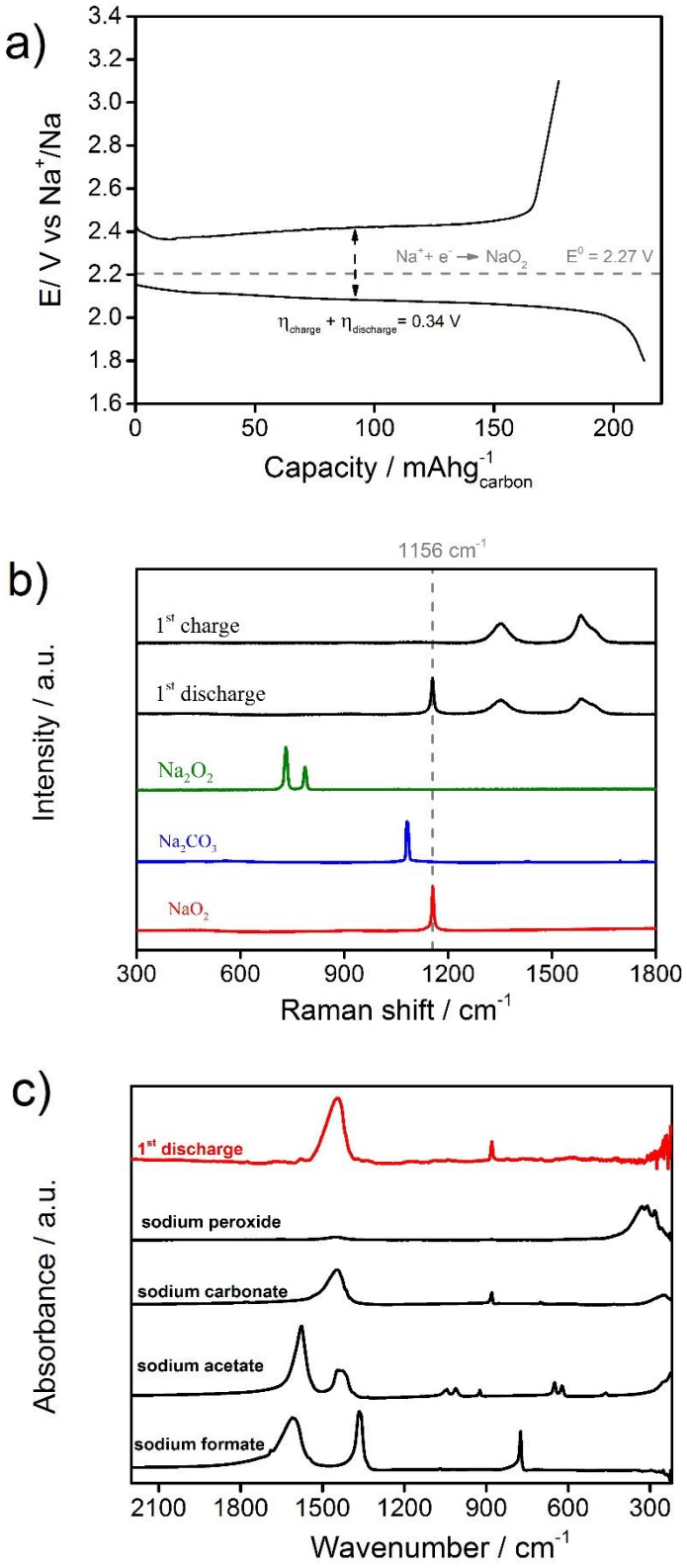

Figure 4.3: a) First galvanostatic discharge/charge cycle; b) FTIR and c) Raman analysis of the GDL H24, Freudenberg carbon cathode after one discharge process in a 0.5 M NaOTf in DEGDME electrolyte at 0.12 mA cm^{-2} current rate.

The PXRD data of the discharged GDL cathode presents all the Bragg reflection peaks related to NaO_2 which has a disordered pyrite structure at room-temperature, space group $Fm\bar{3}m$, with sodium chloride (NaCl) symmetry[4]. Other reflections observed are related to the carbon electrode and the expected side products. Sodium hydroxide (NaOH) reflections are detected in the discharged cathode, however at very low concentration, since a second charge plateau is not observed as is expected for Na-O_2 cells with NaOH as the main reaction product[16].

Based on the galvanostatic profile, Figure 4.3a, the yield of NaO_2 formed upon discharge is 91%, established by the amount of charge which is oxidised at low polarisation. The remaining charge is related to electrolyte degradation products, such as Na_2CO_3, (CH_3COONa) and NaOH detected by FTIR and PXRD.

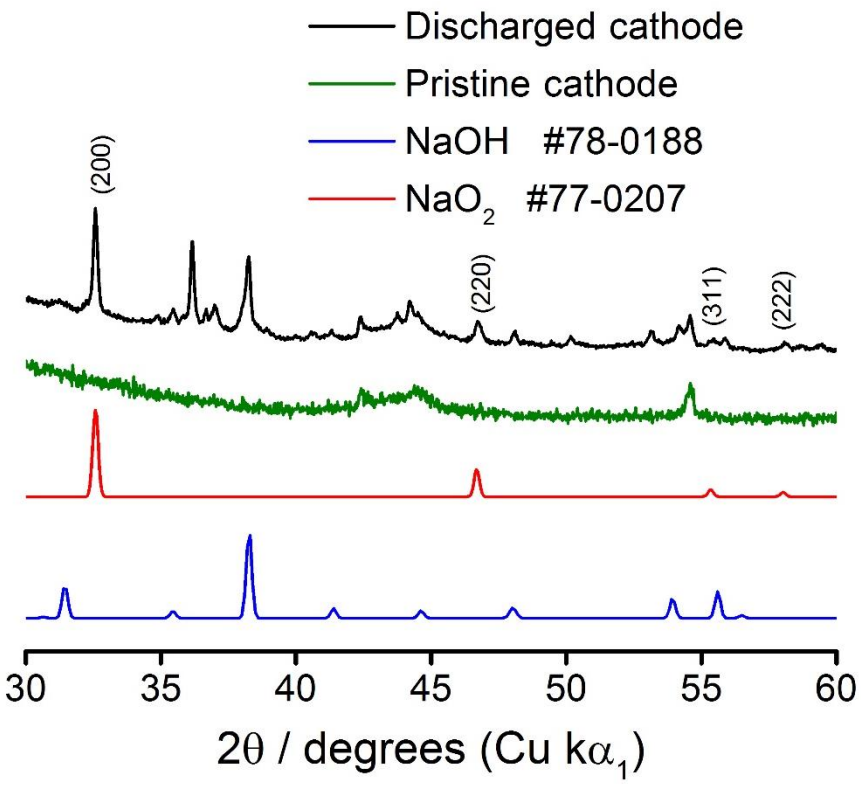

Figure 4.4: PXRD data for GDL H24, Freudenberg carbon cathode after one discharge in a 0.5 M NaOTf in DEGDME electrolyte at 0.12 mA cm^{-2} current rate.

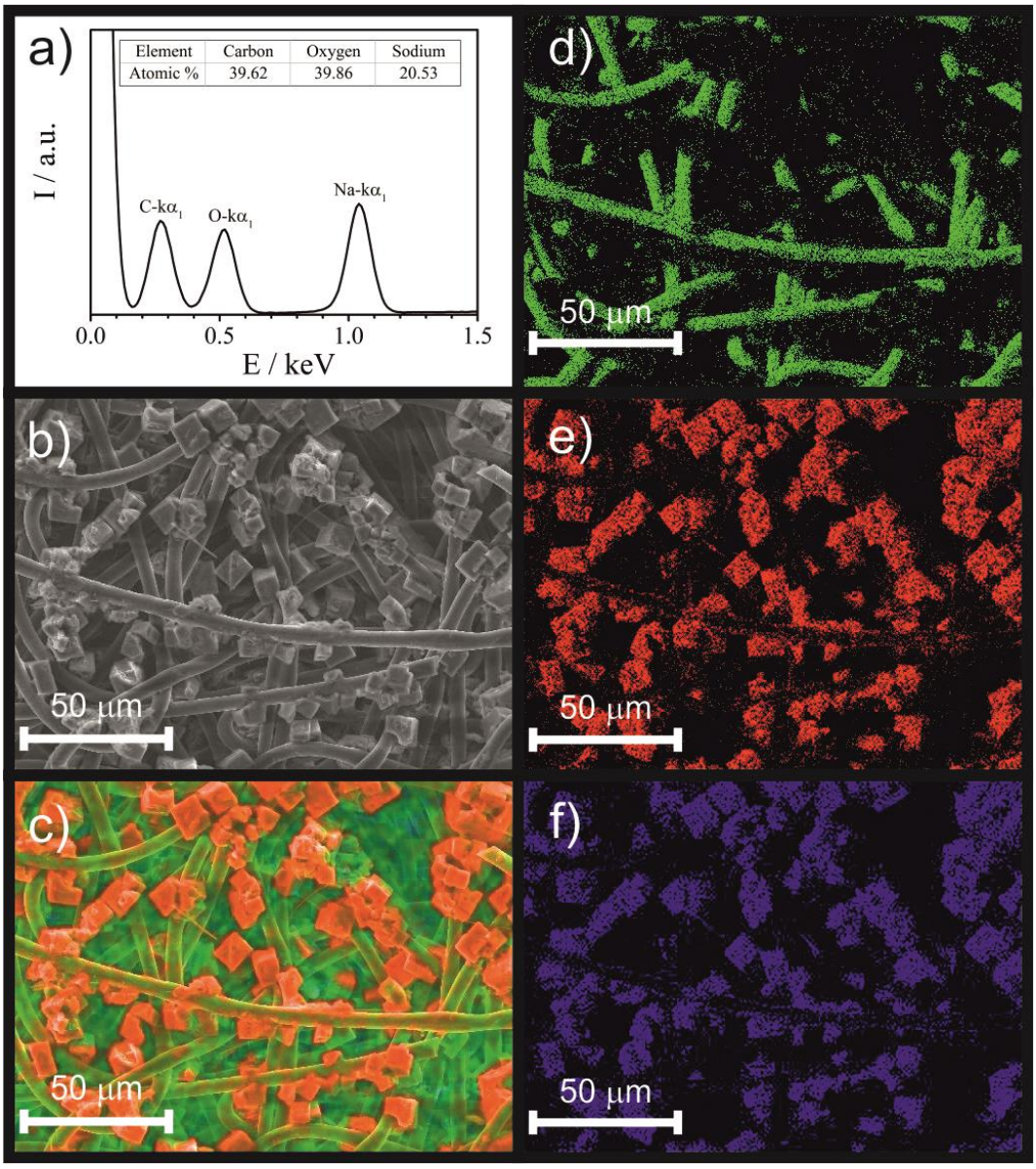

Figure 4.5: SEM and EDS analysis of a discharged cathode showing: a) EDS spectrum, b) SEM image, c) overlay of SEM image and elemental analysis map ("Cameo+", Oxford Instruments) and raw elemental data for d) Carbon, e) Sodium and f) Oxygen.

The morphology of the discharge product observed under the scanning electron microscope is shown in Figure 4.5b. Cubic shaped particles are visible on the carbon fibres through the whole extension of the electrode with an average particle size of 21 µm. In the EDS spectrum, Figure 4.5a, taken from the image

shown in Figure 4.5b, the spectral lines characteristic to sodium and oxygen element register an average atomic ratio of 1:2 respectively, which further corroborates NaO_2 as the main discharge product. The raw element mappings show that the cubes are composed of sodium and oxygen only, no cubic structure is observed on the carbon map. A film composed of sodium and oxygen is observed to grow on the carbon fibre a part from the cubic structures. The conditions in which a NaO_2 film is formed along with cubic precipitates will be discussed in further details in section 4.4.5.

Similar discharge/charge profiles are observed using different carbon cathodes, indicating the cell follows the same discharge mechanism independent of the substrate active material. The effect of different carbon substrates will be discussed in further detail in section 4.4.10.

The electronegativity difference between carbon and oxygen in the glyme backbone creates an electron deficient centre on the alpha carbon (adjacent to the oxygen heteroatom), which is susceptible to a nucleophilic attack from $O_2^{\bullet-}$ generated on the carbon surface during discharge. The proton abstraction leads to an ether peroxide radical intermediate which can undergo oxidative decomposition in the presence of oxygen species to generate the acetate observed in the FTIR spectra, CO_2 and hydroxyl anions.

The nucleophilic oxygenation of carbon dioxide by the superoxide anion in aprotic media is a reaction that is well described in the literature[12, 17], and leads to the formation of Na_2CO_3 and CH_3COONa also detected in the infrared spectroscopy analysis of the discharged cathode.

Scheme 4.2: Degradation mechanism in ether-based electrolytes.

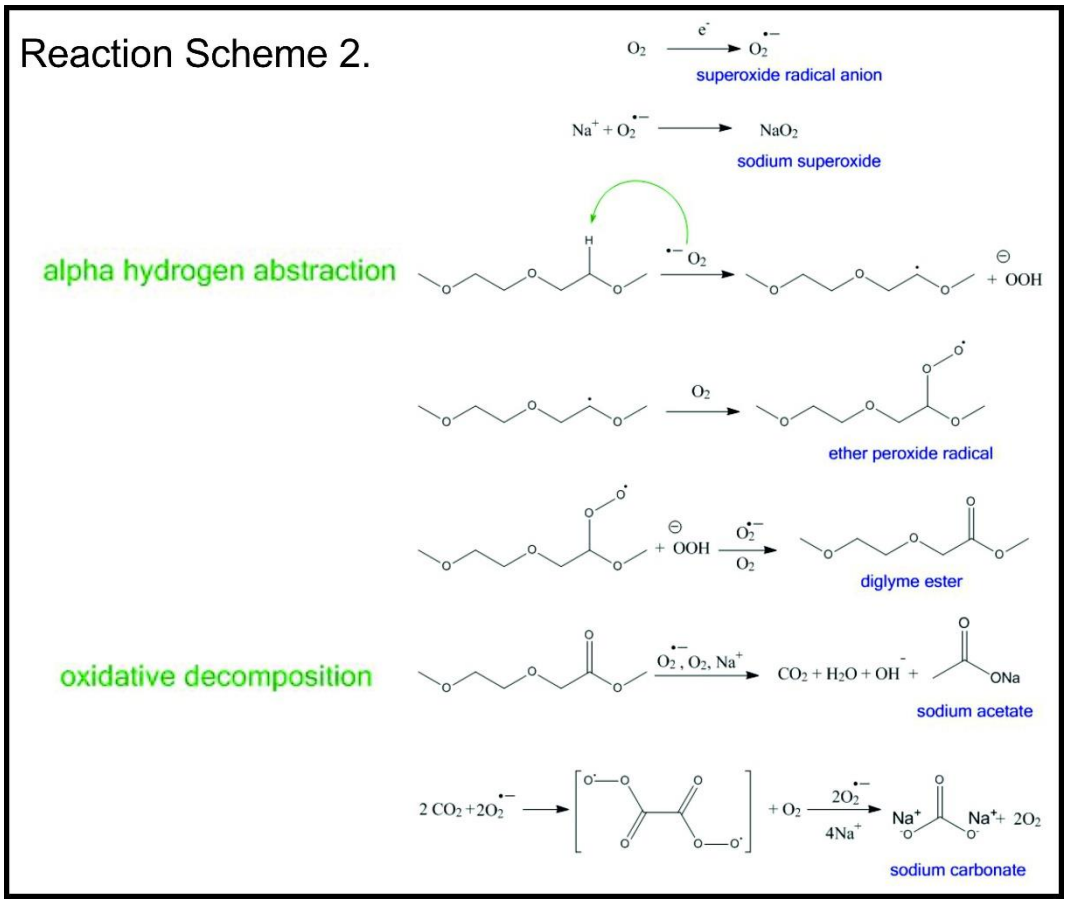

4.4.3 Cyclability

Based on the lesser extent of electrolyte degradation and faster O_2/O_2^- kinetics previously discussed, improved cyclability would be expected of ether-based Na-O_2 cells. The main factor limiting multiple cycling with the present cell configuration was the formation of dendrites during sodium plating (charging step). Figure 4.6 shows a typical potentiometric profile for a Na-O_2 cell where dendritic deposits eventually caused failure by short-circuiting. A characteristic discharge plateau of 2.08 V vs Na^+/Na is observed for the formation of NaO_2 on the cathode surface, followed by the charge at low overpotential as is expected for this reaction.

After only 36 % of the absolute discharge capacity, a potential drop to 0 V vs Na^+/Na occurs when the dendrite growth eventually reaches the positive electrode. After short-circuit, the current flows through the cell, instead of the outer circuit, and the local heat generated dissolves the sodium metal dendrite, causing the potential to fluctuate which dominates the cell reaction. After disassembling the cell, several grey spots are visible on the separator surface (Figure 4.6 inset) related to sodium metal passing through the separators.

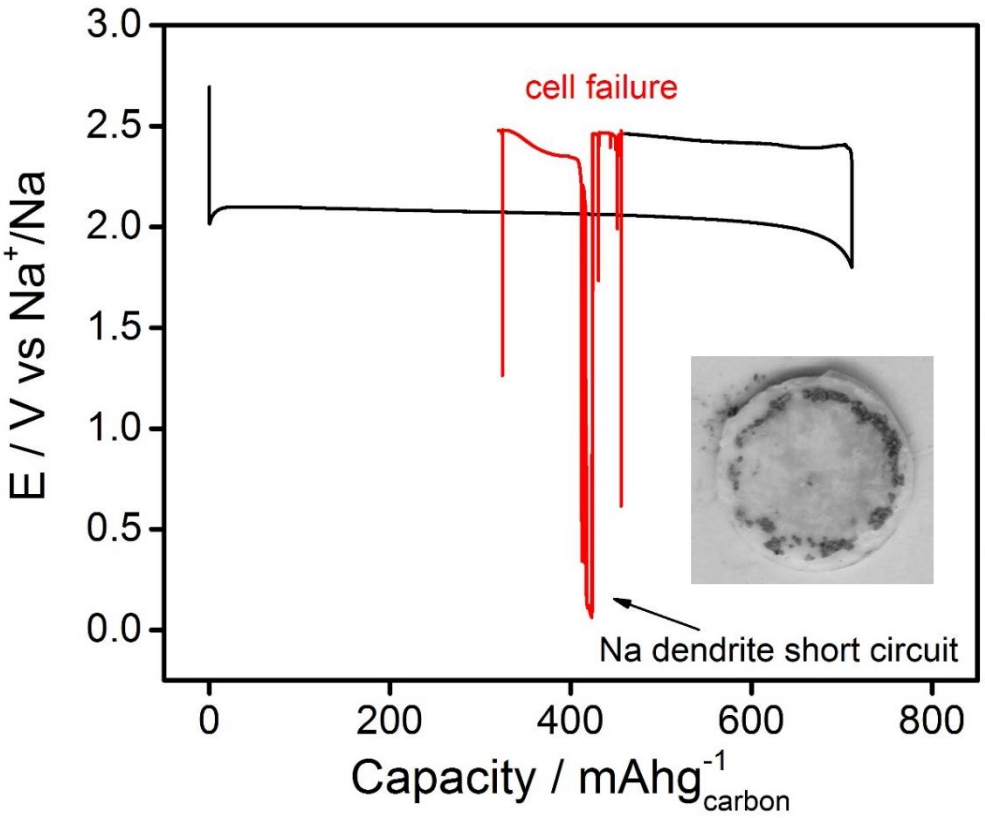

Figure 4.6: First galvanostatic discharge/charge cycle of the P50 Avcarb carbon fibre paper cathode in a 0.5 M NaOTf in DEGDME electrolyte at 0.12 mA cm^{-2} current rate. Inset shows an image of a glass fibre separator after cell failure.

Several attempts were made to overcome or mitigate this problem. Physically increasing the distance between the electrodes (using multiple glass fibre

separators) can delay dendrite formation extending the charge process without solving the short circuiting problem (see Appendix A, Figure A3). This approach represents an increase in the overall weight of the cell, as more electrolyte is needed, and sacrifices specific energy.

Using mechanically stronger ceramic separators (than common glass fibre) also delayed the short-circuiting of the cell (see Appendix A, Figure A4). A report by Monroe *et al.*[18] proposed that dendrites could be suppressed if the shear modulus of the separator was larger than the shear modulus of the lithium metal. However, the accumulation of dendritic nuclei, which were not removed during subsequent discharge, eventually caused cell failure on the second galvanostatic cycle.

Two electrolyte additives that rendered improved cyclability in lithium batteries were tested in Na-O_2 cells (see Appendix A, Figures A5 and A6). Ding *et al.*[19] proposed a "self-healing mechanism" where the addition of cations with lower reduction plating potential than lithium induced an even deposition of the metal anode. The additive cations would form a positive charge around the dendrite nuclei and forcing lithium ion to deposit adjacent to the nuclei more uniformly. Choudhury *et al.*[20] reported the addition of sulfonate enantiomers which were able to lower the electric field at the electrode/electrolyte interface causing lithium to form flat deposits. Both approaches failed to eliminate dendrites in the present Na-O_2 cell configuration. The larger ionic radius and lower metallic bonding (sodium metal is more easily moldable)[21] of sodium makes the formation of dendrites more severe in these systems.

Cycling Na-O_2 cells with capacity limitation instead of a voltage cut off (shallow cycling) can significantly improve cycle life while maintaining capacity

retention, albeit at the penalty of cell capacity. The data shown if Figure 4.7 shows cycling at 222 mAh g^{-1} – 1mAh (28% of the maximum capacity obtained with deep cycling). Stable cycling is observed up to 15 cycles at high coulombic efficiency (91% retention) related to the greater reversibility of the redox couple O_2/NaO_2. Eventually cell failure occurs due to unstable metal deposition.

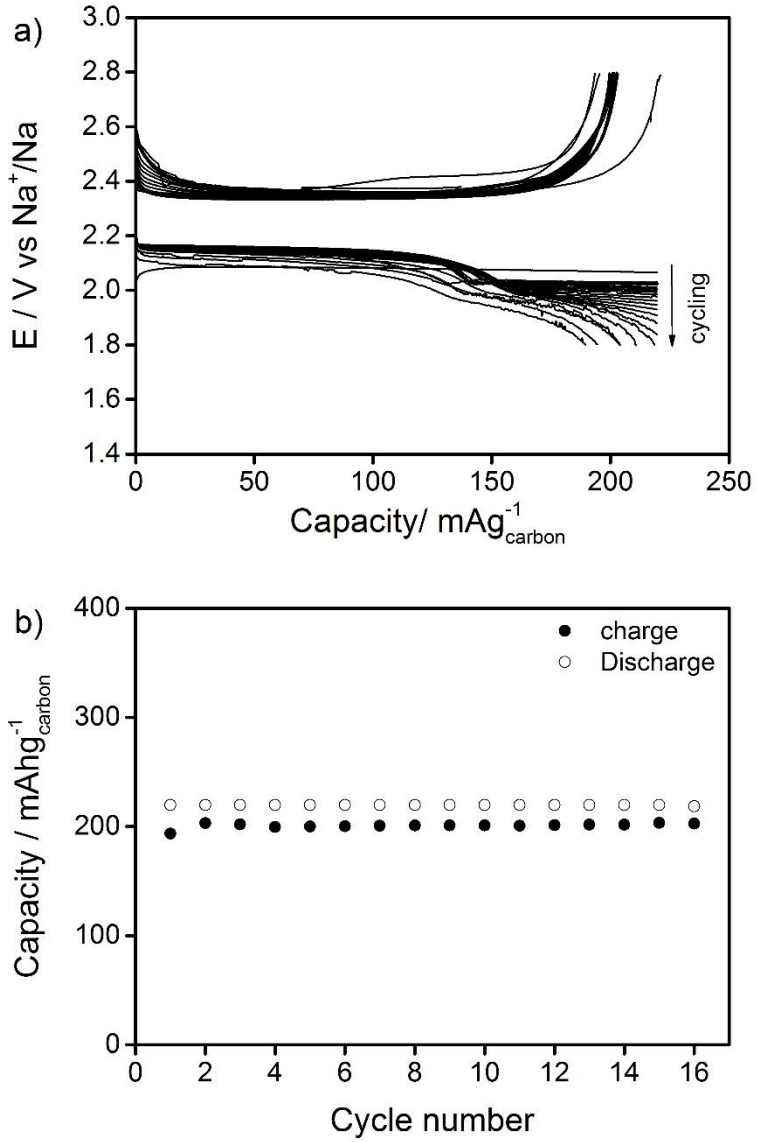

Figure 4.7: a) Galvanostatic discharge/charge profile b) cyclability data of a Na-O_2 cell with capacity cut off at 222 mAh g^{-1} (1 mAh). Current density: 0.12 mA cm^{-2} Electrolyte: 0.5 M NaOTf in DEGDME. Cathode: P50 Avcarb carbon fibre paper.

The primary challenge limiting long cycling of Na-O_2 cells is the metal anode. While a solution to this issue is not established, it is important to optimise and understand fundamental reactions happening at the positive electrode, which will be discussed in the following sections.

4.4.4 Effect of electrolyte solvent chain length

To investigate the effect of varying the ether solvent's chain length on the performance of Na-O_2, three different solvents were employed as electrolytes; DME, DEGDME and TEGDME. Na-O_2 cells were assembled with the same 0.5 M concentration of NaOTf conductive salt and a binder-free carbon fibre paper cathode (Avcarb P50, 10 m^2 g^{-1}). Representative discharge/charge profiles for the three systems are shown in Figure 4.8.

The distinct behaviour in the specific capacity of the cell cycled with TEGDME from the other electrolytes indicates a strong influence of increasing the ether chain length in the performance of the cells. The overall discharge capacity of cells cycled with DME was 575 mAh g^{-1} and cells cycled with DEGDME had very similar capacity 544 mAh g^{-1}. In stark contrast, TEGDME based cells showed much lower capacities, 50 mAh g^{-1}, and a sharper potential decline. The abrupt end observed for the charge process is related to the dendritic issues discussed in the previous section.

Using a shallow cycling procedure (see Appendix A, Figure A7), is possible to demonstrate that DME and DEGDME cells have similar coulombic efficiency and voltage gap.

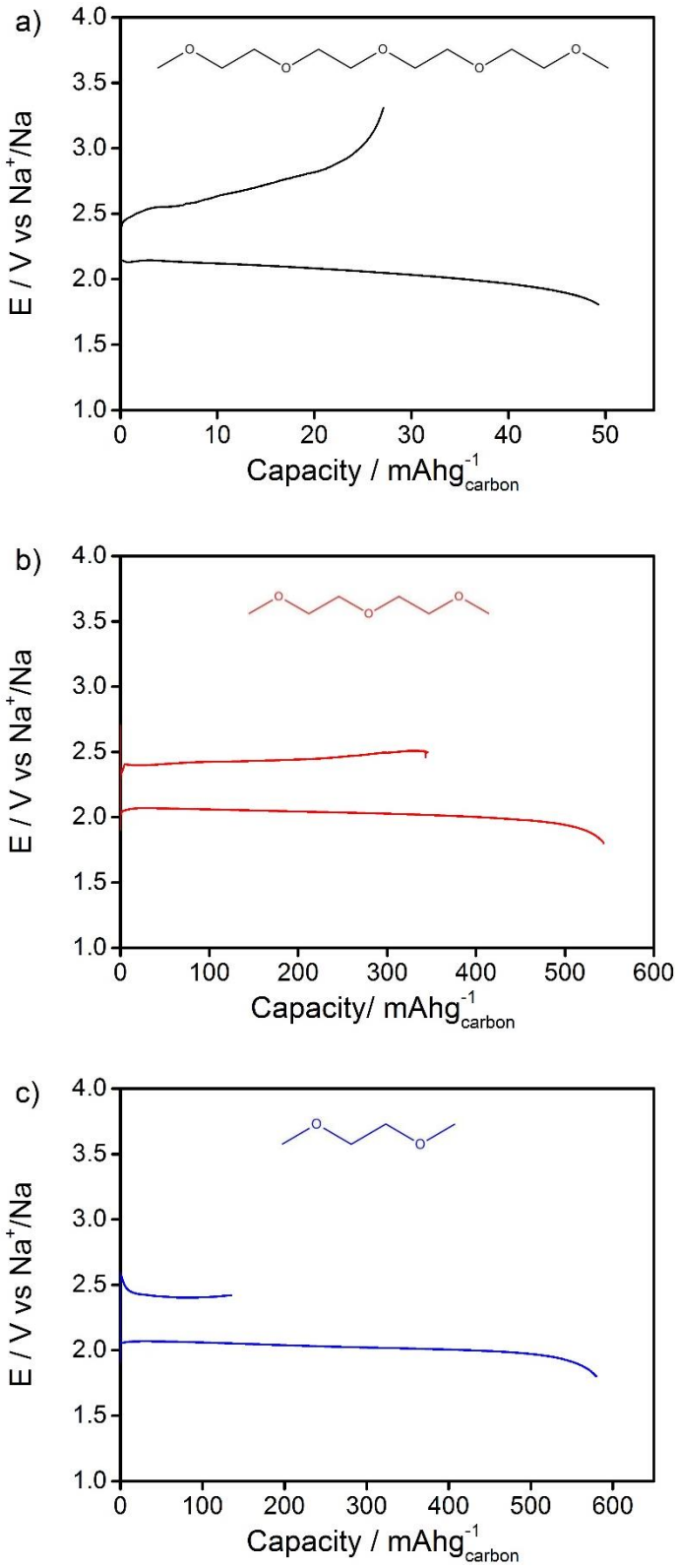

Figure 4.8: First galvanostatic discharge/charge cycle of the P50 Avcarb carbon cathode in a 0.5 M NaOTf in a) **TEGDME**, b) DEGDME and C) DME electrolyte at 0.24 mA cm^{-2} current rate. Insert shows chemical structure of the ether molecules.

It is noteworthy that the three electrolyte systems had comparable water concentration (<10 ppm H_2O, measured with a Karl Fischer coulometer) as the same drying procedure was applied for the solvents and support salt. Trace amounts of H_2O in the non-aqueous electrolyte of Na-O_2 batteries act as a phase-transfer catalyst enhancing the ability of the electrolyte to solvate intermediate chemical species affecting both the specific capacity and the morphology of the discharge products[22]. The same effect is reported for analogous Li-O_2 cells, where increasing H_2O concentration leads to larger toroid shaped Li_2O_2 and higher discharge capacities[23]. Since the three glyme-based cells have the same H_2O concentration, conductive salt concentration, O_2 pressure, cathode and current density, the different capacities shown in Figure 4.8 must be explained by intrinsic feature of the solvents.

One important difference between these electrolytes is the Gutmman donor number (DN) value, which is a measure of the strength of a solvents Lewis basicity and relates to the ability of said solvent molecule to solvate cations in solution[24]. Increasing the chain length of these ethers results in a decrease of the solvent's DN due to an intensification of the chelating ability of oxygen ether atoms towards cations in solution. Namely, the DN values for the three solvents are: 20, 18 and 12 kcal mol^{-1} for DME, DEGDME and TEGDME respectively (collected from the literature)[25-27].

High DN solvents (dimethyl sulphoxide DMSO = 30 kcal mol^{-1}) have greater electron donating properties, Lewis basicity, and produce stronger solvation with sodium cations, while in low DN solvents (acetinitrile ACN = 14 kcal mol^{-1}) this interaction is much weaker[28]. The solvation strength is also dependent on the

electrolyte supporting salt ionic association, however this was kept the same for the three different electrolytes. In analogous Li-O_2 cells, low donor number solvent led to smaller capacities and premature cell death (sharp decrease in voltage)[28], same behaviour of TEGDME cells in Figure 4.8.

Fundamental studies utilising surface-enhanced Raman spectroscopy (SERS) demonstrated that the solvent can control discharge products in Na-O_2 cells. Low DN solvents favoured the formation of Na_2O_2 via a second electron transfer reaction to surface confined superoxide, while high donor number favoured a one-step NaO_2 formation. Indicating that is possible to steer the reaction product by varying the donicity of the solvent used as electrolyte[25].

However, the discharge product of the Na-O_2 cells using different glyme electrolytes was determined via Raman spectroscopy to be NaO_2 in all cases (Figure 4.9). No vibrations associated with the peroxide (730, 787 cm^{-1}) anion were detected. This result indicates that the solvation of the ion pair [Na^+--$O_2^{\bullet-}$] by TEGDME solvent is not weak enough to proceed to the further reduction to Na_2O_2.

In analogous Li-O_2 systems, changing the ether solvent chain length had little influence on nature of discharge products, as in this system, lithium superoxide (LiO_2) is an unstable reaction intermediate and is not expected to be found as a solid final discharge product. Li_2O_2 accompanied by similar electrolyte degradation reactions were detected when discharging Li-O_2 cells using different chain length ether electrolytes[14].

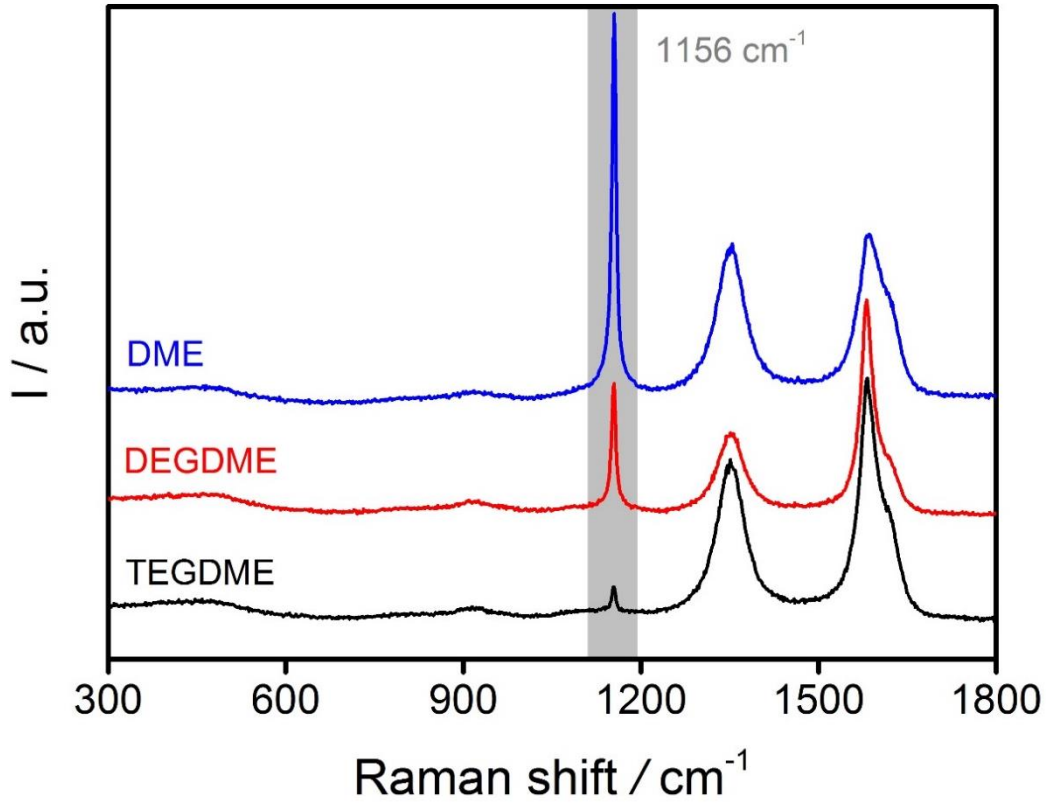

Figure 4.9: Raman spectra of the P50 Avcarb carbon cathode discharged in 0.5 M NaOTf in **TEGDME**, DEGDME and DME electrolytes at 0.24 mA cm^{-2} current rate.

The discharged carbon paper cathodes were further analysed via scanning electron microscopy. The morphology of the discharged products is significantly dependent of the ether chain length, as observed in Figure 4.10. For DEGDME, the expected cubic structure is found throughout the whole extension of the carbon fibre electrode, and higher magnification images indicate that the cubes grow to an average particle size of 6 μm. A similar morphology of large cubic particles was found for the cathode discharges using DME.

Instead, when TEGDME is the chosen electrolyte, the carbon surface is covered by a NaO_2 film. Images at higher magnifications show that the film is composed of small, cubic-like, submicron sized agglomerates.

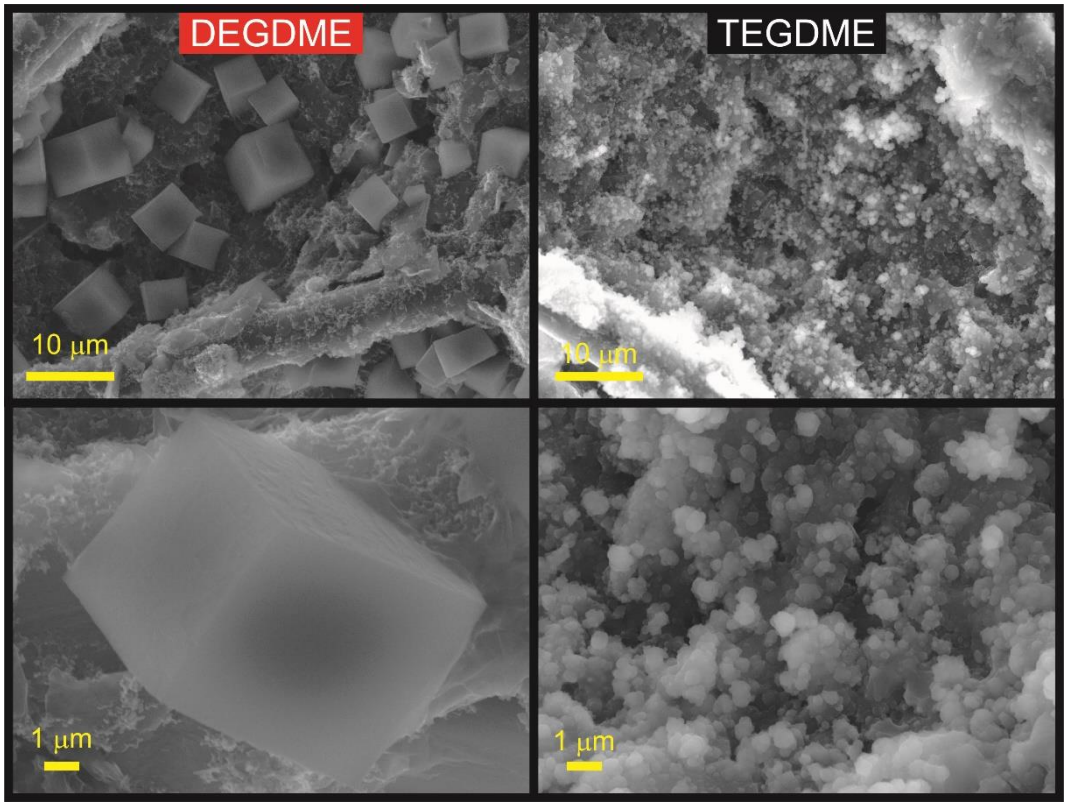

Figure 4.10: SEM analysis of the different discharge product morphology on an Avcarb P50 carbon fibre paper cathode in 0.5 M NaOTf in DEGDME and **TEGDME** electrolytes at 0.24 mA cm^{-2} current rate.

As previously outlined, NaO_2 is the main discharge product for Na-O_2 cells working in dry conditions. Since NaO_2 has the electronic structure of a wide band gap semiconductor, a direct electrochemical deposit of large superoxide cubes is not expected[29]. Instead a solution precipitation mechanism is widely accepted in the literature[26, 29, 30]. The first step being the one electron reduction of O_2 dissolved in the electrolyte at the cathode surface to generate $O_2^{\bullet-}$ in solution. The $O_2^{\bullet-}$ then binds with sodium ions forming NaO_2 which is then solvated by the electrolyte into solution. As the process follows, the NaO_2 saturates in solution and is precipitated as large cubic crystals on the cathode. In the case of TEGDME, due to both a lower donicity character and a stronger long ether chain chelation of sodium ions, the

solvation energy is higher which leads to the film-like NaO_2 and poses a barrier to the growth of large crystals. The opposite situation occurs for DME and DEGDME, where higher capacities and larger superoxide crystals are observed due to much stronger solvation energy of reaction intermediates.

The results obtained for Na-O_2 cells using different chain length glymes-based electrolytes are in line with the knowledge for analogous Li-O_2 systems. Low DN solvents, such as ACN, induce a surface confined mechanism which results in the formation of thin films of Li_2O_2 that rapidly clogs the electrode surface limiting cell capacity and resulting in large cell polarisation. Whereas high DN solvents, such as DMSO, can strongly solvate the LiO_2 intermediate resulting in a solution route mechanism and avoiding electrode clogging by precipitation of large toroid like Li_2O_2 particles[28].

4.4.5 Characterisation of NaO_2 precipitates at different states of discharge

The nucleation and growth mechanism of NaO_2 precipitates during the discharge of Na-O_2 cells was investigated via *ex situ* atomic force microscopy (AFM) and scanning electron microscopy (SEM) imaging of the P50 Avcarb carbon fibre paper cathodes using a 0.5 M NaOTf DEGDME electrolyte and will be discussed in this section.

The precipitation of the discharge products on practical carbon paper electrodes in Na-O_2 batteries is complex and made up of different elements including film formation (surface confined mechanism) and large cubic crystals (solution mechanism). The control of the morphology and thickness of these

deposits is essential to prolonging the cell reactions and inhibiting early cell "death". To which the realisation of the theoretical energy density of these systems (Na-O_2: 1106 Wh kg^{-1}) will be made.

For such, a systematic investigation of the discharge curve arbitrarily split the discharge plateau into four different stages (Figure 4.11). Each cathode being discharged to an absolute capacity (Q) of 0.25, 0.5, 1 and 2 mA h (55.5, 111, 222 and 444 mAh g^{-1}_{carbon}), at a current density of 0.24 mA cm^{-2} (42 mA g^{-1}_{carbon}), disassembled inside an argon-filled glove box and subsequent analysis without exposure to the atmosphere.

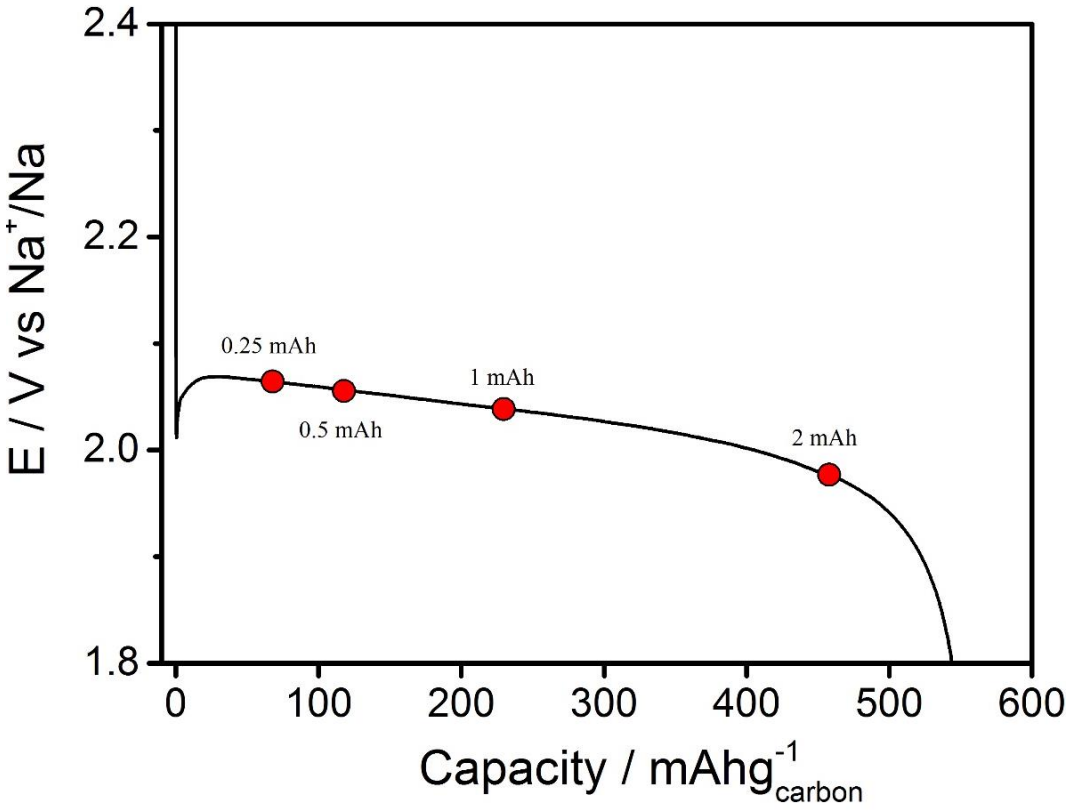

Figure 4.11: Discharge profile of Na-O_2 cells differing depths of discharge to increasing capacities of: 0.25 mAh, 0.5 mAh, 1 mAh, and 2 mAh. Electrolyte: 0.5 M NaOTf in DEGDME.

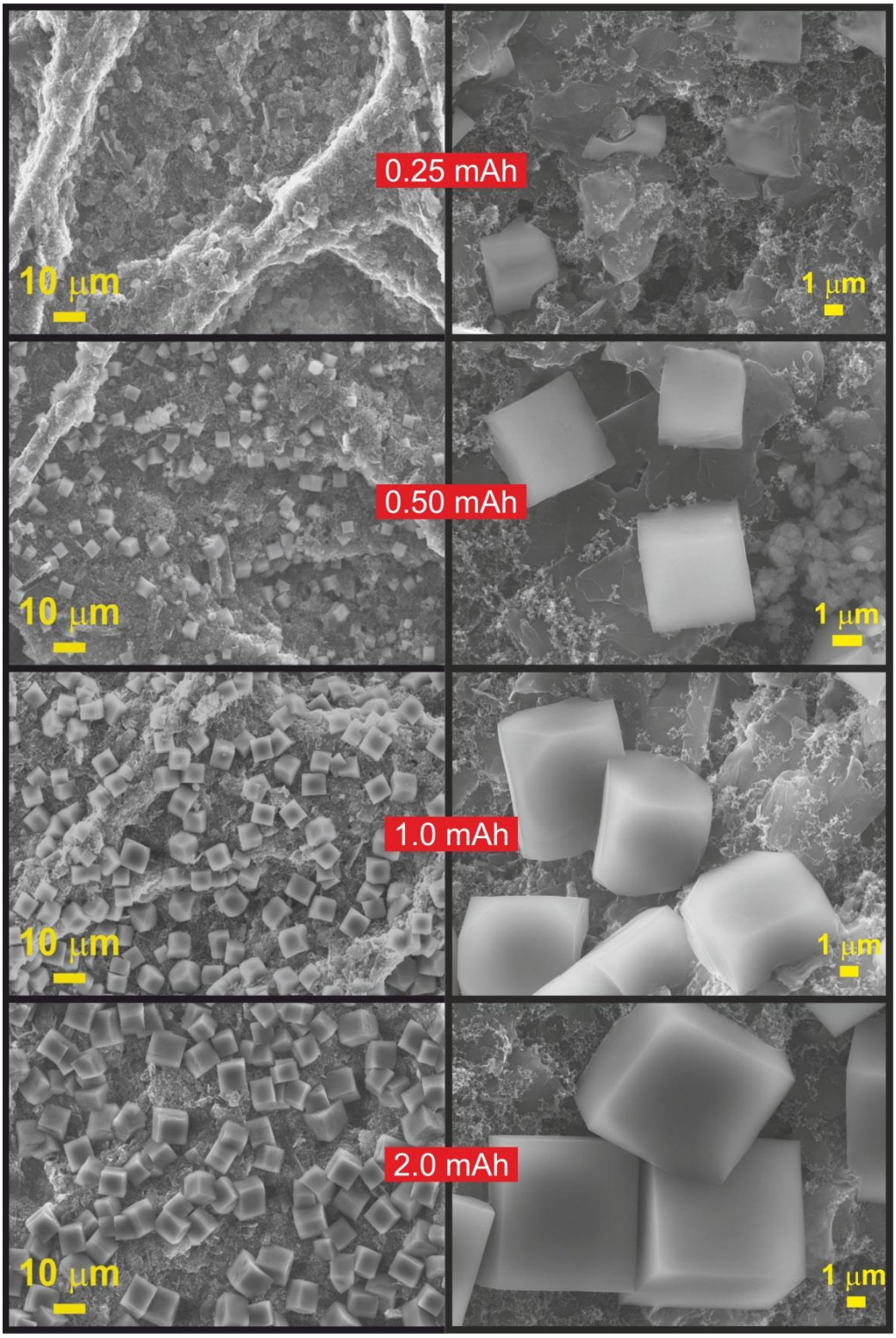

Figure 4.12: Scanning electron microscopy images of carbon fibre cathodes discharged to increasing capacities of: 0.25 mAh, 0.5 mAh, 1 mAh, and 2 mAh at different magnifications.

The cell was discharged to 2.0 V vs Na^+/Na and a 540 mAh g^{-1}_{carbon} capacity is obtained. The shape of the discharge curve is characterised by an initial dip in potential tentatively assigned to the rapid oxygen consumption on the electrode double layer region at the start of the nucleation process followed by a plateau at which NaO_2 is being precipitated from solution at an initial extrapolated potential of 2.10 V vs. Na^+/Na. The NaO_2 cubes gradually grow as the discharge proceeds which decrease the potential across the plateau by 0.2 V to 1.9 V vs. Na^+/Na at which the cell reactions ends characterised by a sharp drop in potential coined as cell death.

The chemical nature of the precipitates formed upon discharge was determined to be phase-pure NaO_2 by Raman spectroscopy (see Figure 4.18 – rate 0.24 mA cm^{-2}).

At the initial stage of discharge (Q = 0.25 mAh), numerous nucleation sites are visible on the carbon substrate at the low magnification images. At high magnifications, it is clear that the NaO_2 nuclei have an imperfect or incomplete cubic structure, possibly indicating that the particles are made up of smaller agglomerate building blocks. Further into the discharge process (Q = 0.5 mAh), perfect cubic particles are already observed, and the coverage density of NaO_2 increase. As the discharge proceeds, a steady growth of the crystal size is evident and a linear relation of particle size with absolute charge is observed up to Q = 1.0 mAh (see Figure 513e). Following that, a 2-fold increase in the discharge capacity only results in 20% increase of the particle size.

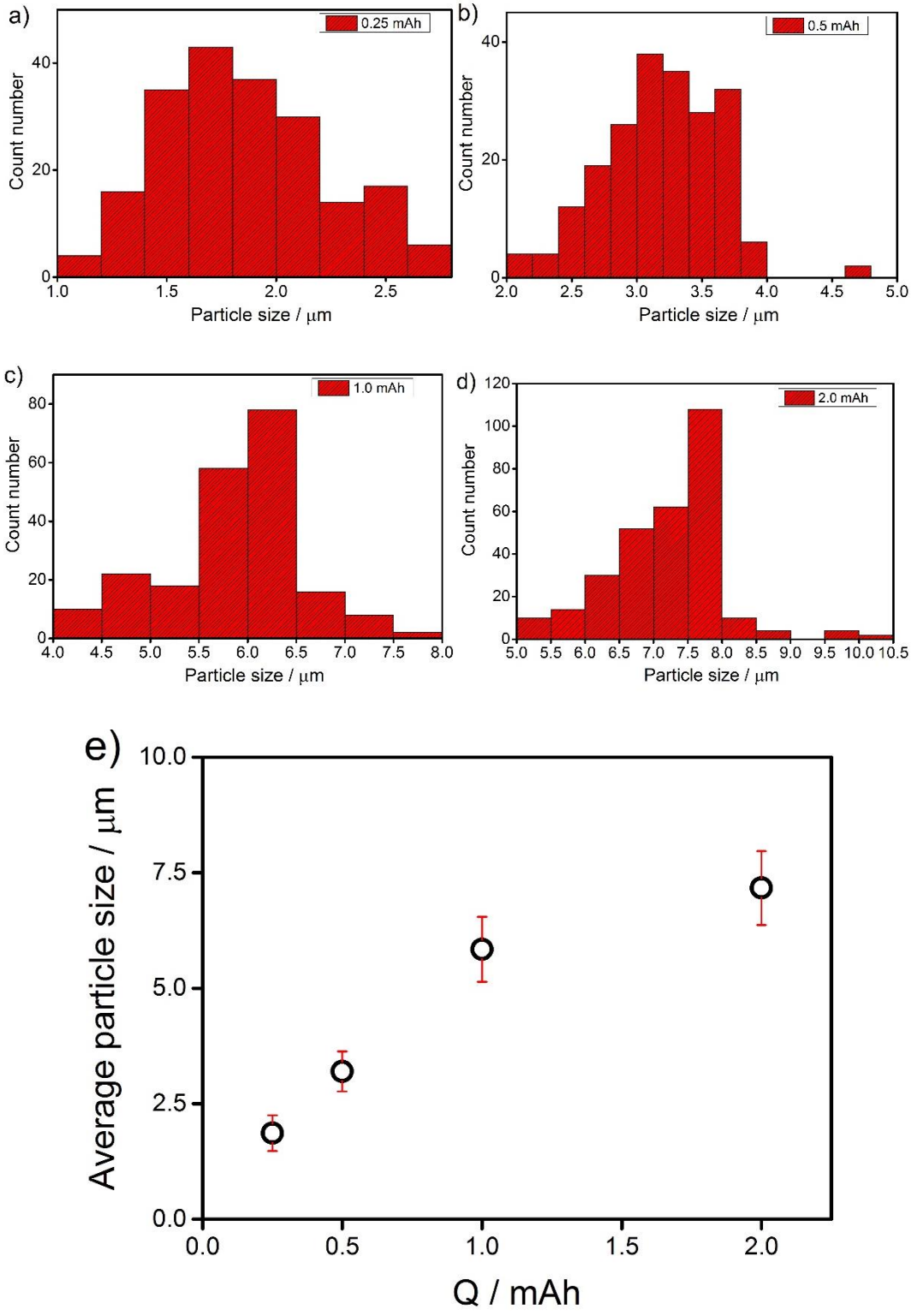

Figure 4.13: Histograms of NaO_2 particle size distribution obtained after discharge to a) 0.25, b) 0.50, c) 1.0 and d) 2.0 mAh absolute capacity. e) NaO_2 particle size vs depth of discharge. Cathode: P50 Avcarb. Electrolyte: 0.5 M NaOTf in DEGDME. Rate: 0.24 mA cm^{-2}. Error bars are standard deviation over 200 counts.

The observation of this inflection point implies that, approaching cell "death" (1.8 V vs Na^+/Na), part of the electrochemical measured charge no longer contributes for the growth of existing crystals. It can be concluded, since NaO_2 is the main discharge product, that the formation of a thin passivating film between the precipitates is taking place, instead of nucleation/growth of the crystals. Based on this observation, it can be hypothesised that a mechanism switch from a solution route (leads to large particles) to a surface confined route (leads to film formation) occurs towards the end of discharge.

The aforementioned film, due to the insulating character of NaO_2[15], is responsible for the premature termination of the discharge process. This termination is described as premature in the light of two reasons: 1) based on the SEM image (Figure 4.12 – Q = 2mAh), the electrode is not passivated and there is still available conductive carbon surface for the oxygen reduction reaction; 2) based on the cathode dimensions (0.785 cm^2 x 0.013 cm, 80% porosity), the density of NaO_2 (ρ= 2.2 g cm^{-3}), the specific capacity obtained for the cell (544 mAh g^{-1} – Figure 4.11) and assuming the one-electron reduction per O_2 reaction (Eq. 4.1) as the only reaction occurring during discharge, only 28% of the maximum theoretical capacity is achieved.

Other reasons for the poor exploitation of the cathode's available pore volume are related to the cell configuration – the cathode is slightly compressed during cell assembly and the current collector blocks the oxygen diffusion into the cathode. Low magnification images show that NaO_2 is preferentially formed on the side where the carbon cathode is in direct contact with the oxygen atmosphere (see Appendix A, Figure A8).

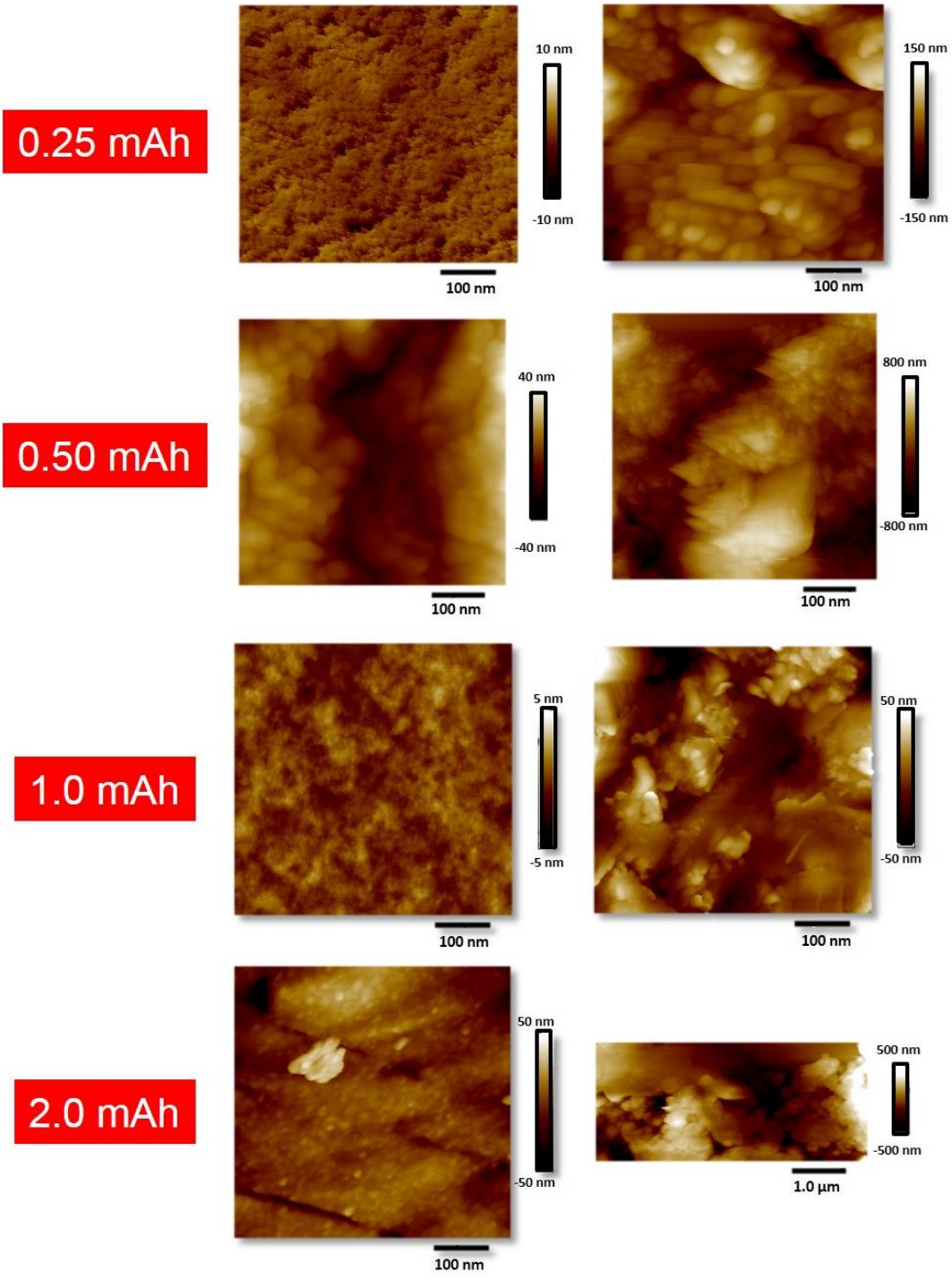

Figure 4.14: AFM images of the film formed between NaO_2 cubes on a P50 Avcarb carbon fibre cathode taken from a Na-O_2 cell discharged to 0.25 mAh, 0.5 mAh, 1 mAh, and 2 mAh absolute capacity. Rate: 0.24 mA cm^{-2}. Electrolyte: 0.5 M NaOTf in DEGDME. AFM analysis undertaken by Dr Iain Aldous.

Ex situ AFM images of Na-O_2 carbon paper cathodes at different depths of discharge has mapped the formation of crystalline cubes of NaO_2 crystals and the surrounding film, Figure 4.14. AFM provides a complementary and more detailed view of the film produced during the discharge process which was not observable on the SEM analysis.

At early stages of nucleation (0.25 mAh) a surface confined film is already observed by scanning with AFM, figure 4.14a, whereby the film is made up of agglomerates of small nanoparticles. This provides new information about the growth mechanism of NaO_2 different from that of SEM whereas film-like deposits were hypothesised to occur only at the end of the discharge. In fact, AFM images of the carbon cathode shows nanoparticles and agglomerates approximately ten nanometres in height, Figure 4.14a and b.

The height across this region is an order of magnitude lower than the NaO_2 cube size of approximately 100 nm in height. Other regions show a much denser and rough film (Figure 4.14b). Here the NaO_2 film is much more uniform and the height of the film is much decreased (20 nm). The insulating layer based on electrochemical impedance studies by Knudsen *et al.*[30] calculated this insulating film to be approximately 11 nm thick under the conditions within their study which qualitatively matches the height of this image, assuming that underneath this area would only be carbon fibres of the carbon paper. This raises the question as to why NaO_2 nanoparticles are found within the film upon fibres and not cube structures at this stage of the discharge. Compared to previous models this observation is different, however significantly the electrochemical quartz mass balance study

(EQCM) used a Au working disc electrode[30, 31]. The uniform structure and hence less surface available nucleation features might be the cause of this discrepancy.

In the carbon fibre paper cathodes discharged to 0.5 mAh the film structure here has changed dramatically in height. The AFM image scale has risen to 800 nm, close to the size of initially formed NaO_2 cubes in these results. The plates are beginning to take some square like features, although they are very rough. The particle sizes as shown in figure 4.14c are even as small as 20 nm in size. Imaging the subsequent discharged cathode at 1 mAh, when looking closely at the film formation, no significant changes are noticed. Similar particle sizes and film formations are present at this depth of discharge, Figure 4.14e and f.

At the final stage of discharge (Q = 2.0 mAh) the AFM image shows an even film made of nanoparticles in a more uniform arrangement (Figure 4.14g). A wider view of this film in Figure 4.14h shows larger plate like features on the surface. Therefore in general once the film is deposited it appears to remain relatively stable apart from the growth of the nanoparticles that we conclude are the main components that make up the NaO_2 cubes on the surface of the electrode.

An attempt to characterise the chemical composition of the film formed between the cubic crystals was made by taking EDS line spectra (Figure 4.15) at different points of the cathode discharged to Q = 2.0 mAh. The spectrum focused on a cubic particle shows a relative atomic ratio of 1:2 for sodium and oxygen indicative of sodium superoxide chemistry. When the beam is focused on the film between the crystals, Spectrum 2, a relative atomic ratio of 1:1 for sodium and oxygen is obtained. No spectral lines related to sulphur and fluorine were detected, ruling out conducting salt contamination on the chemical composition of the film.

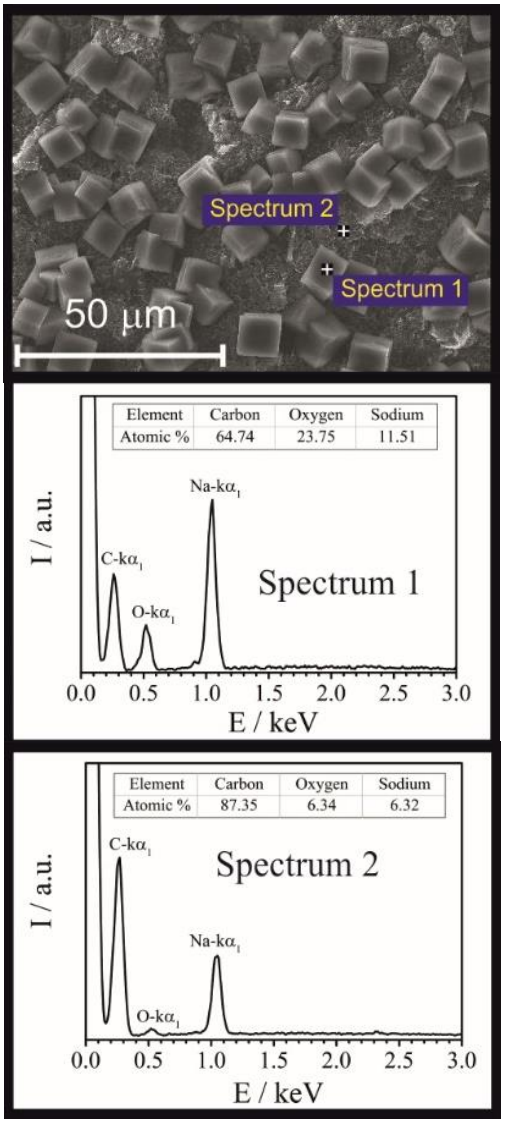

Figure 4.15: EDS spectrum on different focus points of a discharged P50 Avcarb carbon cathode. Rate: 0.24 mA cm^{-2}. Electrolyte: 0.5 M NaOTf in DEGDME. Spectrum 1 was focused on a cubic particle and Spectrum 2 was focused on the carbon fibre.

These results could suggest that the film deposited between cubic particles is actually composed of Na_2O_2, via a surface disproportionation or consecutive electron reduction of NaO_2, as occurs in analogous lithium-oxygen systems[28]. A similar mixed discharge product growth with solution-based (NaO_2) and surface-based (Na_2O_2) mechanisms was proposed by Sun *et al.*[32]. It is also possible that the

1:1 Na:O atomic ratio detected on the film formed on the carbon surface relates to NaOH, a common electrolyte degradation side product in Na-O_2 cells[16].

However, is important to note that the quantification of light elements via EDS is known to be challenging, and the data acquisition in this technique is reliant on the X-ray detector positon related to the topography of the sample. Raman spectra taken between cubic particles only showed the characteristic D and G bands of the carbon substrate and no vibration associated with Na_2O_2 were detected in the FTIR analysis.

Finally, AFM was employed to investigate the topography of the cube itself (Figure 4.16). By applying the AFM tip to the top of a NaO_2 cube, it can be seen that the particle is not a single plate surface as shown by the SEM images. These observations find that small nanoparticle agglomerates ca. 50 nm make up the surface, Figure 4.16a, which is in line with the SEM images taken at low depth-discharge (Figure 4.12, Q = 0.25 mAh), where incomplete cubic shapes are found at start of the nucleation process. Furthermore, when taking a sequentially bigger image of the same surface shows that the cubes surface has defect points along with platelet parts of the surface, Figure 4.16b. This is more complicated than expected and raises many questions as to how these cubes grow at the nanoscale level. The mechanism of growth from a nanoparticle to a micro sized cube is complex and yet to be determined as to the steps that are undertaken in the processes.

Another image of the top of a cube from Figures 4.16c and d reveals an imperfection on the surface. There is a small hole half a micron in width that shows the inner surface of the cube. It appears that the 200 nm into the surface there are nanoparticles of NaO_2 present. The rest of the surface appears to be a single plate,

at this resolution. Further investigation is needed in to characterising the inner structure of the micro particles of NaO_2 formed during the discharge reaction of the Na-O_2 battery. This may be initial evidence for an agglomerated reoriented aggregation mechanism of growth of these particles. In which the outer surface has recrystallized at a certain size of cube to form a single plate leaving a disordered array of single units within the centre of the cube.

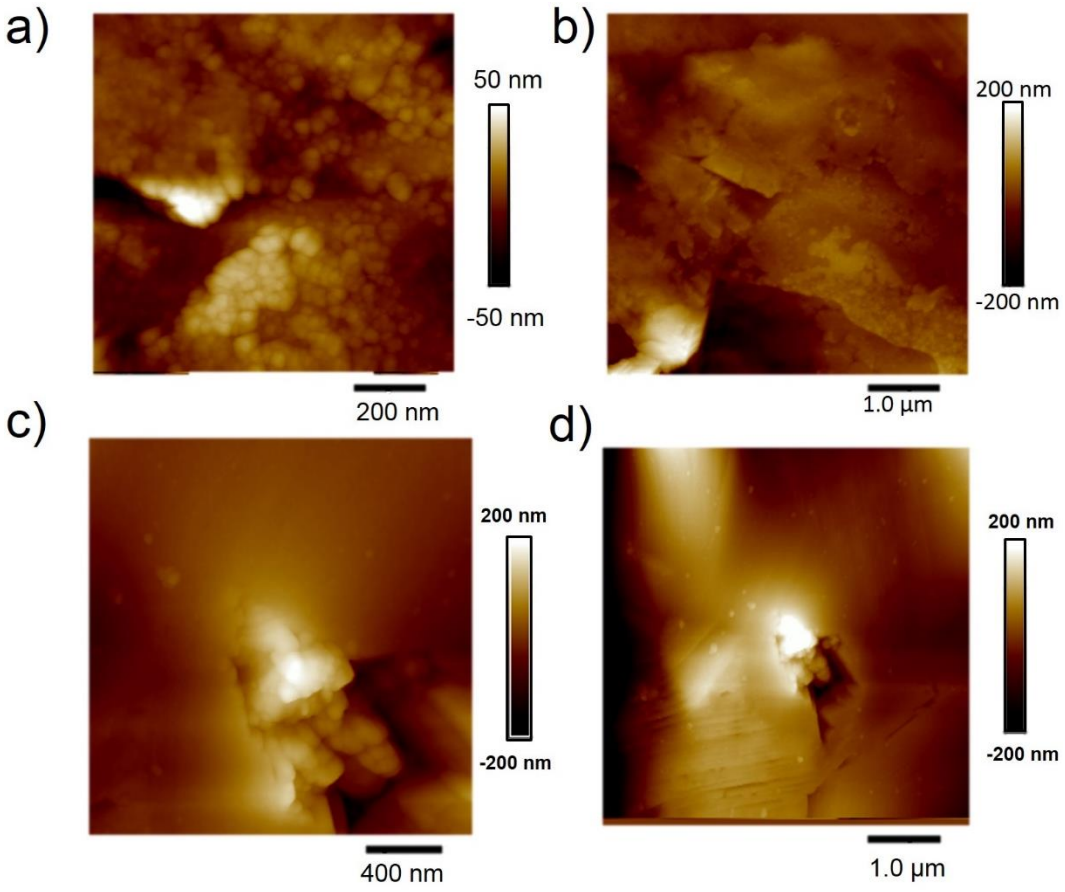

Figure 4.16: AFM images of a) and b) the surface of a NaO_2 cube and c) and d) of a defect on a cubic particle. AFM analysis undertaken by Dr Iain Aldous.

The observation that the micron sized cubic particles are in fact composed of nano-sized agglomerates helps to understand why NaO_2 is the final discharge

product even if Na_2O_2 is the thermodynamically stable phase (Na_2O_2 - $\Delta_rG° = -449.7$ kJ mol^{-1} and NaO_2 $\Delta_rG° = -437.15$ kJ mol^{-1})[6]. NaO_2 has considerable lower nucleation energy at the nanoscale in comparison to Na_2O_2 (see Chapter 1, Figure 1.10[5]) and a conversion to the peroxide upon growing does not take place as the crystal is not a single plate surface.

While the Raman and EDS analysis indicate that the chemical composition on the surface of typical cubic-shaped precipitates is solely NaO_2, the possibility of parasitic products being deposited on top of the cubes should be discarded. Landa-Medrano *et al.*[33] reported a transmission X-ray microscopy study on Na-O_2 battery deposits in which NaO_2 particles were enclosed by an oxygen deficient layer and a side product passivation layer.

4.4.6 Discharge rate effect on capacity, NaO_2 morphology and growth mechanism

If alkali metal-oxygen batteries are to reach its end goal of automotive application, one aspect that must not be overlooked is the increase of rate capability while retaining efficiency. As to date, considerably lower current rates have been reported for metal-oxygen systems when compared to state-of-the-art lithium-ion technology[29, 34].

Batteries should ideally operate under a high current density and low overpotential regimes, especially for electric vehicle batteries which should maintain high performance with increase of current rates. In lithium-ion batteries, the rate capability is primarily limited by intrinsic slow diffusion of electrons and lithium cations within the solid host material[35]. For alkali metal-oxygen batteries,

as the oxygen reduction reaction takes place at a tri-component phase (solid cathode, liquid electrolyte and oxygen gas phase), the solubility and diffusion of oxygen and oxygen reduced species are the limiting factors of rate capability[36].

In this section, the influence of the applied discharge current on the electrochemical performance, NaO_2 discharge mechanism and morphology will be discussed. Na-O_2 cells were assembled with a standard electrolyte combination of 0.5 M NaOTf in DEGDME and a binder carbon fibre paper cathode (P50 Avcarb, 10 m^2 g^{-1}). The cells were discharged at different current rates: 0.12 mAh cm^{-2} (21 mA g^{-1}), 0.24 mA cm^{-2} (42 mA g^{-1}), 0.48 mAh cm^{-2} (84 mA g^{-1}), 0.96 mAh cm^{-2} (168 mA g^{-1}) and 1.92 mAh cm^{-2} (332 mA g^{-1}). The current density was defined by dividing the applied current by the geometric area of the cathode and the specific current was defined by dividing the applied current by the total mass of the cathode. After galvanostatic cycling, the same electrodes were analysed via Raman spectroscopy, AFM and SEM.

Representative discharge profiles are shown in Figure 4.17a. As the current density is increased, the discharge capacity decreases due kinetic limitations of the oxygen reduction reaction taking place. Figure 4.17b shows an inverse correlation between discharge rate and overall capacity which follows a power-law dependence similar to other reports of lithium and sodium oxygen batteries[37-39]. In the same way, the cathodic overpotential ($\eta_c = E - E_{eq}$) increases as rate rises and a flat discharge plateau is observed up to 0.96 mA cm^{-2} which is followed by a sudden drop in potential at cell death.

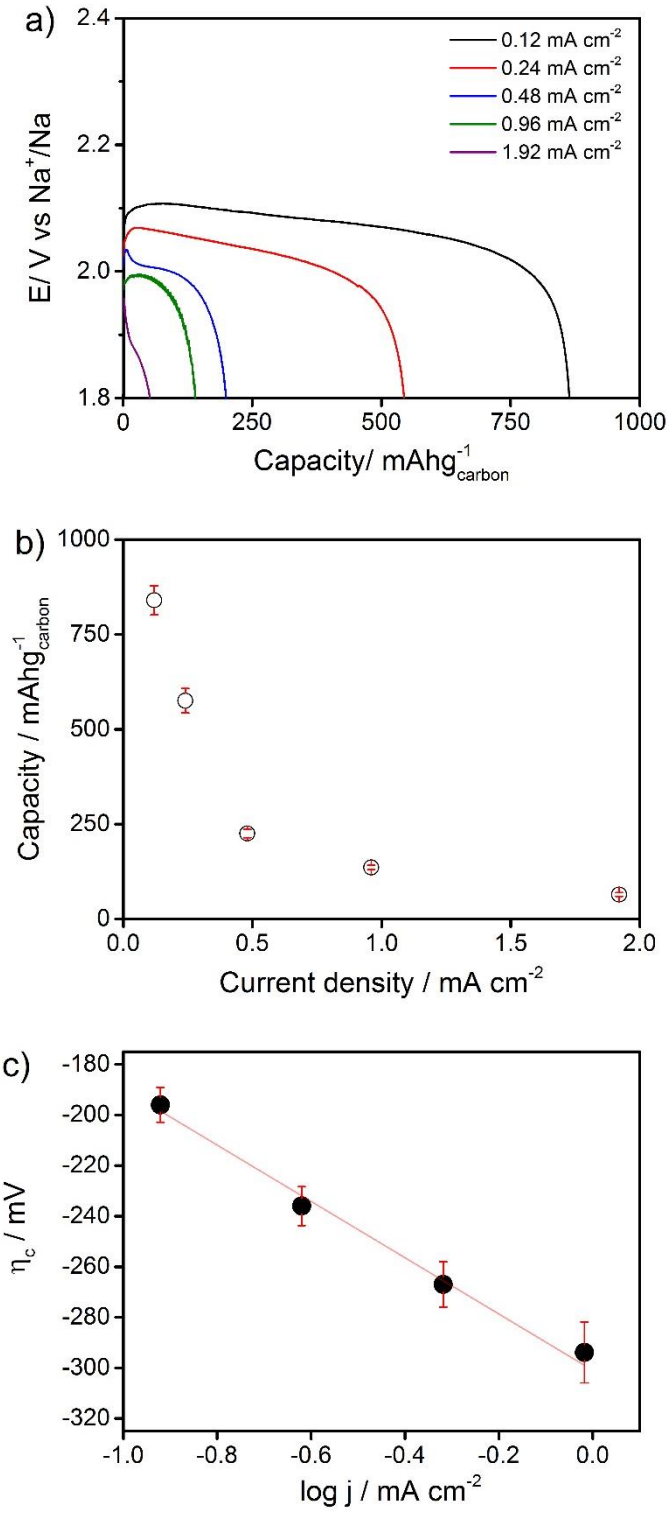

Figure 4.17: a) Discharge profile of Na-O_2 cells at various current densities. b) Correlation between discharge capacity at 1.8 V vs Na^+/Na and current density. c) Tafel plot for the cathodic reaction in Na-O_2 cells. Error bars from standard deviation of at least 3 cells.

In analogous Li-O_2 systems, the origins of the observed overpotentials were hypothesised to be heavily affected by IR drops and mass transport limitations as well as kinetic losses[37, 40]. Comparatively to Li-O_2 cells[38, 41], much lower overpotentials and better rate capabilities are obtained for the Na-O_2 battery. Figure 4.17c shows a Tafel plot of log of current density versus cathodic overpotential which shows a linear dependence indicating a kinetic control on the oxygen reduction reaction[42]. The Tafel slope of 111 mV per decade is very close to the expected for a one electron reaction (118 mV).

At the highest current, 1.92 mA cm^{-2}, the voltage profile is significantly changed and instead of a plateau the voltage declines steadily across the discharge curve. For this reason, and since comparable capacities were not achieved, this electrode was left out of the *ex situ* characterisation.

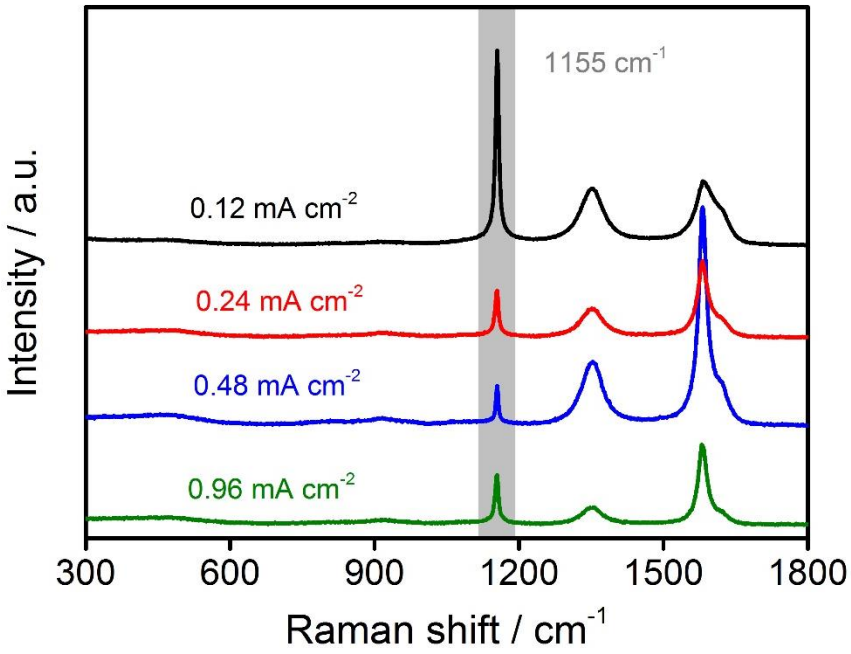

Figure 4.18: Raman spectra of cathodes discharged at various current densities (corresponding to Figure 4.17a). Spectra not normalised.

The one-electron reduction per oxygen to form NaO_2 is the main reaction process for all the current rates employed as evidenced by the presence of an intense peak at 1155 cm^{-1} in the Raman spectra shown in Figure 4.18.

Indeed, other research groups have reported that it is not possible to influence the chemical nature of the discharge product by varying kinetic parameters. This has been proven truth for both situations of NaO_2[16, 43, 44] and Na_2O_2[45] as the discharge product. It is also in line with Li-O_2 battery reports which only detected Li_2O_2 chemistry under different kinetic parameters[38, 41].

The opposite behaviour was reported by Yadegari *et al.*[46], which claimed that at low current densities Na_2O_2 would be the primary reaction product and NaO_2 at elevated current densities. However, these reports are somewhat controversial since the charge curve for different current rates showed three distinct plateau steps, which would not be expected of a one electron oxidation of NaO_2. It was also proposed that polymeric binder decomposition would lead to peroxide formation[46]. The stability of different polymeric binders in the Na-O_2 cell environment will be discussed in further detail in section 4.4.9.

Having proven the reaction product obtained, the growth mechanism of NaO_2 crystal at different current densities was analysed by *ex situ* SEM and the concomitant film formation analysed by *ex situ* AFM. Some variation on the cube size and morphology were observed for a single sample. In general, the particles presented a more constant spatial distribution where the cathode is in direct contact with oxygen gas – between the stainless steel mesh current collectors.

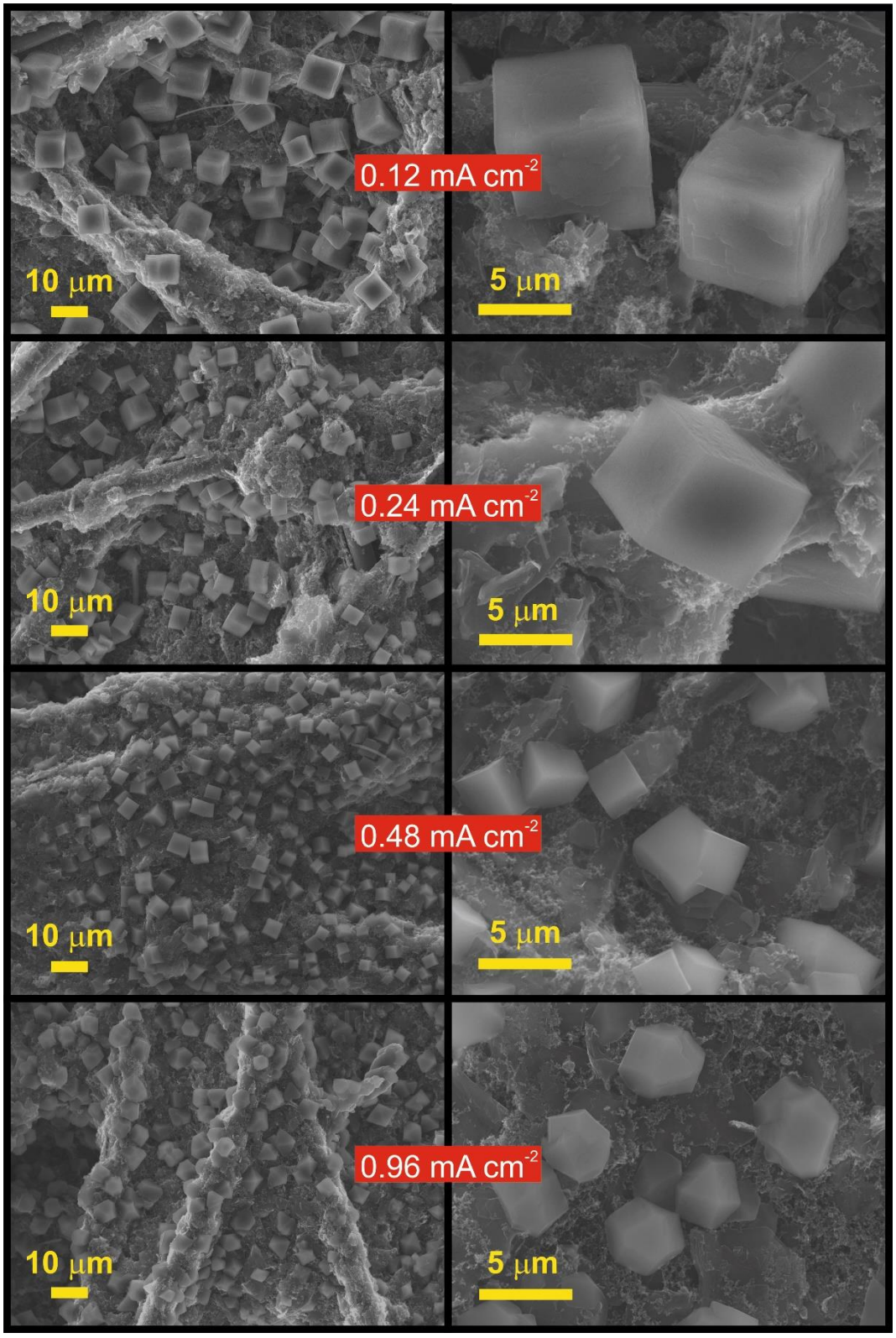

Figure 4.19: Scanning electron microscopy images of carbon fibre cathodes discharged with various current densities at different magnifications. Electrolyte: 0.5 M NaOTf in DEGDME.

Figure 4.19 shows SEM images illustrative of the overall discharge product morphology (when facing the oxygen side of the electrochemical cell) using different current rates at different magnifications. The cathode side facing the electrolyte has significant glass fibre penetration, which impedes an accurate particle size investigation. The same SEM experimental settings were applied for imaging the samples.

Regarding the morphology, only cubic shaped particles are present at low current densities (0.12 – 0.48 mA cm^{-2}). At high rate, (0.96 mA cm^{-2}), the particles assume cuboctahedral and pyramidal shapes. Similar structures and changing morphology at elevated rates have been reported by other research groups[30,42,43]. As for the size of the crystals (measured by the maximal edge length), a linear decrease with increasing current density is obtained for the three lowest current densities after which the particle size stabilises at high rate (Figure 4.20).

As previously discussed, the precipitation of large NaO_2 crystals obeys the following route: initial dioxygen electrochemical reduction → diffusion of superoxide anion radical in solution → nucleation and growth of NaO_2 crystals after saturation in solution. In a low rate regime, the formation of $O_2^{\bullet-}$ radicals is slow and the nucleation process starts in a more dilute solution which results in the growth if isolated, sparse, large clusters (low rates – large particles). In a high rate regime, the solution saturation is faster and the nucleation process takes place in a more concentrated solution, which results in dense smaller clusters (high rates – small particles). This process is analogous to condensation from low-density and high-density gases in classic nucleation theory[47].

The results obtained: an inverse relationship between particle size and the morphological change at high current density are in line with other reports in the literature by Schröder *et al.*[48] and Nichols *et al.*[49]. The opposite trend was reported was reported by Ortiz-Vitoriano *et al.*[39], who observed the growth of large cubic NaO_2 particles at high current rates and smaller cubes at lower current rates. However, Ortiz-Vitoriano's investigation made use of a carbon nanotube based air-cathode that can be quickly blocked on the extremities by the deposition of discharge products, thus limiting dioxygen diffusivity and availability along the carbon structure.

The dioxygen concentration in the electrolyte has a direct influence on the particle size, which is the reason for different particle sizes reported in the present study and by Schröder *et al.*[48] and Nichols *et al.*[49], even though the same electrolyte, same cathode and comparable current densities were employed. The alkali metal oxygen battery testing rig is usually built in-house, so the oxygen is supplied to electrochemical cell at different partial pressure for different research groups, which accounts for variations on the solubility and diffusivity $O_2^{\bullet-}$ within the electrolyte.

Since the different discharged cathodes investigated have virtually the same amount of NaO_2 – were discharged up to the same capacity – the fact that the size of the crystals stagnates at current densities above 0.48 mA cm^{-2} and indicates film-like formation. The power-law shape of the particle size vs current density curve (Figure 4.20) very much resembles the capacity vs current density curve (Figure 4.17b.) which corroborates the idea that some of the charge is not being used in the nucleation growth of NaO_2 cubes. This leads to a conclusion that at a critical current density (which lies between 0.48 and 0.96 mA cm^{-2} for our cell configuration) a

transition from a solution route to a surface confined route mechanism takes place on the discharge process.

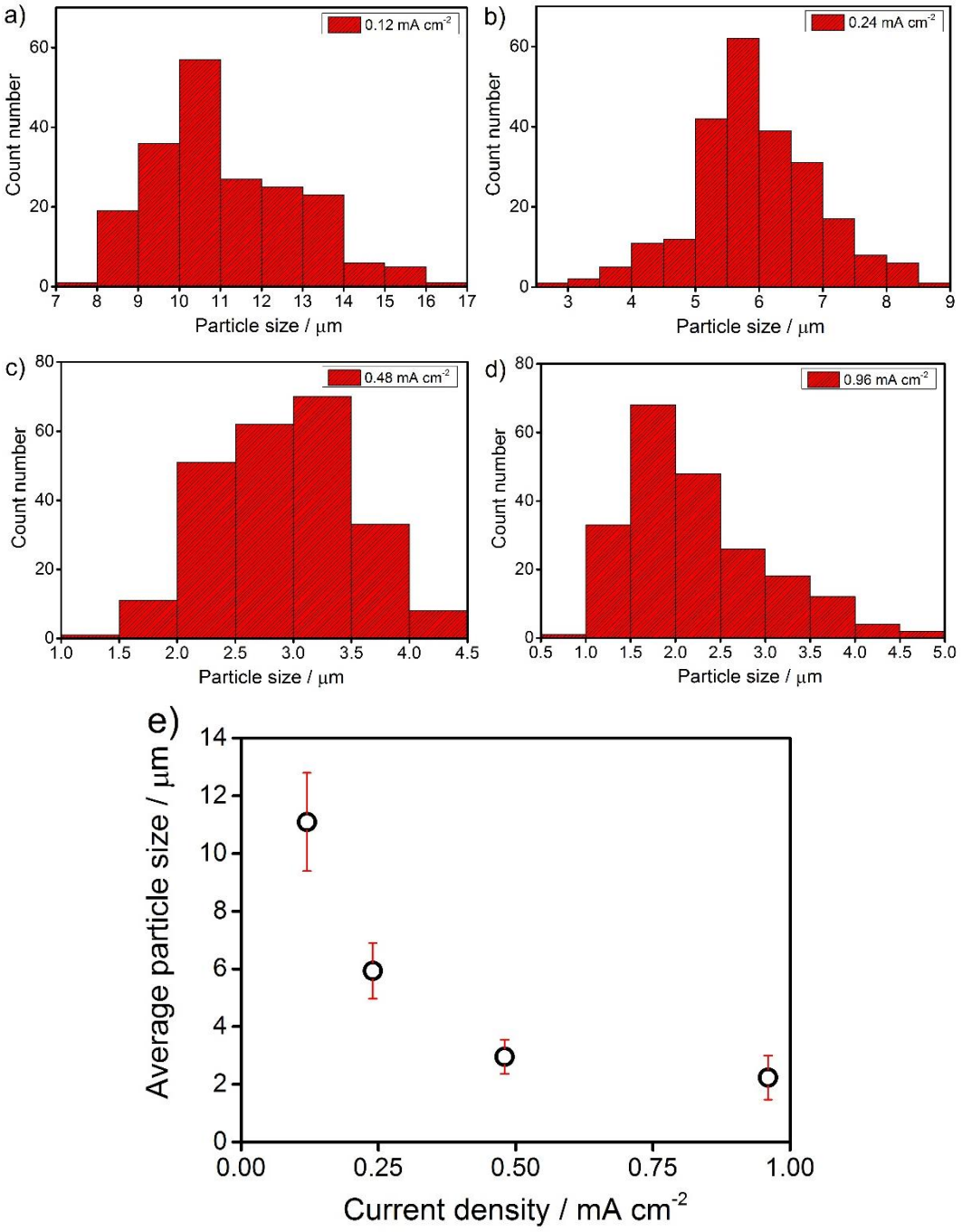

Figure 4.20: Histograms of NaO_2 particle size distribution obtained after discharge at a) 0.12, b) 0.24, c) 0.48 and d) 0.96 mA cm^{-2} current density. e) NaO_2 particle size vs current density. Cathode: P50 Avcarb. Electrolyte: 0.5 M NaOTf in DEGDME. Rate: 0.24 mA cm^{-2}. Error bars are standard deviation over 200 counts.

As previously stated, NaO_2 is a wide band gap insulator (*Eg* = 2.1 eV[29]), which makes this film-like passivation of the carbon surface an undesired cause for early cell "death" and limited rate capability. Knudsen *et al.*[30] and Nichols *et al.*[49] proposed that charge transfer resistance is the main reason for cell "death" at high current densities and pore clogging is more significant at low current densities. Our results are in line with these reports, since a solution route is observed at low current, large NaO_2 particles would cause pore clogging, and a surface route is observed at high currents, insulating film formation increases charge transfer impedance.

An SEM investigation about NaO_2 film formation on the carbon substrate is hindered by charging effects on the sample, which is when electrons from the primary beam build on the surface of insulating samples. Since AFM is a scanning probe microscopy technique and relies on the forces between the tip and the sample, measured by the optical deflection of a laser beam hitting the mechanical lever, it can deliver more information on the topography of non-conducting surfaces without charging issues.

The image of the cathode discharged at a current rate of 0.48 mA cm^{-2} (84 mA g^{-1}_{carbon}) in Figure 4.21b shows nanoparticles agglomerated over the surface of the electrode on the striations of the carbon fibre. Using particle size analysis (Figure 4.21c) it can be seen that there are three sizes of NaO_2 particles on this image of 35, 70, and 100 nm. Based on this observation, it can be inferred that formation has a porous character, instead of being form of a compact layer that would block electron transfer. The porous film would allow electrolyte penetration

and electron exchange at the discharge product/electrode interface. A similar model was proposed by Liu *et al.*[40] for Li-O_2 cell systems.

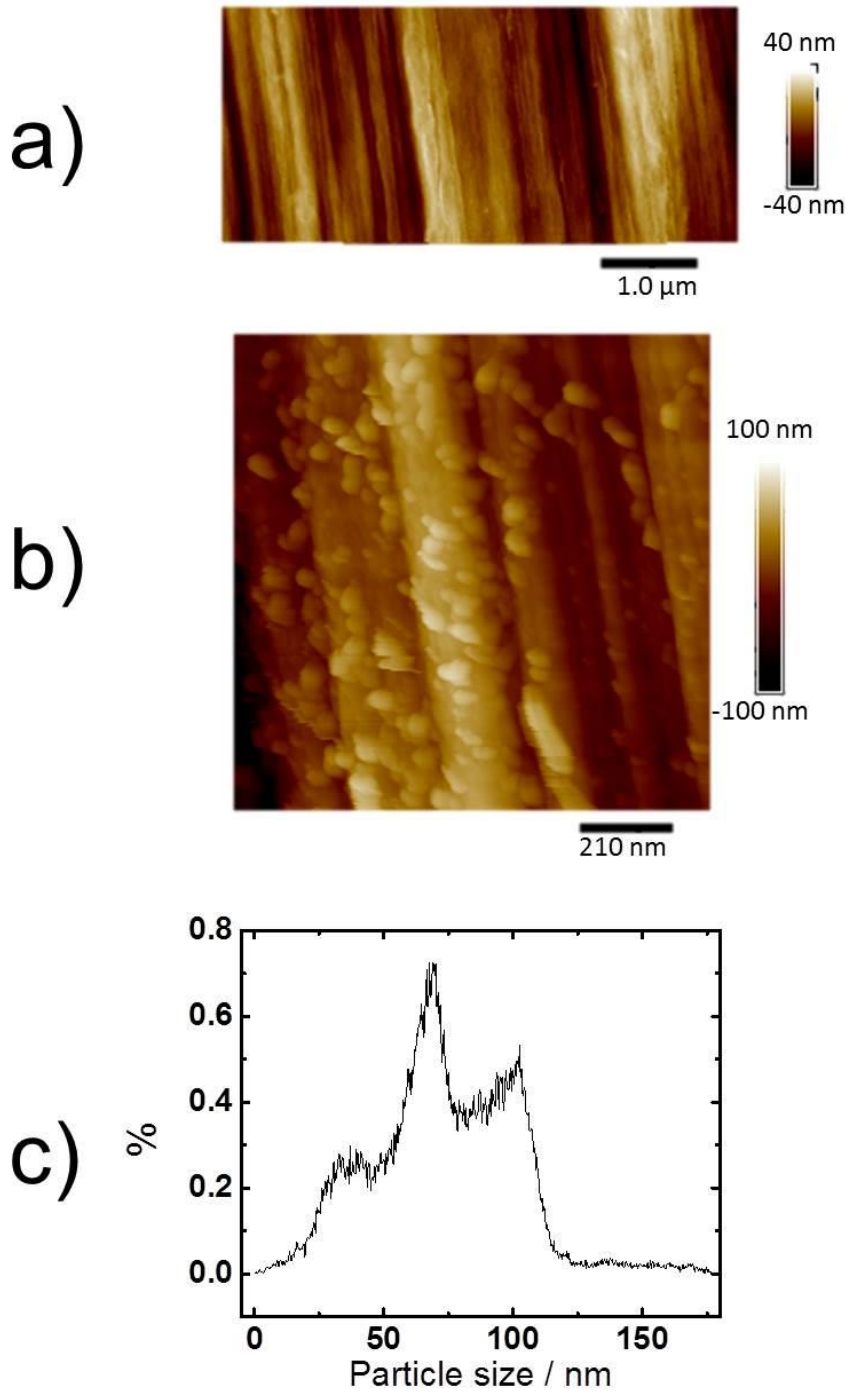

Figure 4.21: AFM image of discharged cathode, 0.48 mA cm^{-2}, with particles of NaO_2 decorating the fibre. b) Particle size analysis. AFM analysis performed by Dr. Iain Aldous.

The chemical composition of the film deposited between the cubes on the P50 Avcarb carbon fibre cathode discharged at 0.96 mA cm^{-2} was analysed via EDS (Figure 4.22), a thicker film is expected for this rate.

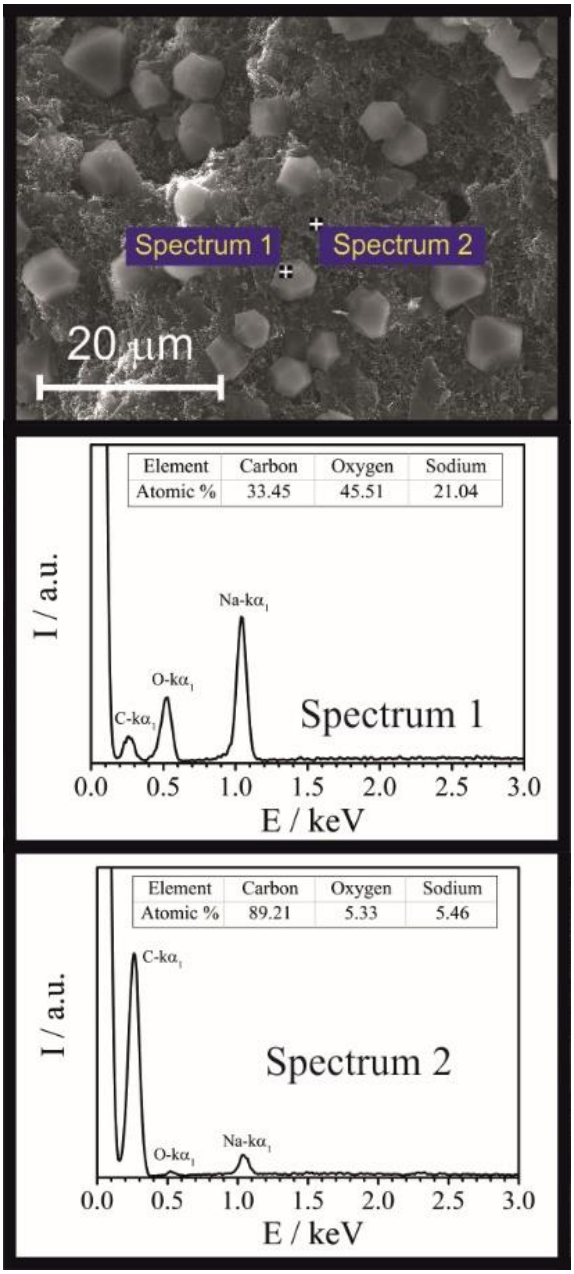

Figure 4.22: EDS spectra on different focus points of the cathode discharged at 0.96 mA cm^{-2}. Spectrum 1 was focused on a cube and Spectrum 2 was focused on the carbon fibre.

The cubic deposits showed a relative atomic ratio of 1:2 for sodium and oxygen and the film deposit showed a relative atomic ratio of 1:1, unchanged from the results obtained when discharging the Na-O_2 cell at 0.24 mA cm^2 current density (Figure 4.15). Once more, the EDS results could be interpreted either as the NaO_2, initial discharge product, undergoing a disproportionation reaction resulting in a Na_2O_2 film between the cubes, or as simply electrolyte degradation resulting in the formation of NaOH. Further investigation is needed to support a Na_2O_2 based film formation claim.

4.4.7 Sodium superoxide stability

A particular intriguing feature of Na-O_2, in contrast to other alkali metal-oxygen systems, is the controversial reports on the final discharge product of the battery. As previously discussed, NaO_2, Na_2O_2, and $Na_2O_2 \cdot 2H_2O$, were detected as a final discharge product for different cell configurations. The final reaction product is intimately linked to the performance of the battery, and the advantages of NaO_2 over LiO_2 – lower combined overpotentials and improved rechargeability – are only obtained when superoxide is the main discharge product. When the cell reaction follows a two-electron reduction of molecular oxygen to produce Na_2O_2, a charging potential much larger than the thermodynamic oxidation of Na_2O_2 is observed due to sluggish kinetics. When $Na_2O_2 \cdot 2H_2O$ is the final product, the charging curve exhibits additional plateaus, which is indicative of side reactions[3].

For the present cell configuration, only phase-pure NaO_2 was detected as a discharge product characterised by Raman spectroscopy. However, the oxygen-oxygen bond vibration, expected at 1156 cm^{-1} when bound to Na^+, was randomly

shifted to lower wavenumbers at 1136 cm^{-1}, which has been associated with $Na_2O_2 \cdot 2H_2O$ on the literature[50]. This observation led to a time-resolved characterisation of the discharge product shown in Figure 4.23.

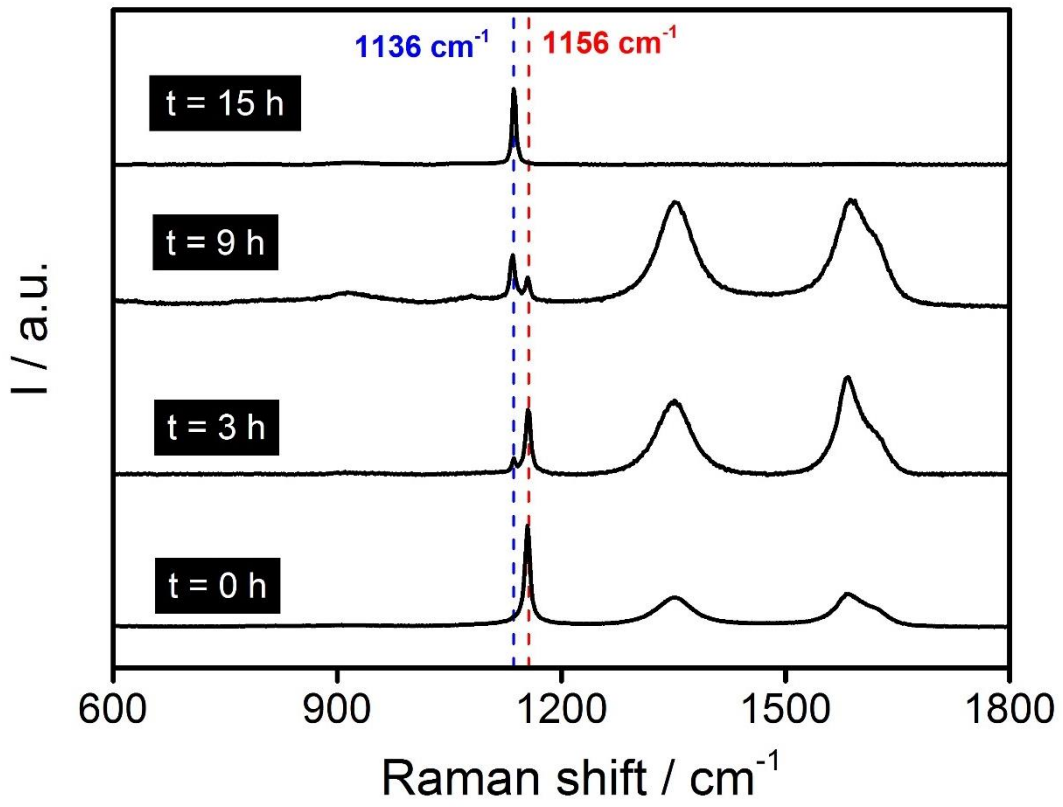

Figure 4.23: Raman spectroscopy analysis after different resting times of the discharge product in Na-O_2 cells using a P50 Avcarb carbon fibre cathode with a 0.5 M NaOTf in DEGDME electrolyte.

When the Raman analysis is undertaken straight after the discharge process (t = 0 h), only a sharp peak at 1156 cm^{-1} is detected. After three hours, the intensity of the 1156 cm^{-1} signal decreases while a peak at 1136 cm^{-1} appears and gradually intensifies. Eventually, the 1156 cm^{-1} signal completely disappears in favour of the 1136 cm^{-1} signal indicating a time transition process. In the spectrum obtained at

t = 15 hours, the absence of the carbon bands simply indicates that the Raman laser was focused solely on top of a solid precipitate.

The assignment of the 1136 cm^{-1} band and the formation of $Na_2O_2 \cdot 2H_2O$ in the discharge of Na-O_2 batteries has been extensively debated in the literature as controversial results have been reported. Ortiz-Vitoriano and *et al.*[39] reported that upon exposure to ambient air, electrochemically formed NaO_2 (1156 cm^{-1}) could be chemically converted to $Na_2O_2 \cdot 2H_2O$ (1136 cm^{-1}), according to the reaction 4.3.

$$2NaO_2 + 2H_2O \rightarrow Na_2O_2 \cdot 2H_2O + O_2 \qquad 4.3$$

This could be indicative, and was speculated, that previous works that reported $Na_2O_2 \cdot 2H_2O$ as a final discharge product[46, 51, 52] had contaminated their sample with atmosphere upon post-discharge characterisation. Intriguingly, the hydrated peroxide transition was not observed when water was purposely added to the electrolyte, indicating the proton source for such transition was the glyme electrolyte[38].

Recently, Bi *et al.*[53] reported results in the same direction, in which altering the cell configuration would cause NaO_2 or $Na_2O_2 \cdot 2H_2O$ to be the final discharge product. The cell configuration that resulted in hydrated peroxide allowed atmosphere contamination. Crystallographic data was provided as evidence for the hydrated peroxide formation. An 1136 cm^{-1} Raman peak was not reported, however an 860 cm^{-1} signal was present in the leaked cell which is assigned to O-O stretching in hydrogen peroxide. This lead to the conjecture that the NaO_2 transition would result in $2NaOH \cdot 2H_2O_2$ instead of $Na_2O_2 \cdot 2H_2O$.

Kim *et al.*[50] reported that electrochemically formed NaO_2 can undergo dissolution and ionisation reactions under rest conditions evidenced by electron spin resonance spectroscopy (ESR) data, which confirmed the presence of superoxide radical anion in solution. Indeed, the solubility of NaO_2 in ether based electrolyte has been reported by other authors[26, 29]. A time-resolved XRD and Raman spectroscopy analysis by Kim *et al.* provided confirmation of the complete conversion of NaO_2 to $Na_2O_2 \cdot 2H_2O$ after a 12 hours rest period of the cathode in a DEGDME-based electrolyte. Similar dissolution processes were reported by Landa-Medrano and *et al.*[54], where the 1136 cm^{-1} Raman signal was observed for an aged cathode after 30 hours. Both studies are in good agreement with the experimental data on presented on Figure 4.23.

Another investigation on the transition of NaO_2 after the discharge process was reported by Sayed *et al.*[55]. The Raman characterisation of the aged cathode showed a signal at 1147 cm^{-1} that was assigned to stretching modes of CH_3-O from sodium methoxide, a common electrolyte degradation parasitic product in metal-oxygen batteries[14]. Evidence of the methoxide bond vibration, which has an intense FTIR signal, was not detected in our investigation.

The reliability of the crystallographic data used to identify $Na_2O_2 \cdot 2H_2O$ as a final discharge product in the aforementioned reports has been called into question[56, 57]. Na_2O_2 can form different hydrated compounds, in which the hydrated molecules are not water of crystallisation, but rather a part of the anion structure[58]. Thus, the XRD data can be wrongly assigned for other possible oxide phases, such as Na_2O_2, $Na_2O_2 \cdot 8H_2O$ and NaOH.

As for the characterisation of the discharge product based on Raman data, a reliable standard for $Na_2O_2 \cdot 2H_2O$ is not available. Nevertheless, Raman spectroscopy can definitively distinguish Na_2O_2 from NaO_2. The fundamental frequencies for the peroxide ion under the influence of sodium ions are expected at 730 cm^{-1} and 787 cm^{-1}, which are assigned to the O_2^{2-} vibration within the unit cell (C_{3h} sites) and at the edge of the unit cell (D_{3h} sites), respectively[59]. While Raman frequency for the superoxide ion is expected at 1156 cm^{-1}. The Raman feature at 1136 cm^{-1}, assigned by Kim and Ortiz-Vitoriano for $Na_2O_2 \cdot 2H_2O$ formation, has been extensively described in the literature as superoxide impurities to commercial Na_2O_2[59-61], occasionally reported at 1141 cm^{-1} possibly due to different experiment conditions – laser source, laser power and exposure time.

In fact, the 1136 cm^{-1} peak has never been reported along with the peroxide ion fundamental frequencies in a discharged cathode, similar to the results previously shown on Figure 4.23. Therefore, is difficult to draw the inference that the shift in the Raman peak from 1156cm^{-1} to 1136cm^{-1} is due to a $Na_2O_2 \cdot 2H_2O$ conversion.

Other techniques such as EDS and XPS are equally incompetent to distinguish NaO_2 from $Na_2O_2 \cdot 2H_2O$, as the same sodium to oxygen atomic ratio is expected on both superoxide and dihydrated peroxide and similar binding energies are expected for the Na1s spectral line.

A similar time-resolved investigation on the morphology of the precipitates was performed by SEM, Figure 4.24. The same electrodes and rest conditions used in the Raman study were employed.

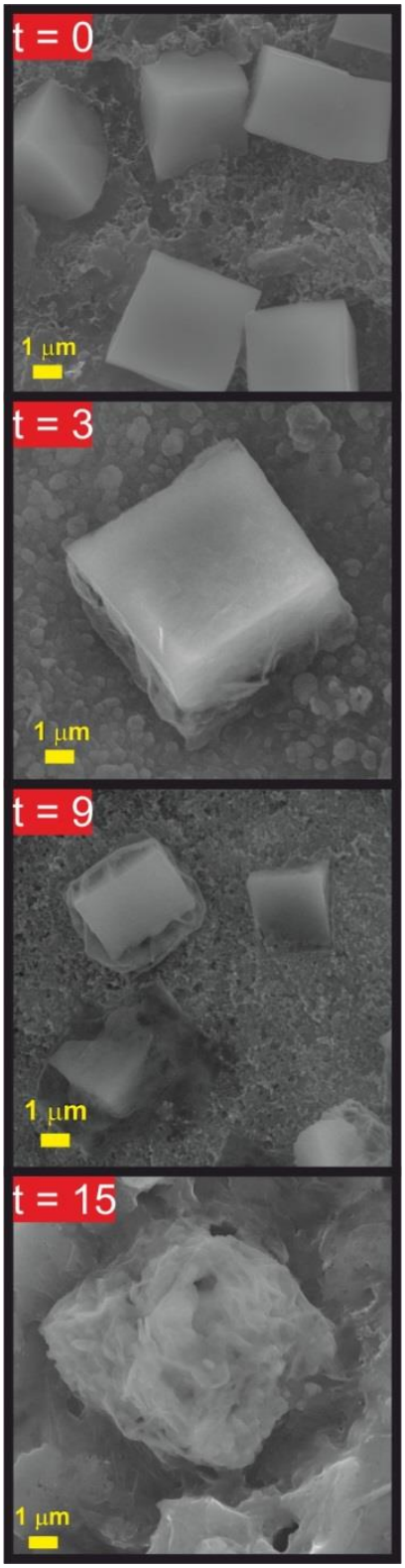

Figure 4.24: SEM analysis after different resting times of the discharge product morphology in Na-O_2 cells using a P50 Avcarb carbon fibre cathode with a 0.5 M NaOTf in DEGDME electrolyte.

The time from removing the electrodes from air tight vials to SEM insertion was generally less than 30 seconds, which is assumed to have little influence on the chemical nature and morphology of the products based on the sharp edges cubes in the non-aged sample (t = 0 hours). SEM micrographs obtained straight after the discharge termination show the widely reported NaO_2 cubic shaped crystals[3]. After 3 hours of the discharged cathode in contact with the electrolyte, the edges of the cubic particles appear smudged or blurred. Since the micron-sized NaO_2 precipitates are visible through the Raman optical microscope, it can be noted that the smudged edges have a signal at 1136 cm^{-1}, while the centre of the cubes at 1156 cm^{-1}.

Increasing the time between discharge and SEM analysis, the blurred edges are more dominant on the crystal morphology, until after 15 hours the cubic shapes completely dissolve bearing resemble to previous reports in which $Na_2O_2 \cdot 2H_2O$ was assumed as the final discharge product[46, 51] and other timer-resolved investigations[50, 54]. The SEM analysis ultimately indicates a dissolution process of NaO_2 in the electrolyte and corroborates the assignment of the 1136 cm^{-1} peak to $Na_2O_2 \cdot 2H_2O$.

The dissolution of NaO_2 and migration of $O_2^{\bullet-}$ into the electrolyte affect significantly the overall electrochemical behaviour of the cell. To investigate the effect of operation conditions, two Na-O_2 cells were cycled up to equivalent absolute capacities under different current densities and the results are presented in Figure 4.25.

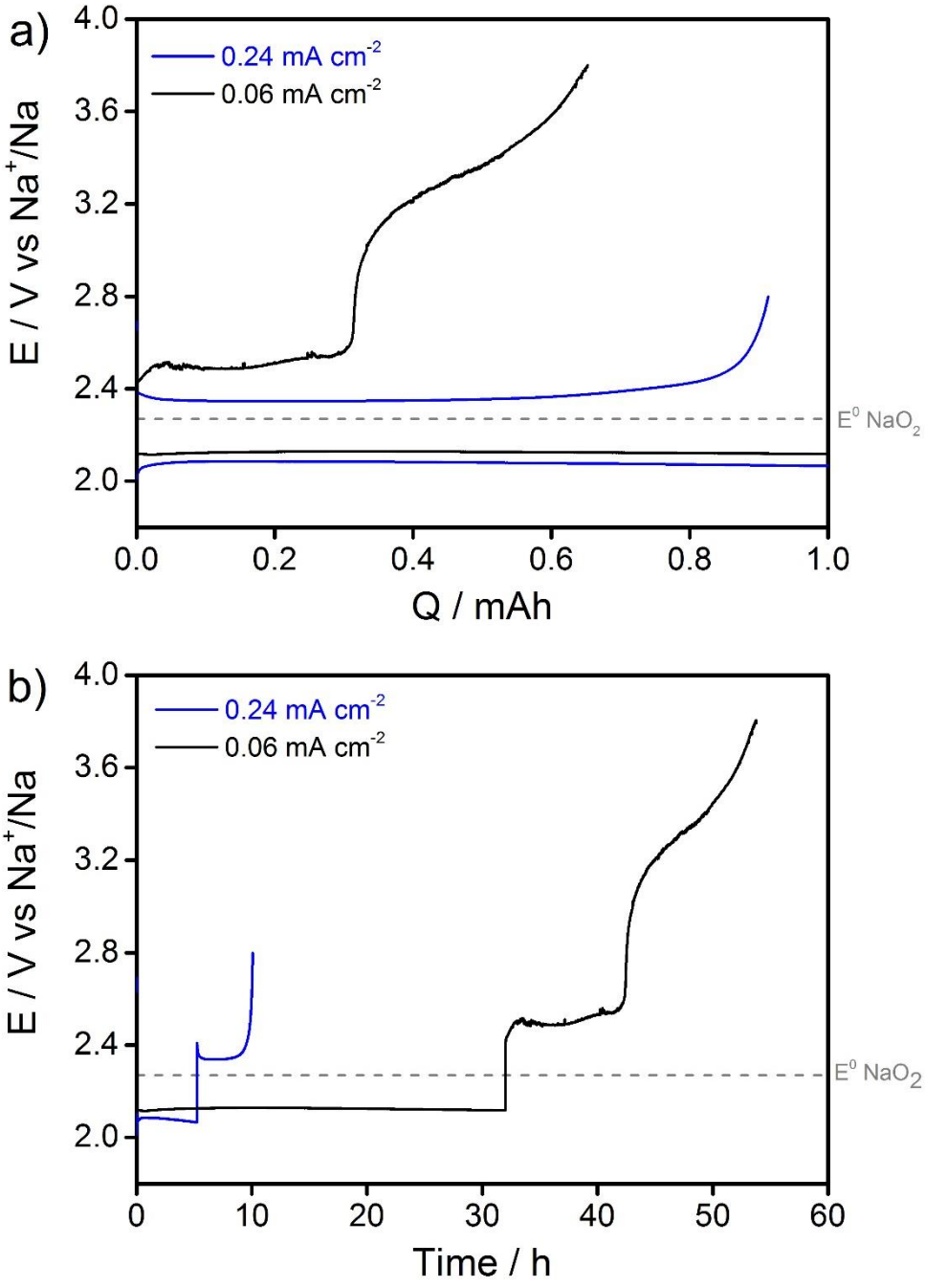

Figure 4.25: First galvanostatic discharge/charge cycle as a function of a) absolute charge and b) cycling time for Na-O_2 cells using a P50 Avcarb carbon fibre cathode with a 0.5 M NaOTf in DEGDME electrolyte at 0.24 and 0.06 mA cm^{-2} current density.

The discharge curve is not expressively affected by the current applied as the same cell chemistry is expected independent of the rate, as discussed in section 4.4.6 (Figure 4.18). The cell discharged at 0.06 mA cm^{-2} has slightly lower overpotential as the $O_2^{\bullet-}$ mass transport is less limited. In contrast, the charge profile is heavily affected by the current applied. For the higher current density (0.24 mA cm^{-2}) cell, the expected behaviour for superoxide based Na-O_2 cells[43] is observed: low charge polarisation (η_{charge} = 80 mV) and high coulombic efficiency (92%).

Even though NaO_2 is the only discharge product in both cases, the lower current density cell exhibited a higher charge overpotential for the first plateau at ~ 2.5 V vs Na^+/Na and the appearance of a second reaction plateau at ~ 3.1 V *vs* Na^+/Na. The larger overpotential for lower current rate, contrary to expected trend, is evidence of the dissolution and migration process, as the cathode is exposed to the cell environment for a longer time, Figure 4.24b.

The shape and plateaus on the charge curves are indicative of reactions taking place on the cell. The additional plateau implies a second reaction other than superoxide decomposition which corroborates the hypothesis of a time-dependent transformation of the discharge product. On the literature[16, 53], the plateau at 3.1 V vs Na^+/Na has been described as sodium hydroxide oxidation based on *in situ* XRD data according equations (4.4 and 4.5), which can only happen if the transition from superoxide to hydrated peroxide indeed occurred.

$$Na_2O_2 \cdot 2H_2O \rightarrow 2NaOH + H_2O_2 \qquad 4.4$$

$$2NaOH \rightarrow 2Na^+ + H_2O_2 + 2e^- \qquad 4.5$$

Based on the aforementioned conversion reaction from NaO_2 to $Na_2O_2 \cdot 2H_2O$, an equimolar amount of water is required for the reaction. During discharge (Figure 4.24a), 1 mAh of NaO_2 was generated, equivalent to 37 x 10^{-6} mol. Based on our cell configuration, 120 μL of electrolyte and 8 ppm of water (H_2O content measured with a Karl Fischer Coulometer), only 0.05 x 10^{-6} mol of water are available to react with NaO_2, which amount to 0.1% of the quantity required. A conclusion can be made that the proton source for the hydrated peroxide transition must come from DEGDME instead of residual water in the electrolyte. A reaction mechanism for the formation of $Na_2O_2 \cdot 2H_2O$ is shown on Scheme 4.3.

Scheme 4.3: NaO_2 dissolution mechanism in DEGDME-based electrolytes.

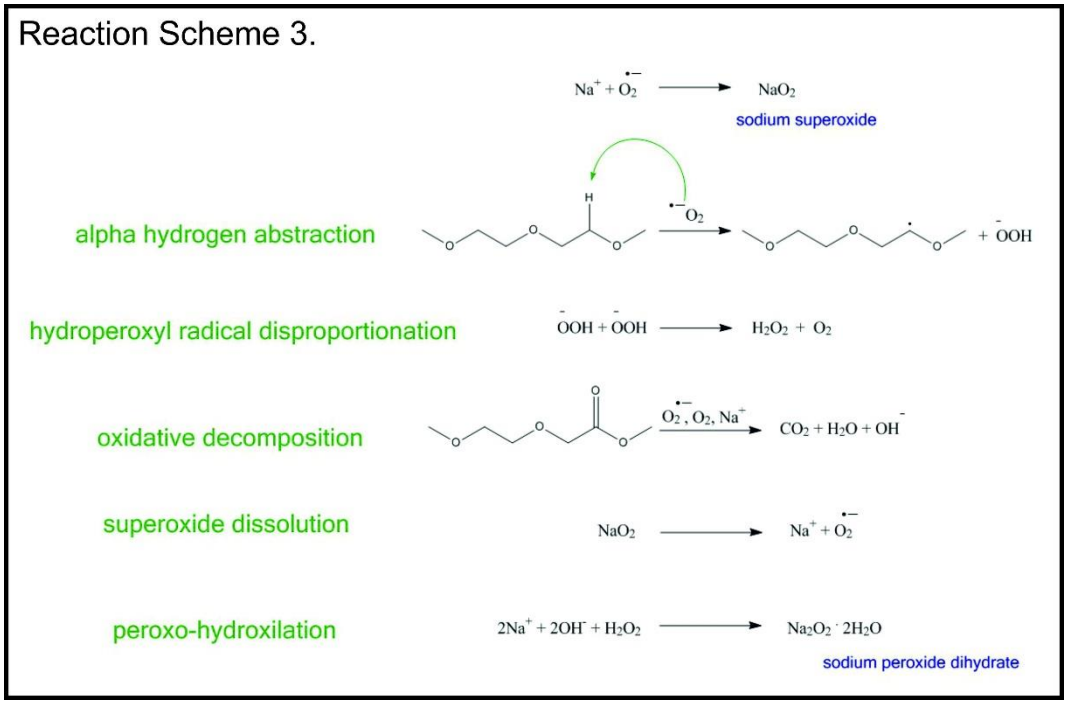

As previously discussed, DEGDME has acid hydrogens bound to the alpha carbon which can react with a strong nucleophile such as the superoxide radical anion or NaO_2 forming hydroperoxyl radicals in the solution. The

disproportionation reaction of hydroperoxyl radical to hydrogen peroxide is well documented in aprotic non-aqueous solvents[62]. Therefore, sodium peroxide dihydrate is generated by a peroxo-hydroxilation reaction proposed by Kim *et al.*[50]. A different reaction mechanism for the $Na_2O_2 \cdot 2H_2O$ is expected when water is purposely added to the electrolyte[16].

4.4.8 Sodium peroxide formation

The Na-O_2 battery based on a two-electron reduction per O_2 to form peroxide suffers from much larger charge polarisation, when compared to superoxide based cells, according to reports by different authors[45, 63-65]. One of the reasons being that a one-electron transfer process is always kinetically favoured[13]. Furthermore, Na_2O_2 has reported sluggish bulk kinetics, while NaO_2 the ionic conductivity is significantly improved[15]. However, if the oxidation of NaO_2 is within the carbon cathode stability towards oxidative degradation (~ 3.83 V vs Na^+/Na)[9], then indeed a practical Na-O_2 cell can be made possible.

Aiming for high power devices, a Na-O_2 battery based on peroxide formation/decomposition is actually preferable since higher theoretical energy densities are generated for this system (4482 Wh l^{-1} for Na_2O_2 in comparison to 2438 Wh l^{-1} for NaO_2).

The formation of Na_2O_2 can be made possible via a chemical disproportionation or consecutive electron reduction of NaO_2. In Li-O_2 cells, Johnson *et al.*[28] observed *in situ* evidence of the disproportionation pathway predominance when using high DN solvents at low overpotentials, while the second electron reduction is dominant at high overpotentials. Ma *et al.*[66] observed

formation of Na_2O_2 via a second electron reduction of NaO_2 when using high DN solvents. Both studies employed cyclic voltammetry with gold electrodes to investigate the oxygen reduction reaction, which is strongly affected by the nature of the electrode material[67].

Based on these cyclic voltammetry studies of O_2 saturated DMSO electrolytes which demonstrated two consecutive electron transfers to be possible[66, 68], an attempt to further reduce electrochemically formed NaO_2 as a sole discharge product by forcing a larger voltage polarisation, under conventional battery test conditions, was made (Figure 4.26). The characterisation of the products formed on the cathode surface via Raman spectroscopy is shown in Figure 4.27.

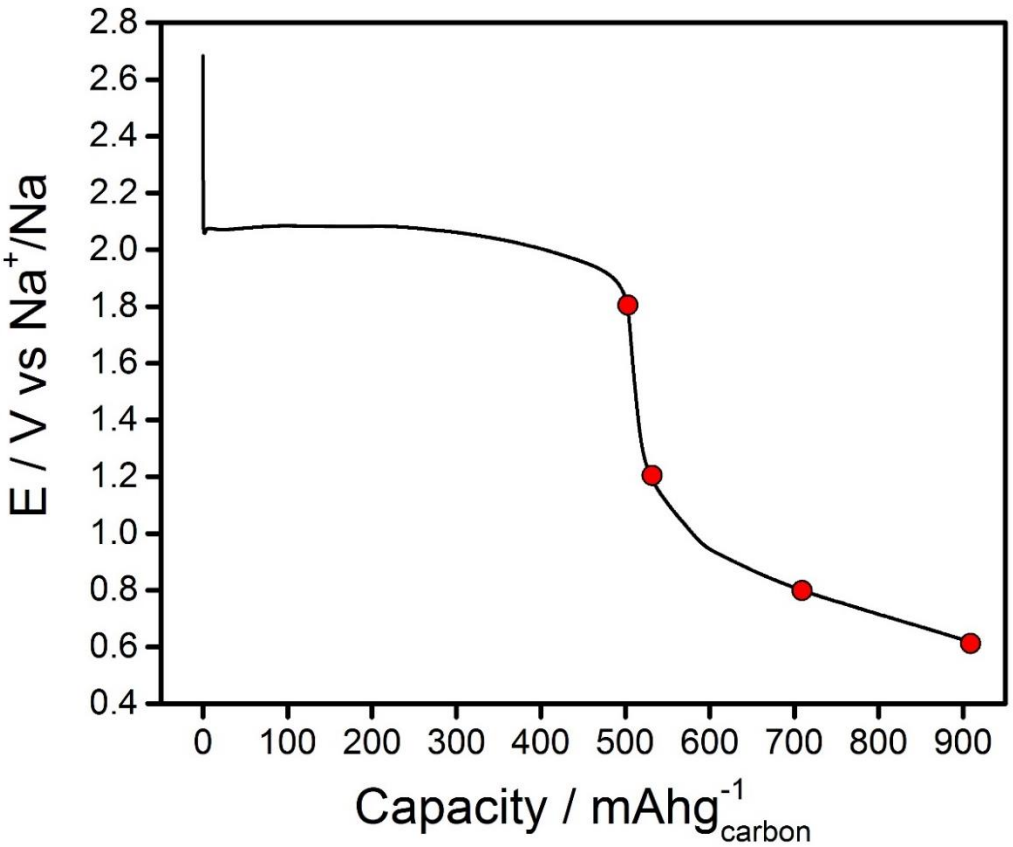

Figure 4.26: Galvanostatic discharge of a Na-O_2 cell using a P50 Avcarb carbon cathode discharged to 0.6 V vs Na^+/Na at 0.24 mA cm^{-2}. Electrolyte: 0.5 M NaOTf in DEGDME.

The discharge curve has a flat potential plateau characteristic of superoxide formation-nucleation-growth followed by a sharp decrease in potential observed at 1.8 V vs Na^+/Na upon surface passivation by a film-lime superoxide deposit, as previously. On the cyclic voltammogram reported by Padmanabhan *et al.*[68] the potential difference between the consecutive reduction peaks is 0.3 V, while in Ma *et al.*[66] report peroxide formation occurs after a 0.5 V cathodic sweep after the NaO_2 formation. However, applying the same potential difference in a Na-O_2 cell a significant additional capacity is not obtained (10 mAh g^{-1}) and no subsequent plateau is not observed, indicating that a second-electron reduction process is not possible. At larger overpotential an increase in capacity is observed outside the electrolyte stability window.

This result further corroborates the NaO_2 deposit mechanism proposed in section 4.4.5. When the film-like deposit formed between cuboid particles reaches a certain thickness, charge transfer is blocked across the electrode interface at "cell death", which impedes the further reduction to peroxide. In cyclic voltammetry experiments, using planar non-porous gold electrodes[25, 68], the reduction of molecular oxygen leads to adsorbed or solvated [Na^+-- $O_2^{\bullet-}$] pairs for which a second-electron reduction is feasible. In practical battery cells, using porous electrodes, the oxygen reduction results in the nucleation and growth of micron-sized, chemically stable, NaO_2 particles, for which charge transfer across the cubes edges has been disregarded as a possible reaction pathway[29].

Raman spectra taken at different discharge potential show solely NaO_2 (1156 cm^{-1}) at 1.8 V vs Na^+/Na; NaO_2 and $Na_2O_2 \cdot 2H_2O$ (1136 cm^{-1}) at 1.2 V vs Na^+/Na; NaO_2, $Na_2O_2 \cdot 2H_2O$ and Na_2CO_3 (1080 cm^{-1}) at 0.8 V vs Na^+/Na; solely

Na_2CO_3 at 0.6 V vs Na^+/Na. Na_2O_2 related vibrations were not detected at any state of discharge.

These results confirm that a second-electron transfer was not possible in practical Na-O_2 cells even at large polarisation. In a recent publication by Schroder *et al.*[56], the same conclusion was obtained while attempting to promote peroxide formation via further reducing electrochemically formed superoxide in an argon atmosphere. Furthermore, the formation of $Na_2O_2 \cdot 2H_2O$ at 1.2 V vs Na^+/Na is in line with the discussion in the previous section. The observation of the transition to hydrated peroxide taking place even with the carbon electrode negatively biased indicates that is indeed a chemical process triggered by the dissolution of electrochemically formed superoxide. Eventually the Raman signal is dominated by Na_2CO_3 due to electrolyte decomposition.

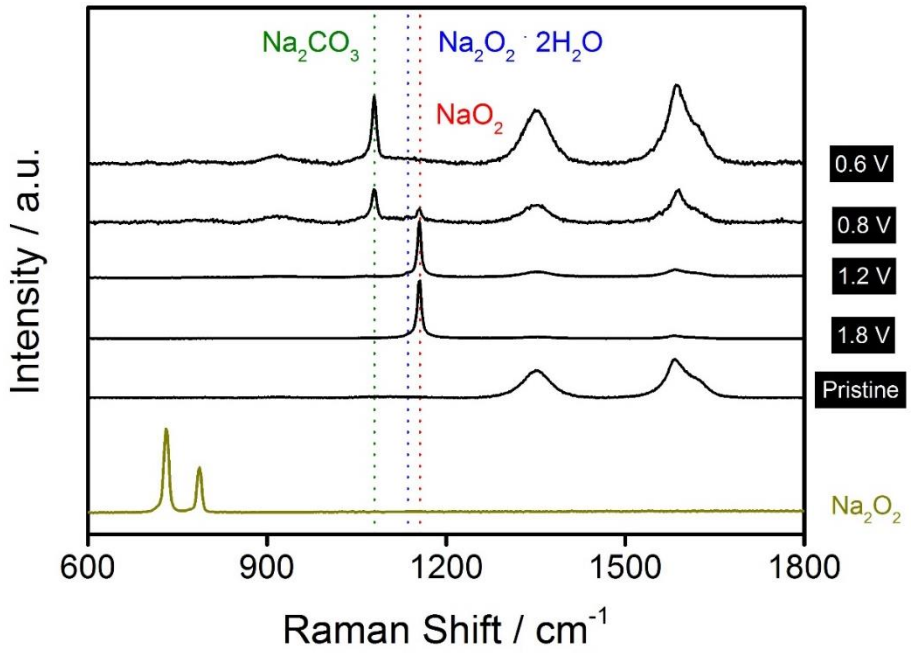

Figure 4.27: Raman spectra of a P50 Avcarb cathode discharged to various potential limits. Rate: at 0.24 mA cm^{-2}. Electrolyte: 0.5 M NaOTf in DEGDME.

4.4.9 Effect of the polymeric binder

A typical positive electrode is comprised of a high surface area carbon and a polymeric binder either connected to a porous current collector or as a self-supporting electrode. Even though the binder only constitutes a small percentage of the overall electrode weight, its stability in practical cells must be taken into consideration.

In Li-O_2 systems, Black *et al.*[69] and Nasybulyn *et al.*[70] identified the instability of PVDF binder by reaction with chemically generated superoxide radical. However, the polymer instability had no influence on the discharge product chemistry of Li-O_2 cells, as Li_2O_2 was identified via PXRD for different binders[69, 70]. Indeed, different research groups have reported stable cycling for Li-O_2 cells using PVDF based carbon cathodes[71-75].

Here, the stability of three polymer binders (CMC, PTFE and PVDF, Figure 4.28) was investigated as well as the effect on the electrochemical performance of a carbon black cathode (Timcal Super C 65, 62 $m^2 g^{-1}$). Na-O_2 cells were assembled using the standard electrolyte (0.5 M NaOTf in DEGDME) at a current density of 0.12 mA cm^2 and an absolute capacity limitation of 1 mAh.

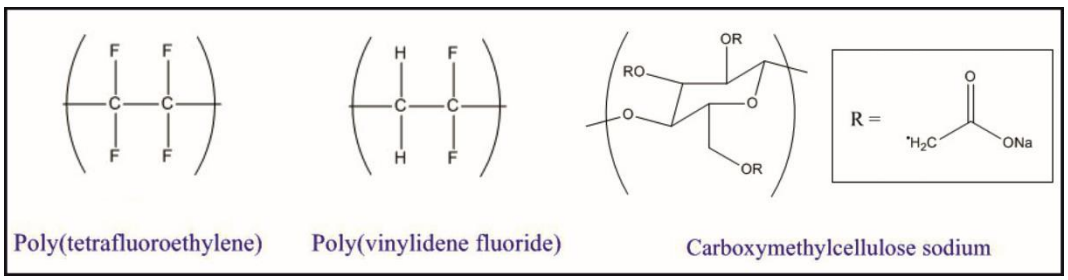

Figure 4.28: Chemical structures of binders utilised in the present work.

The first galvanostatic discharge/charge profile for the four different cathodes and the Raman characterisation of the reaction products are depicted in Figure 4.29a. The performance of carbon black cast with PTFE is very similar to the binder-free cathode, with low combined overpotential and high reversibility (90% for the binder-free cathode and 90% for the PTFE cathode), which is the ideal voltage profile. The formation of phase-pure NaO_2 during discharge in established via Raman spectroscopy and no other side products were detected, confirming the stability of PTFE in Na-O_2 cell chemical environment.

The Na-O_2 cell using a carbon black/CMC cathode presented slightly higher charge overpotential, with monotonically increase of the voltage plateau, and lower capacity retention (76%), which indicates some degree of parasitic reactions. A small peak at 1080 cm^{-1} indicates the presence of Na_2CO_3 together with the 1156 cm^{-1} NaO_2 peak on the discharged cathode. Lithium carbonate has also been reported in Li-O_2 discharged cells using CMC based cathodes due to carbonyl group degradation[70].

The electrochemistry performance of the carbon black/PVDF cell is in stark contrast with the other systems, indicating different cell chemistries. No discharge plateau is observed, instead the voltage steadily decreases which is indicative of mixed reactions. The charge curve presents two distinct voltage processes, a short plateau at low voltage (2.4 V vs Na^+/Na) which is assumed to be superoxide oxidation and one at large overpotential (above 3.6 V vs Na^+/Na) related to oxidation of side product. The ratio of the charge plateaus suggests that the overall cell chemistry is governed by side reactions.

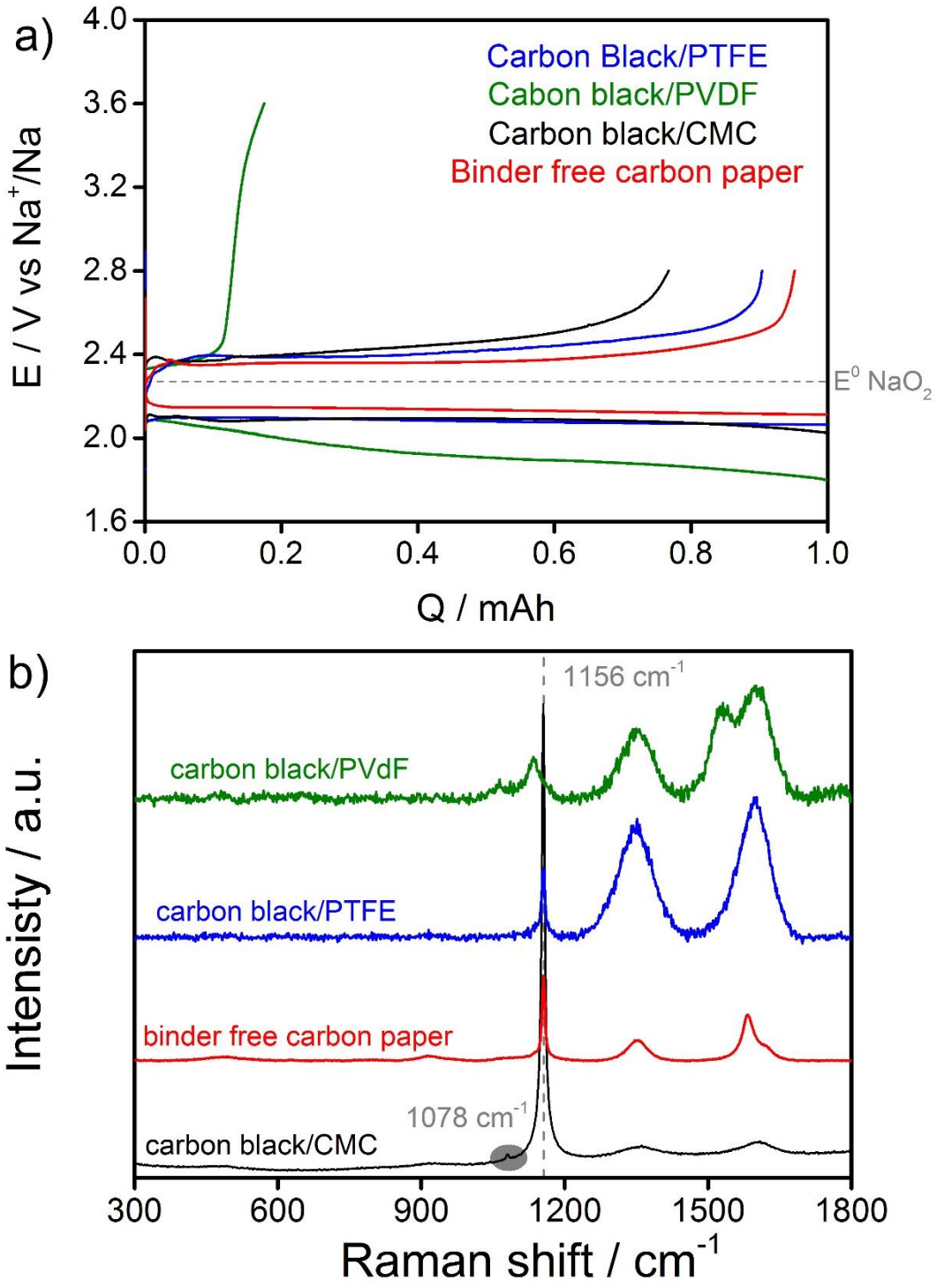

Figure 4.29: a) First Galvanostatic discharge/charge cycle for Na-O_2 cells with carbon black cathodes cast with different binders and 1 mAh absolute capacity limitation. Electrolyte: 0.5 M NaOTf in DEGDME. Rate: 0.12 mA cm^{-2}. b) Raman spectra discharged carbon cathodes.

The Raman spectrum of the discharge carbon black/PVDF cathode exhibits two additional bands at 1134 cm^{-1} and 1531cm^{-1}. Several different locations of the cathode surface were probed under the Raman optical microscope, and the appearance of the two broad bands was reproducible, while a peak at 1156 cm^{-1} (superoxide stretching mode) was not detected. The assignment of the additional Raman features is very controversial on the literature.

Zhai and *et al.*[76] reported similar 1125 cm^{-1} and 1505 cm^{-1} broad bands using an activated carbon/PVDF positive electrode in Li-O_2 cells. The 1125 cm^{-1} signal was assigned to an O-O stretching mode from LiO_2, while the 1505 cm^{-1} signal was assigned to a LiO_2 coupling induced distortion of the graphitic ring vibration mode (G band), supported by DFT evidence of LiO_2 clusters interacting with the carbon surface. It was hypothesised that the outer regions of Li_2O_2 toroids would be composed of superoxide species. The same research group reported a Li-O_2 battery cycling on the formation and decomposition of lithium superoxide based on similar Raman characterisation[71].

Galloway *et al.*[77] reported both the 1123 cm^{-1} (νO-O^-) and the 1520 cm^{-1} (νC-O_2Li) signals *in situ* using a glassy carbon electrode (binder-free), while the latter was not detected using a gold planar electrode. The same research group reported LiO_2 Raman signals using practical battery electrodes (Carbon black/PTFE)[78]. Both studies utilised enhanced Raman techniques, indicating that the superoxide interaction with the graphitic ring is an intrinsically weak scattering process. Since these reduction species are generated via cycling voltammetry, the LiO_2 detected is most likely an absorbed reaction intermediate, instead of a solid discharge product.

In contrast, Papp *et al.*[79] suggested that the LiO_2 assignments (νO-O^- and νC-O_2Li) by Zhai *et al.*[75] were in fact related to PVDF degradation upon cell discharge. An investigation by electrochemical differential mass spectroscopy pointed to a $2e^-/O_2$ process, which ruled out the formation of LiO_2 as a final discharge product.

In the present Na-O_2 cell configuration, the main discharge reaction is the one-electron reduction of molecular oxygen resulting in NaO_2; therefore, the graphitic ring distortion band should be expected for all the polymeric binders based cells in Figure 4.28. The observation of the 1528 cm^{-1} band only when PVDF is employed indicates that the signal is indeed characteristic of the binder.

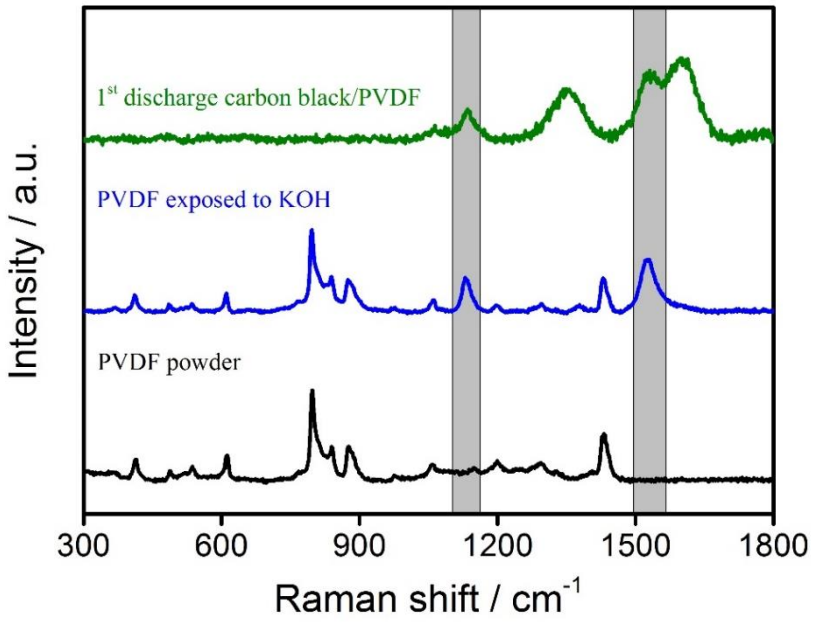

Figure 4.30: Comparison of the discharged carbon black/PVDF cathode Raman characterisation with Raman spectra of PVDF powder and PVDF exposed to KOH.

In fact, the Raman signals detected for the discharged carbon black/PVDF cathode are present in a spectrum of PVDF exposed to potassium hydroxide

(Figure 4.30), in agreement to the report by Papp *et al.*[79]. In this experiment, KOH mimics the superoxide radical anion (even though $O_2^{\bullet-}$ is a much stronger base) inducing the dehydroflurionation reaction which takes place during cell discharge via a one-step concerted elimination mechanism. As a result of the hydrogen abstraction, alternated double bonds are formed in the polymer backbone, which gives rise to the extra bands in the Raman spectrum (Figure 4.29b). The 1134 cm^{-1} signal is assigned to the carbon/carbon single bond stretching mode in the polymer backbone (HC=**CF–CH**=CF) and the 1531 cm^{-1} signal is assigned to the carbon/carbon conjugated bond stretching mode (CF–**CH=CF**–CH)[80].

The same PVDF degradation signals are detected, non-shifted, for different alkali metal-oxygen batteries using a carbon black/PVDF cathode and ether-based electrolytes (see Appendix A, Figure A9). In the Li-O_2 cell, FTIR characterisation of the discharge product demonstrated the formation of Li_2O_2 as the main discharge product, for which the interaction with the carbon surface causing a distortion of the graphitic ring stretching mode is not expected[76]. An additional observation that corroborates the assignment of the 1134 and 1531 cm^{-1} bands to binder degradation, instead of superoxide interaction with the carbon substrate, is the ratio between the intensities of the out of plane disorder induced vibration (D band) and the in plane first order graphitic ring vibration (G band). The I_D/I_G peak intensity ratio for the discharged cathodes cast with different binders remained constant in this study.

Table 4.1: Intensity ratio of D and G Raman bands in discharged carbon black cathodes using different polymeric binders.

Cathode	I_D/I_G
Carbon black/CMC	0.74
Carbon black/PVDF	0.72
Carbon black/PTFE	0.72

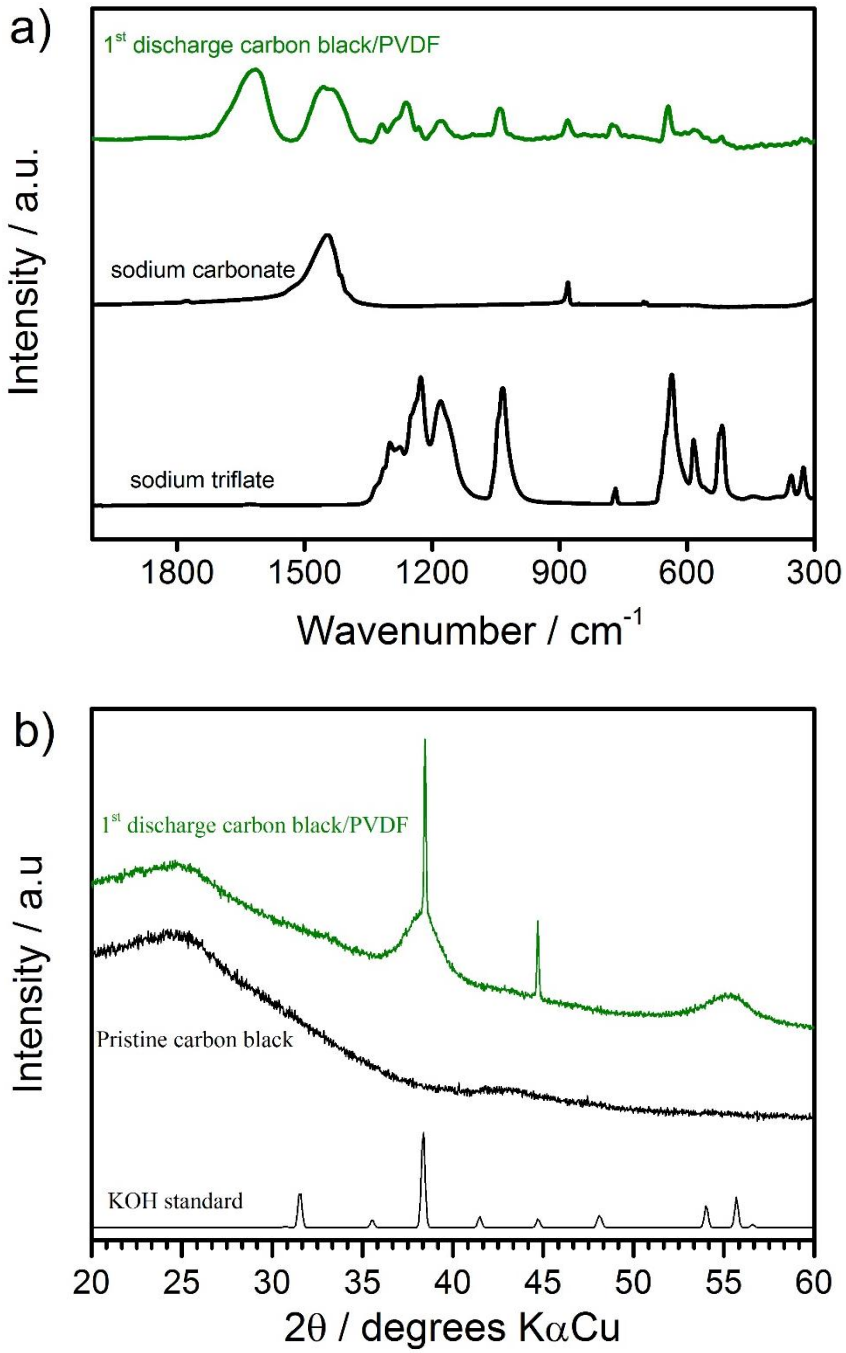

Figure 4.31: a) FTIR and b) PXRD characterisation of carbon black/PVDF cathode discharged in a 0.5 M NaOTf in DEGDME electrolyte at 0.12 mA cm^{-2} rate.

Further characterisation of the carbon black/PVDF cathode by FTIR shows two bands at 1444 and 880 cm^{-1} assigned asymmetric stretch and in-plane bend of the carbonate ion in Na_2CO_3 as a result of glyme degradation. The IR band visible

at 1617 cm^{-1} can in the spectral region of both sodium formate and substituted alkenes, which can arise from binder degradation. The spectra of the discharge cathode still retains signals from the support salt from electrolyte evaporation prior to the analysis.

A mechanism for the degradation processes occurring at the carbon black-PVDF cathode is proposed in Scheme 4.4. The proton abstraction on the PVDF molecule by $O_2^{\bullet-}$ results in the formation of the hydroperoxyl radical (the protonated form of superoxide radical) which is known to promote electrolyte degradation in ether-based solvents[14]. The hydroperoxyl radical disproportionation reaction that ultimately forms sodium hydroxide is also well documented in aprotic non-aqueous solvents[81]. Revees *et al.* reported similar side reactions as a result of PVFD binder degradation via solid-state ^{23}Na NMR spectroscopy[82].

Scheme 4.4: Degradation mechanism of PVDF binder in Na-O_2 cells.

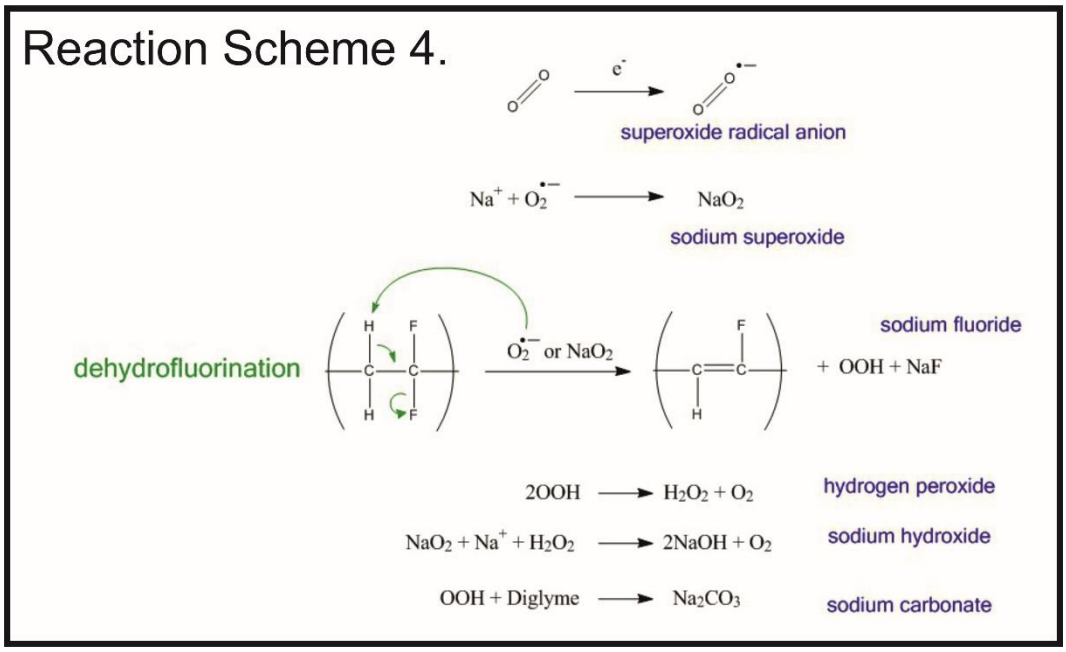

The formation of the aforementioned side products explains the second plateau at high polarisation during charge (Figure 4.29a), as these molecules are more stable than NaO_2 and a higher voltage is required to drive the oxidation reactions. The observation of a lower plateau close to the thermodynamic potential for NaO_2 oxidation can be interpreted as superoxide being electrochemically formed at first in the discharge reaction, and subsequently being degraded to carbonate and hydroxide driven by the PVDF dehydroflurionation reaction.

The morphology of the reaction products on the carbon black surface for different binders was investigated by SEM (Figure 4.32). When using CMC and PTFE, the expected micron-sized cubic structures sparsely distributed on the carbon black carpet were observed, in agreement with the Raman characterisation of NaO_2 as the main reaction product.

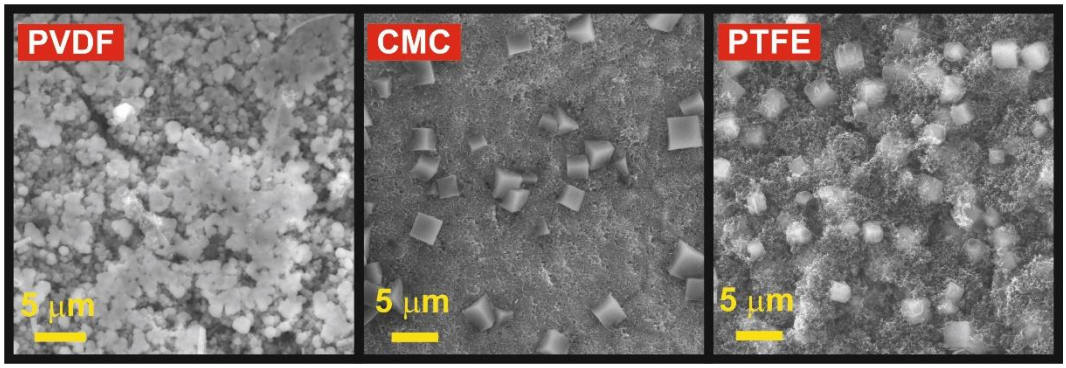

Figure 4.32: SEM micrographs of the carbon black cathodes using different polymer binders discharged in a 0.5 M NaOTf in DEGDME electrolyte at 0.12 mA cm^{-2} rate.

In contrast, when using PVDF, the carbon substrate is not visible and the cathode surface is completely covered by nano-sized globular shapes, similar to the morphology of propylene carbonate based Na-O_2 cells (see Figures 4.2b,c and

B1d). Thus indicating that, for the carbon black/PVDF system, the cell chemistry is dominated by parasitic reactions.

The effect of the binder degradation in Na-O_2 systems is much more detrimental when compared to Li-O_2, where reports by Black *et al.*[68] indicate that the PVDF degradation does not impede the nucleation and growth of the desired Li_2O_2 reaction product in Li-O_2 cells.

4.4.10 Effect of the carbon air-cathode

The design and optimisation of suitable positive electrodes is a central concern on alkali metal-oxygen investigation. Cathodes for alkali metal-oxygen batteries should be catalytic and specific towards ORR/OER – reactions with the electrolyte solvents and conducting salt must be avoided. Allow sufficient electronic and ionic conductivity to ORR/OER reaction sites as well as oxygen mass transport. The cathode stability must be within the cell electrochemical window to avoid oxidative decomposition.

The mechanism studies on NaO_2 growth and nucleation reported here employed only gas diffusion layer electrodes (H24, Freudenberg & Co. and P50, Avcarb). Their well-defined fibre morphology makes them ideal for more fundamental studies, such as ORR/OER kinetics, NaO_2 deposition mechanism and particle size distribution. To obtain high capacity on the positive electrode, however, electrodes with higher porous structures must be assembled to accommodate electronic insulating discharge products avoiding pore clogging and electrode passivation.

Here, an investigation was lead onto the effect of the carbon material in the cathode on Na-O_2 cell performance. For such, five different electrodes are compared: a gas diffusion layer (H24, Freudenberg & Co.), a carbon paper (P50, Avcarb), a graphite felt (GFD 2.5EA, SGL Group) and two conductive carbon black (Ketjenblack EC 600 JD, AkzoNobel and Super C65, Imerys). The carbon black cathodes were prepared using PTFE binder (80% active material, 20% binder) due to superior stability discussed in the previous section. The carbon fibre electrodes are binder-free. Sodium-oxygen cells were assembled using a 0.5 M NaOTf in DEGDME electrolyte (<10 ppm H_2O) at a current density of 0.12 mA cm^{-2}.

The first cycle galvanostatic discharge/charge curves are shown in Figure 4.33a, while the Raman characterisation of discharge products is shown in Figure 4.33b. An overview of the carbon cathodes properties and the maximum capacities achieved are displayed in Table 4.2.

In terms of capacity normalised by carbon active material weight, the Ketjenblack electrode reaches the highest value at 2925 mAh g^{-1}. However, the specific capacity comparison can be misleading due to very low mass loadings associated with low density carbon blacks. When looking at the absolute capacity and areal capacity, the graphite felt is the most effective electrode material with significantly higher capacities obtained (see Appendix A, Figure A10). This is related to the GF higher open porosity (94% of the total electrode volume), which can accommodate larger amounts of NaO_2 deposits. The combination of high porosity and low diameter interwoven carbon fibres with an average diameter of 8 μm maximises the number of three phase regions (where the ORR takes place), which is reported to be directly related to the cell capacity[83].

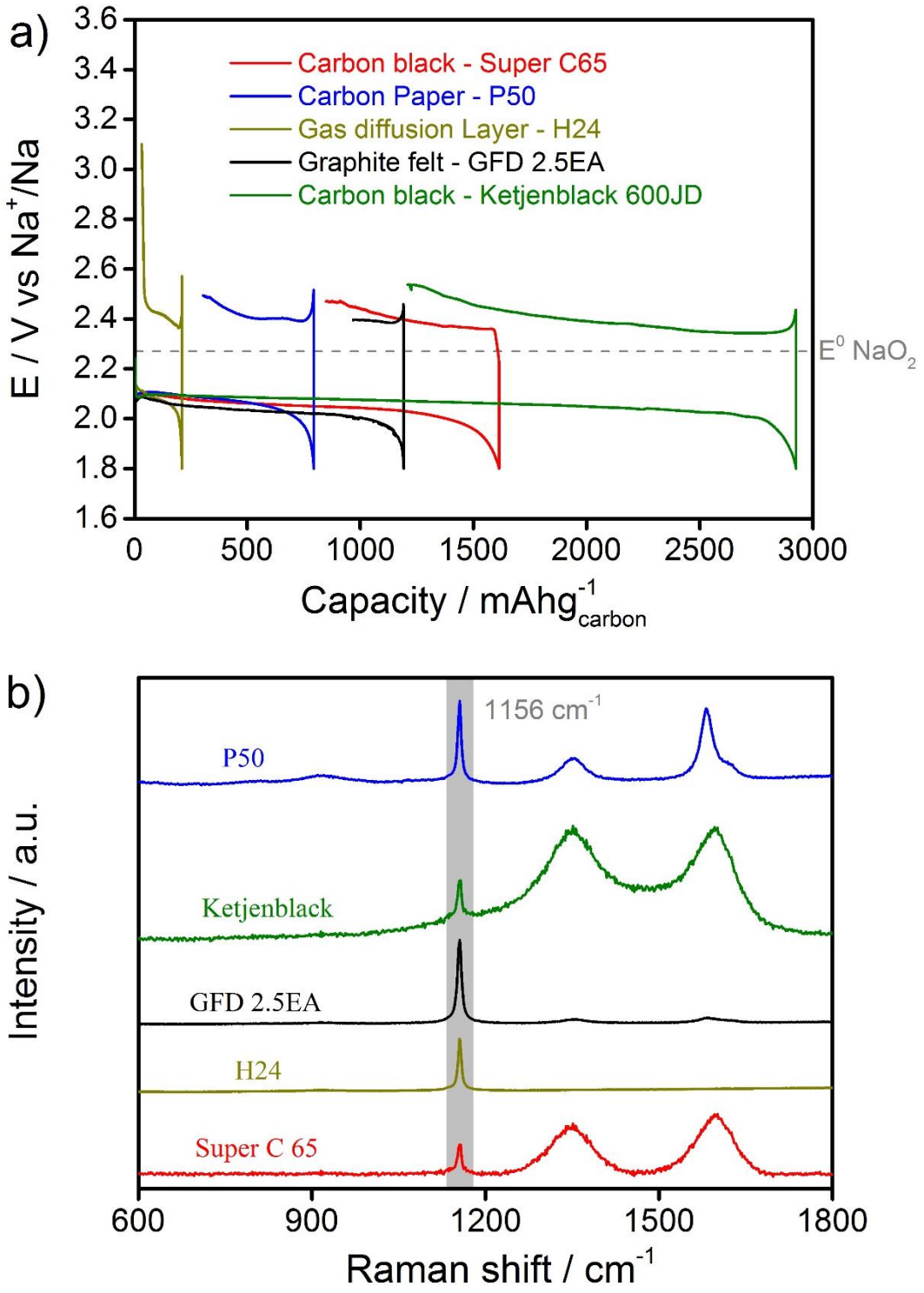

Figure 4.33: a) First galvanostatic discharge/charge curves for Na-O_2 cells using different carbon cathodes with a 0.5 M NaOTf in DEGDME electrolyte at 0.12 mA cm^{-2} rate. b) Raman spectra of the discharged carbon cathodes.

Comparing the capacity obtained in our Na-O_2 batteries with typical lithium-ion batteries reports (in the rage of 3–7 mAh cm^{-2})[84], only the graphite felt electrode shows major improvements. In fact, a capacity requirement calculated for alkali metal-oxygen battery in automotive applications (in the range of 5–30 mAh cm^{-2})[85, 86] is only obtained when using the graphitic felt electrodes.

Table 4.2: Mass loading, BET surface area and average discharge capacities for the five carbon cathodes tested in Na-O_2 cells. Geometric area for all the tested electrodes was 0.785 cm^2.

Carbon	m (mg)	BET (m^2 g^{-1})	Q (mAh)	Q (mAh g^{-1})	Q (mAh cm^{-2})
Super C65	2.2	62	3.6	1614	4.5
P50	4.5	10	3.6	795	4.6
H24	11	1	2.3	212	3.0
GFD 2.5EA	15	0.2	18	1192	23
Ketjenblack	1.2	1454	3.5	2925	2.2

A direct correlation between cell capacity and the accessible surface area was not observed. As previously discussed, the discharge of Na-O_2 cells undergoes a mixed solution and surface mechanism, which results in the concomitant growth of micron-sized particles and nano-sized conformal film. Therefore, other parameters than the available substrate area for oxygen reduction should be responsible for the overall cell capacity.

Looking at the discharge/charge potential hysteresis similar profiles are obtained for electrodes varying significantly the surface area (0.2–1454 m^2 g^{-1}). A flat discharge plateau close to the thermodynamic potential of NaO_2 formation is obtained for all cells. No significant difference in the plateau potential (around 2.08 V vs Na/Na^+) indicates that all the carbon materials are similarly catalytic towards

the ORR. For the oxidation curves, a spike at the beginning of the charging process is observed (a part from the Super C65 cathode) followed by a flat, low overpotential, plateau in all cases. The activation barrier spike is related to the charge transfer resistance between the NaO_2 cubes and the carbon substrate. A more accentuated voltage peak is observed for the GDL H24 cathode which has larger diameter fibres, hence less contact area with NaO_2 precipitates. The capacity retention evaluation was not possible for larger specific capacity cells due to dendrite formation upon charge, as discussed in section 4.4.3.

The formation of NaO_2 via a one-electron per oxygen reduction is confirmed by Raman spectroscopy based on the 1156 cm^{-1} oxygen bond asymmetric stretch peak. This is to be expected for cell configuration and dry O_2 supply employed, where the type of carbon should not interfere in the discharge mechanism[6]. Similar decomposition products were detected for all the different carbon electrodes (Na_2CO_3 and CH_3COONa) by FTIR spectroscopy, indicating that the nature of the carbon electrode does not fundamentally change the electrolyte degradation reactions.

SEM images of the surface of the different electrodes and the discharge products are depicted in Figure 4.34. The images obtained support the formation of NaO_2 as the main discharge product, as cubic precipitates were obtain for all the systems. This observation is in contrast with reports by Yadegari *et al.*[46], which reported that the morphology and chemical nature (peroxide or superoxide) of the discharge products was dependent on the carbon surface area, and in good agreement with Bender *et al.*[6], which reported only cubic-shaped particles for different surface area carbon in Na-O_2 cells.

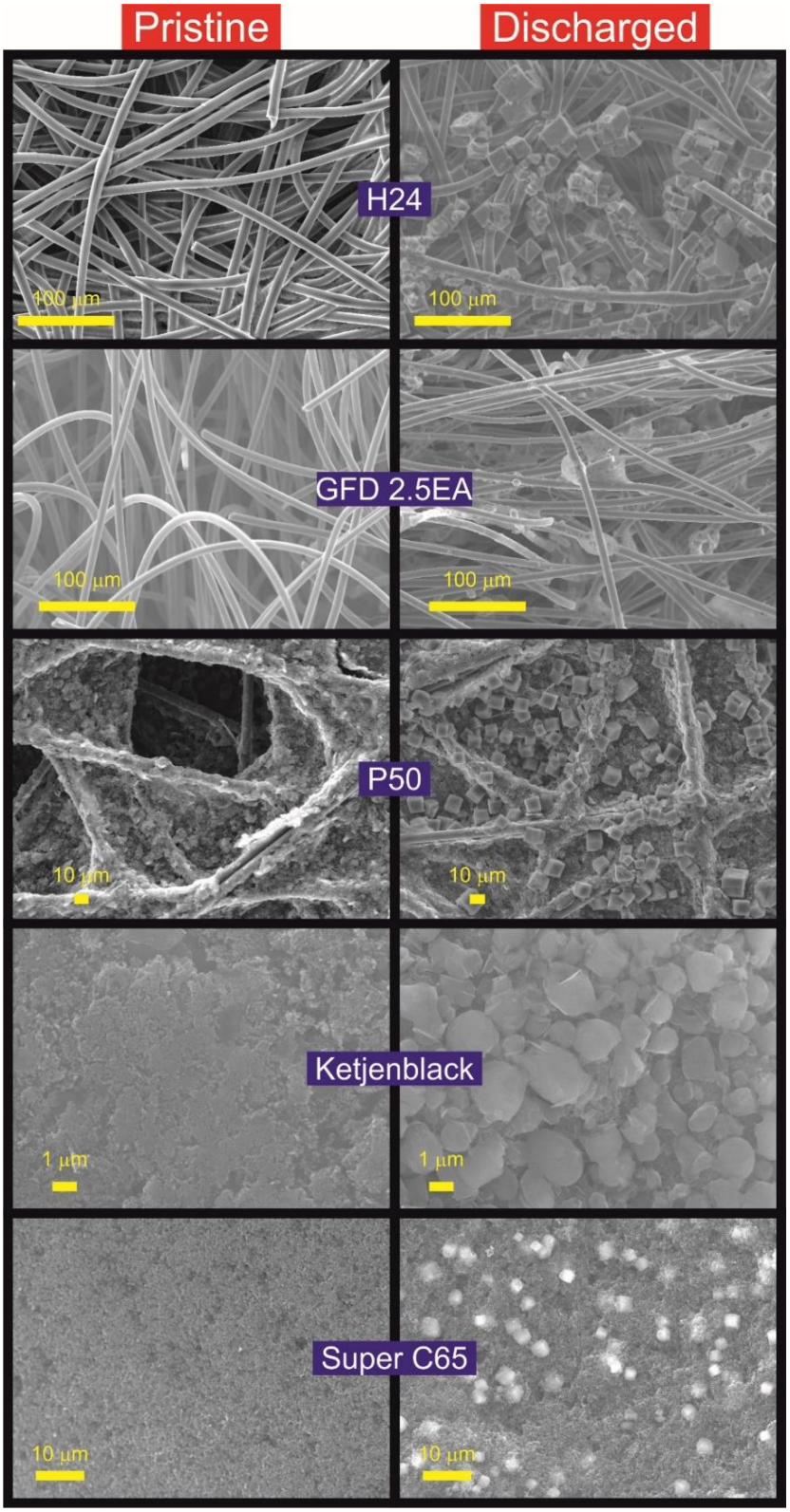

Figure 4.34: SEM analysis of the discharge product morphology for Na-O_2 cells discharged using different carbon cathodes with a 0.5 M NaOTf in DEGDME electrolyte at 0.12 mA cm^{-2} rate.

The cubic particles are not visible in the discharge graphite felt electrode, which can be interpreted as superoxide precipitates being distributed along the electrode's thickness, based on the large volume, higher porosity and larger capacity for this electrode.

Larger NaO_2 cubes were found for low surface area carbon fibre electrodes (H24 and P50) whereas smaller precipitates and higher surface coverage were obtained using high surface area carbon black electrodes (Ketjenblack EC 600 JD and Super C65). This observation is good agreement with the nucleation and growth mechanism proposed in section 4.4.6 when discharging Na-O_2 cells at different current densities. An increase in the surface area has a similar effect as an increase in current rate which ultimately results in the formation of more nucleation sites and leads to the growth of smaller particles, while lower surface area electrode corresponds to the formation less nucleation sites and leads to larger and more sparsely distributed NaO_2 cubes.

Table 4.3: Average particle size of NaO_2 deposit on different carbon cathodes.

Carbon	**Ketjenblack**	**GFD 2.5EA**	**Super C65**	**P50**	**H24**
Particle size (μm)	1.6 ± 0.5	-	2.5 ± 0.7	11.10 ± 1.7	21 ± 5.0

4.4.11 Carbon nanotube cathodes

A common strategy applied to improve the performance of alkali metal-oxygen batteries is to use nanostructured carbon materials as ORR/OER support that provides high surface area and electronic conductivity, resulting in extremely high specific capacities reported for such materials[87].

In Na-O_2 cells, carbon nanotubes were investigated as a positive electrode active material initially by Jian *et al.*[52], which reported high specific capacities (7530 mAh g^{-1}), but comparatively low areal capacity (1.5 mAh cm^{-2}) for a cell chemistry based on the formation/decomposition of $Na_2O_2 \cdot 2H_2O$. Higher specific and areal discharge capacities were reported by Zhao *et al.*[44] (4000 mAh g^{-1} and 5.55 mAh cm^{-2}) and Bender *et al.*[88] (1530 mAh g^{-1} and 3.31 mAh cm^{-2}) for a cell chemistry based on NaO_2 formation/decomposition. However, a clear understanding of what drives the reaction path towards a one- or two-electrons per oxygen reduction was not obtained.

Here, we report Na-O_2 cells using different carbon nanotube cathodes which perform in stark contrast for the same cell configuration and set up. Swagelok cells were assembled using the standard 0.5 M NaOTf in DEGDME electrolyte (<10 ppm H_2O) and cycled at a current density of 0.12 mA cm^{-2}. Two cathodes were investigated, a commercial single wall carbon nanotube (SW CNT – 700 m^2 g^{-1}) and a Ketjenblack conductive carbon/carbon nanotube 1:1 ratio composite electrode (SW CNT-KB 1454 m^2 g^{-1}). The self-supporting electrodes were cast using PTFE binder (80% active material, 20% binder). The first cycle galvanostatic discharge/charge curves are shown in Figure 4.35a, while the Raman

characterisation of discharge products is shown in Figure 4.35b. More detailed information on the cathodes studied is shown in Table 4.4.

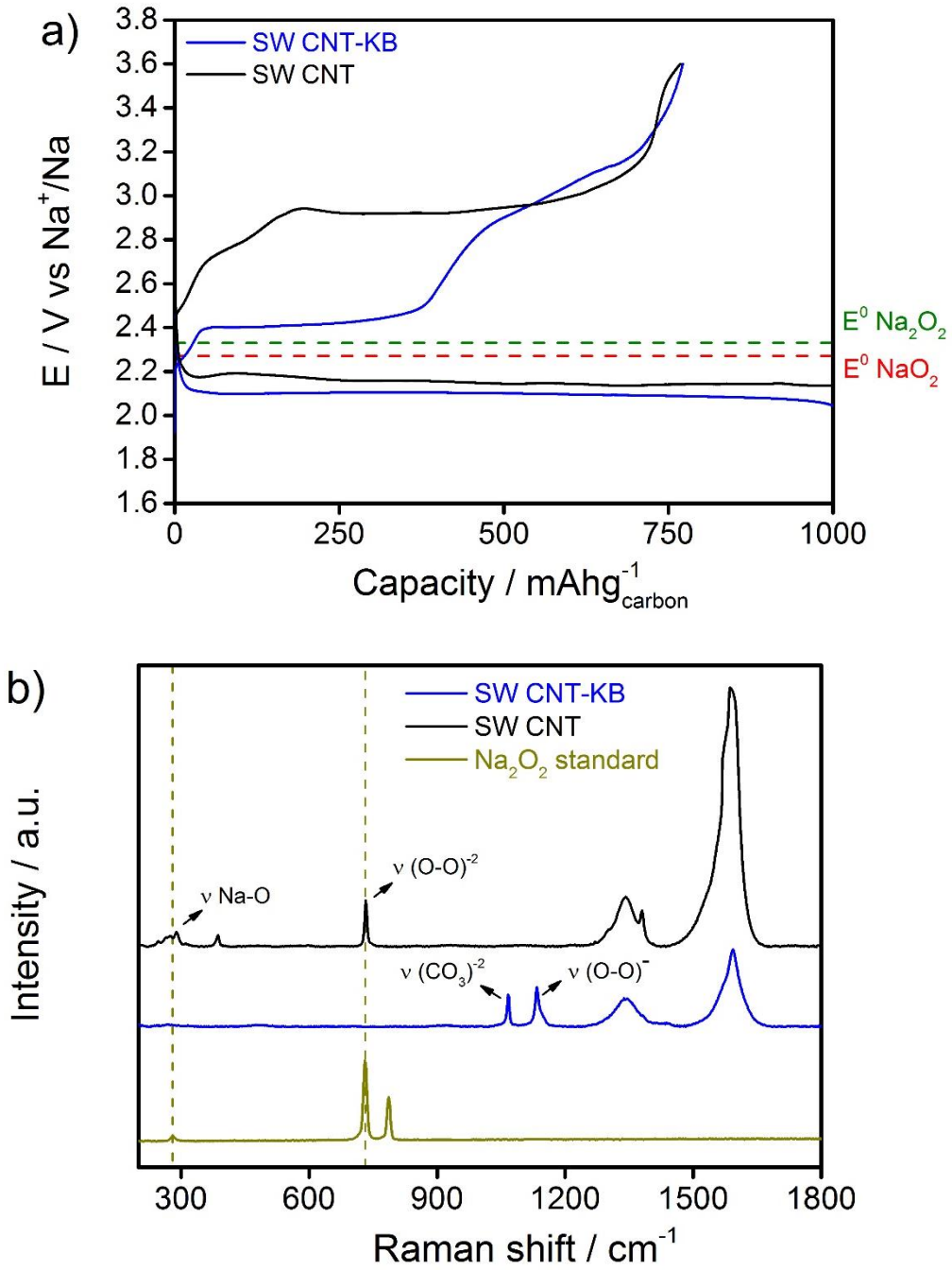

Figure 4.35: a) First Galvanostatic discharge/charge cycle for NaO_2 cells using CNT and CNT-KB cathodes with a 0.5 M NaOTf in DEGDME electrolyte at 0.12 mA cm^{-2} rate. b) Raman analysis of the discharged cathodes

The assessment of the electrochemical behaviour of the SW CNT and the SW CNT-KB Na-O_2 cells reveals important differences for the two electrodes. The pure nanotube cell presents a higher oxygen reduction potential plateau (around 2.15 V vs Na^+/Na) than the composite carbon black cell (around 2.10 V vs Na^+/Na), which could indicate a higher catalytic effect. In fact, the SW CNT cell presented improved absolute and areal capacity considerably higher than lithium-ion systems[84].

Table 4.4: Mass loading and average discharge capacities for the two carbon nanotube based cathodes tested in Na-O_2 cells.

Carbon	m (mg)	Q (mAh)	Q (mAh g^{-1})	Q (mAh cm^{-2})
SW CNT	4.1	4.6	1117	16
SW CNT-KB	2	2.3	1167	8.2

The Raman analysis of the discharge product on the SW CNT cathode surface presents a distinct peak at 733 cm^{-1} (commercial Na_2O_2 – 731 cm^{-1}) and another feature at 287 cm^{-1} (commercial Na_2O_2 – 282 cm^{-1}) which are assigned to peroxide ion vibrations in sodium peroxide. The detection of these Raman bands indicate that for the SW CNT cathode, the cell chemistry follows a two-electron reduction of molecular oxygen and the formation of Na_2O_2 as main discharge product, which has a slightly higher thermodynamic standard potential than NaO_2. The Raman spectrum for the discharged SW CNT-KB electrode shows a peak at 1133 cm^{-1} and another feature at 1066 cm^{-1}, which are assigned to superoxide ion and alkyl carbonate vibrations respectively.

The charge curve for the SW CNT-KB presents two clear plateaus, one at low overpotential (around 2.41 V vs Na^+/Na), associated with the oxidation of NaO_2, and one at larger polarisation (around 3.2 V vs Na^+/Na), associated with the oxidation of Na_2CO_3. The ratio of the oxidation plateaus indicate a superoxide yield of only 36.5%, indicating side reactions dominate the cell operation for this composite cathode.

The charge curve for the Na-O_2 cell using the SW CNT cathode presents only one plateau at 600 mV overpotential, which is higher than the afore reported overpotentials for cells cycling on the formation/decomposition of NaO_2 and is associated with sluggish kinetics for the peroxide oxidation, similar to Li-O_2 cells. The capacity retention of the cell indicates a yield of Na_2O_2 of 69% when charging up to 3.6 V vs Na^+/Na, which is within the carbon stability towards oxidative decomposition[4].

Characterisation of the discharged carbon nanotube cathodes by infrared spectroscopy (Figure 4.36) further confirms the formation of Na_2O_2 for the pure carbon nanotube cell and reveals similar parasitic side reactions products for both battery systems. Common electrolyte degradation products, such as sodium carbonate, sodium formate and sodium acetate are present on the discharged cathodes surface. As was previously discussed, the nature of the carbon cathode does not affect the electrolyte degradation process[14]. The oxygen-oxygen vibration on NaO_2 is not detected, regarding the CNT-KB cell, in the infrared spectra due to the homopolar nature of the bond.

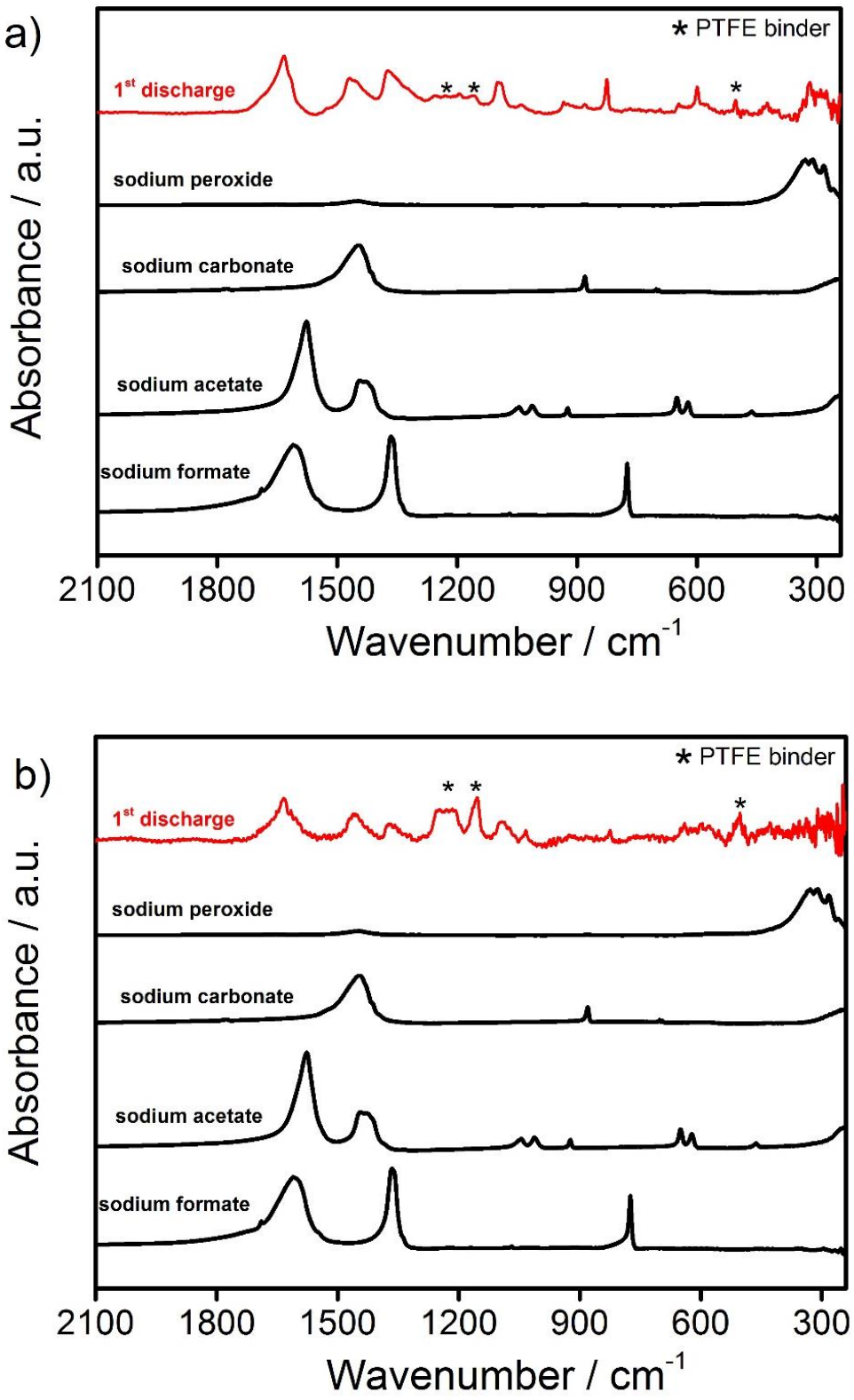

Figure 4.36: FTIR analysis of Na-O_2 cells discharged using a) CNT and b) CNT-KB cathodes with a 0.5 M NaOTf in DEGDME electrolyte at 0.12 mA cm^{-2} rate.

The SEM analysis of the CNT based electrodes reveals significant variation on the morphology of the discharge product (Figure 4.37). In the CNT-KB composite electrode, NaO_2 cubic particles are observed on the carbon surface alongside with smaller agglomerates similar to carbonate based cells (Figure 4.2b and c), in line with Raman analysis showing mixed reaction products. While the SEM analysis of the pure CNT electrode shows the carbon carpet covered with nanometre-sized rod shaped particles, in agreement to other reports of peroxide based Na-O_2 cells[46]. Figure A11 in Appendix A shows lower magnification SEM images that reveals a homogeneous distribution of the discharge products on the carbon surface.

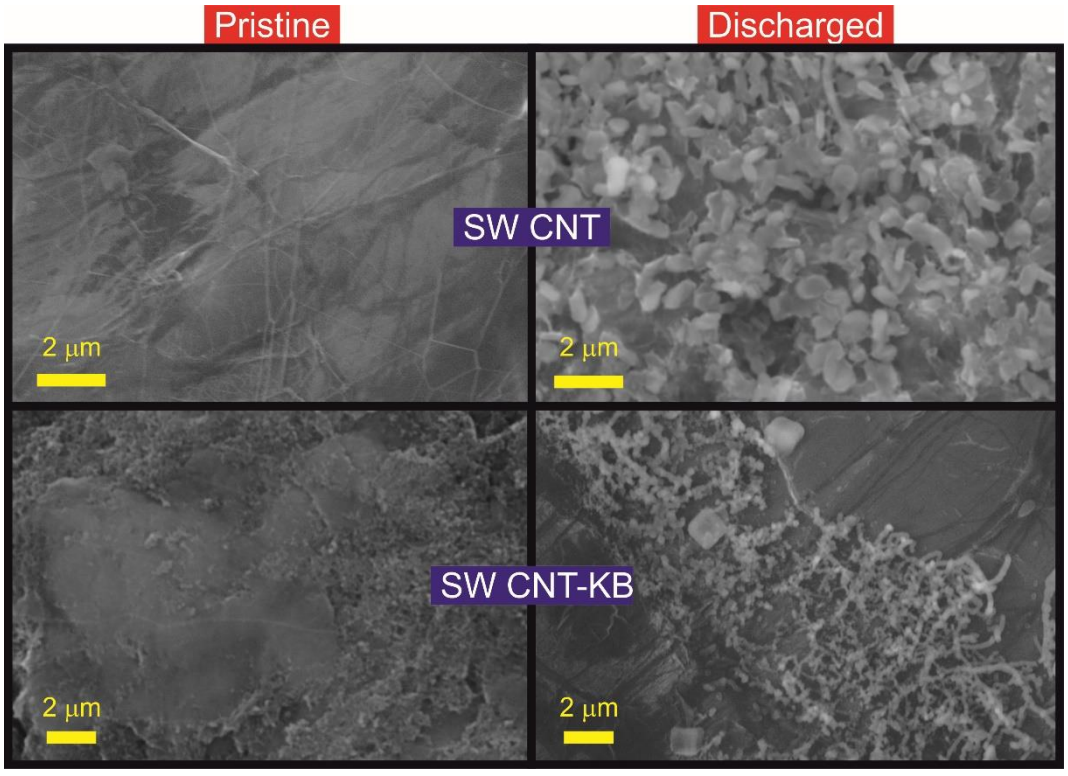

Figure 4.37: SEM analysis of the discharge product morphology for Na-O_2 cells discharged using CNT and CNT-KB cathodes with a 0.5 M NaOTf in DEGDME electrolyte at 0.12 mA cm^{-2} rate.

The formation both NaO_2 and Na_2O_2, while unexpected for the same electrochemical set up (electrolyte, current rate and oxygen partial pressure), can be explained by the sodium oxides phase stability as a function of O_2 partial pressure. Kang *et al.*[5] reported theoretical evidence for Na_2O_2 higher stability at lower O_2 partial pressure, while NaO_2 is metastable. It was hypothesised by the authors that ionic liquid, due to lower dioxygen solubility, would be an example of an electrolyte environment in which the lower O_2 partial pressure would favour the formation of Na_2O_2.

Oxygen diffusivity can be easily blocked at ultra-long carbon nanotube open ends by discharge products[89], which can generate regions of lower O_2 availability along the CNT carpet. This effect was observed by Ortiz-Vitoriano *et al.*[38], which reported larger NaO_2 crystals at the CNT open ends, which implicates oxygen deficiency along the nanotube length.

The obtainment of a one-electron reduction per oxygen reaction resulting in the formation of NaO_2 by other research groups using vertically aligned CNT produced via chemical vapour deposition[10,38], indicates that the present electrode fabrication procedure would benefit from further optimisation aiming to avoid oxygen diffusion blockage.

4.5 Conclusions and future work

This chapter presented an investigation onto several challenges facing the aprotic Na-O_2 battery system. Initially, the instability of organic carbonate electrolytes was demonstrated even with the detection of the desired reaction product (NaO_2). The cell chemistry was governed by electrolyte degradation reactions, which resulted in large voltage polarisation and significant oxidative decomposition.

Ether-based Na-O_2 cell followed the cell chemistry of dioxygen reduction to form NaO_2 upon discharge and its reversible oxidation upon charge. Parasitic reactions were also detected, but to a less extent, allowing higher capacity retention (above 90%) and low cell polarisation.

The negative effect of increasing the ether solvent chain length on the overall cell capacity was demonstrated of TEGDME electrolytes. The lower DN of this electrolyte favoured a surface confined discharge mechanism, resulting in rapid electrode passivation by a film-like deposit and poor electrochemical performance. Higher DN ether solvents (DEGDME and DME) presented similar capacities and coulombic efficiencies and the same micron-sized cubic morphologies of the discharge product. DEGDME was chosen as a standard electrolyte solvent based only on its lower volatility.

Long cycle life, a requirement in any battery system, was found to be limited by dendrite formation upon sodium metal plating, which resulted in short-circuit and eventual cell failure. Several attempt to mitigate their growth were made, and approaches that rendered prolonged cycling in analogous lithium systems did not

succeed in the present cell set up. Sodium metal's higher ionic radius and lower metallic bond strength increase the irregular deposition upon charging. Shallow cycling procedures, based on charge limitation, improved the cycle life on Na-O_2 cells, and the viability of this procedure should be further investigated with better performing carbon cathodes, such as graphitic felts.

The nucleation and growth of NaO_2 precipitates was studied at the course of discharge. A switch from a solution route to a surface confined route was observed towards the end of discharge related to the formation of a film-like deposit and a change in the morphology of the NaO_2 precipitates, observed via SEM analysis. AFM analysis indicates that the precipitation and growth of NaO_2 process goes through an initial film formation, subsequent plate formation, and formation of cubic NaO_2 at the electrode interface.

Furthermore, AFM images suggests that the surface of the cubic precipitates are made up by the agglomeration of aligned nanoparticles ca. 50 nm. This is in line with theoretical calculations[5] reporting lower nucleation energy of NaO_2 compared with Na_2O_2 and is evidence of the former being the preferred discharge product in practical cells.

The dependence of current density on the nucleation and growth of NaO_2 precipitates was further investigated. It was not possible to control the discharge product based on faster kinetics. The surface confined route, which favours the formation of film deposits, was found to be prominent at higher current rates, based on the formation more nucleation sites. The insulating nature of NaO_2 would cause an increase in charge transfer resistance at the electrode interface, limiting rate capability in Na-O_2 cells. AFM images showed a porous nature of this insulating

film, which allows electrolyte penetration and further electron transfer, since the possibility of tunnelling through a NaO_2 films is neglected.

The stability of NaO_2 in DEGDME electrolytes was investigated. A time-resolved dissolution process was observed, casing a shift in the oxygen-oxygen stretching vibration and a degradation of the cubic precipitates, related to the formation of $Na_2O_2 \cdot 2H_2O$. This transition should be avoided, as the dissolution of NaO_2 resulted in higher overpotentials and lower capacity retention.

Analysis of Na-O_2 cells constructed with different polymeric binder showed distinctive cell chemistries. Different from analogous lithium systems, binder instabilities were found to enhance side reactions that cause poor electrochemical performance. The assignment of superoxide induced graphitic ring distortion Raman signals was found to be related to the degradation of PVDF binder. Higher stability and improved rechargeability was found in cells constructed with PTFE binder.

The role of the carbon cathode in the oxygen reduction reaction was investigated. A direct link of between surface area and specific capacity was not observed. However, an inverse relation between surface area and average particle size of NaO_2 precipitates was demonstrated, in line with the nucleation/growth mechanism proposed for different current rates. Higher areal capacities were obtained for a graphitic felt electrode, in which higher porosity resulting in an increase of tri phase regions accounts for the improved performance.

The condition in which the two-electron reduction to form Na_2O_2 takes place were evaluated. It was not possible to force a consecutive electron reduction by applying larger overpotentials at initially formed NaO_2. However, Na_2O_2 formation

was obtained using carbon nanotube electrode, which can block oxygen diffusion causing regions of low oxygen partial pressure favouring the stabilisation of sodium peroxide. Composite electrodes constructed by mixing conductive carbon and carbon nanotubes improved oxygen diffusivity favouring the formation of NaO_2. The Na_2O_2 based cell presented higher charge overpotential, based on sluggish kinetics associated with peroxide oxidation. Therefore, the optimisation of cathode design should be aimed to avoid oxygen diffusion blockage and favouring the superoxide cell chemistry.

4.6 References

1. D. Sharon, D. Hirshberg, M. Afri, A. A. Frimer, M. Noked and D. Aurbach, *J. Solid State Electrochem.*, 2017, 1-18.

2. R. Younesi, M. Hahlin, F. Björefors, P. Johansson and K. Edström, *Chem. Mater.*, 2012, **25**, 77-84.

3. P. Adelhelm, P. Hartmann, C. L. Bender, M. Busche, C. Eufinger and J. Janek, *Beilstein J. Nanotechnol.*, 2015, **6**, 1016.

4. P. Hartmann, C. L. Bender, M. Vračar, A. K. Dürr, A. Garsuch, J. Janek and P. Adelhelm, *Nat. Mater.*, 2013, **12**, 228-232.

5. S. Kang, Y. Mo, S. P. Ong and G. Ceder, *Nano Lett.*, 2014, **14**, 1016-1020.

6. C. L. Bender, P. Hartmann, M. Vračar, P. Adelhelm and J. Janek, *Adv. Energy Mater.*, 2014, **4**.

7. I. Landa-Medrano, C. Li, N. Ortiz-Vitoriano, I. Ruiz de Larramendi, J. Carrasco and T. f. Rojo, *J. Phys. Chem. Lett.*, 2016, **7**, 1161-1166.

8. S. A. Freunberger, Y. Chen, Z. Peng, J. M. Griffin, L. J. Hardwick, F. Bardé, P. Novák and P. G. Bruce, *J. Am. Chem. Soc*, 2011, **133**, 8040-8047.

9. M. M. O. Thotiyl, S. A. Freunberger, Z. Peng and P. G. Bruce, *J. Am. Chem. Soc*, 2013, **135**, 494-500.

10. N. Zhao and X. Guo, *J. Phys. Chem. C*, 2015, **119**, 25319-25326.

11. Z. Zhang, J. Lu, R. S. Assary, P. Du, H.-H. Wang, Y.-K. Sun, Y. Qin, K. C. Lau, J. Greeley and P. C. Redfern, *J. Phys. Chem. C*, 2011, **115**, 25535-25542.

12. J. D. Wadhawan, P. J. Welford, E. Maisonhaute, V. Climent, N. S. Lawrence, R. G. Compton, H. B. McPeak and C. E. Hahn, *J. Phys. Chem. B*, 2001, **105**, 10659-10668.

13. J. Weiss, *Nature*, 1958, **181**, 825-826.

14. S. A. Freunberger, Y. Chen, N. E. Drewett, L. J. Hardwick, F. Bardé and P. G. Bruce, *Angew. Chem. –Int. Edit.*, 2011, **50**, 8609-8613.

15. S. Yang and D. J. Siegel, *Chem. Mater.*, 2015, **27**, 3852-3860.

16. R. Pinedo, D. Weber, B. Bergner, D. Schröder, P. Adelhelm and J. Janek, *J. Phys. Chem. C*, 2016, **120**, 8472-8481.

17. J. L. Roberts Jr, T. S. Calderwood and D. T. Sawyer, *J. Am. Chem. Soc*, 1984, **106**, 4667-4670.

18. C. Monroe and J. Newman, *J. Electrochem. Soc.*, 2005, **152**, A396-A404.

19. F. Ding, W. Xu, G. L. Graff, J. Zhang, M. L. Sushko, X. Chen, Y. Shao, M. H. Engelhard, Z. Nie and J. Xiao, *J. Am. Chem. Soc*, 2013, **135**, 4450-4456.

20. S. Choudhury, C. T.-C. Wan, W. I. Al Sadat, Z. Tu, S. Lau, M. J. Zachman, L. F. Kourkoutis and L. A. Archer, *Sci. Adv.*, 2017, **3**, e1602809.

21. A. Wang, X. Hu, H. Tang, C. Zhang, S. Liu, Y. Yang, Q. Yang and J. Luo, *Angew. Chem.*, 2017.

22. C. Xia, R. Black, R. Fernandes, B. Adams and L. F. Nazar, *Nat. Chem.*, 2015, **7**, 496-501.

23. N. B. Aetukuri, B. D. McCloskey, J. M. García, L. E. Krupp, V. Viswanathan and A. C. Luntz, *Nat. Chem.*, 2015, **7**, 50-56.

24. V. Gutmann, *Coordination Chem. Rev.*, 1976, **18**, 225-255.

25. I. M. Aldous and L. J. Hardwick, *Angew. Chem. –Int. Edit.*, 2016, **55**, 8254-8257.

26. L. Lutz, W. Yin, A. Grimaud, D. Alves Dalla Corte, M. Tang, L. Johnson, E. Azaceta, V. Sarou-Kanian, A. Naylor and S. Hamad, *J. Phys. Chem. C*, 2016, **120**, 20068-20076.

27. K. Abraham, *J. Electrochem. Soc.*, 2015, **162**, A3021-A3031.

28. L. Johnson, C. Li, Z. Liu, Y. Chen, S. A. Freunberger, P. C. Ashok, B. B. Praveen, K. Dholakia, J.-M. Tarascon and P. G. Bruce, *Nat. Chem.*, 2014, **6**, 1091-1099.

29. P. Hartmann, M. Heinemann, C. L. Bender, K. Graf, R.-P. Baumann, P. Adelhelm, C. Heiliger and J. r. Janek, *J. Phys. Chem. C*, 2015, **119**, 22778-22786.

30. K. B. Knudsen, J. E. Nichols, T. Vegge, A. C. Luntz, B. D. McCloskey and J. Hjelm, *J. Phys. Chem. C*, 2016, **120**, 10799-10805.

31. I. Landa-Medrano, I. R. de Larramendi, N. Ortiz-Vitoriano, R. Pinedo, J. I. R. de Larramendi and T. Rojo, *J. Power Sources*, 2014, **249**, 110-117.

32. Q. Sun, J. Liu, X. Li, B. Wang, H. Yadegari, A. Lushington, M. N. Banis, Y. Zhao, W. Xiao and N. Chen, *Adv. Funct. Mater.*, 2017, **27**.

33. I. Landa-Medrano, A. Sorrentino, L. Stievano, I. R. de Larramendi, E. Pereiro, L. Lezama, T. Rojo and D. Tonti, *Nano Energy*, 2017, **37**, 224-231.

34. L. Grande, E. Paillard, J. Hassoun, J. B. Park, Y. J. Lee, Y. K. Sun, S. Passerini and B. Scrosati, *Adv. Mater.*, 2015, **27**, 784-800.

35. B. Scrosati, J. Hassoun and Y.-K. Sun, *Energy Environ. Sci.*, 2011, **4**, 3287-3295.

36. P. Hartmann, D. Grübl, H. Sommer, J. r. Janek, W. G. Bessler and P. Adelhelm, *J. Phys. Chem. C*, 2014, **118**, 1461-1471.

37. V. Viswanathan, K. S. Thygesen, J. Hummelshøj, J. K. Nørskov, G. Girishkumar, B. McCloskey and A. Luntz, *J. Chem. Phys.*, 2011, **135**, 214704.

38. L. D. Griffith, A. E. Sleightholme, J. F. Mansfield, D. J. Siegel and C. W. Monroe, *ACS Appl. Mater. Inter.*, 2015, **7**, 7670-7678.

39. N. Ortiz-Vitoriano, T. P. Batcho, D. G. Kwabi, B. Han, N. Pour, K. P. C. Yao, C. V. Thompson and Y. Shao-Horn, *J. Phys. Chem. Lett*, 2015, **6**, 2636-2643.

40. J. Liu, S. K. Rahimian and C. W. Monroe, *Phys. Chem. Chem. Phys.*, 2016, **18**, 22840-22851.

41. B. D. Adams, C. Radtke, R. Black, M. L. Trudeau, K. Zaghib and L. F. Nazar, *Energy Environ. Sci.*, 2013, **6**, 1772-1778.

42. V. Viswanathan, J. Nørskov, A. Speidel, R. Scheffler, S. Gowda and A. Luntz, *J. Phys. Chem. Lett.*, 2013, **4**, 556-560.

43. P. Hartmann, C. L. Bender, J. Sann, A. K. Dürr, M. Jansen, J. Janek and P. Adelhelm, *Phys. Chem. Chem. Phys.*, 2013, **15**, 11661-11672.

44. N. Zhao, C. Li and X. Guo, *Phys. Chem. Chem. Phys.*, 2014, **16**, 15646-15652.

45. W. Liu, Q. Sun, Y. Yang, J.-Y. Xie and Z.-W. Fu, *Chem. Commun.*, 2013, **49**, 1951-1953.

46. H. Yadegari, Y. Li, M. N. Banis, X. Li, B. Wang, Q. Sun, R. Li, T.-K. Sham, X. Cui and X. Sun, *Energy Environ. Sci.*, 2014, **7**, 3747-3757.

47. D. W. Oxtoby, *J. Phys.: Condens. Matter*, 1992, **4**, 7627.

48. D. Schröder, C. L. Bender, M. Osenberg, A. Hilger, I. Manke and J. Janek, *Sci. Rep.*, 2016, **6**, 24288.

49. J. E. Nichols and B. D. McCloskey, *J. Phys. Chem. C*, 2017, **121**, 85-96.

50. J. Kim, H. Park, B. Lee, W. M. Seong, H.-D. Lim, Y. Bae, H. Kim, W. K. Kim, K. H. Ryu and K. Kang, *Nat. Commun.*, 2016, **7**.

51. J. Kim, H.-D. Lim, H. Gwon and K. Kang, *Phys. Chem. Chem. Phys.*, 2013, **15**, 3623-3629.

52. Z. Jian, Y. Chen, F. Li, T. Zhang, C. Liu and H. Zhou, *J. Power Sources*, 2014, **251**, 466-469.

53. X. Bi, R. Wang, L. Ma, D. Zhang, K. Amine and J. Lu, *Small Methods*, 2017.

54. I. Landa-Medrano, R. Pinedo, X. Bi, I. Ruiz de Larramendi, L. Lezama, J. r. Janek, K. Amine, J. Lu and T. Rojo, *ACS Appl. Mater. Inter.*, 2016, **8**, 20120-20127.

55. S. Y. Sayed, K. P. Yao, D. G. Kwabi, T. P. Batcho, C. V. Amanchukwu, S. Feng, C. V. Thompson and Y. Shao-Horn, *Chem. Commun.*, 2016, **52**, 9691-9694.

56. D. Schröder, C. L. Bender, R. Pinedo, W. Bartuli, M. G. Schwab, Ž. Tomović and J. Janek, *Energy Technology*, 2017.

57. C. L. Bender, D. Schröder, R. Pinedo, P. Adelhelm and J. Janek, *Angew. Chem. –Int. Edit.*, 2016, **55**, 4640-4649.

58. F. A. Cotton, *Progress in inorganic chemistry*, John Wiley & Sons, 2009.

59. H. Eysel and S. Thym, *Zeitschrift für anorganische und allgemeine Chemie*, 1975, **411**, 97-102.

60. J. Evans, *J. Chem. Soc. D: Chem. Comm.*, 1969, 682-683.

61. J. Creighton and E. Lippincott, *J. Chem. Phys.*, 1964, **40**, 1779-1780.

62. D. H. Chin, G. Chiericato Jr, E. J. Nanni Jr and D. T. Sawyer, *J. Am. Chem. Soc*, 1982, **104**, 1296-1299.

63. Q. Sun, Y. Yang and Z.-W. Fu, *Electrochem. Commun.*, 2012, **16**, 22-25.

64. Y. Li, H. Yadegari, X. Li, M. N. Banis, R. Li and X. Sun, *Chem. Commun.*, 2013, **49**, 11731-11733.

65. W.-M. Liu, W.-W. Yin, F. Ding, L. Sang and Z.-W. Fu, *Electrochem. Commun.*, 2014, **45**, 87-90.

66. S. Ma, W. C. McKee, J. Wang, L. Guo, M. Jansen, Y. Xu and Z. Peng, *Phys. Chem. Chem. Phys.*, 2017, **19**, 12375-12383.

67. C. Zhang, F.-R. F. Fan and A. J. Bard, *J. Am. Chem. Soc*, 2009, **131**, 177.

68. J. P. Vivek, N. G. Berry, J. Zou, R. J. Nichols and L. J. Hardwick, *J. Phys. Chem. C*, 2017, **121**, 19657-19667.

69. R. Black, S. H. Oh, J.-H. Lee, T. Yim, B. Adams and L. F. Nazar, *J. Am. Chem. Soc*, 2012, **134**, 2902-2905.

70. E. Nasybulin, W. Xu, M. H. Engelhard, Z. Nie, X. S. Li and J.-G. Zhang, *J. Power Sources*, 2013, **243**, 899-907.

71. J. Lu, Y. J. Lee, X. Luo, K. C. Lau, M. Asadi, H.-H. Wang, S. Brombosz, J. Wen, D. Zhai and Z. Chen, *Nature*, 2016, **529**, 377-382.

72. J. Lu, Y. Lei, K. C. Lau, X. Luo, P. Du, J. Wen, R. S. Assary, U. Das, D. J. Miller and J. W. Elam, *Nat. Commun.*, 2013, **4**, ncomms3383.

73. K.-N. Jung, J.-I. Lee, J.-H. Jung, K.-H. Shin and J.-W. Lee, *Chem. Commun.*, 2014, **50**, 5458-5461.

74. J.-B. Park, J. Lee, C. S. Yoon and Y.-K. Sun, *ACS Appl. Mater. Inter.*, 2013, **5**, 13426-13431.

75. H.-G. Jung, J. Hassoun, J.-B. Park, Y.-K. Sun and B. Scrosati, *Nat. Chem.*, 2012, **4**, 579-585.

76. D. Zhai, H.-H. Wang, K. C. Lau, J. Gao, P. C. Redfern, F. Kang, B. Li, E. Indacochea, U. Das and H.-H. Sun, *J. Phys. Chem. Lett.*, 2014, **5**, 2705-2710.

77. T. A. Galloway and L. J. Hardwick, *J. Phys. Chem. Lett.*, 2016, **7**, 2119-2124.

78. T. A. Galloway, L. Cabo-Fernandez, I. Aldous, F. Braga and L. Hardwick, *Faraday Discussions*, 2017.

79. J. K. Papp, J. D. Forster, C. M. Burke, H. W. Kim, A. C. Luntz, R. M. Shelby, J. J. Urban and B. D. McCloskey, *J. Phys. Chem. Lett.*, 2017, **8**, 1169-1174.

80. G. Ross, J. Watts, M. Hill and P. Morrissey, *Polymer*, 2000, **41**, 1685-1696.

81. D. Sawyer, J. Roberts, T. Calderwood, H. Sugimoto, M. McDowell and P. Wardman, *Philos. Trans. R. Soc. London*, 1985, **311**, 483-503.

82. Z. E. Reeve, C. J. Franko, K. J. Harris, H. Yadegari, X. Sun and G. R. Goward, *J. Am. Chem. Soc*, 2017, **139**, 595-598.

83. W. Xu, J. Xiao, D. Wang, J. Zhang and J.-G. Zhang, *J. Electrochem. Soc.*, 2010, **157**, A219-A224.

84. J. Christensen, P. Albertus, R. S. Sanchez-Carrera, T. Lohmann, B. Kozinsky, R. Liedtke, J. Ahmed and A. Kojic, *J. Electrochem. Soc.*, 2011, **159**, R1-R30.

85. D. Aurbach, B. D. McCloskey, L. F. Nazar and P. G. Bruce, *Nat. Energy*, 2016, **1**, 16128.

86. K. G. Gallagher, S. Goebel, T. Greszler, M. Mathias, W. Oelerich, D. Eroglu and V. Srinivasan, *Energy Environ. Sci.*, 2014, **7**, 1555-1563.

87. W. W. Yin and Z. W. Fu, *ChemCatChem*, 2017, **9**, 1545-1553.

88. C. L. Bender, W. Bartuli, M. G. Schwab, P. Adelhelm and J. Janek, *Energy Technology*, 2015, **3**, 242-248.

89. N. Ding, S. W. Chien, T. A. Hor, R. Lum, Y. Zong and Z. Liu, *J. Mater. Chem.*, 2014, **2**, 12433-12441.

Chapter 5.
Aprotic Potassium-Oxygen Battery Systems

5.1 Abstract

Several aspects of the underlying chemistry of aprotic room-temperature potassium-oxygen batteries are discussed in this chapter. Using ether based electrolytes, the stability of different cell components was investigated and the main cell chemistry was proven to be a one-electron oxygen reduction by *ex situ* Raman, PXRD, SEM and EDS analysis. The effect of increasing current density on cell performance and morphology of potassium superoxide precipitates was determined. The stability of different polymeric binders during K-O_2 cells cycling is also discussed. The main factor found to limit cycle life, as well as maximum specific capacity, were parasitic reactions taking place on the K metal anode surface. Different electrolyte combinations were employed and the conditions in which a protective surface layer or a passivating surface layer is formed on the metal anode were determined. The chemical nature of the surface layer was characterised by Raman, FTIR and XPS. The cyclability of K-O_2 cells was enhanced when using highly concentrated electrolytes and a blended electrolytes containing ionic liquid ether solvents. Finally, the electrochemical performance of an alternative anode material (K_3Sb) was evaluated and further insight on the alloying reaction between potassium and antimony is provided by *in situ* Raman characterisation.

5.2 Introduction

Non aqueous potassium-oxygen ($K\text{-}O_2$) batteries emerged in 2013 as an alternative to the many challenges facing analogous lithium-oxygen systems, such as sluggish kinetics during OER and electrolyte/cathode degradation during cell operation[1]. Based on the formation and decomposition of potassium superoxide (KO_2) the theoretical specific energy of $K\text{-}O_2$ (935 Wh kg^{-1}) is lower than the $Li\text{-}O_2$ (3505 Wh kg^{-1}) and the sodium-oxygen ($Na\text{-}O_2$, 1106 Wh kg^{-1}) counterparts. However, the investigation of potassium batteries can be justified by its superior electrochemical performance and the possibility of developing low-cost, high efficiency energy storage systems. The first $K\text{-}O_2$ cell, reported by Ren *et al.*[1, 2], showed the lowest ever reported potential gap in alkali metal-oxygen cells (less than 50 mV) and excellent round-trip efficiency (around 95%).

The improved electrochemical behaviour is related to higher conductivity of the discharge product[3] and less parasitic reactions upon cycling[1, 2]. Within alkali metal-oxygen systems, the desired reaction products are very sparingly soluble in most electrolyte employed, therefore, a new phase is formed during the discharge process and the conductivity of this oxide phase is related to the efficiency of the charge process. Differing from lithium peroxide (Li_2O_2), KO_2 is a wide band gap semiconductor at temperatures above -23 ^oC[3].

The lesser extent of electrolyte degradation is related to the higher stability of the superoxide radical ion ($O_2^{\bullet -}$) in potassium containing solutions based on the hard soft acid base theory (HSAB). Monovalent cations with larger radius are softer Lewis acids and have stronger coordination of a soft base such as the superoxide

radical anion. In a situation where the ion pairs [K^+--$O_2^{\bullet -}$] are strongly associated, the superoxide radical anion is less free to react undesirably with the electrolyte[4]. For this reason, potassium salts have been utilised as additive to Li-O_2 cells promoting the desired solution route mechanism[5, 6].

Whether or not secondary K-O_2 batteries can be achieved will depend on the investigation of more stable interfaces with the highly reducing metal anode, which can degrade electrolyte components raising safety concerns. In K-O_2 cells, the combination of reactive oxygen intermediates with the highly electropositive metal anode makes electrolyte stability an even greater challenge.

Thus, developing electrolyte combinations that could effectively passivate the potassium surface against the $O_2^{\bullet -}$ nucleophilic attack or investigating alternative negative electrode materials would be of great interest towards achieving a practical K-O_2 battery.

This chapter will evaluate the stability and determine the potential application of different cell components in the K-O_2 battery, such as carbon cathode, polymeric binder, electrolyte solvents and support salts and metal anode. An alternative to K metal anodes will also be investigated for suitability in K-O_2 cells using a prepotassiated, intermetallic, K_3Sb anode material.

5.3 Experimental Methods

This section provides specific experimental conditions for the results discussed in this chapter. For more detailed information see: Chapter 2. Experimental procedures and techniques.

5.3.1 Electrolyte preparation

The selected solvents 1,2 dimethoxyethane (DME) and diethylene glycol dimethyl ether (DEGDME) were distilled and dried over freshly activated molecular sieves (4 Å). The ionic liquid 1-butyl-1-methylpyrrolidinium bis(trifluoromethylsulfonyl)imide ([PYR 14][TFSI]) was used without further purification. The solvents were stored in an argon filled glovebox (<0.1 ppm H_2O and <0.1 ppm O_2). Potassium hexafluorophosphate (KPF_6), potassium trifluoromethanesulfonate (KOTf), potassium bis (fluorosulfonyl)imide (KFSI) and potassium bis (trifluoromethanesulfonyl)imide (KTFSI) were used as supporting salts and dried under vacuum at 80°C at least 12 hours. The electrolyte solutions were prepared inside an argon filled glovebox and H_2O content measured with a Karl Fischer Coulometer. Electrolytes were found to have <30 ppm water.

5.3.2 Carbon cathode preparation

The air-cathodes consisted of different carbon materials: gas diffusion layer (H24, Freudenberg & Co.), carbon paper (P50, Avcarb), single wall carbon nanotube (Elicarb), and conductive carbon black (Ketjenblack EC 600 JD, AkzoNobel and Super C65, Imerys). The composite electrodes were prepared using

poly(tetrafluoroethylene) (PTFE) binder (80% active carbon material, 20% binder) by mixing into a slurry with ethanol. The putty like mixture was put in a calender and pressed to a thickness of 100 μm to obtain self-supporting films. The electrodes were punched into 10 mm disk then dried at 120°C under vacuum for at least 12 hours. For the investigation into the influence of the polymeric binder, section 5.4.7, the electrodes were cast via the same procedure, but using poly(vinylidene fluoride) (PVDF) and carboxymethylcellulose sodium (CMC) instead. The binder-free carbon fibre electrodes were dried in a similar manner.

5.3.3 Swagelok cell assembly

K-O_2 cells were assembled using a custom built Swagelok set up. Potassium metal was used as an anode, roll pressed and cut into a 0.785 cm^2 discs. Two Whatman glass fibre separators (GF-G grade, 470 μm) were impregnated with 0.12 mL of the chosen electrolyte. The separators went through the same cleaning and drying process as the cathodes. Different carbon materials were used as cathodes as 10 mm diameter discs. The cathodes were held by a stainless steel current collector containing holes to allow O_2 access. The assembled Swagelok cells were transferred in a sealed glass chamber to the O_2 line station. The chamber was purged with dry O_2 for 10 minutes, and the cell rested for 3 hours at the open-circuit potential (OCP) prior to discharge. The galvanostatic discharge was performed using a Bio-Logic MPG-2 battery cycler. The discharge rate was based on the geometric cross-sectional area of the cathodes. All potentials are referenced against K^+/K.

5.3.4 Cell disassembly, cathode and anode characterisation

After electrochemical measurements, the Swagelok cells were disassembled inside the glovebox without atmosphere exposure. The positive electrodes were washed twice with dry DME, 10 minutes each time. Finally the electrodes were dried in the glovebox vacuum chamber for at least 12 hours. The K metal anodes were washed and dried via the same procedure.

Fourier-transform infrared (FTIR) data was collected on a Nicolet 6700 spectrometer (Thermo Fisher Scientific) by grinding portions of the discharged cathode into CsI pellets. Data was collected in transmission mode inside a nitrogen filled glove box.

Raman data was recorded on a Renishaw in via microscope with a 532 nm laser (2 mW cm^{-2}) in a gas-tight cell (ECC-Opto-STD, El-Cell GmBH) focussed through a microscope (Leica) via a 50x objective lens (Leica). The cathodes placed behind a quartz window to allow viewing of the electrode.

Powder X-ray diffraction data was obtained using a PANalytical X'Pert Pro diffractometer (Mo Kα1) in Bragg-Brentano geometry. The carbon cathodes were sealed in borosilicate glass capillary tubes under an inert atmosphere (argon filled glovebox) using silicon rubber to seal. After removing the capillary from the glove box they were heat sealed with a blowtorch.

Scanning electron microscopic (SEM) images were recorded with a JEOL JSM-7001F field emission electron microscope fitted with energy dispersive X-ray spectroscopy (EDS) analysis equipment (Oxford Instruments INCAx-act X-ray detector).

X-ray photoelectron spectroscopy (XPS) experiments were performed in a standard ultrahigh vacuum surface science chamber consisting of a PSP Vacuum Technology electron energy analyser (angle integrating ± 10^{o}) and a dual anode Mg Kα (1253.6 eV) X-ray source. The base pressure of the system was 2×10^{-10} mbar, with hydrogen as the main residual gas in the chamber. The spectrometer was calibrated using Au 4f7/2 at 83.9 eV. XPS spectra were fitted using Voigt functions after Shirley background removal. The overall resolution is 0.2 eV.

5.3.5 Sb-C nanocomposite preparation and coin cell assembly

A mixture of Super C65 (Imerys) and "bulk" commercial antimony powder (Sigma-Aldrich; ~100 mesh) was weighed out in a 30:70 (by weight) ratio to a total of 1 g. The mixture was ball milled in a planetary mill (Fritsch Premium Line 7 Ball Mill) for 22 h at 1000 rpm. The milling was performed under ambient atmosphere with zirconia grinding balls (5 mm diameter).

Composite electrodes were fabricated by casting an aqueous mixture of antimony active material (commercial or Sb-C nanocomposite): carbon black Super C65 (Imerys):CMC in a ratio of 64:21:15% (by weight) on an copper foil current collector.

Coin cells were assembled inside an argon filled glovebox (<0.1 ppm H_2O and <0.1 ppm O_2) using CR2025 cell parts. K metal counter electrodes were prepared by roll pressing and cutting into 1.13 cm^2 discs. Whatman glass fibre separators were impregnated with 0.5 M KPF_6 in ethylene carbonate (EC) and diethyl carbonate (DEC) (1:1 v/v) electrolyte. The commercial Sb and Sb-C

nanocomposite were used as anodes. Electrochemical cycling was carried out at 30°C (Maccor Series 4200 battery cycler).

5.3.6 In situ Raman characterisation

Self-supporting electrodes were fabricated for the *in situ* Raman experiments by casting an aqueous mixture of antimony active material (commercial or Sb-C nanocomposite): carbon black Super C65 (Imerys):CMC in a ratio of 40:22:35% (by weight) on a glass slide and cutting into 0.28 cm^2 discs.

Raman data was recorded on a Renishaw in via microscope with a 633 nm laser (2 mW cm^{-2}) focussed through a microscope (Leica) via a 50x objective lens (Leica). K-ion half cells were assembled using an *in situ* Raman cell (ECC-Opto-STD, El-Cell GmBH) with a K metal counter electrode, Whatman glass fibre separators impregnated with 0.5 M KPF_6 in EC:DEC (1:1 v/v) and antimony active material anode.

5.4 Results and Discussion

5.4.1 Stability of ether based electrolytes

The utilisation of ether solvents in K-O_2 batteries was first investigated due to ether electrolytes greater stability reported for Li-O_2 and Na-O_2 systems[7]. In contrast to Na-O_2 cells[8], different cell chemistries have not been reported and only KO_2 has been reported as the reaction product. Therefore, organic carbonate electrolytes can be disregarded based on the instabilities previously reported for other alkali metal batteries[9].

K-O_2 cells were assembled using a 0.25 M KPF_6 in DME electrolyte and a binder free gas diffusion layer carbon cathode (H24, Freudenberg & Co., $1 m^2 g^{-1}$). The cell operated at a current density of 0.12 mA cm^{-2} between a voltage window of 2.0 V and 3.0 V vs K^+/K, within the stability of the carbon electrode towards oxidative decomposition[10].

The first galvanostatic discharge/charge cycle is shown in Figure 5.1a. Characterisation of the cell reaction products was made by Raman spectroscopy (Figure 5.1b), FTIR (Figure 5.1c), PXRD (Figure 5.2) and SEM (Figure 5.3).

A flat plateau characteristic of single discharge reaction is observed at 2.41 V vs K^+/K near the thermodynamic potential for KO_2 formation. Likewise, a flat charge plateau is observed at 2.54 V vs K^+/K followed by an increase in potential towards the end of the oxidation process related to an increase in the charge transfer resistance in the positive electrode. The low combined overpotential results in outstanding capacity retention of 95.2%, which is higher than analogous Na-O_2 and Li-O_2 cells (see Appendix B, Figure B1).

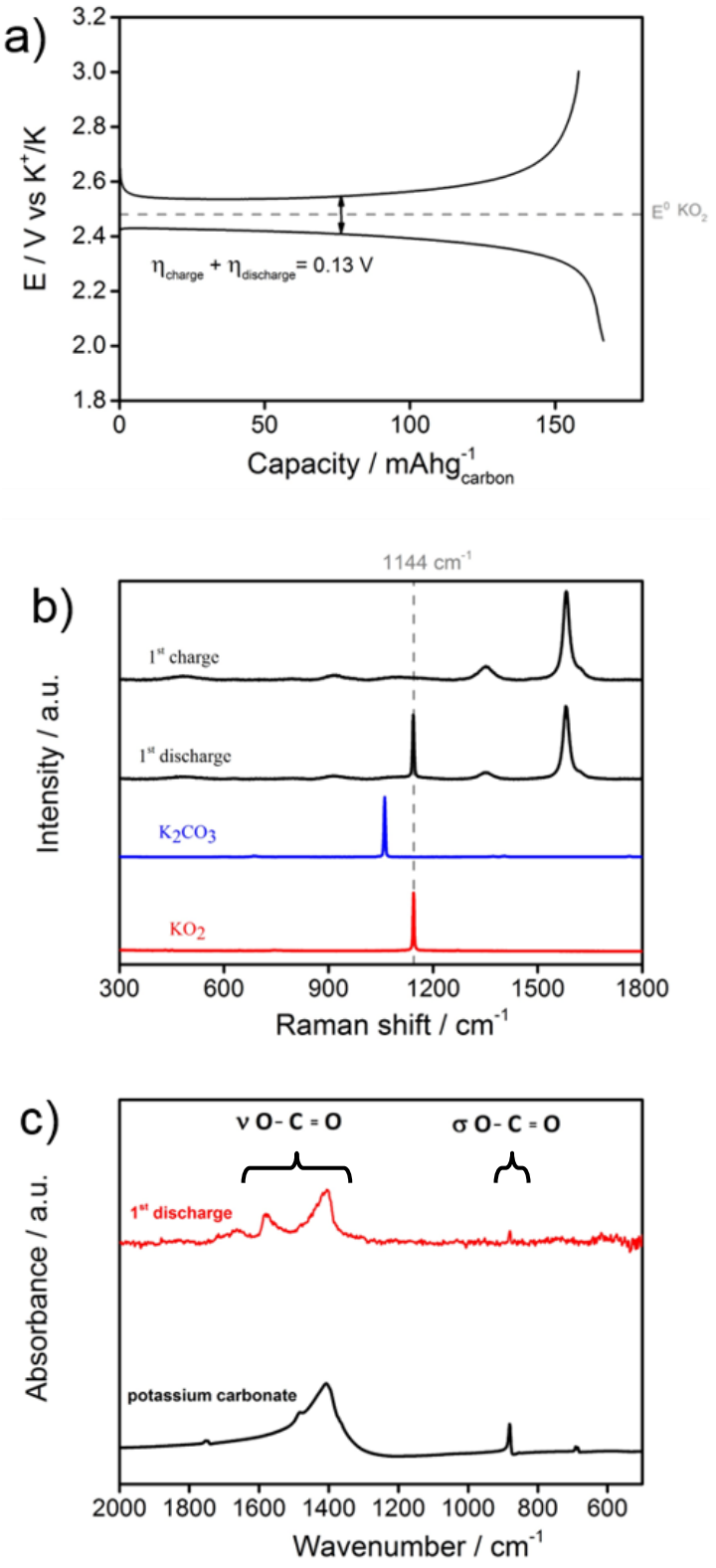

Figure 5.1: a) First galvanostatic discharge/charge cycle. b) FTIR and c) Raman analysis of the GDL H24, Freudenberg carbon cathode after one discharge process in a 0.25 M KPF_6 in DME electrolyte at 0.12 mA cm^{-2} current rate.

The Raman spectrum taken on cathode surface shows a sharp peak at 1144 cm^{-1} which is assigned to the oxygen–oxygen asymmetric stretch mode in potassium superoxide accompanied by the carbon substrate signature bands. In comparison to the Raman spectrum of an otherwise identical Na-O_2 cell, the O–O stretching signal appears shifted to lower wavenumbers, which is an effect of the potassium counter-ion. Due to the larger ionic radius in K^+, the electric charge is more dispersed, thus making the O–O superoxide vibration less energetic.

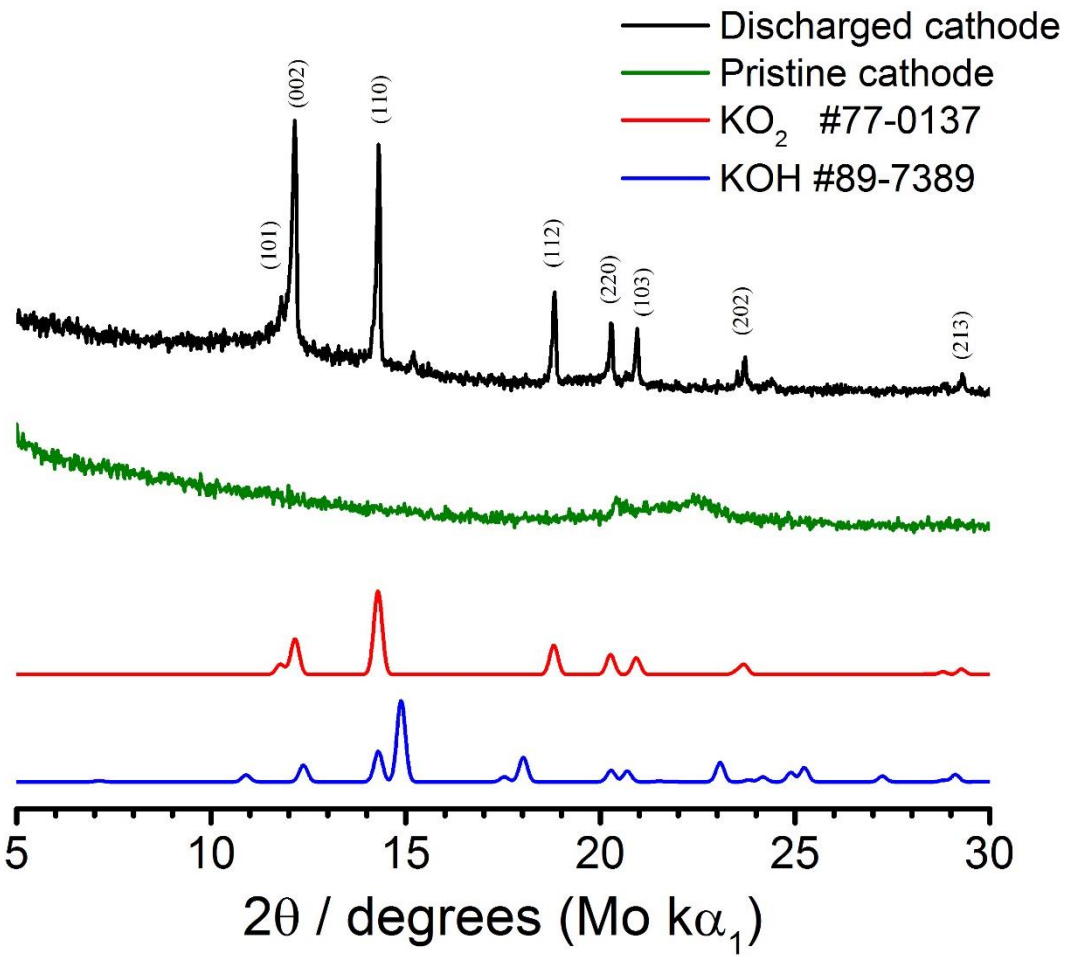

Figure 5.2: PXRD analysis of a discharged GDL H24, Freudenberg carbon cathode in 0.25 M KPF_6 in DME electrolyte at 0.12 mA cm^{-2} current rate.

PXRD data shows phase-pure potassium superoxide as the main reaction product in agreement with the Raman analysis. At room-temperature, KO_2 possesses the crystal structure of calcium carbide (CaC_2), which is a tetragonal lattice with superoxide ions face centred (space group F4/mmm)[11]. In contrast to PXRD data for the discharge cathode in a sodium cell (see Chapter 4, Figure 4.4), no evidence for side products were found. Therefore, Raman and x-ray diffraction data indicate that the main cell reaction is the one electron reduction of molecular oxygen during the discharge (1) and the subsequent decomposition of potassium superoxide upon charge (2).

Discharge $K^+ + e^- + O_2 \rightarrow KO_2$ 5.1

Charge $KO_2 \rightarrow K^+ + e^- + O_2$ 5.2

Further characterisation of the GDL cathode by infrared spectroscopy indicates some degree of electrolyte decomposition. Two vibration bands at 1404 cm^{-1} and 879 cm^{-1} assigned to asymmetric stretch and in-plane asymmetric bend of the carbonate ion in potassium carbonate (K_2CO_3). A vibration mode at 1580 cm^{-1} related to asymmetric stretching of carboxylate moieties indicates potassium formate (HCO_2K) as another side reaction product. Based on the galvanostatic cycling profile it can be estimated that the yield of side reactions is only 4.8%.

No evidence of potassium peroxide (K_2O_2) as a possible discharge product was detected via Raman, PXRD or FTIR analysis. Based on the higher thermodynamic stability of KO_2, is unlikely that a chemical disproportionation reaction could occur, in contrast to lithium systems where LiO_2 is unstable resulting in Li_2O_2 as the final reaction product[12].

The proposed reaction mechanism for the DME electrolyte degradation in potassium-oxygen cells is similar to the analogous DEGDME electrolyte sodium-oxygen system. In fact, linear chain ether electrolytes were found to give rise to similar parasitic reaction products in lithium-oxygen cells[7] and the same outcome was observed in this investigation.

Scheme 5.1: Degradation mechanism in KO_2 cells using ether-based electrolytes.

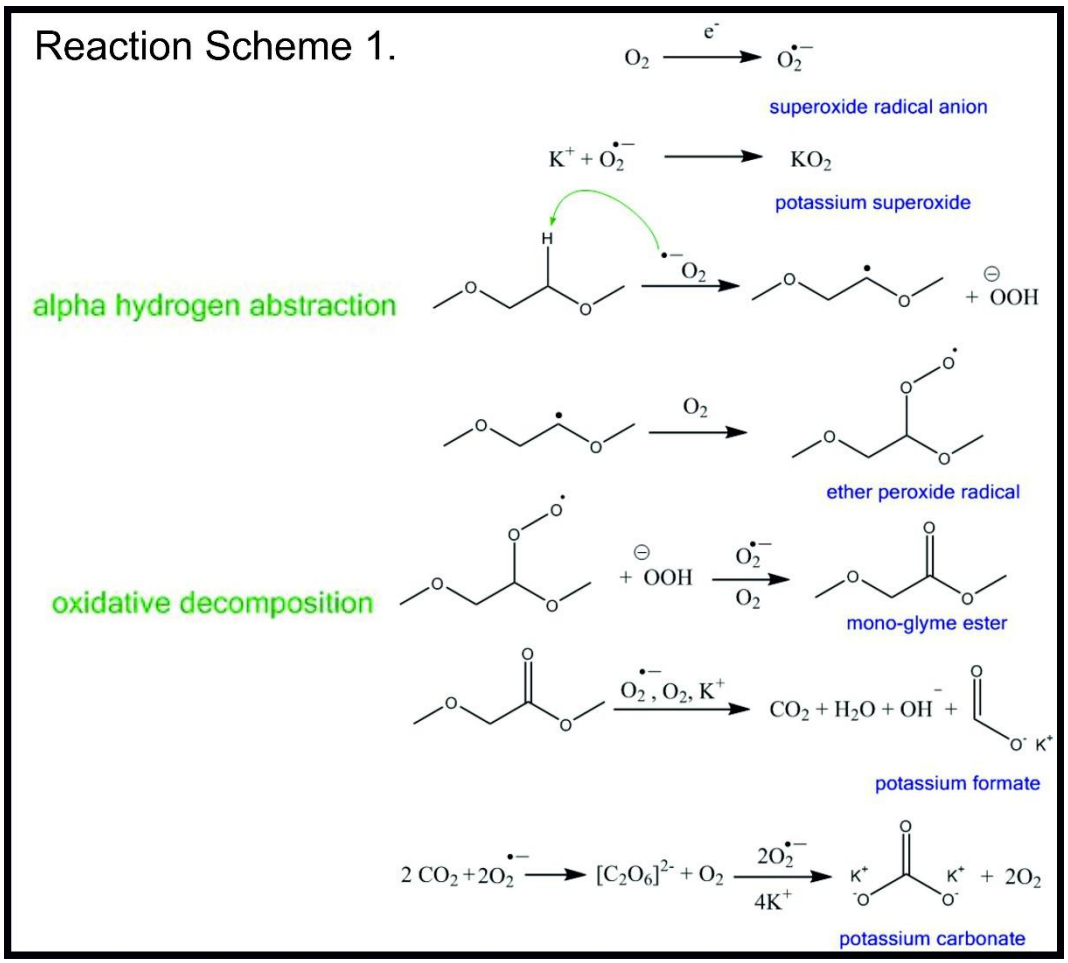

The reaction scheme 1 starts with the one-electron reduction of molecular oxygen forming the superoxide radical anion. This reactive intermediate reacts with both potassium ions in solution and the electrolyte solvent by a nucleophilic attack

on the acid hydrogen atom. The ether peroxide radical formed subsequently can undergo oxidative decomposition reactions, resulting in the formation of K_2CO_3 and HCO_2K, or esterification reactions resulting in methoxy (oxo)acetic anhydride, which has been detected in Li-O_2 and Na-O_2 cells[7, 13]. The latter was not detected in the present K-O_2 cell configuration, also indicating improved electrolyte stability.

The detection of electrolyte degradation products is obviously undesirable; however, it does not prevent the realisation of a practical potassium-oxygen battery as they are kinetically supressed by a more favourable superoxide main reaction. Electrolyte decomposition processes are common in lithium-ion batteries, as well as other cell components such as binder, current collectors, positive and negative electrode, resulting in the reduction of lithium ions inventory, loss of active material and eventual capacity fade[14]. The minimisation of such processes, by means of voltage and capacity limitations for instance, assures the long cyclability typical of this battery system.

The morphology of KO_2 precipitates deposited on the carbon fibre surface was investigated by SEM (Figure 5.3b). The cathode surface appears covered by cubic shaped particles with particle size around 10 μm. As previously discussed, the discharge process in alkali metal-oxygen cells follows two competitive routes: a surface confined mechanism and a solution mechanism[15, 16] (different mechanisms shown in Figure 1.15). The observation of large precipitates indicates solution based discharge mechanisms, associated with higher capacities and improved capabilities, which is the same behaviour observed for Na-O_2 cells (Chapter 4, section 4.45).

The EDS spectrum, Figure 5.3a, shows Kα transition lines with energy associated to potassium and oxygen and an atomic ratio close to 1:2 is observed, which further corroborates the chemical nature of potassium superoxide. In the raw element mappings, cubic shapes are present on the K and O map, but absent in the C map, in good agreement with previous Raman and PXRD data.

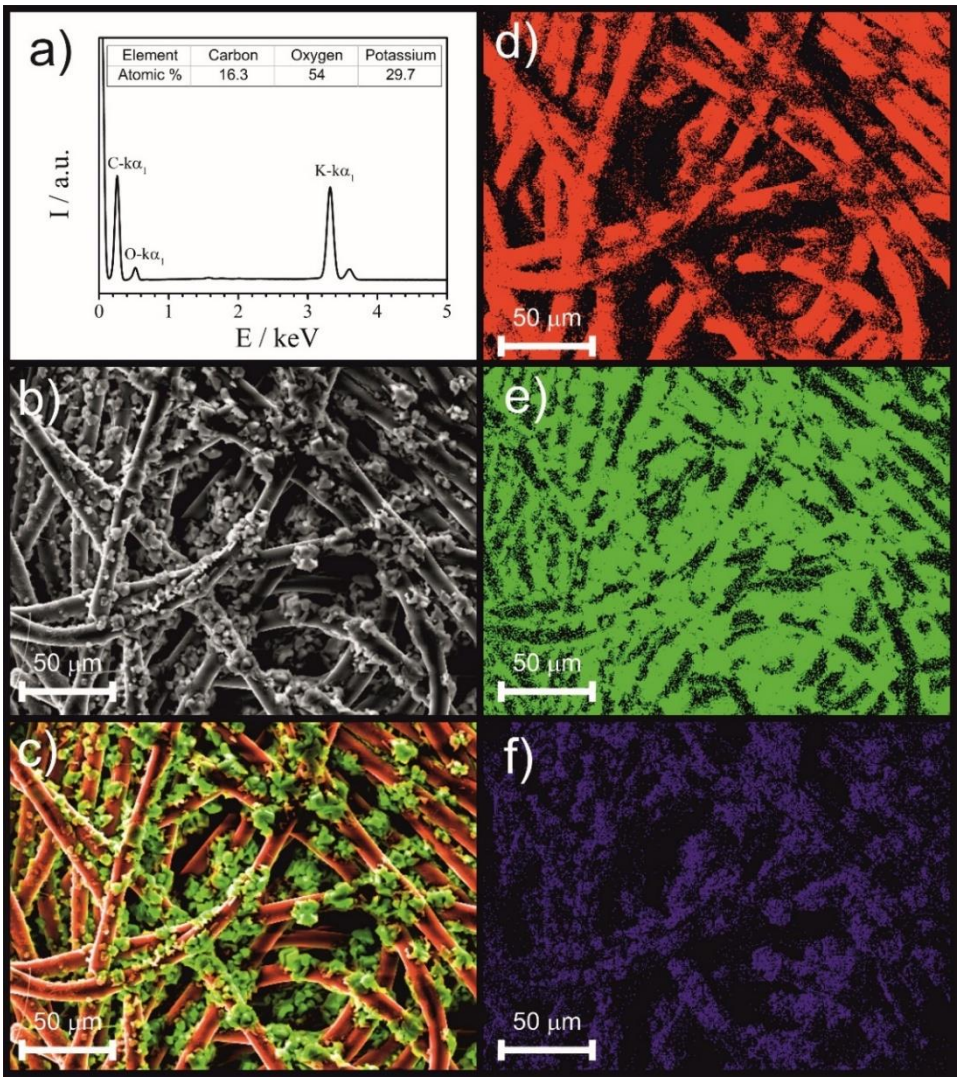

Figure 5.3: SEM and EDS analysis of a GDL Avcarb P50 carbon cathode after one discharge in a 0.25 M KPF_6 in DME electrolyte at 0.12 mA cm^{-2} current rate showing: a) EDS spectrum, b) SEM image, c) overlay of SEM image and elemental analysis map ("Cameo+", Oxford Instruments) and raw elemental data for d) carbon, e) potassium, f) oxygen.

The selection of suitable electrolytes for K-O_2 is considerably more challenging than other alkali metal systems. Aprotic organic solvents for which promising results of their use as electrolytes in analogous lithium-oxygen cells have been reported, such as DMSO[17] and DMA[18] are not compatible with the potassium metal and undergo reductive decomposition (see Appendix B, Figure B2).

Furthermore, an investigation onto the effect of increasing the ether solvent chain length, which proved to have direct impact on the cell capacity and discharge mechanism of Na-O_2 cells, was not possible due incompatibility with the metal anode (see Appendix B, Figure B2). Increasing the chain length of glymes results in a higher chelating character of the solvent towards potassium ions favouring dissolution processes. Shortly after introducing potassium to a DEGDME and TEGDME solution, the metal surface turns blue which is associated to solvated electrons[19, 20]. It was confirmed that a K-O_2 cell using a DEGDME electrolyte follows the same one-electron mechanism resulting in the formation of potassium superoxide after discharge (see Appendix B, Figure B3). The charge process shows voltage fluctuation which cause cell failure associated with the metal dissolution.

Only short length ether (DME) showed chemical stability in contact to the metal anode, and is the main electrolyte media used in this chapter.

5.4.2 Cyclability

Similar to Na-O_2 systems, the main factors found to limit long cycle life in K-O_2 cells were issues associated with the metal reactivity, resulting from mainly oxygen crossover on the anode. To illustrate that, Figure 5.4 shows the two first

cycles of a potassium oxygen using 0.25 M KPF_6 in DEGDME electrolyte in combination with a carbon cathode. The first galvanostatic cycle shows the expected high reversibility of the single electron redox couple O_2/KO_2 with low voltage gap. After the second discharge process, the internal resistance of the cell increases and no charge capacity is obtained causing cell failure.

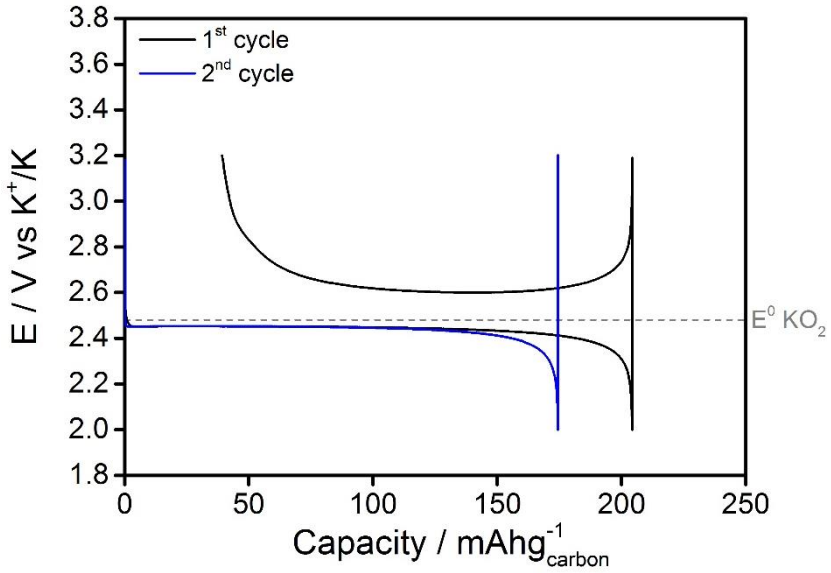

Figure 5.4: Two galvanostatic discharge/charge cycles of a K-O_2 cell using a carbon cathode and a 0.25 M KPF_6 in DME electrolyte at a 0.12 mA cm^{-2} rate.

When disassembling the cell after the second galvanostatic cycle, it was observed that the potassium metal anode was covered by a yellow surface layer characteristic of potassium superoxide[3] (see inset on Figure 5.5). Insight on the chemical nature this surface layer as obtained upon Raman spectroscopy characterisation subsequent to cell failure. Peaks associated with the stretching vibration of O-O (1144 cm^{-1}), O-C=O (1060 cm^{-1}) and O-H (3560 cm^{-1}) were detected, indicating a qualitative composition of the passivation layer formed by potassium superoxide, potassium carbonate and potassium hydroxide. Similar

anode side reaction products (lithium carbonate and lithium hydroxide) were reported for analogous lithium-oxygen cells using ether-based electrolytes[21].

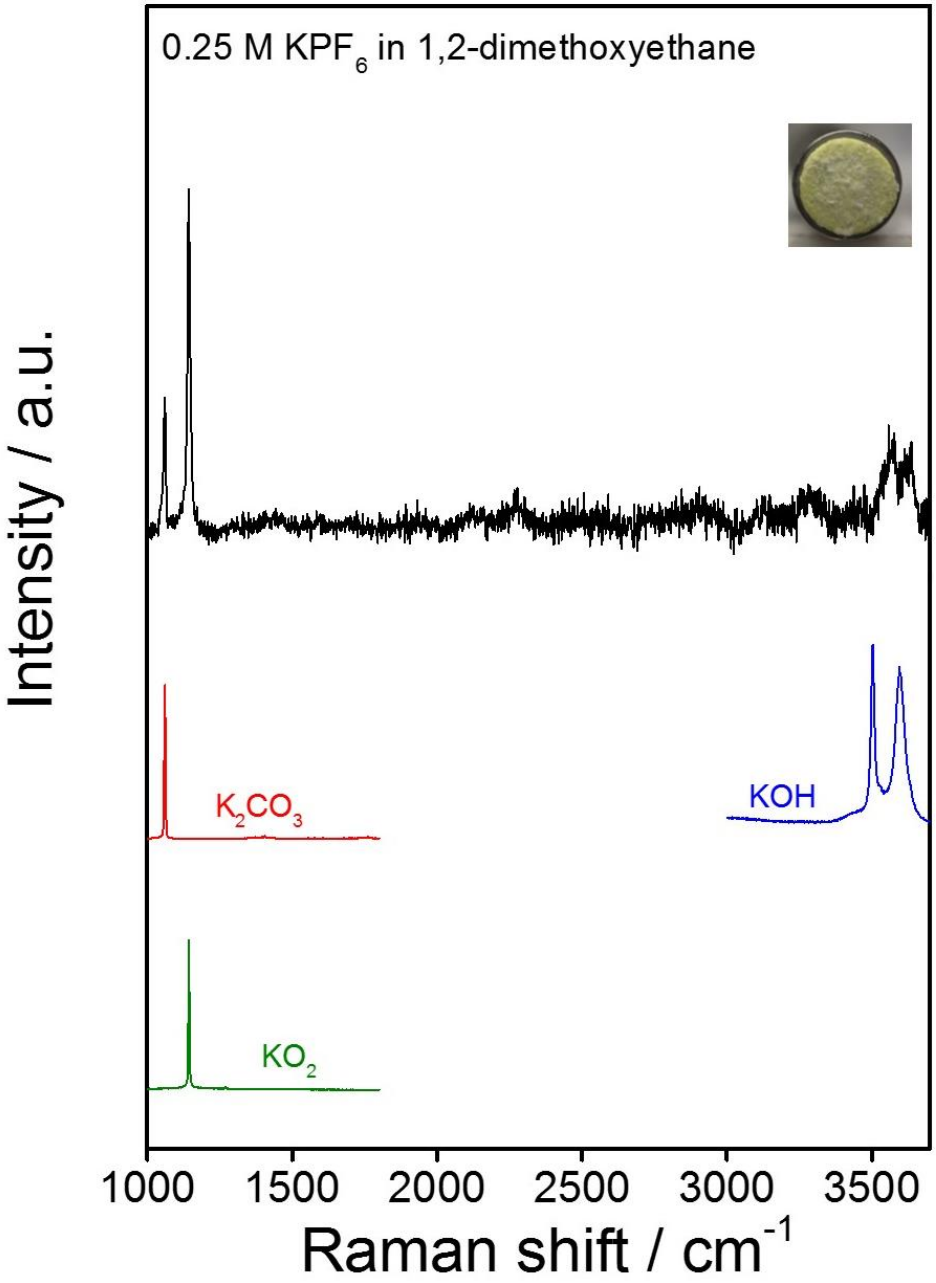

Figure 5.5: Raman spectra of the surface layer formed on the K metal anode after one galvanostatic cycle in a K-O_2 cell using DME in combination with KPF_6 electrolyte. Inset shows a photograph of the metal anode.

The observation of KO_2 is a result of the aforementioned crossover of O_2 species from the porous cathode reacting at the surface of the potassium anode. Potassium carbonate and potassium hydroxide are detected as a result of electrolyte degradation reactions, which can be triggered by the hydrogen abstraction in the DME molecule by the superoxide radical anion (Reaction scheme 1). Ren *et al.*[2] reported DFT calculations in which the same side reaction products were obtained by C-O bond cleavage on the ether molecule. It was proposed that DME would be negatively charged localised at the methylene groups ($–CH_2–$) by the highly reducing potassium metal, making it susceptible to O_2 binding which would cause the carbon-oxygen bond cleavage. The same composition of the passivation layer was reported (KO_2, K_2CO_3 and KOH)[3]. The accumulation of insoluble and insulating products at the metal anode surface is responsible for the increase in internal cell resistance that blocks electron transfer and mass transport through the electrode interface (Figure 5.4) and limits cycle life.

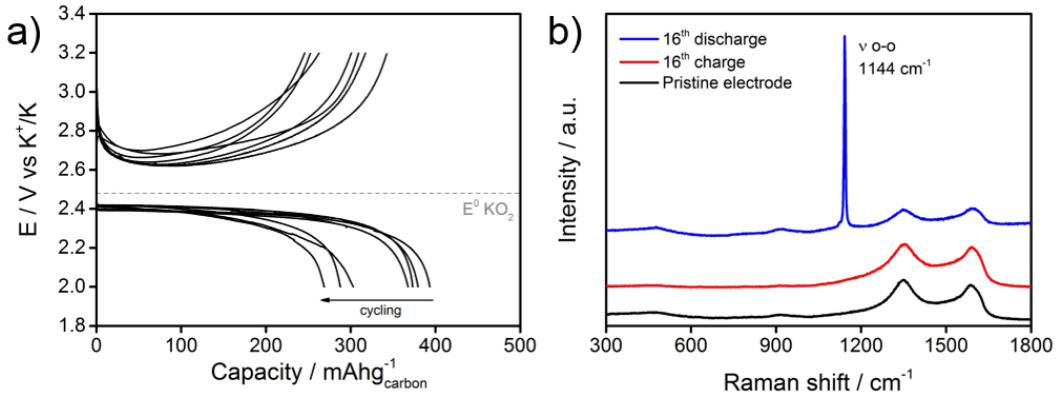

Figure 5.6: a) additional cycling obtained after anode replacement in a K-O_2 cell using 0.25 M KPF_6 in DEGDME electrolyte and a carbon cathode. b) Raman characterisation of the discharged cathode after 16 discharge/charge cycles.

As a proof that the formation of a passivation surface layer on the anode limits cyclability, when the anode is replaced after cell failure for a fresh potassium metal, additional cycling is obtained (Figure 5.6a) and Raman characterisation of reaction products after 16 galvanostatic cycles indicates the cell runs on the formation and decomposition of KO_2.

5.4.3 Effect of electrolyte salt

To investigate possible electrolyte alternatives which can mitigate the formation of an insulating layer on the anode surface thus prolonging cycle life, different potassium support salts were evaluated in combination with DME solvent. Although limited by the choice of the electrolyte solvent, the selection of different support salt has been reported to significantly alter the composition of the SEI in lithium batteries based on inherent chemical instability of the salt in relation to the metal anode[22].

Four different potassium salt anions were evaluated: hexafluorophosphate (KPF_6), trifluoromethanesulfonate (KOTf), bis (fluorosulfonyl)imide (KFSI) and bis (trifluoromethanesulfonyl)imide (KTFSI). The chemical structure of the anions is shown in Figure 5.7. K-O_2 cells were prepared in conjunction with a carbon fibre paper cathode (Avcarb, P50, 10 m^2 g^{-1}) and underwent galvanostatic discharge/charge cycling (Figure 5.8a). Subsequent analysis of the reaction products of the cell were performed via Raman spectroscopy and PXRD (Figures 5.8b and 5.8c).

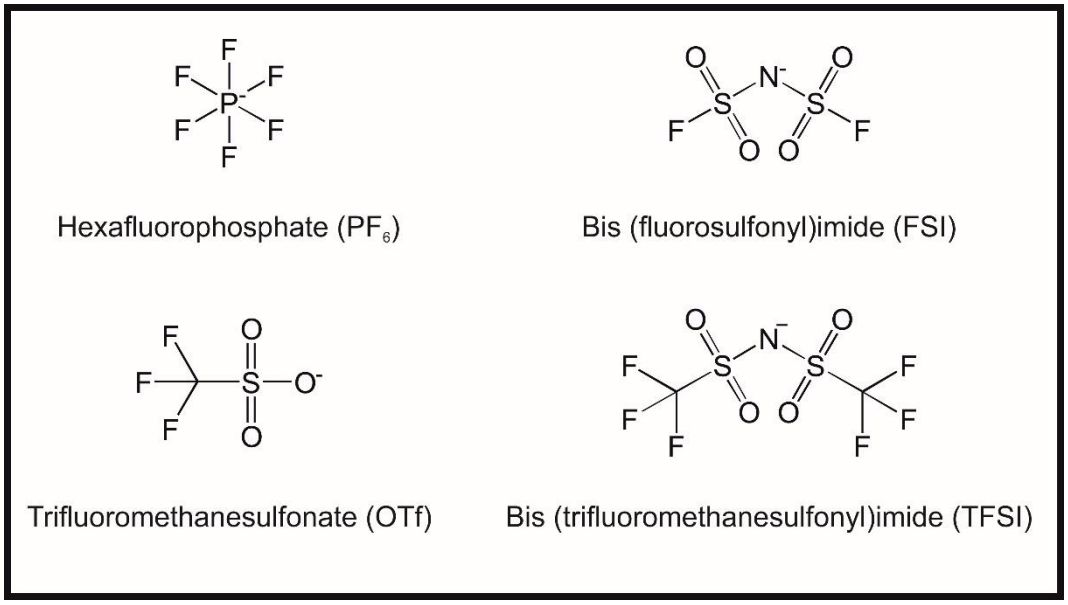

Figure 5.7: Chemical structure of the potassium support salt anions investigated.

The electrolyte salt anion was found to have a major influence on the electrochemical performance of K-O_2 cells. For KPF_6, a reversible charge process (98%) with low overpotential was obtained with higher capacities compared to the other cells. The observation of higher capacities for the KPF_6 cell is counter intuitive in light to the lower ionic association (IA) strength of this anion. As previously discussed, IA plays a key role in solvating superoxide intermediates and promoting a solution route discharge mechanism which leads to larger capacities[25]. The strength of electron donation from the salt anion to the K^+ in the [K^+--$O_2^{\bullet -}$] ion pair is as follows: KTFSI > KFSI > KOTf > KPF_6, collected from the literature[23, 24]. A direct link with the discharge capacity was not observed.

For the KFSI cell, despite of a stable discharge process, no charge capacity is obtained even at larger potential cut-off, indicating irreversible reactions. In fact, KFSI cells could not be recharged even at limited capacity, shallow cycling procedure (see Appendix B, Figure B4).

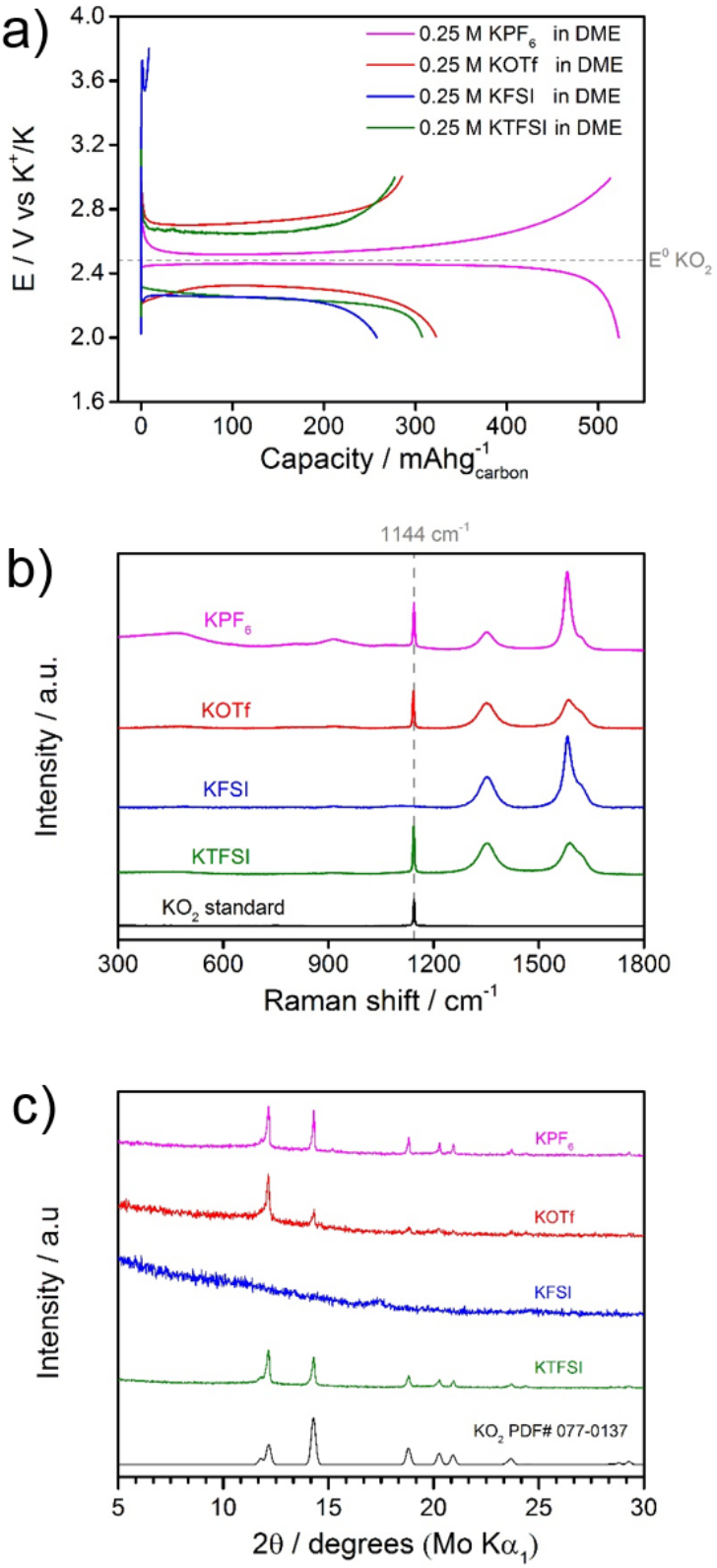

Figure 5.8: a) Potential vs capacity profile for K-O_2 cells using DME with 0.25 M KPF_6, KOTf, KFSI and KTFSI in DME electrolyte; b) Raman spectra and c) PXRD patterns of discharged Avcarb P50 carbon fibre cathodes at 0.12 mA cm^{-2} rate.

Post discharge analysis of the KFSI cell did not identify the formation of KO_2 on the cathode surface. Furthermore, FSI salts additives have been used as stable SEI former in lithium batteries based on the reduction of less protected sulfonyl groups resulting in the formation of lithium fluoride[22, 25]. Stable stripping and plating of K anode using KFSI electrolyte have been reported on the literature for K-ion cells[26]. Therefore, it can be hypothesised that, in K-O_2 cells, the degradation of the FSI^- anion is intensified by the superoxide anion radical attack on the electrophilic sulphur centre. Similar degradation of the FSI^- anion were reported in lithium systems[27]. While this nucleophilic attack is sterically hindered by CF_3 moieties in KOTf and KTFSI.

KOTf and KTFSI cells also presented high reversibility (88% and 80% respectively), but large voltage hysteresis are observed. The observation of larger overpotentials is normally related to different cell reactions taking place during the discharge/charge process. However, Raman and PXRD analysis show compelling evidence of sole crystalline KO_2 being the discharge product.

Since the electrolyte anion had no influence on the cathodic reaction, it can be inferred that processes happening at the anode are responsible for the larger voltage gap. To investigate the chemical nature of the SEI formed upon cycling, both KOTf and KTFSI cells were disassembled inside an argon glove-box and the surface layer formed on the metal anode was analysed (Figure 5.9).

The KOTf anode was covered by a yellow powder, similar to KPF_6 cells. Raman spectra show the same composition of the SEI: KO_2 from oxygen crossover and K_2CO_3 and KOH from electrolyte decomposition. Again, this insulating layer was responsible for the limit cyclability obtained for KOTf cells.

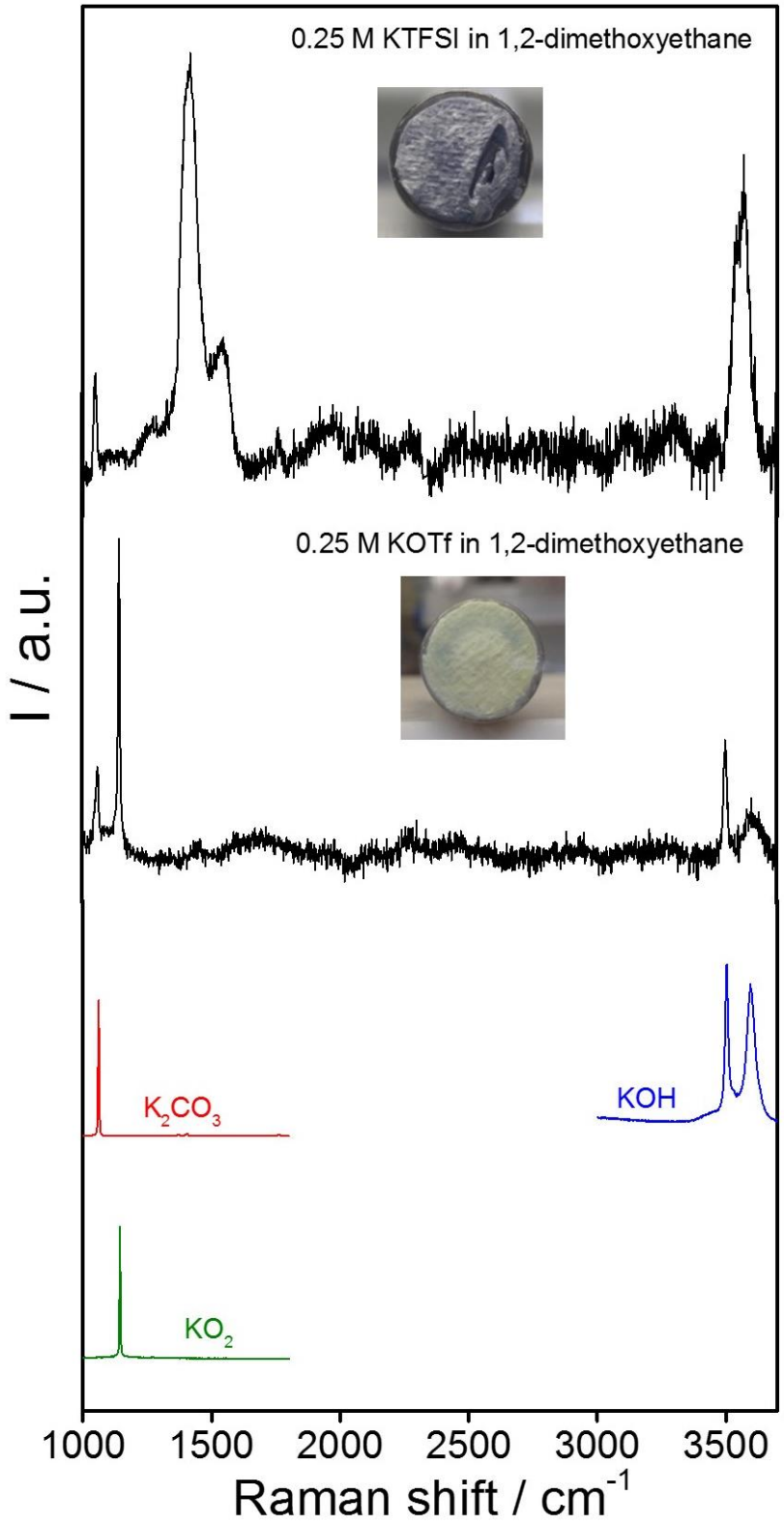

Figure 5:9 Raman spectra of the surface layer formed on the K metal anode after one galvanostatic cycle in a K-O_2 cell using DME in combination with KOTf and KTFSI electrolyte. Inset shows photographs of the metal anodes.

In contrast, KTFSI cells formed a light grey anode surface layer and Raman analysis did not show the presence of KO_2 (1144 cm^{-1}) in its composition, but K_2CO_3 and KOH were still detected as a result of DME degradation. Two additional bands at 1407 cm^{-1} and 1545 cm^{-1} are tentatively assigned to CH_3-S asymmetric deformation[28]. Similar results were reported by Ren *et al.*[29] when comparing KPF_6 and KTFSI electrolytes for K-O_2 cells.

This result indicates that the SEI formed when using KTFSI is impermeable to O_2, effectively avoiding oxygen crossover, while still allowing K^+ transport through the film. The larger cell polarisation (400 mV) in contrast to KPF_6 cells (70 mV), is due to low mobility of large K^+ through this compact thin layer, since there was no difference in the cell reaction. The enhanced stability of the K metal anode encourages the use of TFSI based electrolytes to achieve improved cycle life.

5.4.4 KTFSI based K-O_2 cells

The attainment of a stable surface layer using KTFSI, but not using KOTf, indicates that possible component of the SEI are related to cleavage of $–SO_2–CF_3$ moieties. Therefore, an attempt of tuning the protective layer was made by simply increasing the KTFSI concentration in solution. The use of highly concentrated electrolytes (above conventional 1 mol dm^{-3} standard) has been recently investigated as a new family of electrolytes with potential to obtain stable cycling using alkali metal anodes[30]. Li-ion[31], Na-ion[32] and K-ion[26] cells have achieved improved cycle life and inhibition of dendritic formation using high concentrated ether electrolytes. Notably, higher specific capacities are achieved in alkali metal-

oxygen cells, making the suppression of anode instabilities considerably more challenging for these systems.

K-O_2 cells were assembled increasing the support salt concentration, namely 0.25, 0.5, 1.0, 3.0 and 5.0 M KTFSI in DME in combination with a carbon fibre paper cathode (Avcarb P50, 10 m^2 g^{-1}). The cells operated at a current density of 0.12 mA cm^{-2} between a voltage window of 2.0 V and 3.0 V vs K^+/K.

The shallow cycling data in Figure 5.10 with a capacity limitation of 50 mAh g^{-1} shows that systematically increasing the KTFSI concentration successfully prolongs cycle life and enhances coulombic efficiency. The same voltage gaps was obtained for all cells (400 mV), indicating similar cell chemistry.

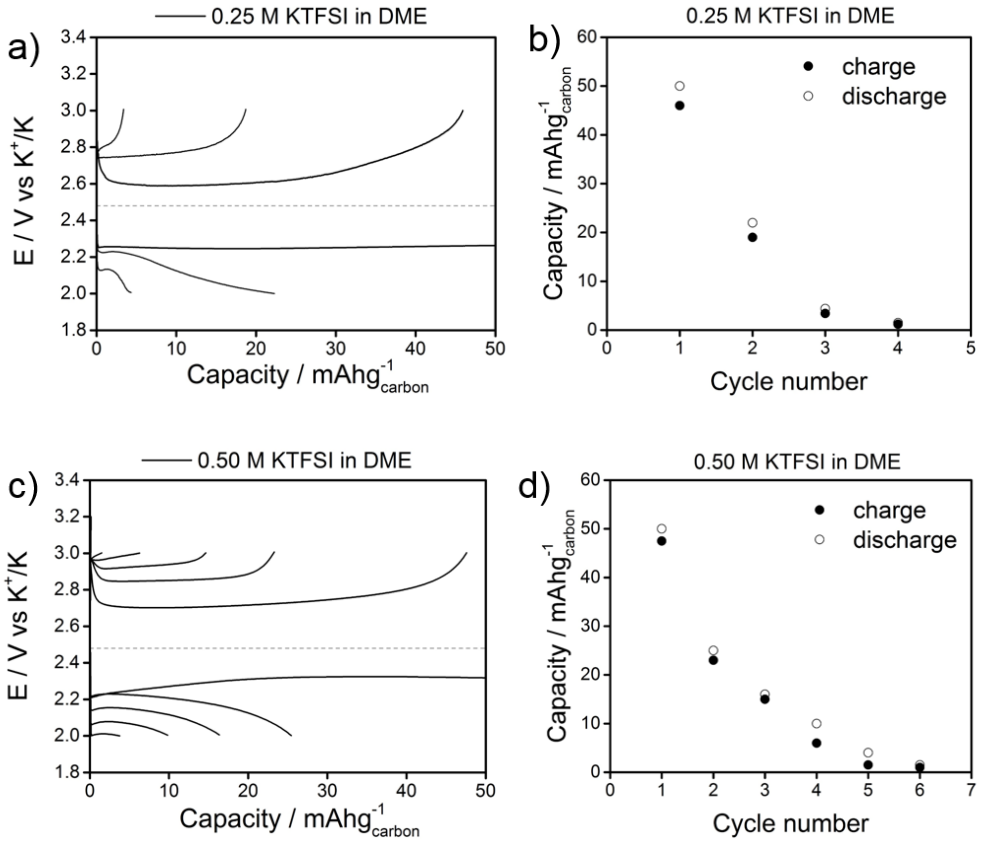

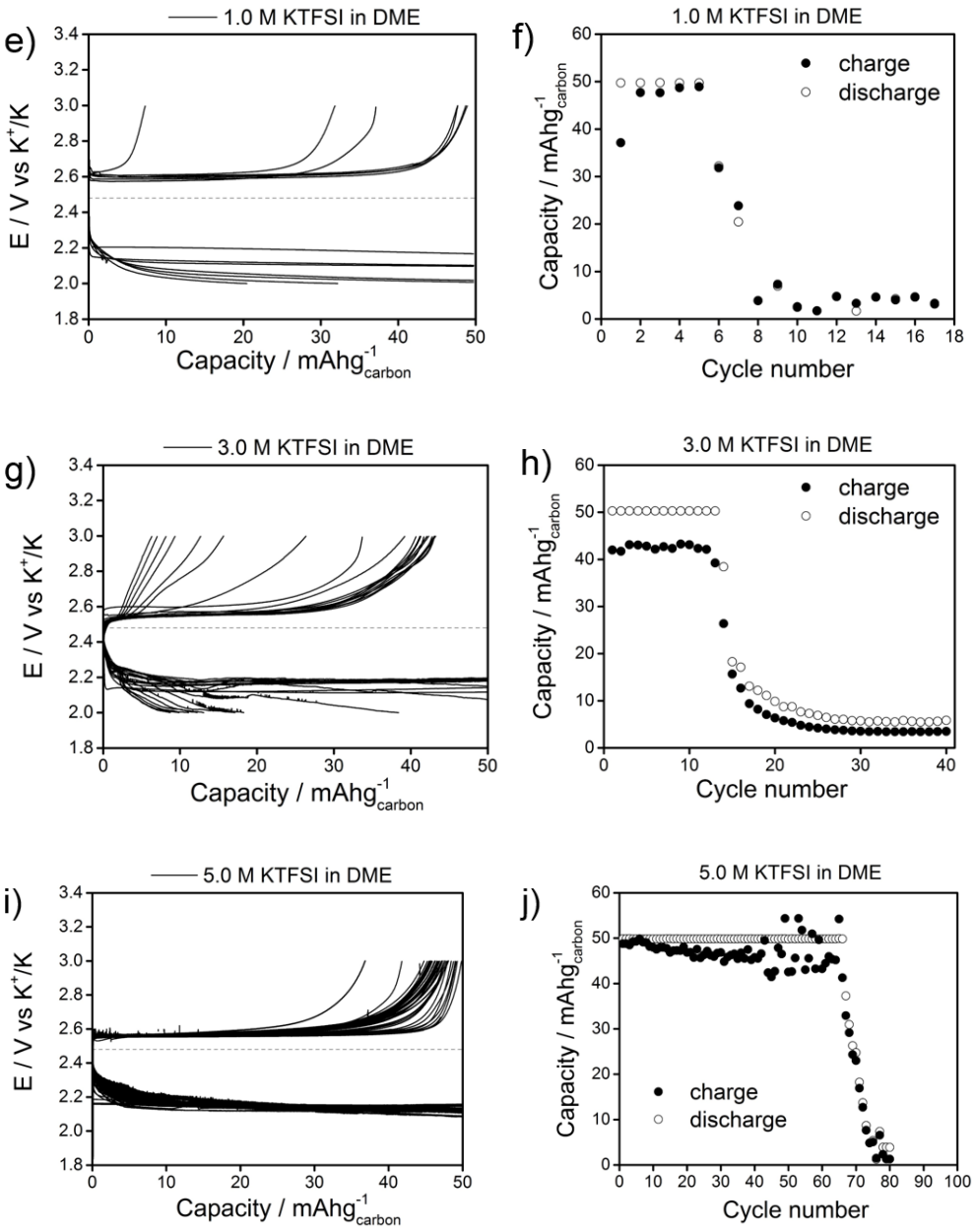

Figure 5.10: Potential vs capacity profile and cycling data for K-O_2 cells using a) and b) 0.25 M, c) and d) 0.50 M, e) and f) 1.0 M, g and h) 3.0 M and i) and j) 5.0 M KTFSI in DME electrolyte. Cathode: Avcarb P50. Rate: 0.12 mA cm^{-2}. The dotted horizontal lines mark the thermodynamic potential for KO_2 formation.

The best performing cell using a 5 M KTFSI in DME solution (Figure 5.10i and j), presented stable cycling with 93 % capacity retention up to 66 cycles, after which the capacity faded rapidly and only negligible capacities were obtained.

Analysis of the 5 M KTFSI/DME cell after cycling reveals that capacity fade occurs due to instabilities in both the anode and the cathode. Raman analysis (Figure 5.11a) shows a single KO_2 peak after the first discharge and the accumulation of electrolyte degradation products (K_2CO_3) on the cathode surface upon continuous cycling.

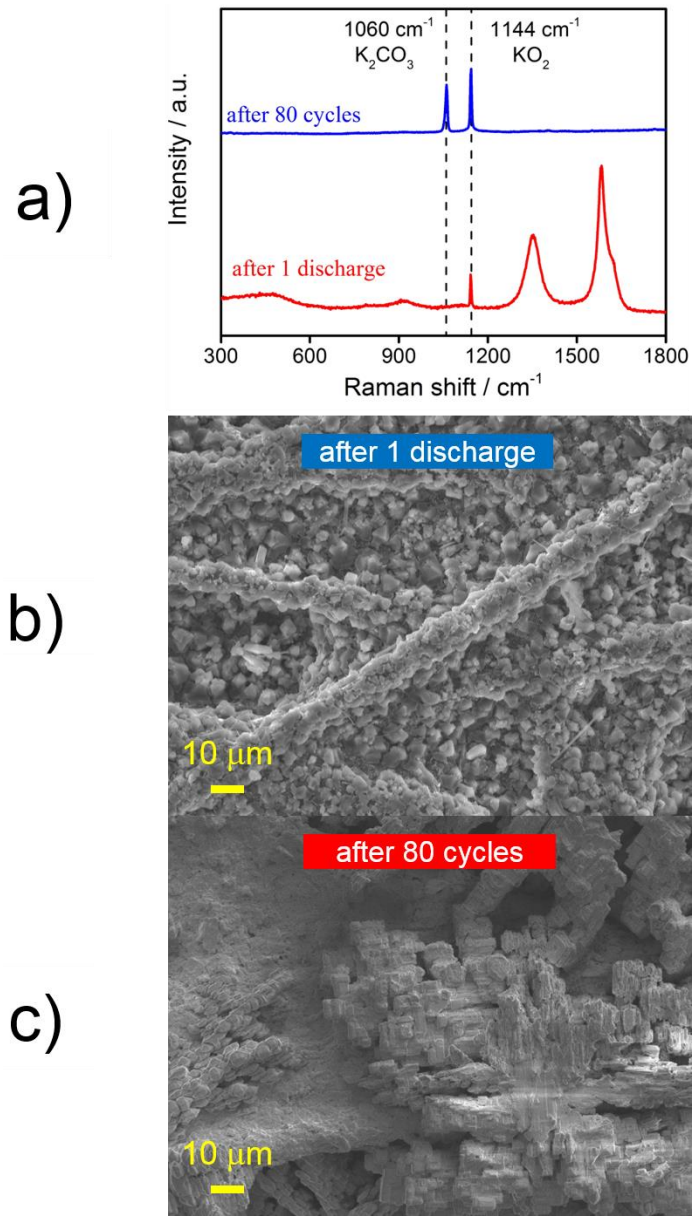

Figure 5.11: a) Raman and b) and c) SEM analysis of the cathode reaction products after 1 discharge and after 80 cycles in a K-O_2 cell using 5.0 M KTFSI in DME electrolyte and an Avcarb P50 cathode. Rate: 0.12 mA cm^{-2}.

SEM images in Figure 5.11b and c further corroborates the Raman data. After the first discharge process, sparsely distributed cubic particles are observed on the carbon substrate while after 80 cycles the carbon is completely covered by a mixture of cubic particles and an insulating film which causes charge build-up on the images. As a consequence, the Raman mapping of the cathode after 80 cycles does not show any carbon D and G bands, indicating complete passivation of the conductive surface.

On the anode side, when disassembling the cell, it can be seen that after 80 successive striping/plating cycles the protective layer is disrupted allowing fresh K metal in contact with the O_2 containing electrolyte resulting in the formation of KO_2. Figure B5 in Appendix B shows that the surface layer after one galvanostatic cycle remains intact and after long cycling oxygen crossover is detected. Furthermore, the disruption of the protection layer causes dendrites to short circuit the cell, observed in the discharge/charge cycling and on the glass fibre separators (see Figure B6, Appendix B).

To further investigate the components of the protective SEI formed upon cycling K-O_2 cells using highly concentrated electrolytes, FTIR (Figure 5.12) and XPS (Figure 5.13) measurements of the surface layer were performed. After electrochemical measurements, the metal anode was washed repeatedly with DME to avoid contamination the support salt.

FTIR analysis further confirms the ether solvent degradation products that compose the anode protective surface layer: KOH (3504 cm^{-1}), K_2CO_3 (1405 and 882 cm^{-1}) and carboxylates (potassium formate or potassium acetate 1663 cm^{-1}). Other components arise from degradation of the support salt. The two bands at 797

and 742 cm^{-1} assigned to asymmetric and symmetric stretch modes of the SNS group[33] are not present in the surface layer, indicating nitrogen sulphur bond cleavage induced by the K anode. A signal at 1071 cm^{-1} associated with in-plane -SO_2- symmetric stretch[34] further supports the decomposition of KTFSI.

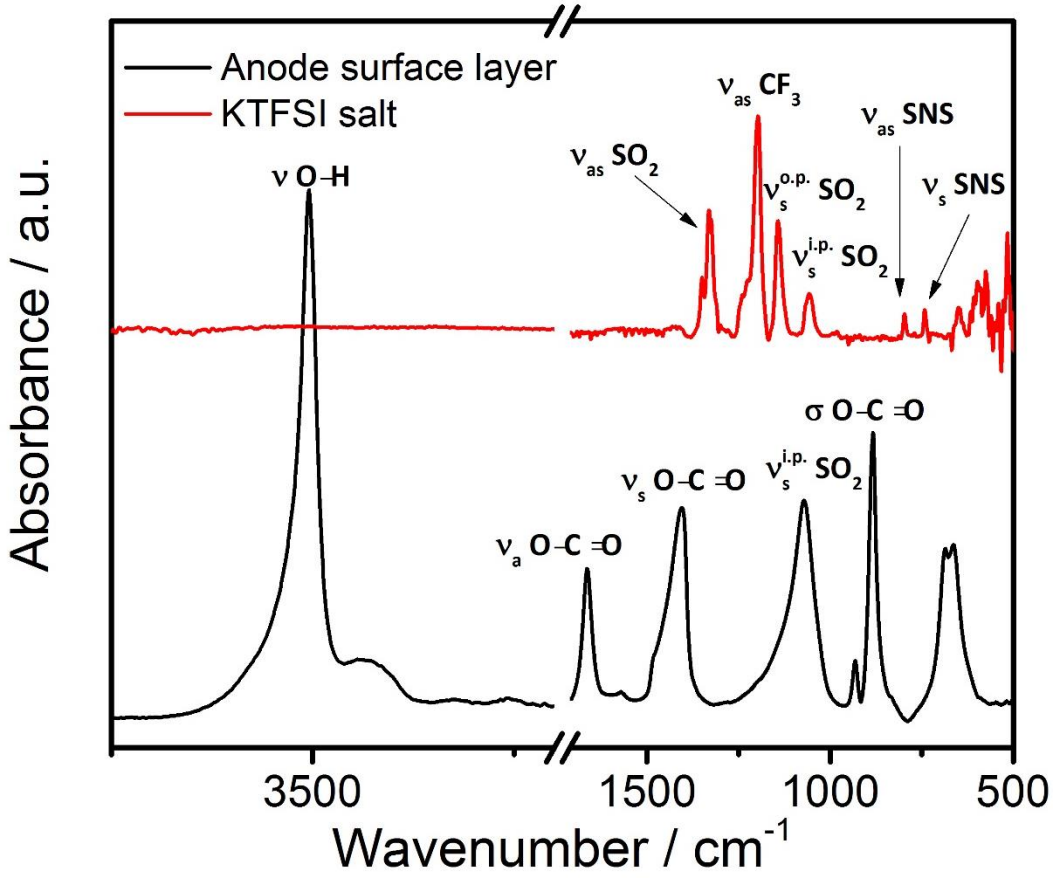

Figure 5.12: FTIR spectra of the surface layer formed on the metal anode after one galvanostatic cycle in a K-O_2 cell using a 5 M KTFSI in DME electrolyte. The spectra of KTFSI salt is shown for comparison.

XPS analysis was performed to gain further insight on the chemical composition of the anode protective surface layer. The S 2p spectrum in Figure 5.13a shows two peaks at 168.9 and 165.3 eV related to the presence of sulphate (SO_4^{2-} – 89%) and sulphite groups (SO_3^{2-} – 11%), respectively. This is in

agreement with the FTIR detection of sulphur-oxygen vibrations, which can arise from cleavage of the nitrogen sulphur bond and further reaction with oxygen dissolved in the electrolyte. Comparing the surface layer obtained with highly concentrated 5.0 M KTFSI with the results report by Ren *et al.*[29] using standard 1.0 M KTFSI solution, less sulphite is detected and S^{2-} was not detected. Potassium sulphide (K_2S) can obtained as a result of further reduction of sulphite species, which are obtained as a result of further reduction of sulphate species, thus indicating less reductive decomposition using highly concentrated electrolytes.

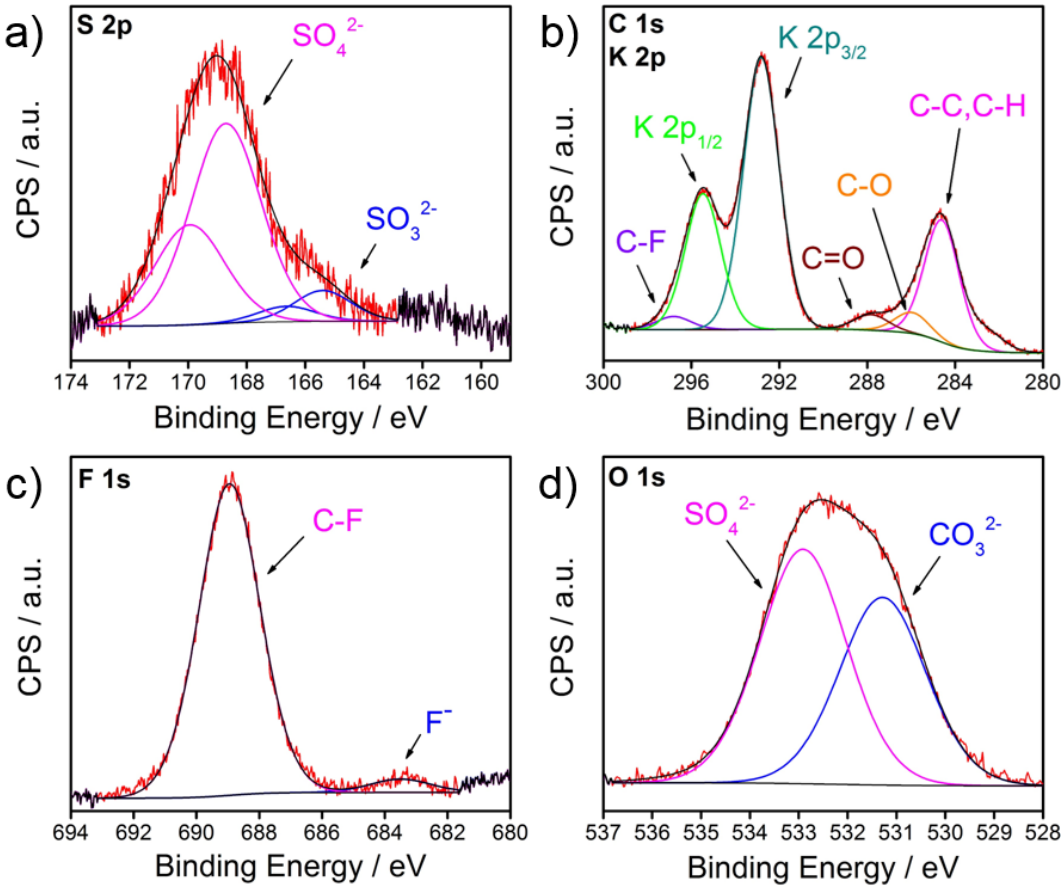

Figure 5.13: XPS spectra of the surface layer formed on the metal anode after one galvanostatic cycle in a K-O_2 cell using 5M KTFSI in DME electrolyte: a) S 2p, b) C 1s and K 2p, c) F 1s and d) O 1s. (XPS analysis performed by Jose A. C. Clemente).

The C 1s spectra in Figure 5.13b shows the presence of C-O, C=O, C-C/C-H (sp^3) species in agreement with the Raman and FTIR characterisation of electrolyte degradation products (carbonate and carboxylates). The O 1s spectrum shows sulphate and carbonate species from both KTFSI and DME decomposition. Finally, the F 1s spectrum shows two signals at 689 and 683.5 eV related to C-F (96%) and F^- (11%) species. The comparative area ratio of both fluorine species indicate inappreciable cleavage of the C-F bonds in CF_3 groups in the KTFSI molecule resulting in the formation of KF. A higher percentage of KF was reported when using standard KTFSI electrolytes[29].

The combination of Raman, FTIR and XPS analysis of the surface layer formed on potassium anodes in K-O_2 batteries using KTFSI/DME electrolyte shows that the SEI is formed of both ether and support salt degradation products. This process is similar to the formation of a stable SEI layer on graphite anodes in lithium-ion batteries, which is composed of organic carbonate degradation products and lithium salt degradation.

Further attempts to tune the K metal protective layer were made by the application of an ionic liquid mixed with DME as an electrolyte media in K-O_2 cells. Ionic liquids are room-temperature molten salts, due to week ionic interactions of large organic cations with delocalised charge anions compared to conventional ionic compounds. ILs have been extensively studied as an alternative to conventional electrolytes for electrochemical applications, based on their high chemical stability, large electrochemical window, intrinsic electrolytic conductivity and negligible volatility[35].

However, the application of ILs in alkali metal oxygen batteries is hindered by low O_2 solubility and poor cathode wettability related to the high viscosity of these compounds[36]. A strategy to address these shortcomings is the use of blended electrolytes containing ILs and molecular solvents. A mixture of ILs and glymes have been reported to enhance the sluggish transport properties and increase O_2 solubility[37, 38].

Here, K-O_2 cells were assembled using a blend of N-butyl-N-methylpyrrolidinium bis(trifluoromethanesulfonyl)imide [PYR14][TFSI] and 1,2 dimethoxyethane (DME) at different ratios using a 1 M KTFSI salt concentration. A carbon fibre paper cathode (Avcarb, P50) was used and the cell cycled between 2.0 and 2.8 V vs K^+/K at a 0.12 mA cm^{-2} current rate.

Figure 5.14 shows cycling data for the 1.0 M KTFSI in 1:1 DME: [PYR14][TFSI] and 1.0 M KTFSI in 3:1 DME:[PYR14][TFSI] electrolyte blends, a pure ether solvent cell is shown for comparison. The pure ionic liquid and the 1:3 DME:[PYR14][TFSI] blend cells did not achieve comparable capacities, possibly due to issues associated with wettability and high viscosity of the IL.

The reaction product of K-O_2 cells using IL blends electrolytes was confirmed to be crystalline KO_2 by PXRD without signs of other side reactions (see Appendix B, Figure B7), which accounts for the good coulombic efficiency of the cells. The reversibility of the one-electron redox couple O_2/O_2^- in the presence of metal ions in [PYR14][TFSI] electrolytes has been reported by Allen *et al.*[39]. The PYR14 anion is a softer Lewis acid than other alkali metal ions, resulting in weaker electrostatic association with the superoxide anion and improved ORR/OER reversibility[39].

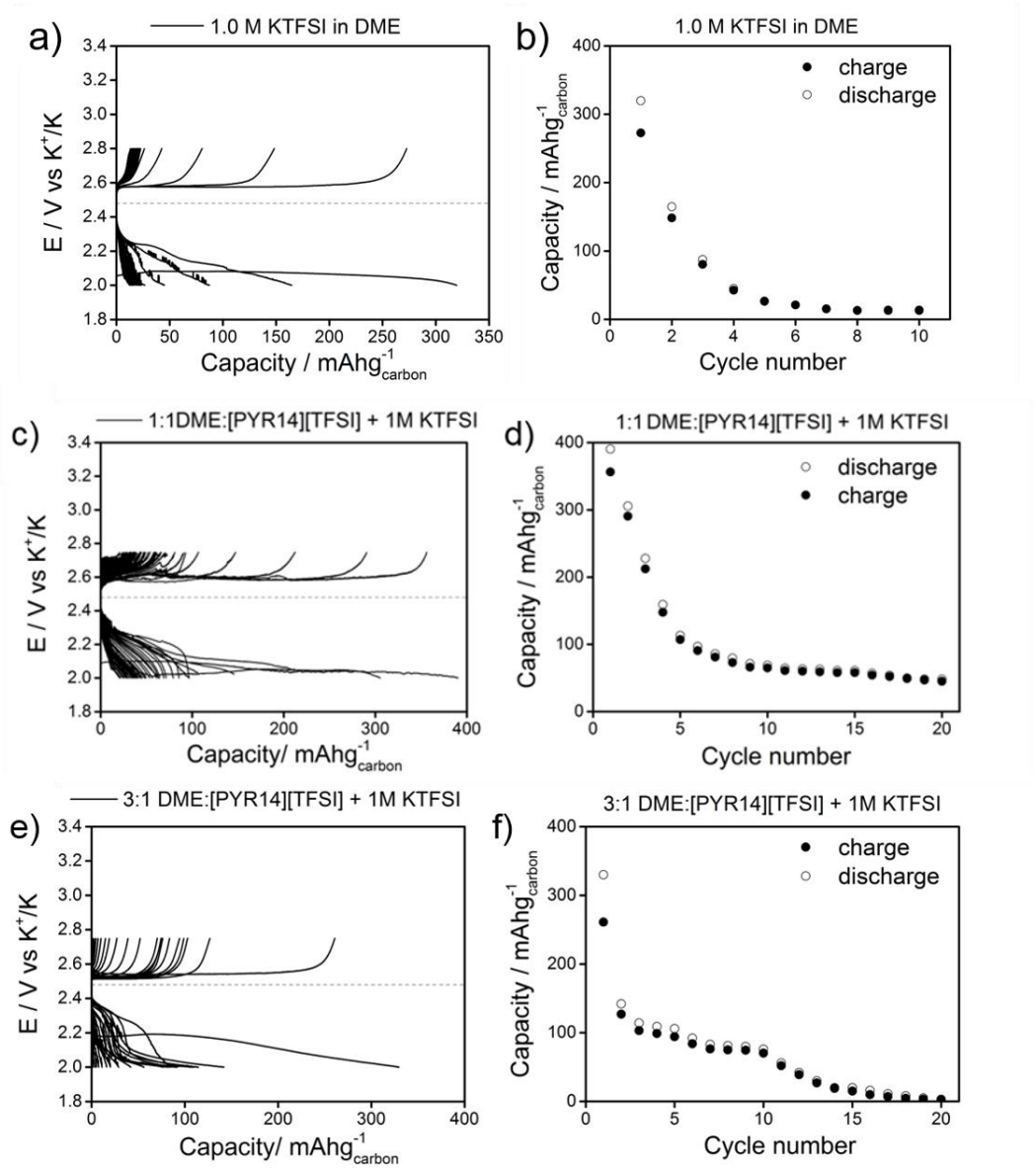

Figure 5.14: Potential vs capacity profile and cycling data for K-O_2 cells using a) and b) 1 M KTFI in DME, c) and d) 1 M KTFSI in 1:1DME: [PYR14][TFSI] and e) and f) 1 M KTFSI in 3:1 DME: [PYR14][TFSI] Cathode: Avcarb P50. Rate: 0.12 mA cm^{-2}. The dotted horizontal lines mark the thermodynamic potential for KO_2 formation.

The addition of ionic liquid to the ether electrolyte resulted in a modest improvement in the cyclability of the K-O_2 cells, as significant capacity fade was observed for both blended electrolytes. Similar to the highly concentrated electrolytes, a Raman analysis of the surface layer formed on the K anode (Figure

5.15), shows that a protective SEI is formed after the first cycle – no oxygen crossover is observed. After consecutive cycling, KO_2 along with ether decomposition product are detected, indicating the protective layer is disrupted.

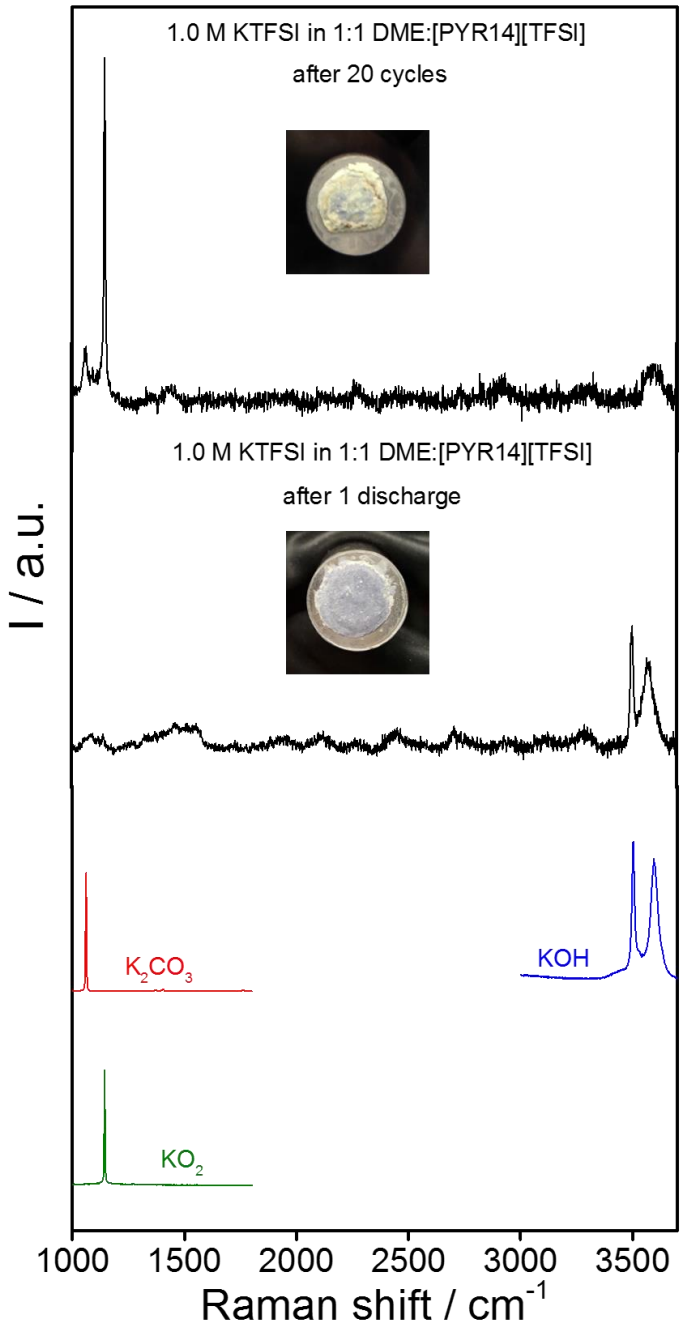

Figure 5.15: Raman spectra of the surface layer formed on the K metal anode after 1 discharge and after 20 galvanostatic cycles in a K-O_2 cell using 1 M KTFSI in 1:1DME: [PYR14][TFSI] electrolyte.

The composition of the anode surface layer formed after one galvanostatic discharge while using the blended 1:1DME:[PYR14][TFSI] electrolyte was investigated by FTIR (Figure 5.16) and XPS (Figure 5.17).

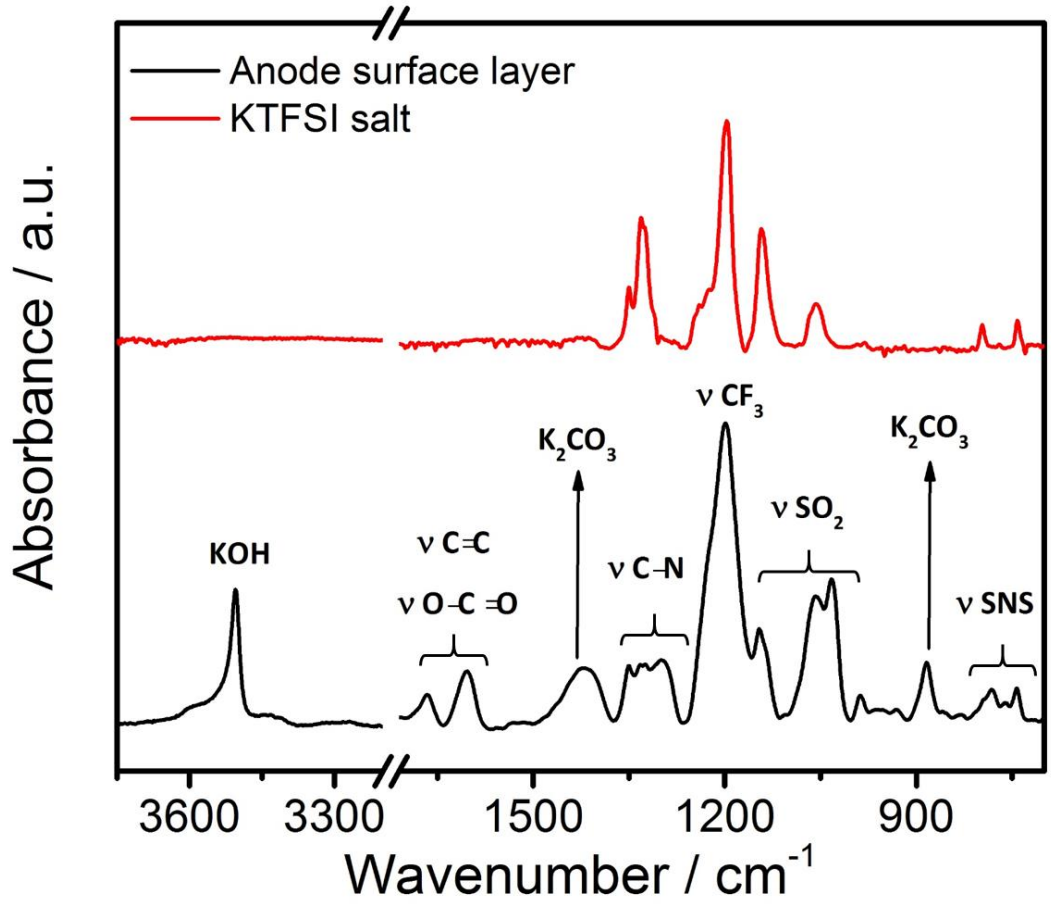

Figure 5.16: FTIR spectra of the surface layer formed on the K metal anode after one galvanostatic cycle in a K-O_2 cell using a 1.0 M KTFSI in 1:1DME:[PYR14][TFSI] electrolyte. The spectra of KTFSI salt is shown for comparison.

In the FTIR spectra, the same ether degradation products are detected in line with the previous analysis. The surface layer seems to retain some of the vibrations associated with the ionic liquid anion, such as the CF_3 asymmetric stretching (1199 cm^{-1}), -SO_2- symmetric stretching (1142 cm^{-1}) and both the asymmetric and

symmetric stretching of SNS (783 and 742 cm^{-1}). Furthermore, fragments of the ionic liquid cation decomposition are observed. The IR bands at 1350, 1325 and 1295 cm^{-1} are in the region associated with the C-N stretching in tertiary amines and a signal at 1660 cm^{-1} is assigned to C=C vibration in isolated alkene[28]. The electrophilic centre in the methylpyrrolidinium cation makes it susceptible to anodic oxidation (see Appendix B, Figure B8). The decomposition of [PYR14][TFSI] in Li-O_2 cells was reported by Piana *et al.*[40], producing tertiary amines and alkene fragment as a result of reduction by the lithium metal. A higher extent of ionic liquid decomposition is expected on K-O_2 cells based on the more reactive anode.

In the XPS analysis of the protection layer composition, the S 2p spectrum shows the formation of sulphate, indicating TFSI decomposition via N-S bond cleavage. Sulphite was not detected, however, since XPS is a surface sensitive technique, the data acquisition for heavier elements is hindered by the lighter elements degradation product, such as alkenes, carbonates and carboxylates. The peak at 169 eV is tentatively assigned to sulphate. The low CPS obtained is related to glass fibre contamination on the surface. Other possible electrolyte degradation products, such as K_2S and KF were also not detected. The C 1s spectrum shows the existence of species associated with DME and PYR14 decomposition and the F 1s spectrum indicates the retainment of CF_3 species from the KTFSI molecule. The O 1s spectrum further confirms the formation of K_2CO_3 from glyme degradation and K_2SO_4 from KTFSI reduction by the anode. Superoxide species were not detected, in line with the Raman analysis, confirming that the surface layer formed with 1.0 M KTFSI in 1:1 DME: [PYR14][TFSI] electrolyte inhibits oxygen crossover.

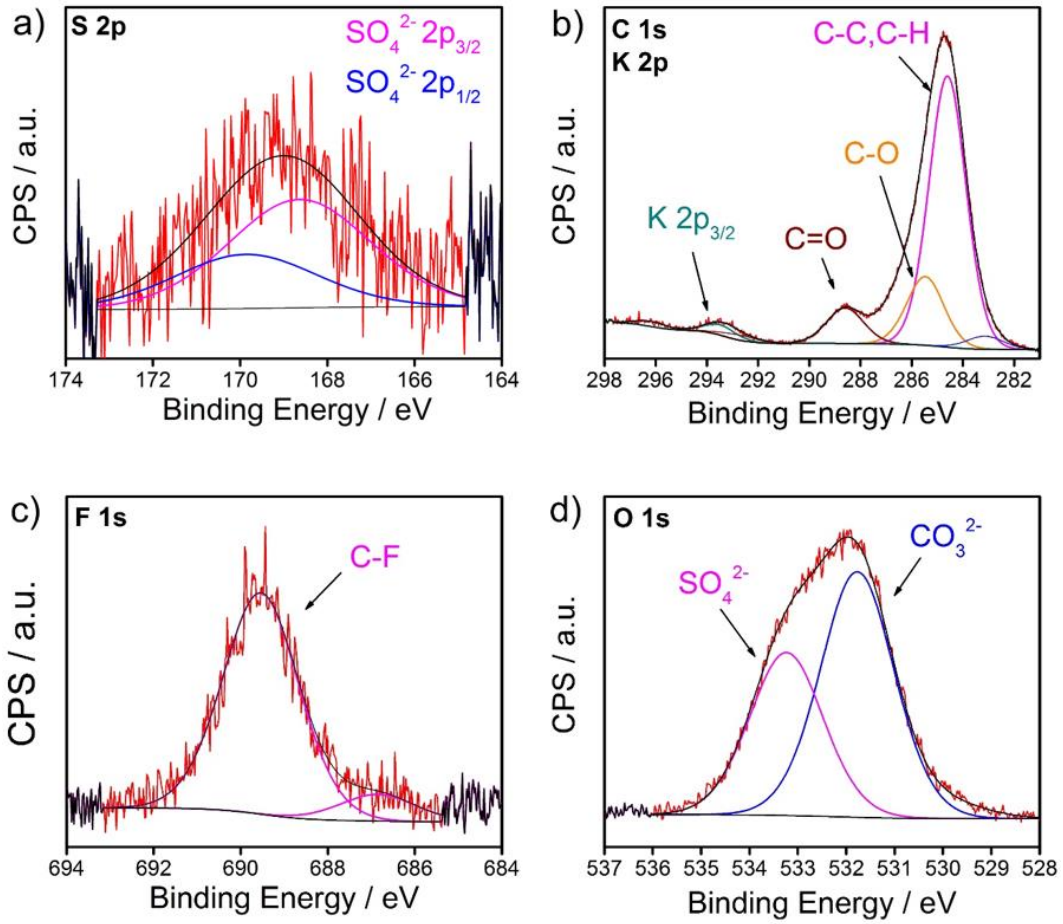

Figure 5.17: XPS spectra of the surface layer formed on the metal anode after one galvanostatic discharge in a K-O_2 cell using in a K-O_2 cell using a 1.0 M KTFSI in 1:1DME:[PYR14][TFSI] electrolyte: : a) S 2p, b) C 1s and K 2p, c) F 1s and d) O 1s. (XPS analysis performed by Jose A. C. Clemente).

5.4.5 Alternative K_3Sb anode material

One alternative to circumvent the safety hazard and reactivity issues associated with the use of K metal anode is to replace it with intercalation or intermetallic materials. In analogous lithium systems, the concept of a metal-free cell was first introduced by Hassoun *et al.*[41] using a lithiated silicon-carbon anode. Other intermetallic materials, such as aluminium-carbon[42] and tin-carbon[43] have

been employed and rendered enhanced cyclability. Intercalation carbon negative electrodes have also been investigated in Li-[44] and Na-O_2[45] batteries.

Antimony is a compound with excellent potential for the development of low cost anodes. Fast alloying reaction kinetics have been reported for this material, which has a high theoretical gravimetric capacity of 660 mAh g^{-1} corresponding to the formation of AM_3Sb (AM = Li, Na and K)[46, 47]. However, a major issue for the implementation of Sb anodes is the structural damage caused by a huge volume expansion upon cycling, resulting in rapid capacity fade and limited rate capability[48].

A well-accepted strategy to overcome this issue is to have the antimony particles embedded in a conductive matrix (e.g. carbon or nickel), acting as a confining buffer that tolerates large volume expansion[49]. Other attractive route is the synthesis of Sb nanoparticles, the benefits arise from the size confinement reducing particle deformation and cracking, resulting in improved conduction pathways[50]. The shorter AM^+ diffusion length and higher electrode/electrolyte interface enhances rate capability[51]. Therefore, Sb-C nanocomposites were investigated as possible alternative potassium storage negative electrodes for K-O_2 batteries.

The Sb-C nanocomposites were obtained via a simple mechanical milling route of commercial Sb "bulk" particles and conductive carbon black (Super C 65, Imerys) as reported by other authors[49, 52]. The morphology analysis of the composite material by SEM (Figure 5.18) shows that the particle size is reduced from large micron-sided, on the commercial Sb, to agglomerated nanoparticles with a broadly size range of 100 nm.

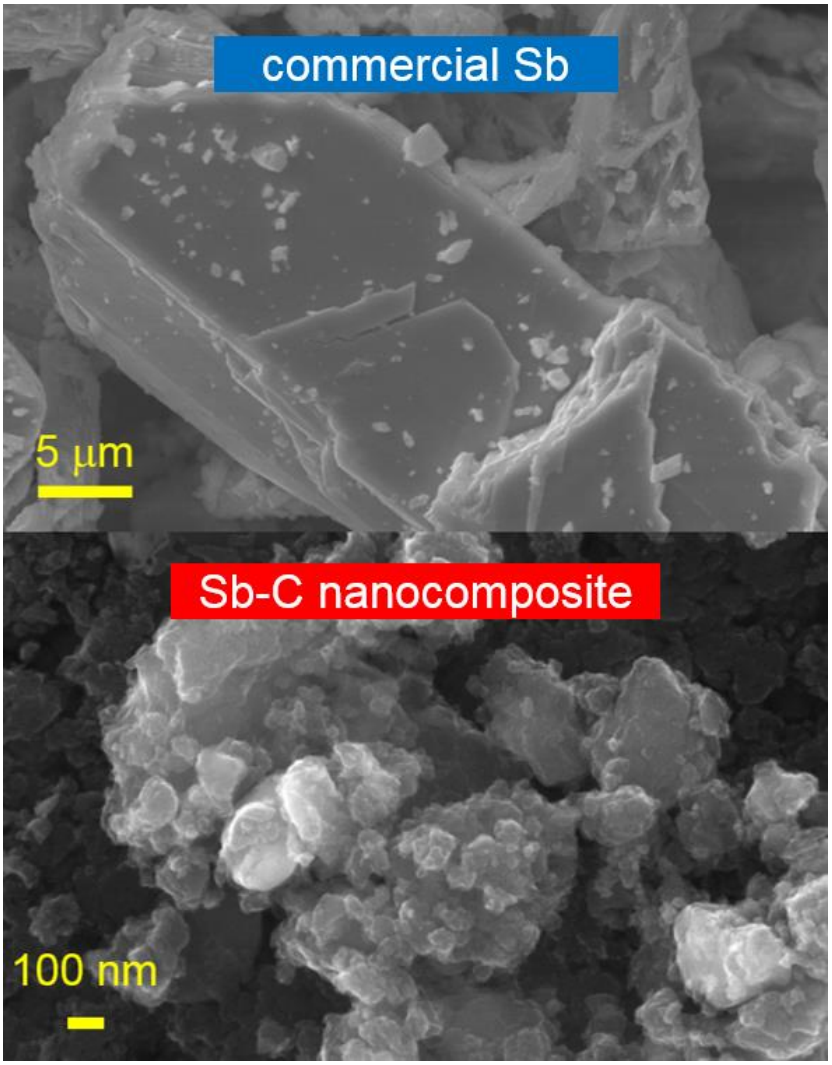

Figure 5.18: SEM images of bulk Sb particles and ball milled C-Sb composite.

The electrochemical performance of K-ion half cells using Sb-C nanocomposite as a working electrode was evaluated in 0.5 M KPF_6 EC:DEC (1:1 v/v) electrolyte and compared with the commercial material (Figure 5.19). The cells were galvanostatically cycled at a C/2 rate, C-rate being defined as the current applied to fully discharge/charge K_3Sb within one hour (660 A g^{-1}). The first cycle for both materials exhibits larger capacities than the theoretical value, which is a common behaviour associated with SEI formation happening from irreversible electrochemical degradation of the electrolyte.

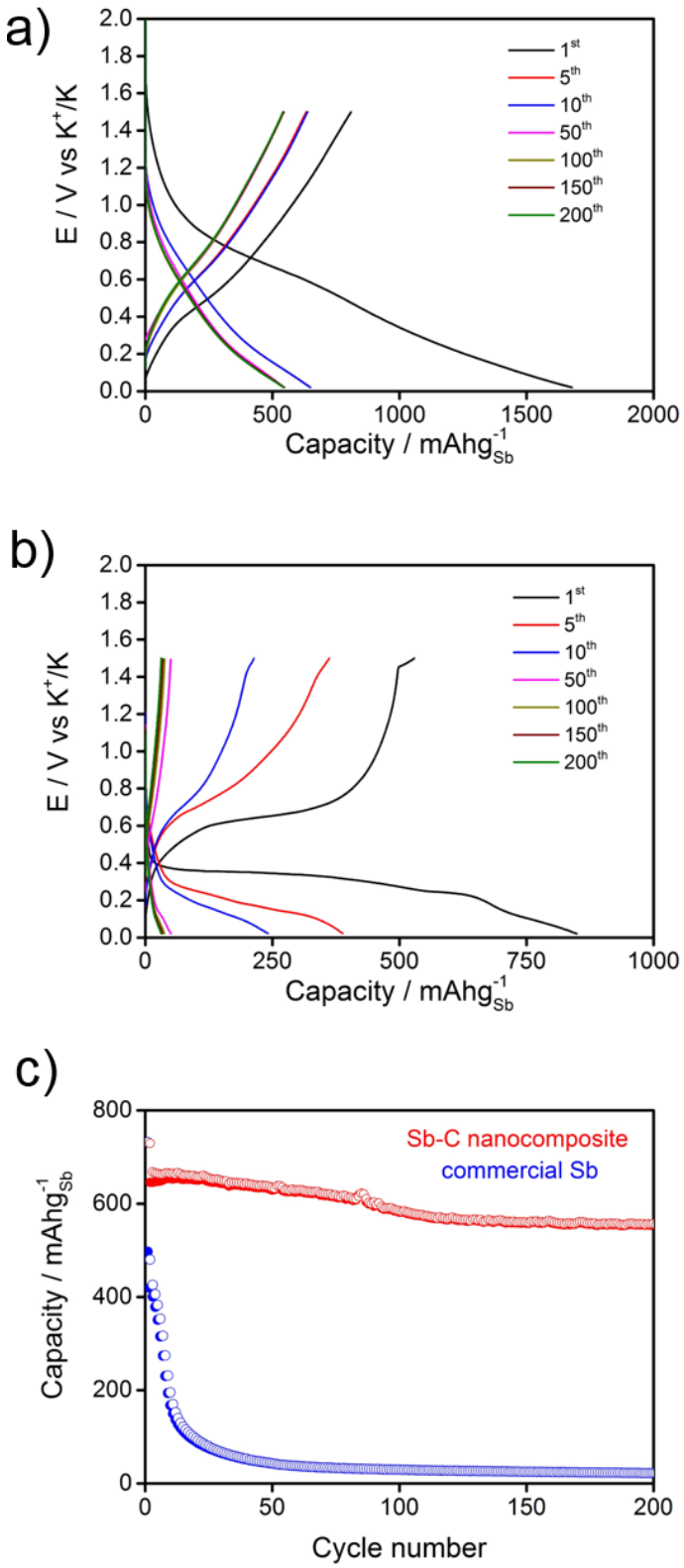

Figure 5.19: 200 cycles of galvanostatic discharge/charge for K-ion half cells using a) Sb-C nanocomposite and b) commercial Sb as anode material and at C/2 rate; c) cycling data. Electrolyte: 0.5 M KPF_6 in EC:DEC.

The SEI is stabilised on the subsequent cycles and a discharge capacity of 649 mAh g^{-1}_{Sb} is obtained for the Sb-C nanocomposite, which approaches the 3 K storage capacity (98.5 % of the theoretical value). High coulombic efficiency is obtained for the initial discharge/charge cycles – 98%. The cyclability data show good capacity retention over 200 cycles (84%), especially considering the capacity fade observed for other anode materials associated with the large potassium ion radius[53]. In contrast, the commercial "bulk" Sb half-cell delivers an initial capacity of 480 mAh g^{-1}_{Sb} and exhibits rapid capacity face after only 20 cycles. Indicating that the carbon nanocomposite effectively mitigates stress and strain related to the volumetric change.

The potentiodynamic profiles of both cells reveal significant difference in the alloying reaction between the materials. For the commercial Sb, a distinct dealloying (discharge) plateau is observed at ~0.35 V vs K^+/K and an alloying (charge) plateau is observed at ~0.65 V vs K^+/K. The assignment of the electrochemical processes occurring at different stages of potassiation is challenging based on different stable phases reported for the binary phase diagram of Sb-K[54]. However, a similar alloying reaction to sodium systems is expected and the formation of a KSb (1:1) intermediate is tentatively assigned following: Sb (rhombohedral) → KSb (amorphous) → K_3Sb (cubic)[47]. A similar phase transition has observed for other carbon-antimony materials[52].

The Sb-C nanocomposite shows a monotonically potential variation upon cycling without the observation of distinct discharge/charge plateaus. The less defined load curves are characteristic of nanostructured electrode materials[50] and

can be attributed to low crystallinity of the Sb-C composite at the nanoscale and rapid amorphisation upon cycling[49].

The rate capability of the Sb-C nanocomposite was further investigated. Figure 5.20 shows good rate capability indicating facile alloying kinetics. High coulombic efficiency (99%) is maintained for the highest rate. A capacity retention of 22% is obtained at 8C, which is lower comparing to Li-ion and Na-ion using Sb anode materials[55], but a significant improvement in comparison to carbon-based K-ion anodes[53, 56].

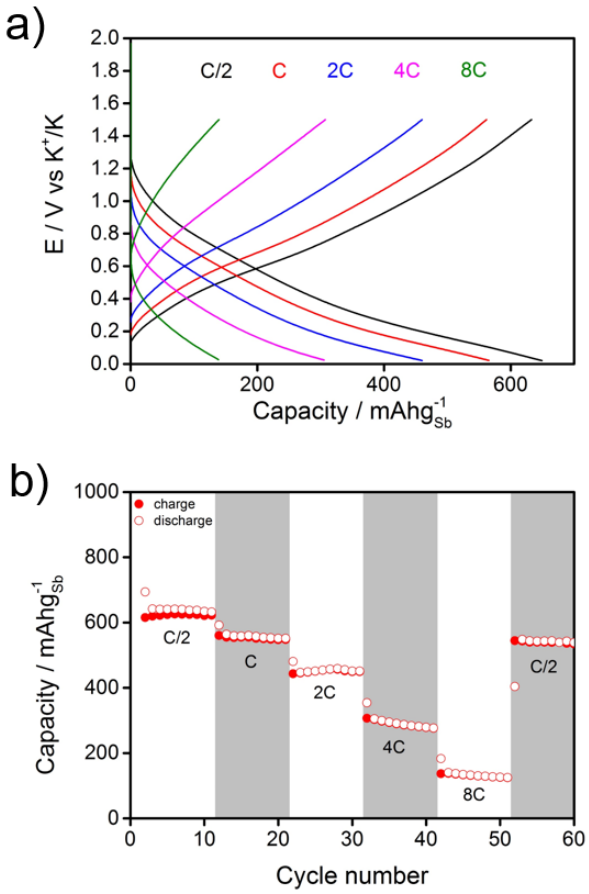

Figure 5.20: a) Discharge/charge curves for K-ion half cells using Sb-C nanocomposite as anode material at various current rates: from C/2 to 8C and b) cyclability plot of Sb-C nanocomposite showing the capacity at varying C-rate. Electrolyte: 0.5 M KPF_6 in EC:DEC.

To gain further insight onto the electrochemical processes undergone upon potassiation/depotassiation reactions, *in situ* experiments were performed on both Sb anode materials. The experiments were carried out on the same 0.5 M KPF_6 EC:DEC electrolyte and same active materials. However, to cast self-supporting electrodes and allow the Raman laser on the material, a higher binder content was necessary. Therefore, a lower rate (C/10) was employed to minimise overpotentials.

Figure 5.21 shows the *in situ* Raman data for the commercial Sb electrode. At the open circuit potential, two Raman features are observed at 113 cm^{-1} and 150 cm^{-1}, assigned to the E_g and A_{1g} bands respectively, which are related to pure longitudinal vibrations (A_{1g}) and pure transverse vibrations (E_g) of Sb atoms in the rhombohedral structure[57].

Upon potassiation (discharge), the Sb Raman peaks monotonically decrease in intensity without further changes in the spectra, indicating a stability of the initial Sb (rhombohedral) phase down to ~0.8 V vs K^+/K. The intensity decrease of the A_{1g} peak is notably more pronounced, until 0.38 V vs K^+/K where it splits into two components at 143 cm^{-1} and 152 cm^{-1}. A straightforward assignment of these new components is not yet provided, however, based on the reported phase transition at this potential[47,52], it can be related to the loss of crystallinity due to the KSb intermediate.

At the end of discharge, 0.02 V vs K^+/K, the A_{1g} peak is no longer observed, indicating full conversion to the K_3Sb phase. The E_g signal is still detected at higher wavenumbers, indicating that the transverse Sb-Sb vibrations are more energetic at the cubic K_3Sb structure. Both E_g and A_{1g} modes are recovered upon depotassiation, suggesting that the long range order is recovered.

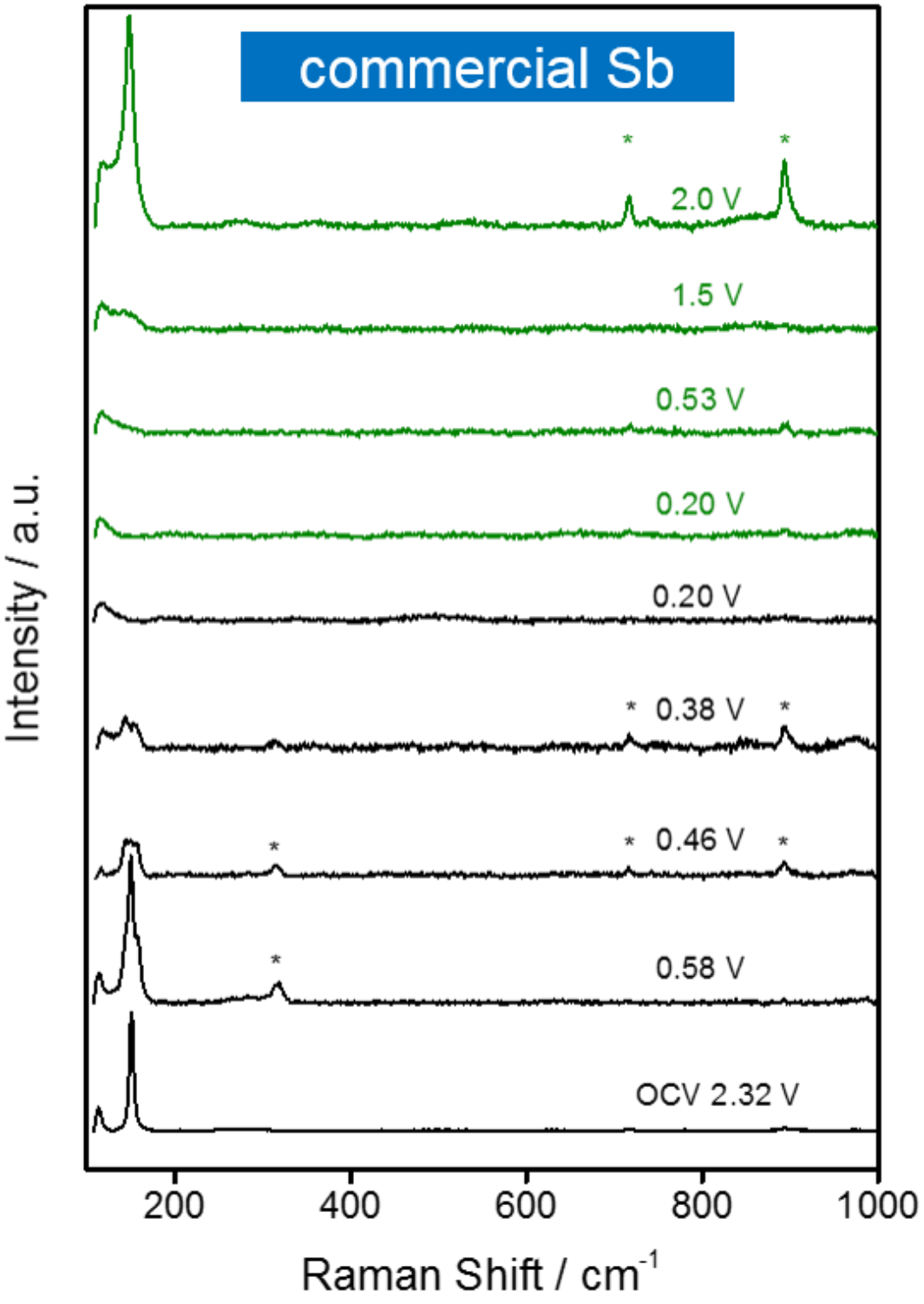

Figure 5.21: *In situ* Raman spectroscopy data of a K-ion half-cell over one discharge (black spectra) and charge (green spectra) cycle using a bulk Sb anode at a C/10 rate. Electrolyte: 0.5 M KPF_6 in EC:DEC. Label: * Peaks related to the electrolyte.

The Raman observed response during K-Sb alloying reaction is similar to the report by Drewett *et al.*[55] for an analogous sodium system using a bulk Sb anode.

Figure 5.22 shows the *in situ* Raman data for a discharge process using the Sb-C nanocomposite. Upon potassiation, a decrease in the intensity of the long range order vibration modes of Sb is observed. In contrast to the commercial Sb, the A_{1g} vibration does not fade at 0.02 V, demonstrating some retainment of the long ordered structure. This can be related to the formation of an under potassiated final species ($K_{3-x}Sb$), as has been proposed by other authors for the sodium-antimony system[55, 58].

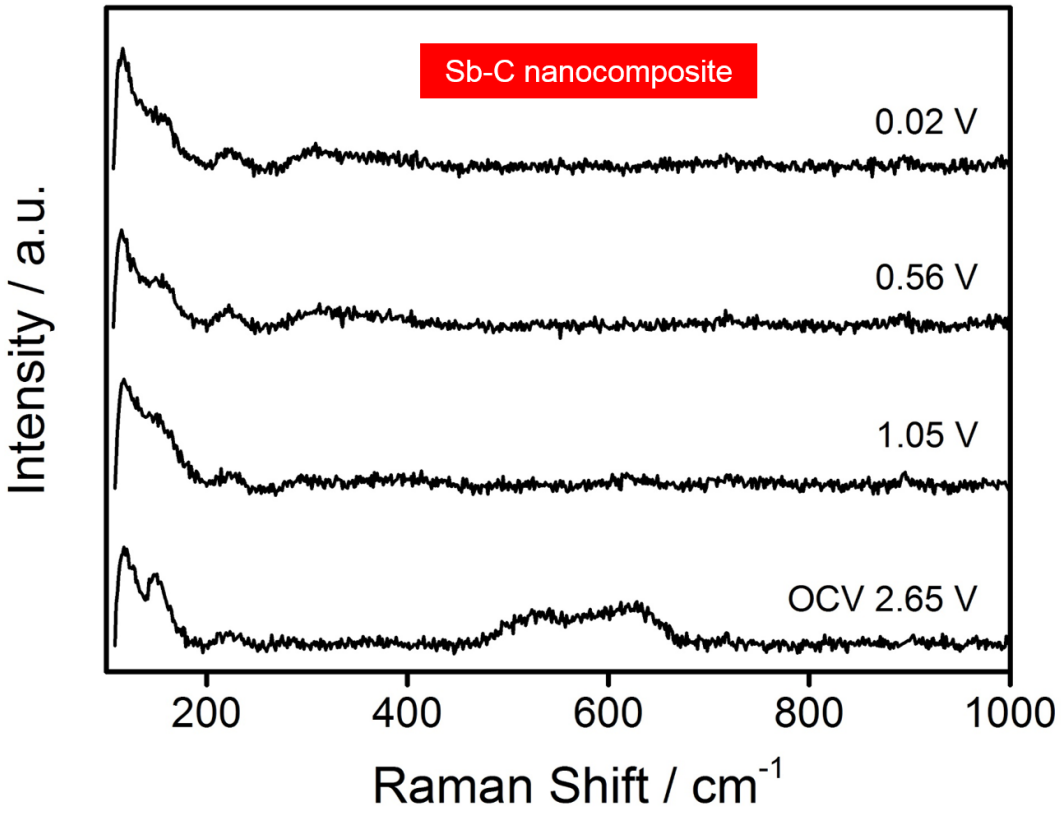

Figure 5.22: *In situ* Raman spectroscopy data of a K-ion half-cell over one discharge cycle using a ball milled C-Sb anode at a C/10 rate. Electrolyte: 0.5 M KPF_6 in EC:DEC.

As a proof of concept, a K-O_2 cell was assembled using a carbon cathode in combination with a K_3Sb anode, which was prepared by discharging the Sb-C nanocomposite anode in a K-ion half cell. It was possible to obtain a full galvanostatic discharge/charge cycle with high reversibility (Figure 5.23a). The combined processes during cell operation is shown in Eq. 5.3. However, a larger cell polarisation with limited capacity is observed when using the potassiated Sb anode in comparison to a conventional cell. The larger overpotential relates to the inherent lower ionic conductivity of the K_3Sb anode, and is similar to other reports of intermetallic anode in Li-[41] and K-O_2[52] cells.

$$xO_2 + K_xSb \leftrightharpoons xKO_2 + Sb \qquad 5.3$$

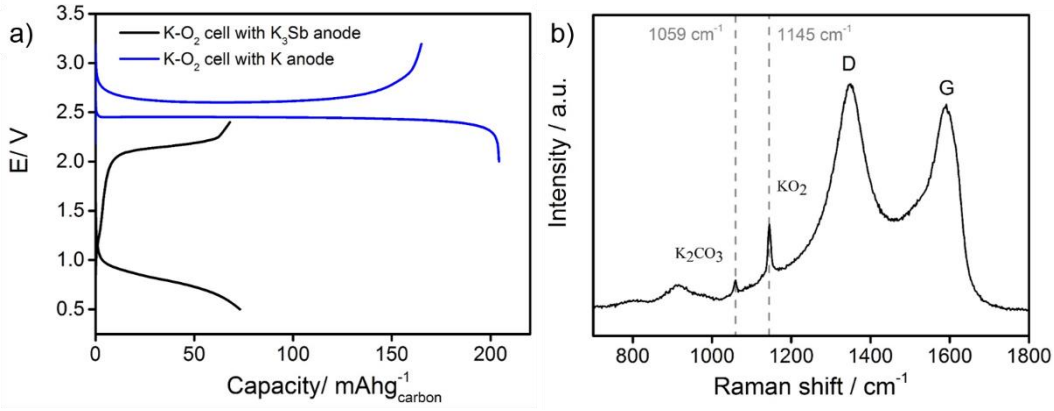

Figure 5.23: a) First galvanostatic discharge/charge cycle of K-O_2 cells using a potassium metal anode (blue) and a K_3Sb anode (black) with a carbon cathode at 0.12 mA cm^{-2} rate using a 0.25 M KPF_6 in DME electrolyte; b) Raman analysis of the discharge product formed on the K-O_2 cell using K_3Sb anode.

The formation of the desired reaction product, KO_2, during discharge was confirmed by Raman spectroscopy analysis of the carbon cathode. K_2CO_3 was also detected due to the lower voltages required to depotassiate the antimonide anode. The formation of K_2CO_3 can arise from either electrolyte degradation or KO_2

decomposition at large cathodic overpotential. This is in agreement to the behaviour of Na-O_2 cells at similar voltages (see Chapter 4, Figure 4.27).

5.4.6 Current density effect on capacity, KO_2 morphology and growth mechanism

Despite instabilities associates with the K metal anode, it is important to optimise and investigate processes occurring at positive electrode of the aprotic K-O_2 battery system. Initially, an investigation was carried out to determine the effect of current density on the cell performance and discharge products morphology. K-O_2 cells were assembled using a carbon fibre paper cathode (Avcarb, P50) in combination with a 0.25 KPF_6 in DME electrolyte. The cells were discharged at different current rates: 0.12 mAh cm^{-2} (21 mA g^{-1}), 0.24 mA cm^{-2} (42 mA g^{-1}), 0.48 mAh cm^{-2} (84 mA g^{-1}) and 0.96 mAh cm^{-2} (168 mA g^{-1}). After galvanostatic cycling, the same electrodes were analysed via Raman spectroscopy and SEM.

Representative potentiodynamic profiles of the different rates employed are shown in Figure 5.24a. As the current rate increases, larger overpotentials accompanied by reduced capacity (Figure 5.24b) are obtained, related to kinetic limitations of the ORR/OER. Viswanathan *et al.*[59] argue that the observed voltage polarisation, especially for high current densities, originate from iR drops caused by intrinsic cell impedance for a two-electrode set up. It is noteworthy that high coulombic efficiency is maintained even for the higher rate cells (91 % using 0.96 mA cm^{-2} rate). Thus, indicating very facile kinetics and reversible behaviour during K-O_2 cells operation.

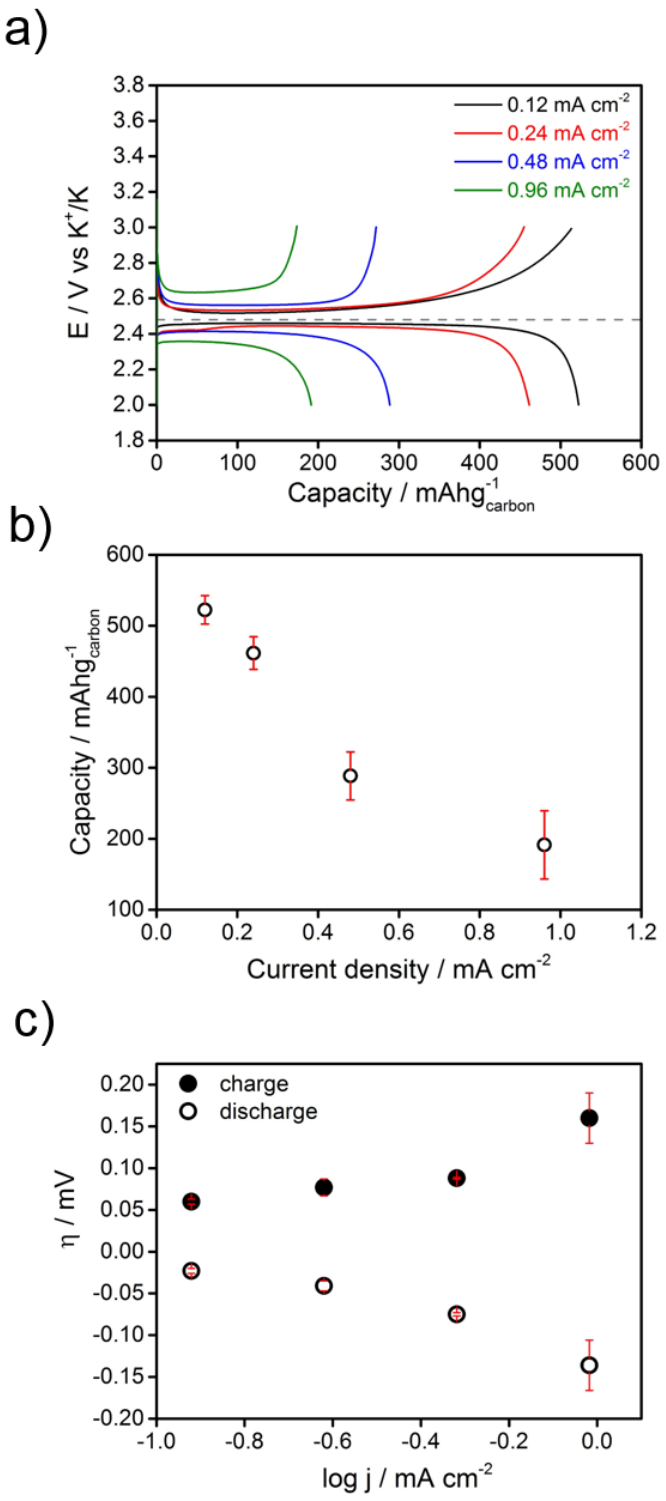

Figure 5.24: First galvanostatic discharge/charge cycle of K-O_2 cells using a carbon cathode (Avcarb, P50) and 0.25 KPF_6 in DME electrolyte at various current densities, b) Correlation between discharge capacity at 2.0 V vs K^+/K and current density and c) Tafel plots for the cathodic and anodic reaction in K-O_2 cells. (Error bars from standard deviation of at least 3 cells).

Figure 5.24c shows a Tafel plot of logarithm of the current density (log j) versus overpotential ($\eta = E - E^0$). Similar to Na-O_2 cells, a linear dependence is obtained, indicating kinetic control on the cell electrochemical processes. The Tafel slopes obtained (ORR = 119 mV; ERR = 102 mV) are close to the "typical" one-electron reaction (118 mV)[60]. A deviation from the linear η-log j behaviour is observed at high currents (0.96 mA cm^{-2}) causing a curvature in the Tafel plot, which has also been reported by other authors in analogous alkali metal-oxygen systems[59, 61]. Safari *et al.*[62] proposed that the experimental deviations on the expected linear behaviour derive from a discrepancy between the reduction rate of adsorbed oxygen species and adsorbed LiO_2 species with the chemical disproportionation reaction. However, a second electron reduction or disproportionation of KO_2 is not expected based on a higher thermodynamic stability compared to K_2O_2.

In agreement with the Tafel plots, the dominant process in K-O_2 cells operating at different rates was found to be the formation of KO_2 via Raman analysis of discharged cathodes (Figure 5.25). The detection of solely the superoxide stretching mote at 1144 cm^{-1} indicates very little extent of electrolyte degradation, in line with the high reversibility of the cells.

Similar to the behaviour of Na-O_2 cells (see Chapter 4, Figure 4.18), increasing the current rate of K-O_2 cells does not fundamentally effect the reaction products being formed, as no K_2O_2 was detected. This is in agreement to other reports in Li-[63], Na-[64] and K-O_2[65] systems using similar ether electrolytes and in contrast to reports by Yadegari *et al.*[66], which reported that low current rates would favour a two-electron reduction pathway in Na-O_2 systems.

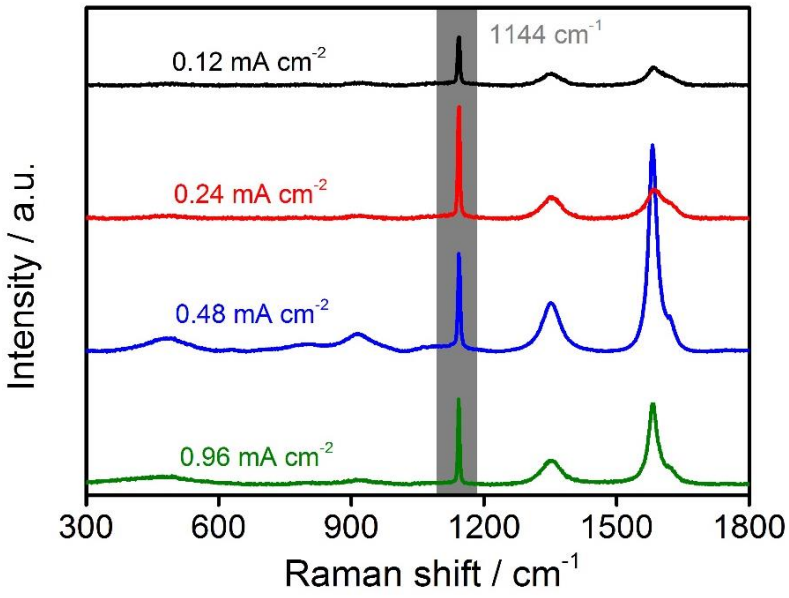

Figure 5.25: Raman spectra of discharged carbon fibre (Avcarb P50) cathodes at various current densities in K-O_2 cells using a 0.25 KPF_6 in DME electrolyte. (Spectra not normalised).

Having proven that the discharge of K-O_2 cells follows a one-electron reduction per molecular process for the different rates analysed, the growth mechanism of KO_2 crystals was investigated via *ex situ* SEM. Images were taken from the cathode side in direct contact with oxygen gas to avoid glass fibre contamination.

Figure 5.26 shows SEM images representative of the discharge products formed on the carbon fibre surface at different magnification. The same microscope settings were applied for imaging the samples. The growth of numerous cubic-like particles on the carbon carpet is seen for all current rates. KO_2 presents a tetragonal structure at room temperature with a displacement of the O_2^- ion related to the c-axis within the crystal structure[11]. In comparison to Na-O_2 cells, less perfect cubes are obtained, as NaO_2 presents a pyrite-type crystal structure with cubic symmetry[67].

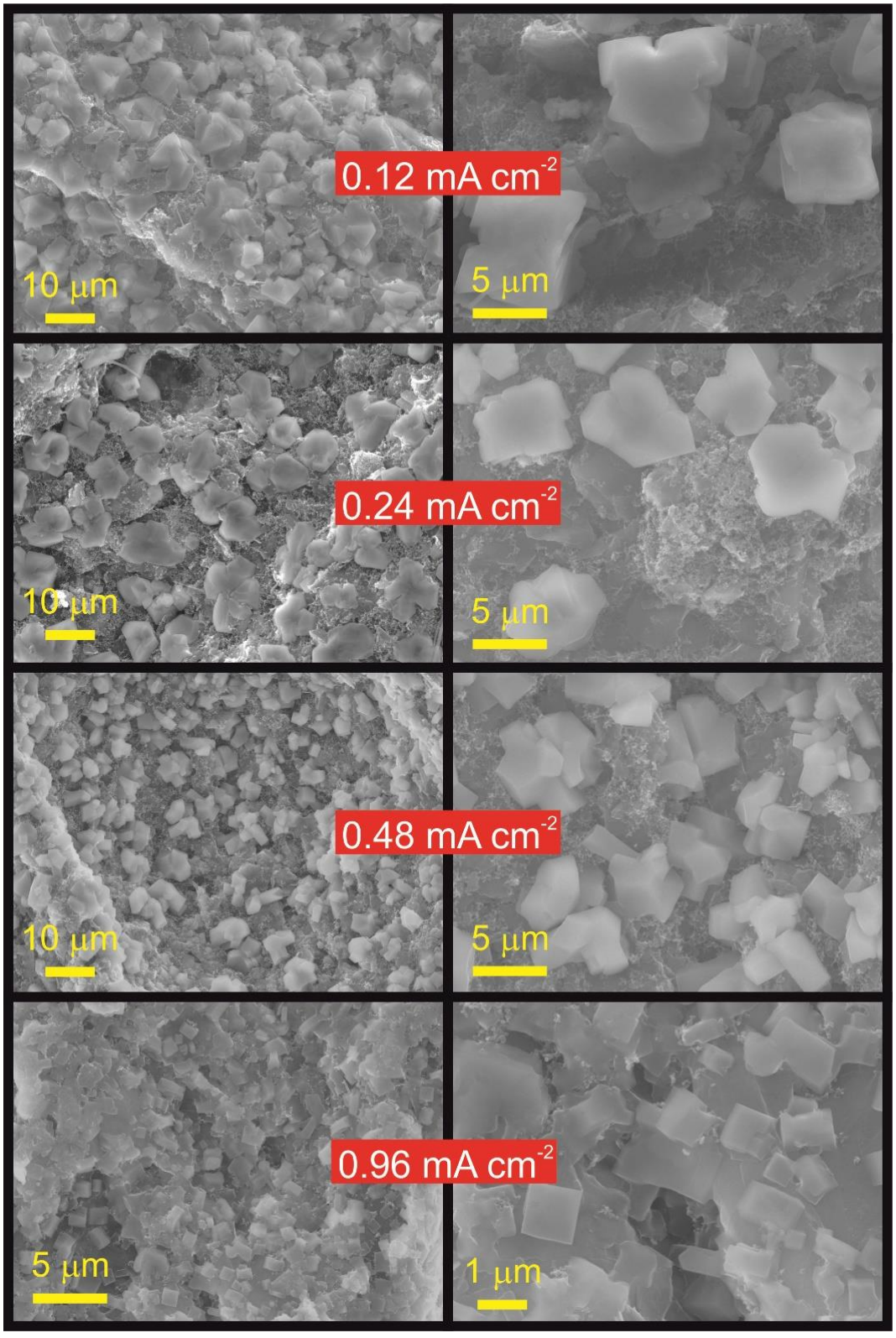

Figure 5.26: Scanning electron microscopy images at different magnifications of carbon fibre cathodes (Avcarb P50) discharged in K-O_2 cells at various current densities. Electrolyte: 0.25 M KPF_6 in DME.

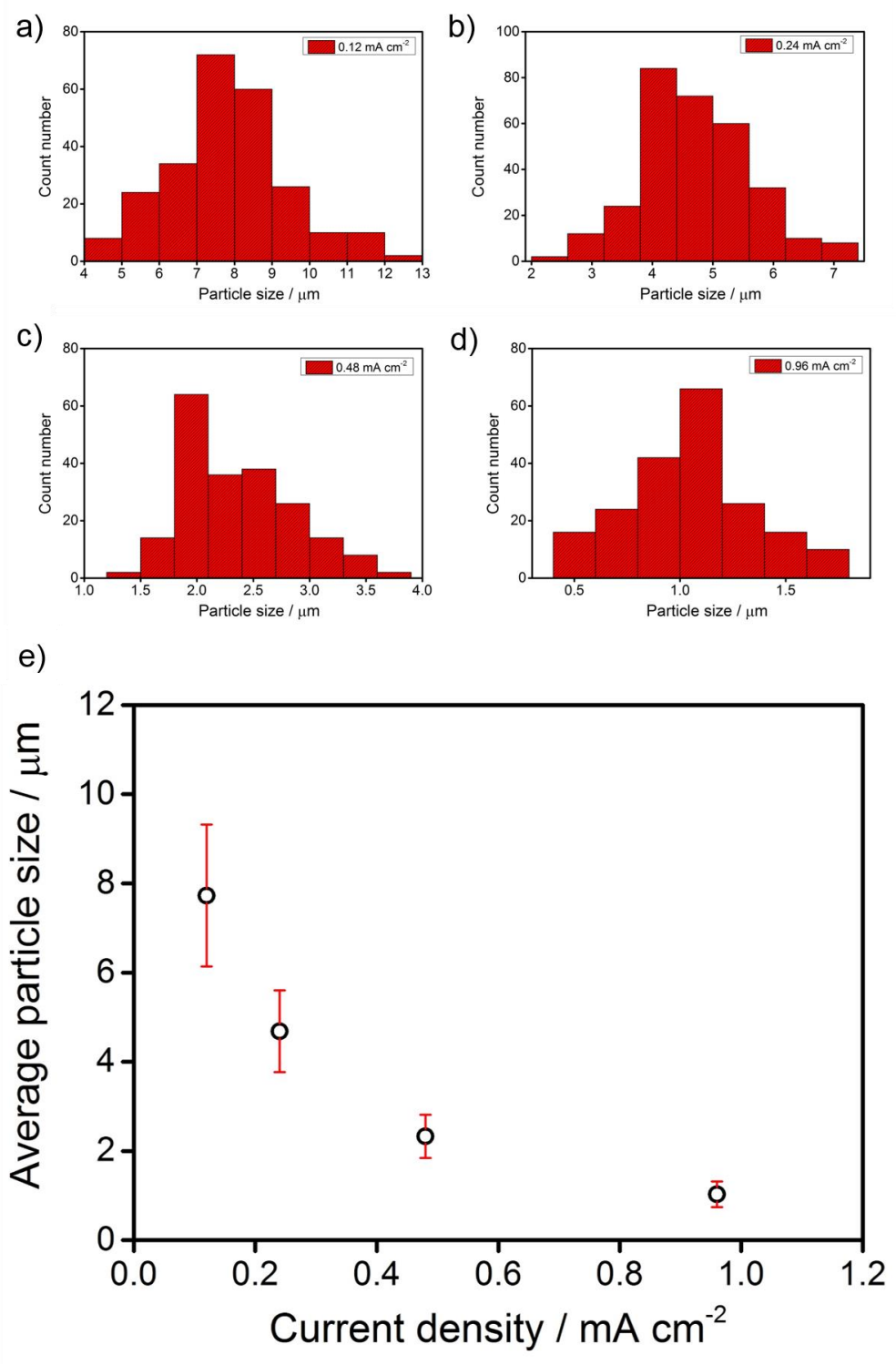

Figure 5.27: Histograms of particle size distribution obtained after one discharge process in K-O_2 cells using carbon cathodes (Avcarb P50) in combination with a 0.25 M KPF_6 in DME electrolyte at a) 0.12, b) 0.24, c) 0.48 and d) 0.96 mA cm^{-2}. e) Particle size of KO_2 precipitates vs current density. Error bars are standard deviation over 200 counts.

The obtainment of micron-sized cubic-like KO_2 precipitates, instead of a conformal film, indicates that the discharge follows a solution precipitation-precipitation mechanism. Although theoretical calculations show that KO_2 has a lower band gap than NaO_2 and Li_2O_2[3, 68, 69], direct electron transfer growth of KO_2 should not occur implying a solution route upon the reduction of dissolved oxygen species at the carbon surface analogous to the growth of NaO_2[70].

The average size of KO_2 crystals decreases with increasing current density (Figure 5.27). Na-O_2 cells using analogous ether-based electrolytes and carbon fibre cathode followed a similar trend (see Figure 4.20). The first step of the discharge solution route is the reduction of molecular oxygen dissolved in the electrolyte at the carbon surface. The nucleation of KO_2 and growth of large particles occurs when the electrode interface is saturated with $[K^+\text{--}O_2^{\bullet-}]$ ion pairs. As previously discussed, high current rates favour the formation of smaller cubic particles because the initial nucleation takes place in a locally more concentrated solution. This results in the formation of dense nuclei cluster which grow into smaller particles. The opposite situation takes place at low currents, resulting in more sparsely distributed nuclei which grow into larger KO_2 particles. Xiao *et al.*[65] reported a similar trend for K-O_2 cells using a DME-based electrolyte. Different experimental set up and oxygen partial pressure accounts for the difference in average particle size reported.

In contrast to Na-O_2 cells, increasing current density did not induced a change in morphology of the K-O_2 precipitates. When discharge sodium cells at high current rates, a change from cubic NaO_2 particles to cuboctahedra particles takes place (see Figure 4.19) as a result of a concomitant film formation. The growth

of an insulating film between NaO_2 cubes was responsible for limited capacity obtained due to blocking of the conductive carbon surface increasing the cell impedance[71]. For K-O_2 cells, the cubic particles obtained at 0.96 mA cm^{-2} and the inverse proportion between current density and particle size indicate that a conformal film is not deposited during discharge.

5.4.7 Effect of the polymeric binder

As previously discussed, polymeric binders are an important part of the composition of air-cathodes in alkali metal-oxygen cells. Typically, the binder molecules are on the surface of the carbon electrode and in direct contact with electrolytes and strong nucleophiles, consequently highly susceptible to degradation processes. In Li-O_2 cells, Black *et al.*[72] and Nasybulyn *et al.*[73] reported the instability of PVDF, a commonly used polymeric binder. In Na-O_2 cells, the degradation of PVDF was found to have a major influence on the cell performance (see Figure 4.29). Binder degradation induced NaO_2 decomposition resulting in high charge overpotentials and limited coulombic efficiency. Thus far, the stability of polymeric binder and its effect on the electrochemistry of K-O_2 cells has not been reported.

Different polymeric binders (CMC, PTFE and PVDF – chemical structure shown in Figure 4.28) were used to cast carbon black cathodes (Timcal Super C 65, 62 $m^2 g^{-1}$). K-O_2 cells were assembled in conjunction with a 0.25 M KPF_6 in DME electrolyte and underwent galvanostatic discharge and spectroscopic analyses (Figure 5.28). A binder-free carbon fibre (Avcarb, P50) was used for comparison.

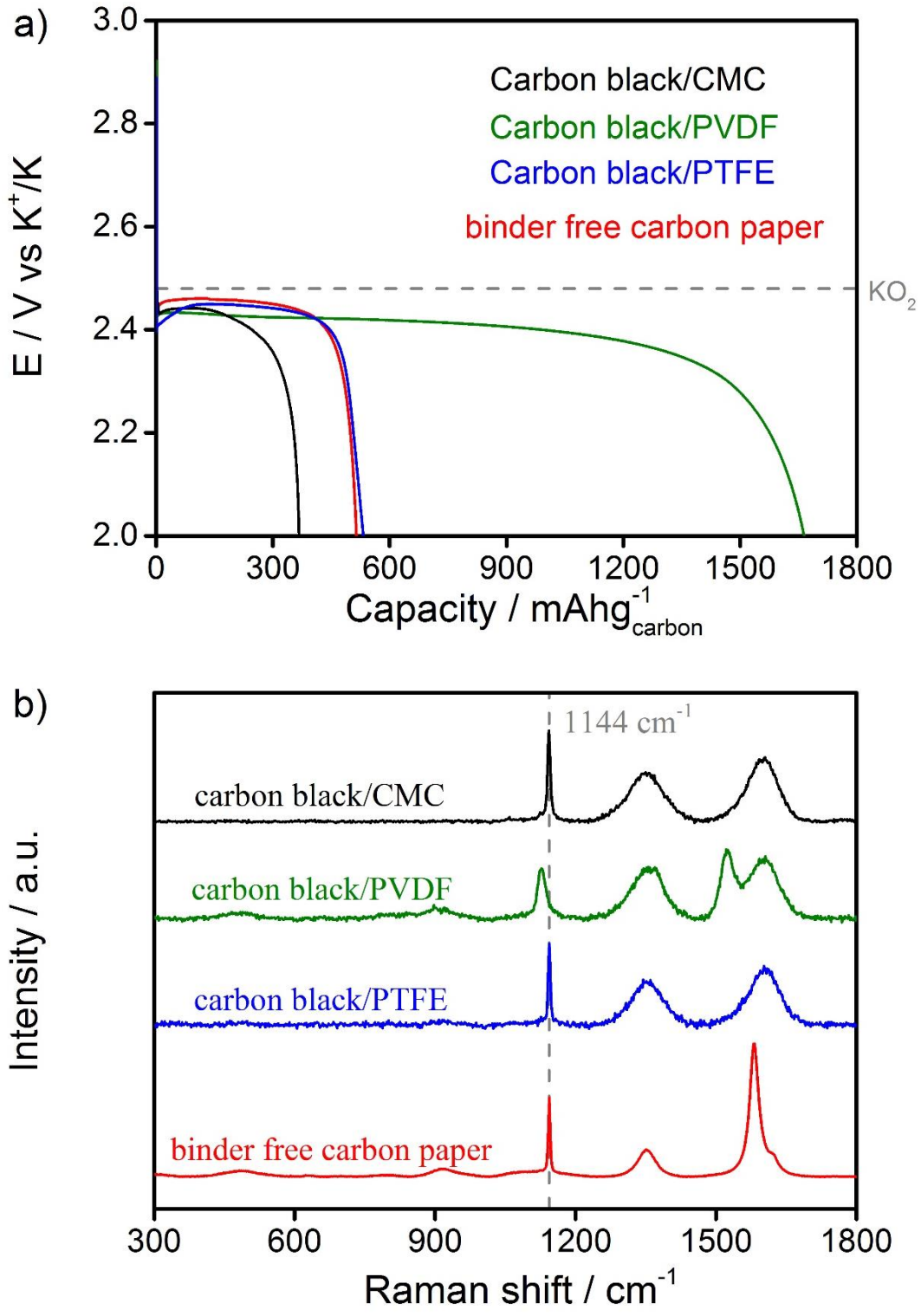

Figure 5.28: a) Electrochemical data at 0.12 mA cm^{-2} of K-O_2 cells discharged using carbon black cathodes cast with different polymeric binders using a 0.25 M KPF_6 in DME electrolyte. b) Raman spectra of discharged carbon black cathodes cast with different polymeric binders.

The discharge profiles obtained already shows differences from sodium systems. The KO_2 cell using carbon black/PVDF, as well as the other cells, presents a flat plateau discharge indicative of a single electrochemical reaction. This contrast with its behaviour in Na-O_2 cells where a descending curve was obtained.

The main reaction product for the carbon black/PTFE cell and the carbon black/CMC cell was the desired KO_2, as evidenced by the O-O symmetric stretching mode of the superoxide anion visible at 1144 cm^{-1}. This suggest stability of PTFE and CMC during K-O_2 cells operation, in agreement with previous literature[72, 73].

The Raman spectrum of the discharged carbon black/PVDF cathode shows additional bands at 1127 cm^{-1} and 1522 cm^{-1}. The assignment of these extra Raman bands visible in discharge Li-O_2 cathodes has been debated on the literature. Lu *et al.*[74] reported similar broad signals corresponding to the superoxide stretch in LiO_2 (at 1123 cm^{-1}) and to the interaction between LiO_2 and the graphitic carbon (1505 cm^{-1}). Unlike Lu, Papp *et al.*[75] assigned these bands to degradation of PVDF binder via $O_2^{\bullet-}$ induced hydrogen abstraction. However, Galloway *et al.*[76, 77] observed the νC-O_2Li signal at 1520 cm^{-1} using binder free glassy carbon electrodes and PTFE based carbon black electrodes.

In K-O_2 cells, the one-electron per oxygen reduction is the main cell chemistry observed using different binders, therefore, the νC-O_2Li signal should be also expected for the carbon black/PTFE and carbon black/CMC cells. The additional Raman bands observed on the spectra discharged carbon black/PVDF cathodes are also observed when PVDF powder reacts with KOH (Figure 5.29) promoting a dehydroflurionation reaction described on the literature[78]. The

mechanism of PVDF degradation in K-O_2 cells is analogous to Na-O_2 systems (see Scheme 4.4).

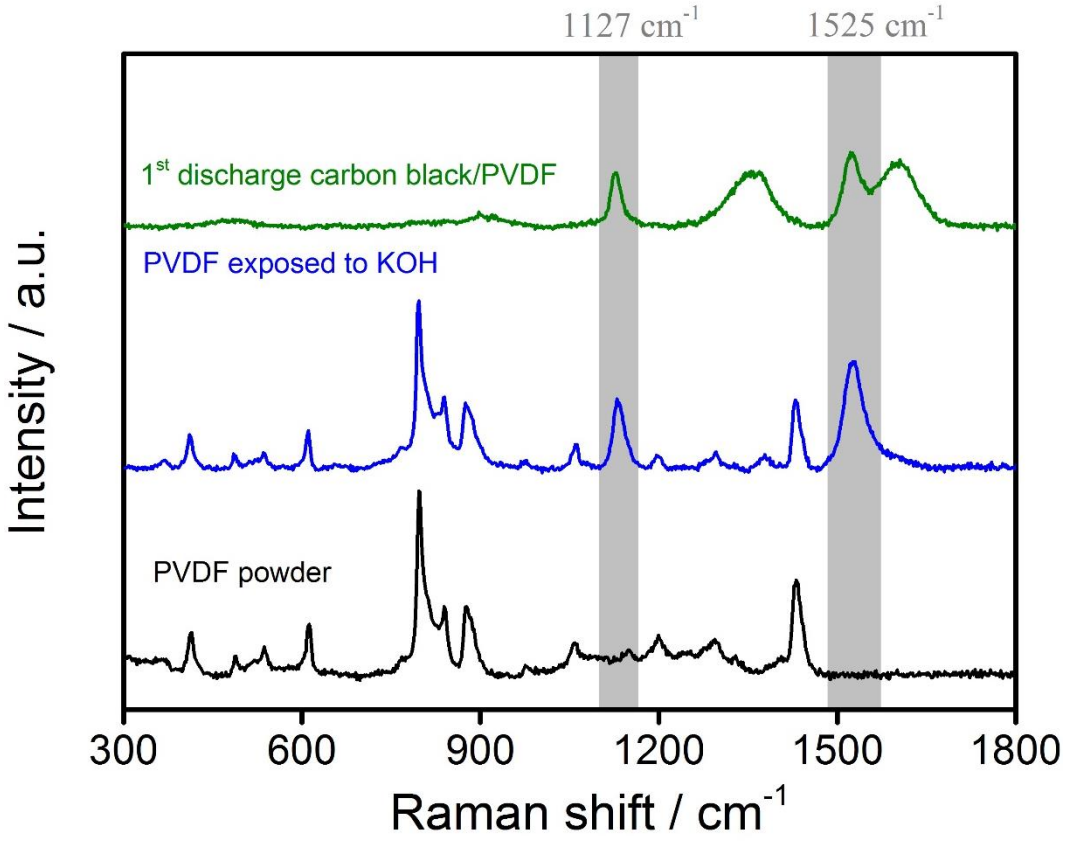

Figure 5.29: Comparison of the discharged carbon black/PVDF cathode Raman analysis with Raman spectrum of PVDF powder and PVDF exposed to KOH.

Furthermore, a Raman mapping of the three polymeric binder carbon cathodes after discharge shows a constant ratio between the carbon D and G bands. The ratio of intensity of D and G bands is a measure of disorder degree of the carbon material. The G corresponds to the in-plane motion of sp^2 C atoms in the graphitic ring and chains[79]. Therefore, a LiO_2 induced distortion of the graphitic ring, as reported by Lu *et al.*[74], would have an effect on the I_D/I_G ratio of the discharge cathode, which is not observed (Table 5.1).

Table 5.1: Intensity ratio of D and G Raman bands in discharged carbon black cathodes using different polymeric binders.

Cathode	I_D/I_G
Carbon black/CMC	0.97
Carbon black/PVDF	0.97
Carbon black/PTFE	0.95

Supplementary characterisation of the carbon black/PVDF cathode was performed by PXRD (Figure 5.30) and SEM (Figure 5.31) after one discharge process. PXRD data shows that, despite the PVDF degradation observed on the Raman spectrum, KO_2 is the main discharge product of the cell. This is corroborated by SEM images of the discharged carbon black/PVDF cathode showing micron-sized cubic particles similar to the discharge product morphology on the CMC and PTFE cathode.

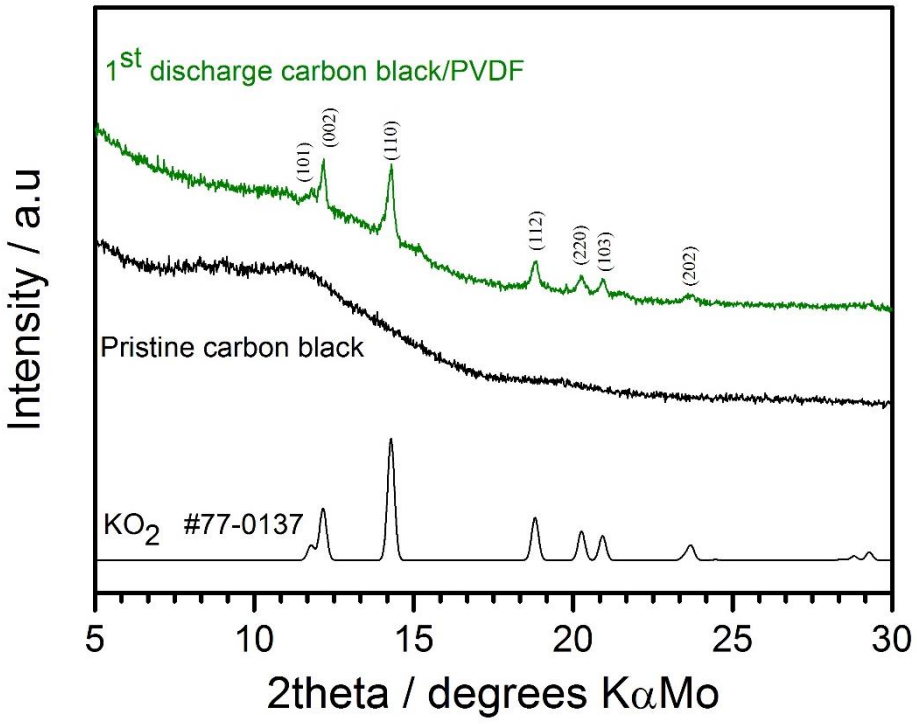

Figure 5.30: PXRD characterisation of a discharged carbon black/PVDF cathode in a K-O_2 cell using a 0.25 M KPF_6 in DME electrolyte.

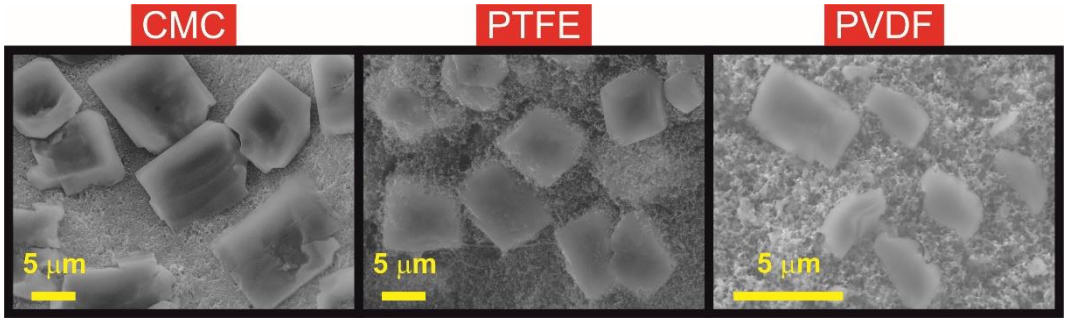

Figure 5.31: SEM micrographs of the discharge products obtained in K-O_2 cells using carbon black cathodes cast with different polymer binders in combination with a 0.25 M KPF_6 in DME electrolyte.

The formation of KO_2 despite PVDF binder degradation is in stark contrast to Na-O_2 cells using the same carbon black/PVDF cathode in analogous ether-based electrolytes (Chapter 4, Figure 4.31). For sodium systems NaO_2 was not formed upon discharge, instead, Na_2CO_3, CH_3COONa and NaOH were detected as a result of binder and electrolyte degradation (see Figure 4.31).

This is evidence of the higher stability of KO_2 in ether-based electrolytes, as it does not undergoes the same dissolution/ionisation process[80] as NaO_2, resulting in the formation of $Na_2O_2{\cdot}2H_2O$. Raman spectra taken of discharge cathodes in K-O_2 cells after 12 hours resting period (see Appendix B, Figure B9) shows the same superoxide anion stretch vibration and the formation of $K_2O_2 \cdot 2H_2O$ was not detected. This is a result of the lower solubility of KO_2 in glyme solvents[81], which triggers the ionisation process that causes a shift in the Raman spectra[80]. For analogous Na-O_2 cells, the solubility of NaO_2 was reported by Hartmann *et al.*[70].

Furthermore, Li_2O_2 (the desired reaction product) was detected during oxygen reduction upon discharge of Li-O_2 cells despite of PVDF binder degradation[72]. Li_2O_2 is also insoluble in ether-based electrolytes[82].

5.4.8 Effect of the carbon air-cathode

The requirements to design better a positive electrode (also referred as air-cathode) in K-O_2 cells are analogous to other alkali metal-oxygen cells. The challenges to overcome arise KO_2, the main reaction product of the cell, being a strong oxidiser[83], insoluble in ether solvents[81] and a wide band gap semiconductor[3]. Therefore, the ideal cathode architecture must be able to accommodate the insoluble discharge product whilst still providing available conductive surface for O_2 transport and reduction. In contrast to Li-O_2 cells and NaO_2 cells, only the solution route mechanism, which results in the growth of large cubic particles, has been observed upon discharge of K-O_2 cell, making the pore volume of the electrode more important than surface area[84, 85].

A significant issue associated the charge process of Li-O_2 cells is the auto-oxidation of the carbon electrode, observed at potentials above 3.5 V vs Li^+/Li[10], which results in the accumulation of parasitic product that limit cycle life. For K-O_2 cells however, the fast, reversible, reaction of the KO_2/O_2 redox couple results in low charge polarisation, making carbon a viable positive electrode material.

A study to determine the effect of the carbon material in the positive electrode on the reaction chemistry and performance of K-O_2 cells was carried out. Five different electrodes were compared: a gas diffusion layer (H24, Freudenberg & Co.), a carbon paper (P50, Avcarb), a commercial single wall carbon nanotube (SW CNT), two conductive carbon black (Ketjenblack EC 600 JD, AkzoNobel and Super C65, Imerys). Self-supporting carbon black and SW CNT electrodes were prepared using PTFE binder (80% active material, 20% binder). K-O_2 cells were

assembled using a 0.25 M KPF_6 in DME electrolyte and underwent galvanostatic discharge at 0.12 mA cm^{-2} current density. Subsequent analysis of the reaction products of the cell were performed via Raman spectroscopy and SEM.

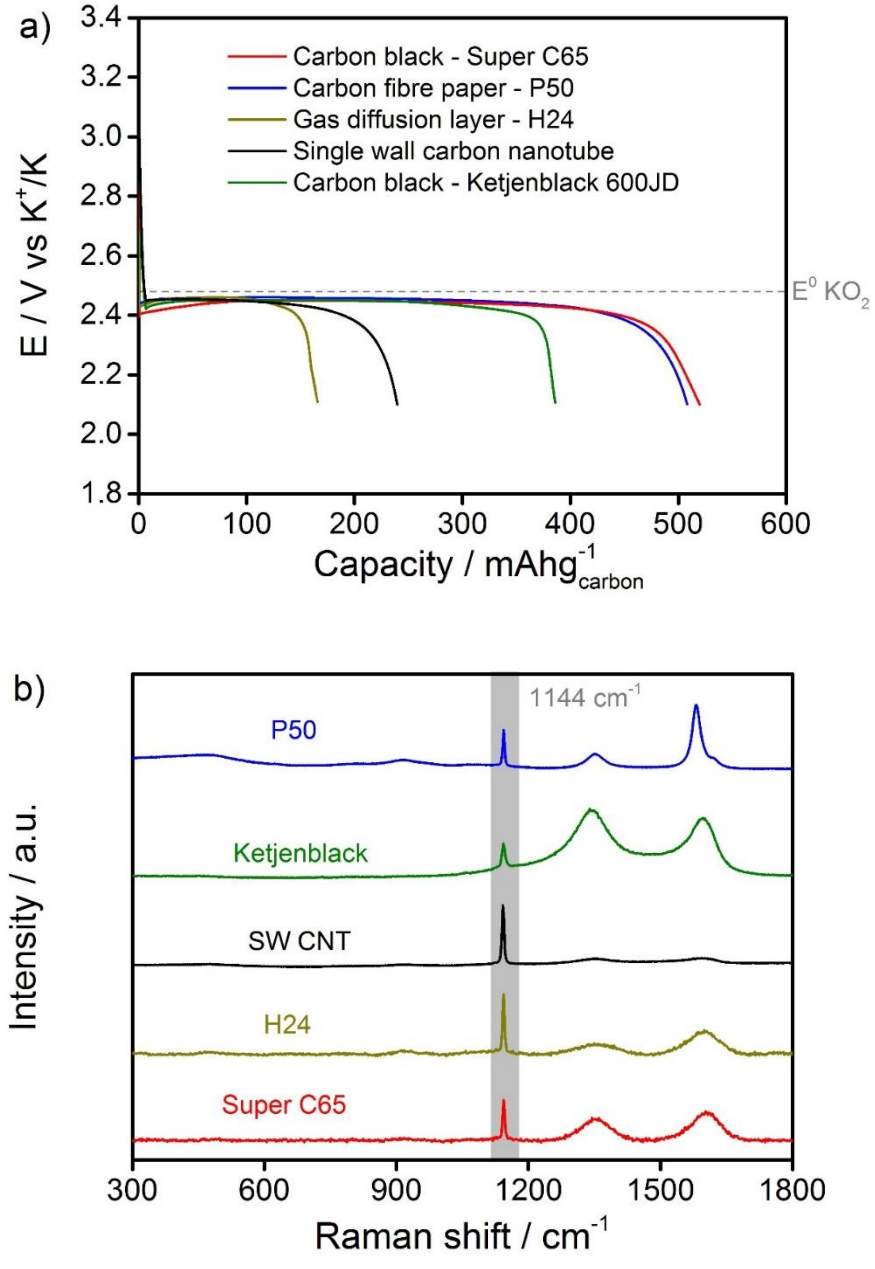

Figure 5.32: a) Electrochemical data at 0.12 mA cm^{-2} of K-O_2 cells discharged using different carbon cathodes using a 0.25 M KPF_6 in DME electrolyte. b) Raman spectra of discharged cells with different carbon cathodes.

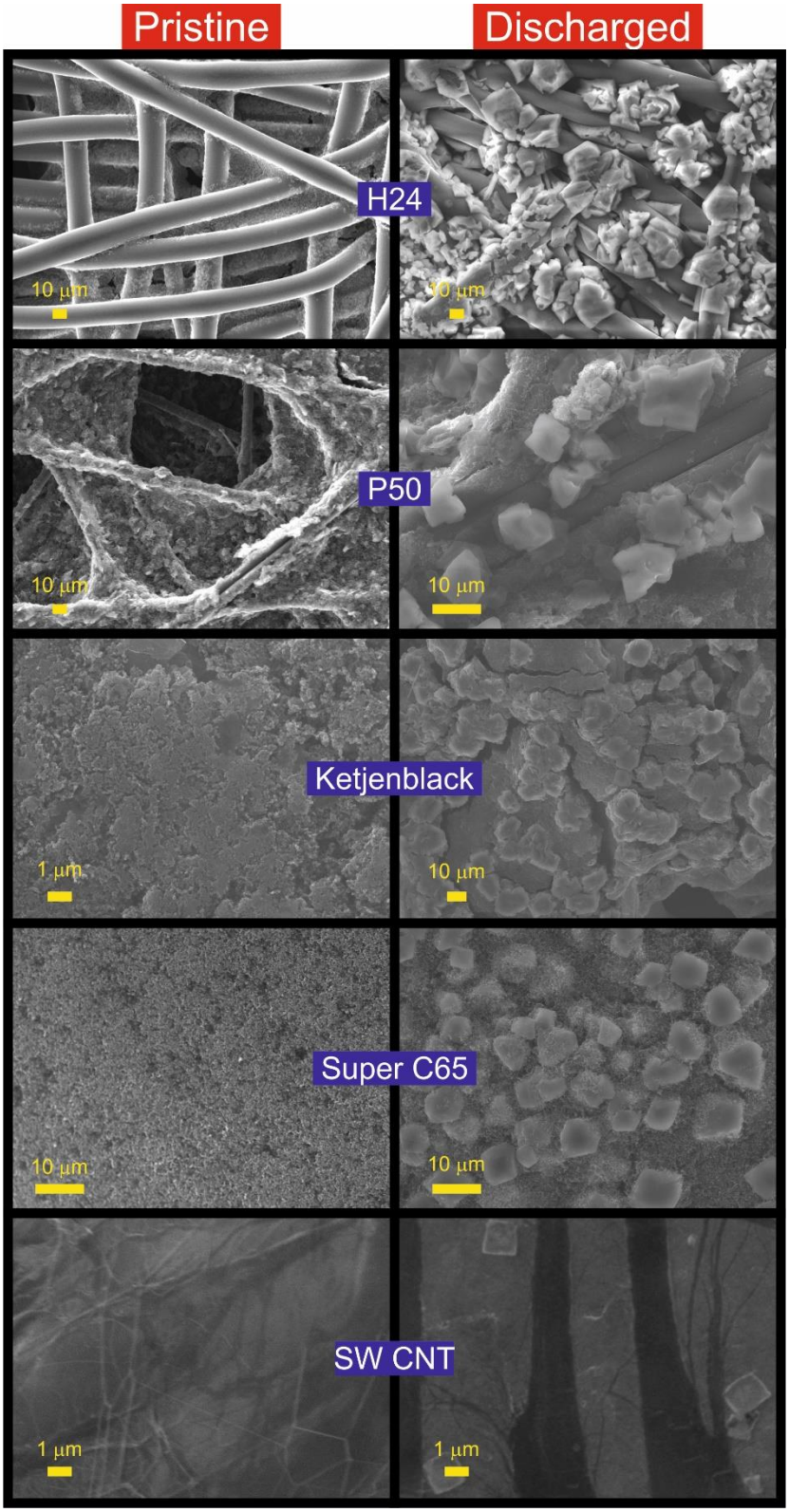

Figure 5.33: SEM images of pristine and discharged carbon electrodes in K-O_2 cells using a 0.25 M KPF_6 in DME electrolyte at 0.12 mA cm^{-2}.

The discharge profiles shown in Figure 5.32a are similar for carbon electrodes covering a wide range of properties. The oxygen reduction happens at low overpotential for all cells (~30 mV) as a result of the faster kinetics of O_2^- in solutions with cations of lower charge density, and is comparable to other reports on the literature[1, 65].

The type of carbon was found to have no influence at all in the reaction chemistry of the cells. Raman spectroscopy analysis of the carbon surface after discharge (Figure 5.32b) shows only the 1144 cm^{-1} superoxide ion stretching peak in KO_2, indicating that the cell chemistry follows a one-electron per oxygen reduction. The formation of KO_2 upon discharge of the different carbon cathode cells was further confirmed by SEM analysis (Figure 5.33). Only cubic shaped particles were observed on the surface of the carbon substrates, independent of the type of carbon. This is in good agreement with a report by Xiao *et al.*[65] in ether-based K-O_2 cells.

Evidence for electrolyte degradation products, such as K_2CO_3 and HCO_2K, was not detected on the Raman analysis, which is in line with reports of Li- and Na-O_2 systems where the same electrolyte degradation products were reported for different carbon cathodes. The type of carbon does have an effect on oxidative decomposition, however, this is not observed in K-O_2 cells.

In contrast to Na-O_2 cells, the one-electron formation of KO_2 was observed for the SW CNT cell. The CNT structure in the positive electrode has been reported to induce O_2 diffusion blockage at the open ends, creating regions of local low oxygen saturation[85]. This characteristic explained the two-electron formation of Na_2O_2 in Na-O_2 cells using SW CNT cathode (Figure 4.35), since peroxide is the

stable phase at low O_2 partial pressure[86]. In K-O_2 cells however, KO_2 is the thermodynamically stable compound as the superoxide phase stability increases going down the periodic table[68, 87]. A KO_2 based K-O_2 battery is more desirable aiming for high rate capability devices, due to the kinetically favoured one-electron process[88].

A direct correlation between carbon surface area and cell capacity was not obtained for the electrodes evaluated (Table 5.2). The carbon black (Ketjenblack) electrode, which presented the highest capacity in Na-O_2 cells (Figure 4.33) attributed to its high surface area and mesopore volume, was found to have one of the lowest capacities. The highest gravimetric capacity was obtained for the cathode with the highest mass loading (P50).

Table 5.2: Mass loading, BET surface area and average discharge capacities for the five carbon cathodes tested in K-O_2 cells.

Carbon	m (mg)	BET ($m^2 g^{-1}$)	Q (mAh)	Q (mAh g^{-1})	Q (mAh cm^{-2})
Super C65	2.2	62	1.2	532	1.5
P50	4.5	10	2.3	508	2.9
H24	11	1	1.8	166	2.3
SW CNT	1.9	700	0.5	244	0.64
Ketjenblack	1.6	1454	0.6	386	2.12

The inconsistency of the maximum achieved capacity and the carbon properties in the positive electrode are attributed to instabilities related to reactive metal anode. As discussed in section 5.4.2, the growth of a passivating layer as a result of oxygen crossover and C-O bond cleavage in the ether electrolyte increases the internal resistivity of the cells and ultimately terminates the discharge process.

To illustrate that, Figure 5.34 shows a SW CNT cathode cell which underwent full discharge, at 0.12 mA cm^{-2} current density, achieving a specific capacity of 244 mAh g^{-1}. The cell was disassembled inside an argon filled glove box, and the anode, which was covered by a yellow surface layer, was replaced by a fresh K metal anode. The cell underwent a consecutive discharge recovering the same OOR overpotential. An additional 241 mAh g^{-1} capacity is obtained until the metal anode is again passivated blocking electron transfer though the cells. Thus, proving that the anode reactivity is indeed responsible for the early cell death.

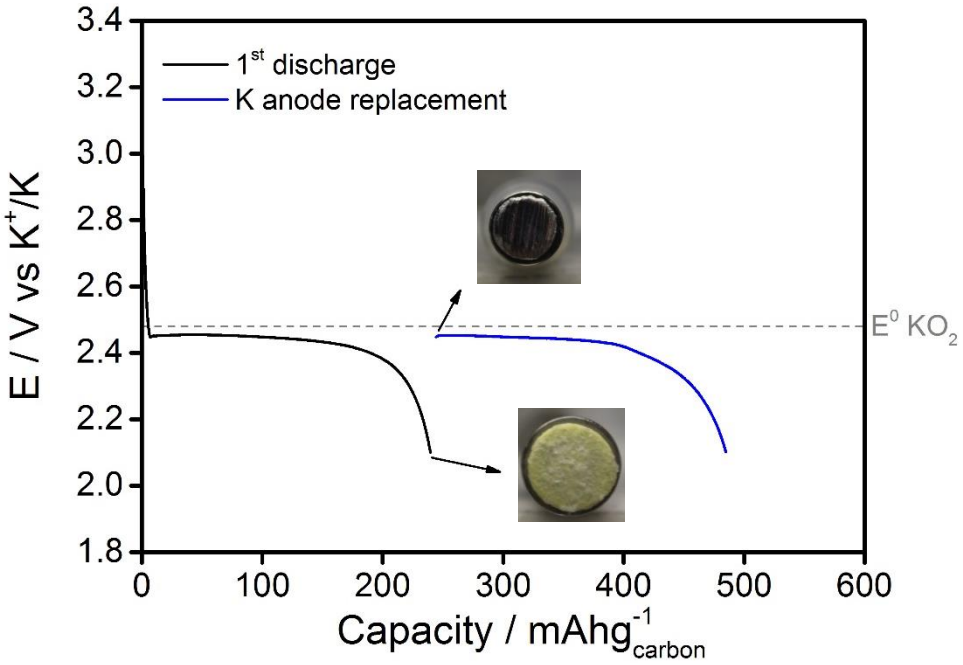

Figure 5.34: Electrochemical data at 0.12 mA cm^{-2} of a K-O_2 cells discharged using a SW CNT cathode and a 0.25 M KPF_6 in DME electrolyte. A fresh K metal anode was replaced after the first discharge. Inset shows photographs of the metal anodes.

Moreover, using the carbon fibre cathode (P50) as an example, based on the electrode dimensions (0.785 cm^2 x 0.013 cm, 80% porosity), the density of KO_2 (ρ= 2.14 g cm^{-3}), the cell's capacity (508 mAh g^{-1} – Figure 5.32a) and assuming the

one-electron per O_2 reduction reaction (Eq. 5.1), only 13% of the maximum theoretical capacity is achieved. This indicates a substandard exploitation of the cathode available reactive surface.

5.5 Conclusions and future work

In summary, ether-based K-O_2 cells followed a one-electron per oxygen reduction as the main reaction chemistry. The formation of phase-pure KO_2 was demonstrated via *ex situ* Raman and PXRD analysis of the carbon cathode. Highly reversible cells were obtained (~ 95%) as a result of the stability of the $O_2^{\bullet -}$ in electrolytes containing the low density K^+ cation, based on the HSAB theory. Electrolyte degradation products (K_2CO_3 and HCO_2K) in a minor extent were detected by FTIR as a result of hydrogen abstraction on the ether molecule by the superoxide radical anion.

The effect of current density was evaluated and K-O_2 cells retained high coulombic efficiency at high rates due to faster kinetics of the O_2/KO_2 redox couple. Increasing current density did not influence the discharge product chemistry and morphology as solely KO_2 was detected. The KO_2 crystal average size had an inverse proportion with current density. This indicates that the discharge mechanism undergoes a solution route, which contrast to the observation of Na-O_2 cell, in which a mixed solution and surface confined route is obtained. The solution route is favourable aiming for high capacity cells, as the surface confined route can lead to the passivation of the carbon surface.

The stability of different polymeric binders commonly used to cast air-cathode for alkali metal-oxygen cells was investigated. The degradation of PVDF in the K-O_2 cell environment by $O_2^{\bullet -}$ induced dehydroflurionation reaction was observed on the Raman characterisation. In contrast to Na-O_2 cells, the desired one-electron per oxygen reduction process was demonstrated by PXRD analysis despite

of binder degradation. This is attributed to the higher stability of KO_2, for which a dissolution/ionisation process, resulting in hydrated species, was not observed. The Raman spectrum of the discharged carbon black/PVDF cathode showed additional bands at 1127 cm^{-1} and 1522 cm^{-1} which are assigned to binder degradation, instead of superoxide interaction with the graphitic ring of the carbon electrode.

The K metal anode reactivity with the ether solvent and O_2 molecules dissolved in the electrolyte was found to limit discharge capacity and cyclability of K-O_2 cells, resulting in the formation of an insulating surface layer on the metal anode. K_2CO_3, KOH and KO_2 were determined as the main components of the surface layer when using KPF_6 and KOTf in DME electrolytes. When using a KFSI in DME electrolyte, the cell was not successfully recharged due to the formation of a KF insulating layer on the carbon surface.

When a KTFSI in DME electrolyte was employed, a protective, O_2 impermeable, layer was formed as KO_2 was no longer detected on the anode surface. The protective layer composition was found to be mixture of DME degradation (K_2CO_3, KOH) and KTFSI degradation (K_2SO_4, K_2SO_3 and KF).

Enhanced battery cycling was obtained for a highly concentrated KTFSI electrolyte and a blended electrolytes containing [PYR14][KTFSI] and DME. The protective layer was eventually disrupted by the consecutive stripping/plating cycles resulting in oxygen crossover. Further work needs to be carried out to increase the cycleable capacity to more appealing values, whilst maintaining the stability of the protective SEI.

An antimony-carbon nanocomposite was investigated as a potential anode material for safer, long cycling, K-O_2 cells. The ball milled antimony presented

good electrochemical performance with initial discharge capacity of 649 mAh g^{-1}_{Sb}, corresponding to 98% of the maximum theoretical capacity. The improved cyclability obtained for the nanocomposite (84% after 200 galvanostatic cycles), is related to the buffer effect of the carbon matrix on the volume expansion of antimony particles. At high rates, the material remained high reversible alloying reaction and a rate capability of 22% at 8C was obtained.

Insight into the alloying reaction between antimony and carbon was provided by *in situ* Raman. Upon potassiation of the Sb-C nanocomposite, the Raman peak at 152 cm^{-1} (related to longitudinal Sb-Sb vibration) does not completely fade, possibly indicating the formation of underpotassiated species. The depotassiation reaction was not possible to be followed through *in situ* Raman characterisation due to electrolyte interference. Further work needs to be carried out to determine whether the long range order is recovered upon charge. A proof of concept K-O_2 cell using a K_3Sb anode and a carbon cathode was successfully cycled with the formation of the desired KO_2 product, encouraging further research on this anode material.

5.6 References

1. X. Ren and Y. Wu, *J. Am. Chem. Soc*, 2013, **135**, 2923-2926.
2. X. Ren, K. C. Lau, M. Yu, X. Bi, E. Kreidler, L. A. Curtiss and Y. Wu, *ACS Appl. Mater. Inter.*, 2014, **6**, 19299-19307.
3. A. U. Khan and S. Mahanti, *J. Chem. Phys.*, 1975, **63**, 2271-2278.
4. C. O. Laoire, S. Mukerjee, K. Abraham, E. J. Plichta and M. A. Hendrickson, *J. Phys. Chem. C*, 2010, **114**, 9178-9186.
5. I. Landa-Medrano, M. Olivares-Marín, B. Bergner, R. Pinedo, A. Sorrentino, E. Pereiro, I. Ruiz de Larramendi, J. r. Janek, T. Rojo and D. Tonti, *J. Phys. Chem. C*, 2017, **121**, 3822-3829.
6. S. Matsuda, Y. Kubo, K. Uosaki and S. Nakanishi, *J. Phys. Chem. Lett.*, 2017, **8**, 1142-1146.
7. S. A. Freunberger, Y. Chen, N. E. Drewett, L. J. Hardwick, F. Bardé and P. G. Bruce, *Angew. Chem. -Int. Edit.*, 2011, **50**, 8609-8613.
8. P. Adelhelm, P. Hartmann, C. L. Bender, M. Busche, C. Eufinger and J. Janek, *Beilstein J. Nanotechno.*, 2015, **6**, 1016.
9. S. A. Freunberger, Y. Chen, Z. Peng, J. M. Griffin, L. J. Hardwick, F. Bardé, P. Novák and P. G. Bruce, *J. Am. Chem. Soc*, 2011, **133**, 8040-8047.
10. M. M. Ottakam Thotiyl, S. A. Freunberger, Z. Peng and P. G. Bruce, *J. Am. Chem. Soc*, 2012, **135**, 494-500.
11. F. Halverson, *J. Phys. Chem. Solids*, 1962, **23**, 207-214.
12. D. Sharon, D. Hirshberg, M. Afri, A. A. Frimer, M. Noked and D. Aurbach, *J. Solid State Electrochem.*, 2017, 1-18.
13. R. Black, A. Shyamsunder, P. Adeli, D. Kundu, G. K. Murphy and L. F. Nazar, *ChemSusChem*, 2016, **9**, 1795-1803.
14. C. R. Birkl, M. R. Roberts, E. McTurk, P. G. Bruce and D. A. Howey, *J. Power Sources*, 2017, **341**, 373-386.
15. L. Johnson, C. Li, Z. Liu, Y. Chen, S. A. Freunberger, P. C. Ashok, B. B. Praveen, K. Dholakia, J.-M. Tarascon and P. G. Bruce, *Nat. Chem.*, 2014, **6**, 1091-1099.

16. I. M. Aldous and L. J. Hardwick, *Angew. Chem. -Int. Edit.*, 2016, **55**, 8254-8257.
17. Z. Peng, S. A. Freunberger, Y. Chen and P. G. Bruce, *Science*, 2012, **337**, 563-566.
18. W. Walker, V. Giordani, J. Uddin, V. S. Bryantsev, G. V. Chase and D. Addison, *J. Am. Chem. Soc*, 2013, **135**, 2076-2079.
19. P. E. Mason, T. Buttersack, S. Bauerecker and P. Jungwirth, *Angew. Chem. -Int. Edit.*, 2016, **55**, 13019-13022.
20. F. Dainton, D. Wiles and A. Wright, *J. Chem. Soc.*, 1960, 4283-4289.
21. R. S. Assary, J. Lu, P. Du, X. Luo, X. Zhang, Y. Ren, L. A. Curtiss and K. Amine, *ChemSusChem*, 2013, **6**, 51-55.
22. X. B. Cheng, R. Zhang, C. Z. Zhao, F. Wei, J. G. Zhang and Q. Zhang, *Adv. Sci.*, 2016, **3**.
23. L. Lutz, D. Alves Dalla Corte, M. Tang, E. Salager, M. Deschamps, A. Grimaud, L. Johnson, P. G. Bruce and J.-M. Tarascon, *Chem. Mater.*, 2017, **29**, 6066-6075.
24. D. Sharon, D. Hirsberg, M. Salama, M. Afri, A. A. Frimer, M. Noked, W. Kwak, Y.-K. Sun and D. Aurbach, *ACS Appl. Mater. Inter.*, 2016, **8**, 5300-5307.
25. H. Kim, F. Wu, J. T. Lee, N. Nitta, H. T. Lin, M. Oschatz, W. I. Cho, S. Kaskel, O. Borodin and G. Yushin, *Adv. Energy Mater.*, 2015, **5**.
26. N. Xiao, W. D. McCulloch and Y. Wu, *J. Am. Chem. Soc*, 2017, **139**, 9475-9478.
27. G. G. Eshetu, S. Grugeon, G. Gachot, D. Mathiron, M. Armand and S. Laruelle, *Electrochim. Acta*, 2013, **102**, 133-141.
28. G. Socrates, *Infrared and Raman characteristic group frequencies: tables and charts*, John Wiley & Sons, 2004.
29. X. Ren, M. He, N. Xiao, W. D. McCulloch and Y. Wu, *Adv. Energy Mater.*, 2017, **7**.
30. Y. Yamada and A. Yamada, *J. Electrochem. Soc.*, 2015, **162**, A2406-A2423.

31. J. Qian, W. A. Henderson, W. Xu, P. Bhattacharya, M. Engelhard, O. Borodin and J.-G. Zhang, *Nat. Commun.*, 2015, **6**.
32. R. Cao, K. Mishra, X. Li, J. Qian, M. H. Engelhard, M. E. Bowden, K. S. Han, K. T. Mueller, W. A. Henderson and J.-G. Zhang, *Nano Energy*, 2016, **30**, 825-830.
33. S. Wen, T. Richardson, D. Ghantous, K. Striebel, P. Ross and E. Cairns, *J. Electroanal. Chem.*, 1996, **408**, 113-118.
34. I. Rey, P. Johansson, J. Lindgren, J. Lassegues, J. Grondin and L. Servant, *J. Phys. Chem. A*, 1998, **102**, 3249-3258.
35. M. Armand, F. Endres, D. R. MacFarlane, H. Ohno and B. Scrosati, *Nat. Mater.*, 2009, **8**, 621-629.
36. T. Zhang and Z.-Y. Wen, *J. Phys. Chem. C*, 2017, **121**, 5968-5973.
37. J. Xie, Q. Dong, I. Madden, X. Yao, Q. Cheng, P. Dornath, W. Fan and D. Wang, *Nano Lett.*, 2015, **15**, 8371-8376.
38. A. R. Neale, P. Goodrich, T.-L. Hughes, C. Hardacre, S. C. Ball and J. Jacquemin, *J. Electrochem. Soc.*, 2017, **164**, H5124-H5134.
39. C. J. Allen, J. Hwang, R. Kautz, S. Mukerjee, E. J. Plichta, M. A. Hendrickson and K. Abraham, *J. Phys. Chem. C*, 2012, **116**, 20755-20764.
40. M. Piana, J. Wandt, S. Meini, I. Buchberger, N. Tsiouvaras and H. A. Gasteiger, *J. Electrochem. Soc.*, 2014, **161**, A1992-A2001.
41. J. Hassoun, H.-G. Jung, D.-J. Lee, J.-B. Park, K. Amine, Y.-K. Sun and B. Scrosati, *Nano Lett.*, 2012, **12**, 5775-5779.
42. Z. Guo, X. Dong, Y. Wang and Y. Xia, *Chem. Commun.*, 2015, **51**, 676-678.
43. G. A. Elia, D. Bresser, J. Reiter, P. Oberhumer, Y.-K. Sun, B. Scrosati, S. Passerini and J. Hassoun, *ACS Appl. Mater. Inter.*, 2015, **7**, 22638-22643.
44. J. Chun, H. Kim, C. Jo, E. Lim, J. Lee and Y. Kim, *ChemPlusChem*, 2015, **80**, 349-353.
45. C. L. Bender, B. Jache, P. Adelhelm and J. Janek, *J. Mater. Chem.*, 2015, **3**, 20633-20641.
46. L. Baggetto, P. Ganesh, C.-N. Sun, R. A. Meisner, T. A. Zawodzinski and G. M. Veith, *J. Mater. Chem.*, 2013, **1**, 7985-7994.

47. A. Darwiche, C. Marino, M. T. Sougrati, B. Fraisse, L. Stievano and L. Monconduit, *J. Am. Chem. Soc*, 2012, **134**, 20805-20811.
48. W. Luo, J.-J. Gaumet and L.-Q. Mai, *Rare Metals*, 2017, 1-18.
49. J. Qian, Y. Chen, L. Wu, Y. Cao, X. Ai and H. Yang, *Chem. Commun.*, 2012, **48**, 7070-7072.
50. A. S. Aricò, P. Bruce, B. Scrosati, J.-M. Tarascon and W. Van Schalkwijk, *Nat. Mater.*, 2005, **4**, 366-377.
51. P. G. Bruce, B. Scrosati and J. M. Tarascon, *Angew. Chem. -Int. Edit.*, 2008, **47**, 2930-2946.
52. W. D. McCulloch, X. Ren, M. Yu, Z. Huang and Y. Wu, *ACS Appl. Mater. Inter.*, 2015, **7**, 26158-26166.
53. Z. Jian, W. Luo and X. Ji, *J. Am. Chem. Soc*, 2015, **137**, 11566-11569.
54. J. Sangster and A. Pelton, *J. Phase Equilib.*, 1993, **14**, 510-514.
55. N. E. Drewett, I. M. Aldous, J. Zou and L. J. Hardwick, *Electrochim. Acta*, 2017, **247**, 296-305.
56. Z. Jian, Z. Xing, C. Bommier, Z. Li and X. Ji, *Adv. Energy Mater.*, 2016, **6**.
57. O. Degtyareva, V. V. Struzhkin and R. J. Hemley, *Solid State Commun.*, 2007, **141**, 164-167.
58. P. K. Allan, J. M. Griffin, A. Darwiche, O. J. Borkiewicz, K. M. Wiaderek, K. W. Chapman, A. J. Morris, P. J. Chupas, L. Monconduit and C. P. Grey, *J. Am. Chem. Soc*, 2016, **138**, 2352-2365.
59. V. Viswanathan, J. Nørskov, A. Speidel, R. Scheffler, S. Gowda and A. Luntz, *J. Phys. Chem. Lett.*, 2013, **4**, 556-560.
60. A. J. Bard, L. R. Faulkner, J. Leddy and C. G. Zoski, *Electrochemical methods: fundamentals and applications*, wiley New York, 1980.
61. N. Ortiz-Vitoriano, T. P. Batcho, D. G. Kwabi, B. Han, N. Pour, K. P. C. Yao, C. V. Thompson and Y. Shao-Horn, *J. Phys. Chem. Lett.*, 2015, **6**, 2636-2643.
62. M. Safari, B. Adams and L. Nazar, *J. Phys. Chem. Lett.*, 2014, **5**, 3486-3491.
63. B. D. Adams, C. Radtke, R. Black, M. L. Trudeau, K. Zaghib and L. F. Nazar, *Energy Environ. Sci.*, 2013, **6**, 1772-1778.

64. N. Zhao, C. Li and X. Guo, *Phys. Chem. Chem. Phys.*, 2014, **16**, 15646-15652.
65. N. Xiao, X. Ren, M. He, W. D. McCulloch and Y. Wu, *ACS Appl. Mater. Inter.*, 2016, **9**, 4301-4308.
66. H. Yadegari, Y. Li, M. N. Banis, X. Li, B. Wang, Q. Sun, R. Li, T.-K. Sham, X. Cui and X. Sun, *Energy Environ. Sci.*, 2014, **7**, 3747-3757.
67. G. F. Carter and D. Templeton, *J. Am. Chem. Soc*, 1953, **75**, 5247-5249.
68. O. Gerbig, R. Merkle and J. Maier, *Adv. Funct. Mater.*, 2015, **25**, 2552-2563.
69. Y. N. Zhuravlev, N. Kravchenko and O. Obolonskaya, *Russ. J. Phys. Chem. B*, 2010, **4**, 20-28.
70. P. Hartmann, M. Heinemann, C. L. Bender, K. Graf, R.-P. Baumann, P. Adelhelm, C. Heiliger and J. r. Janek, *J. Phys. Chem. C*, 2015, **119**, 22778-22786.
71. K. B. Knudsen, J. E. Nichols, T. Vegge, A. C. Luntz, B. D. McCloskey and J. Hjelm, *J. Phys. Chem. C*, 2016, **120**, 10799-10805.
72. R. Black, S. H. Oh, J.-H. Lee, T. Yim, B. Adams and L. F. Nazar, *J. Am. Chem. Soc*, 2012, **134**, 2902-2905.
73. E. Nasybulin, W. Xu, M. H. Engelhard, Z. Nie, X. S. Li and J.-G. Zhang, *J. Power Sources*, 2013, **243**, 899-907.
74. J. Lu, Y. J. Lee, X. Luo, K. C. Lau, M. Asadi, H.-H. Wang, S. Brombosz, J. Wen, D. Zhai and Z. Chen, *Nature*, 2016, **529**, 377-382.
75. J. K. Papp, J. D. Forster, C. M. Burke, H. W. Kim, A. C. Luntz, R. M. Shelby, J. J. Urban and B. D. McCloskey, *J. Phys. Chem. Lett.*, 2017, **8**, 1169-1174.
76. T. A. Galloway and L. J. Hardwick, *J. Phys. Chem. Lett.*, 2016, **7**, 2119-2124.
77. T. A. Galloway, L. Cabo-Fernandez, I. Aldous, F. Braga and L. Hardwick, *Faraday Discuss.*, 2017.
78. G. Ross, J. Watts, M. Hill and P. Morrissey, *Polymer*, 2000, **41**, 1685-1696.
79. A. C. Ferrari and J. Robertson, *Phys. Rev. B*, 2000, **61**, 14095.

80. J. Kim, H. Park, B. Lee, W. M. Seong, H.-D. Lim, Y. Bae, H. Kim, W. K. Kim, K. H. Ryu and K. Kang, *Nat. Commun.*, 2016, **7**.
81. K. U. Schwenke, S. Meini, X. Wu, H. A. Gasteiger and M. Piana, *Phys. Chem. Chem. Phys.*, 2013, **15**, 11830-11839.
82. G. Girishkumar, B. McCloskey, A. Luntz, S. Swanson and W. Wilcke, *J. Phys. Chem. Lett.*, 2010, **1**, 2193-2203.
83. M. Hayyan, M. A. Hashim and I. M. AlNashef, *Chem. Rev.*, 2016, **116**, 3029-3085.
84. S. Meini, M. Piana, H. Beyer, J. Schwämmlein and H. A. Gasteiger, *J. Electrochem. Soc.*, 2012, **159**, A2135-A2142.
85. N. Ding, S. W. Chien, T. A. Hor, R. Lum, Y. Zong and Z. Liu, *J. Mater. Chem.*, 2014, **2**, 12433-12441.
86. S. Kang, Y. Mo, S. P. Ong and G. Ceder, *Nano Lett.*, 2014, **14**, 1016-1020.
87. C. Knights and B. Phillips, *J. Nucl. Mater.*, 1979, **84**, 196-206.
88. J. Weiss, *Nature*, 1958, **181**, 825-826.

Chapter 6.
Conclusions and Future work

In the investigation of Li-O_2 systems, hypercrosslinked polymers based on benzene and pyrrole monomers were heat treated under different conditions and utilised to fabricate positive electrodes with varying properties. The utilisation of these materials in ether based Li-O_2 cells provided guidelines for the design of more efficient cathodes. The nitrogen heteroatom doping was found to have little effect on both cell capacity and electro activity towards the ORR/OER. The larger pore volume of the electrode allowed larger capacities to be obtained at lower cell polarisation.

A tertiary amine (DABCO) was utilised as an electrolyte additive in ether based Li-O_2 cells using typical carbon fibre cathodes. The addition of DABCO was found to have little effect on the discharge of the cell, whereby Li_2O_2 accompanied by common electrolyte degradation products were detected. During the charge process, however, a significant effect of reducing cell polarisation in 1 V was observed. The DABCO additive acts as a physical singlet oxygen quencher, mitigating parasitic reactions associated with the formation of this reactive intermediate. Therefore it can be concluded that the main reason for large voltage gaps observed in Li-O_2 cells is electrolyte/cathode degradation, rather than Li_2O_2 conductivity limitations.

Although Li-O_2 cells have not shown stable cycling, both hypercrosslinked polymer carbon cathodes and DABCO additives presented promising results. A

sensible future work on this system would be the integration of both materials in a Li-O_2 cell. Furthermore, potentially more stable electrolytes which promote a solution route mechanism could also be evaluated, such as DMSO. An interesting cell configuration would be the integration of DABCO with other redox mediators (such as 2,2,6,6-tetramethyl-1-piperidinyloxy – TEMPO), in a dual additive configuration, for which promising results have been reported in the literature.

In the investigation of Na-O_2 systems, insight into what drives the discharge of the cell to the formation of different reaction products was provided. NaO_2 was the main discharge product detected for the present cell configuration and its formation was observed even in organic carbonate electrolytes, which are known to be unstable against superoxide radical attack. In ether based electrolytes, NaO_2 underwent a dissolution/ionisation process resulting in the formation of $Na_2O_2{\cdot}2H_2O$, explaining some of the reports in the literature. This transition, however, should be avoided, as larger polarisation and lower coulombic efficiencies were obtained for the oxidation of $Na_2O_2{\cdot}2H_2O$. Na_2O_2 was detected when discharging Na-O_2 cells using carbon nanotube cathodes, for which limited oxygen diffusion favours the formation of the peroxide product, in agreement with the phase stability of this system reported in the literature.

Two reaction mechanism were found to compete during the galvanostatic discharge of Na-O_2 cells, a solution route (results in the formation of micron-sized cubic particles) and a surface confined route (results in film formation). Limited capacity and larger cell polarisation were obtained using TEGDME as the electrolyte solvent. Nano sized deposits were observed on the SEM images of discharged cathodes. This is an effect of the lower donor number and higher

chelating property of the solvent promoting the solution route mechanism. Using high current densities the same solution route was obtained with a significant amount of film formation approaching cell death. The film formation was investigated via AFM analysis, which provided valuable information regarding the nucleation process of the cell. Both the film and the cubic NaO_2 particles were found to be composed of nanometric agglomerates, for which the formation of superoxide is favoured based on lower surface energy, as reported in the literature. In general, the reaction pathway which induces film formation should be avoided in order to obtain high capacity devices.

The stability of PVDF, a commonly employed polymeric binder, was found to be a more significant issue in Na-O_2 cells compared to other alkali metal-oxygen systems. The investigation showed that carbon black cathodes cast with PVDF were completely covered with electrolyte degradation products, in contrast to other binders which allowed the reversible formation/decomposition of NaO_2. In Li-O_2 and K-O_2 cells using PVDF to cast carbon black cathodes, the desired reaction product (Li_2O_2 and KO_2, respectively) were obtained. This can be an effect of the dissolution/ionisation process of NaO_2 causing further degradation of the cell components.

Any further work in the Na-O_2 battery will be on developing more stable anode interfaces or alternative anode materials. The main factor found to hinder long cycle life was the short circuit of the cell caused by dendrite formation when plating the metal anode.

Finally, the investigation onto non-aqueous K-O_2 cells revealed faster kinetics and higher reversibility associated with one electron reduction/oxidation of

KO_2. This is an effect of the less favourable interaction of the superoxide anion intermediate by larger, less charge localised cations (softer acids) in agreement with the HSAB theory.

The main factor which limited not only cyclability, but also cell capacity was oxygen crossover, which is the reaction of dissolved oxygen on the anode surface. A passivating layer growth was detected and its components were determined to be ether decomposition (K_2CO_3 and KOH) and KO_2. Investigating different electrolyte combinations, a stable SEI was formed when KTFSI was employed as supporting salt. The stability of the surface layer was enhanced with increasing the TFSI concentration in solution. Improved cyclability was obtained at the expense of discharge capacity, while in full discharge cells the protective layer was disrupted by the consecutive stripping/plating cycles.

Further work in K-O_2 batteries should also be aimed towards the development of stable electrolyte interfaces with the metal anode. Especially since the replacement of the passivated anode allowed cycling under the formation/decomposition of only KO_2, indicating high reversibility of the cathodic reaction.

An antimony-carbon nanocomposite was investigated as a possible anode alternative to the unstable potassium metal. In half cells, long cycling with low irreversible capacity was obtained as a result of the buffering effect of carbon mitigating volumetric changes. An ether based K-O_2 cell was constructed and successfully galvanostatic cycled. Although promising results were obtained, further work is necessary to evaluate whether or not this material is a feasible replacement for the potassium metal.

CURRICULUM VITAE

Filipe Braga Nogueira

Personal

Date of birth: 21/04/1988

Place of Birth: Recife – Brazil

Nationality: Brazilian

Education

2006 – 2010

Bachelor in Science, Chemistry

Federal University of Pernambuco, Pernambuco – Brazil

Undergraduate Research Monograph title: *Electrochemical Evaluation of The Inhibitors Tolad 4410, DCI-6A and Sodium Sulphite for The Protection of Carbon Steel in Aqueous Saline Environments.*

2010 – 2012

Masters in Chemistry

University of Sao Paulo, Sao Paulo – Brazil

Masters Dissertation title: *Self Assembly of Poly(o-methoxyaniline) and Vanadium Pentoxide Nanoparticles as Cathodes for Lithium-ion Batteries in Ionic Liquid.*

2013 – 2018

PhD in Chemistry

University of Liverpool, Liverpool – UK

Stephenson Institute for Renewable Energy

Thesis title: *Electrochemical Testing of Alkali Metal-Oxygen Batteries*

Publications

(1) Iftekhar, M.; Drewett, N.; Armstrong, A.; Hesp, D.; Braga, F.; Ahmed, S.; Hardwick, L. *Journal of The Electrochemical Society* 2014, *161*, A2109.

(2) Benedetti, T. M.; Carvalho, T.; Iwakura, D. C.; Braga, F.; Vieira, B. R.; Vidinha, P.; Gruber, J.; Torresi, R. M. *Solar Energy Materials and Solar Cells* 2015, *132*, 101.

(3) Wu, T.-H.; Hesp, D.; Dhanak, V.; Collins, C.; Braga, F.; Hardwick, L. J.; Hu, C.-C. *Journal of Materials Chemistry A* 2015, *3*, 12786.

(4) Galloway, T. A.; Cabo-Fernandez, L.; Aldous, I.; Braga, F.; Hardwick, L. *Faraday Discussions* 2017.

(5) Serwar, M., Ali Rana, U.; Siddiqi, H.; Khan, S. Ud-Din, Ali, F.; Al-Fatesh, A.; Adomkevicius, A.; Coca-Clemente, J. A.; Cabo-Fernandez, L.; Braga, F.; Hardwick, L. RSC Advances, 2017, 86, 54626-54637.

(6) Aldous, I.; Braga, F.; Walsh, J.; Neri, G.; Cowan, A.; Hardwick, J. *Singlet oxygen as a charging intermediate in the oxidation of alkali metal oxygen batteries* **(In preparation)**. Data relating to Chapter 3.

(7) Braga, F., Aldous, I.; Hardwick, J. *Characterisation of NaO_2 precipitates on practical carbon electrodes for Na-O_2 cells.* **(In preparation).** Data relating to Chapter 4.

(8) Braga, F., Hardwick, J. *The Role of binder decomposition on sodium and potassium-oxygen batteries.* **(In preparation)**. Data relating to Chapters 4 and 5.

Appendix A.

Data relating to: Chapter 4.Aprotic sodium-oxygen battery systems

4.4.1 Stability of organic carbonate based electrolytes

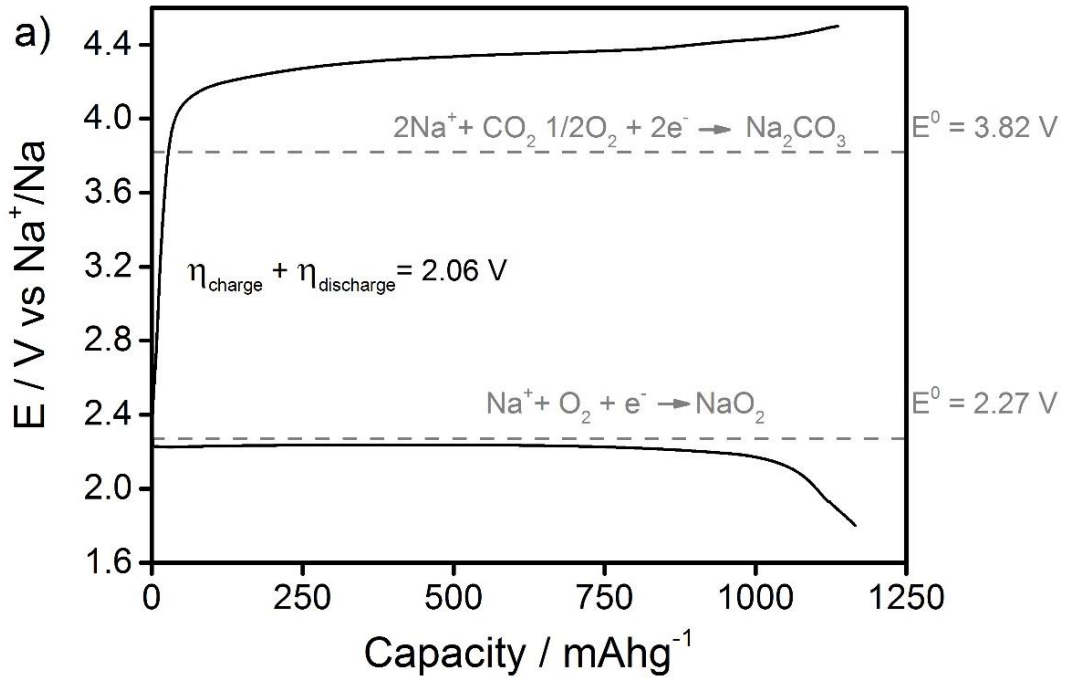

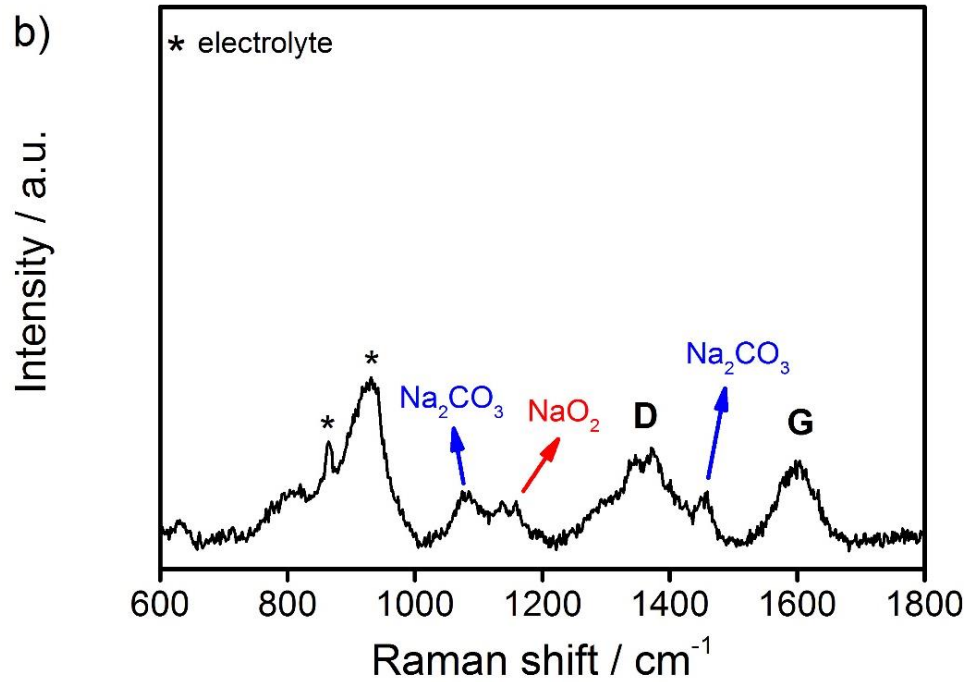

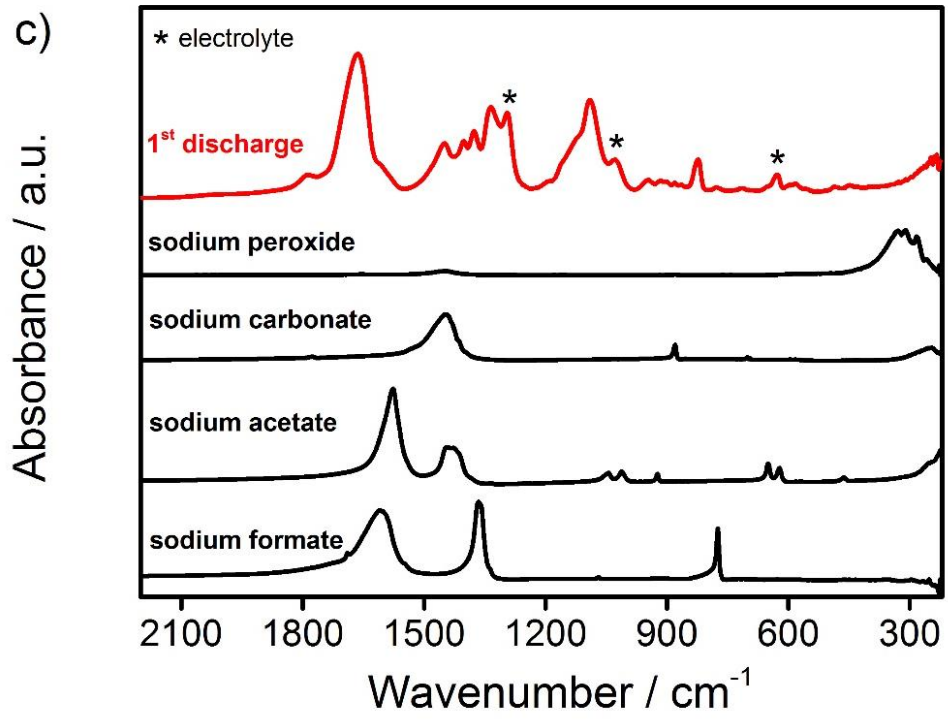

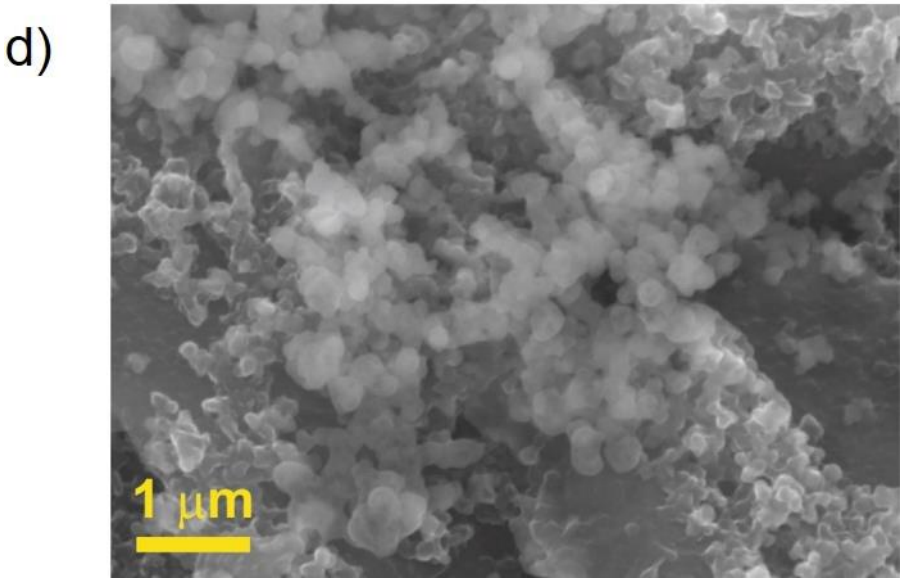

Figure A1: a) First galvanostatic discharge/charge cycle; b) FTIR, c) Raman and d) SEM analysis of the Super C65, Imerys carbon black cathode after one discharge process in a 1.0 M $NaPF_6$ in PC electrolyte at 0.12 mA cm^{-2} current rate.

4.4.2 Stability of ether based electrolytes

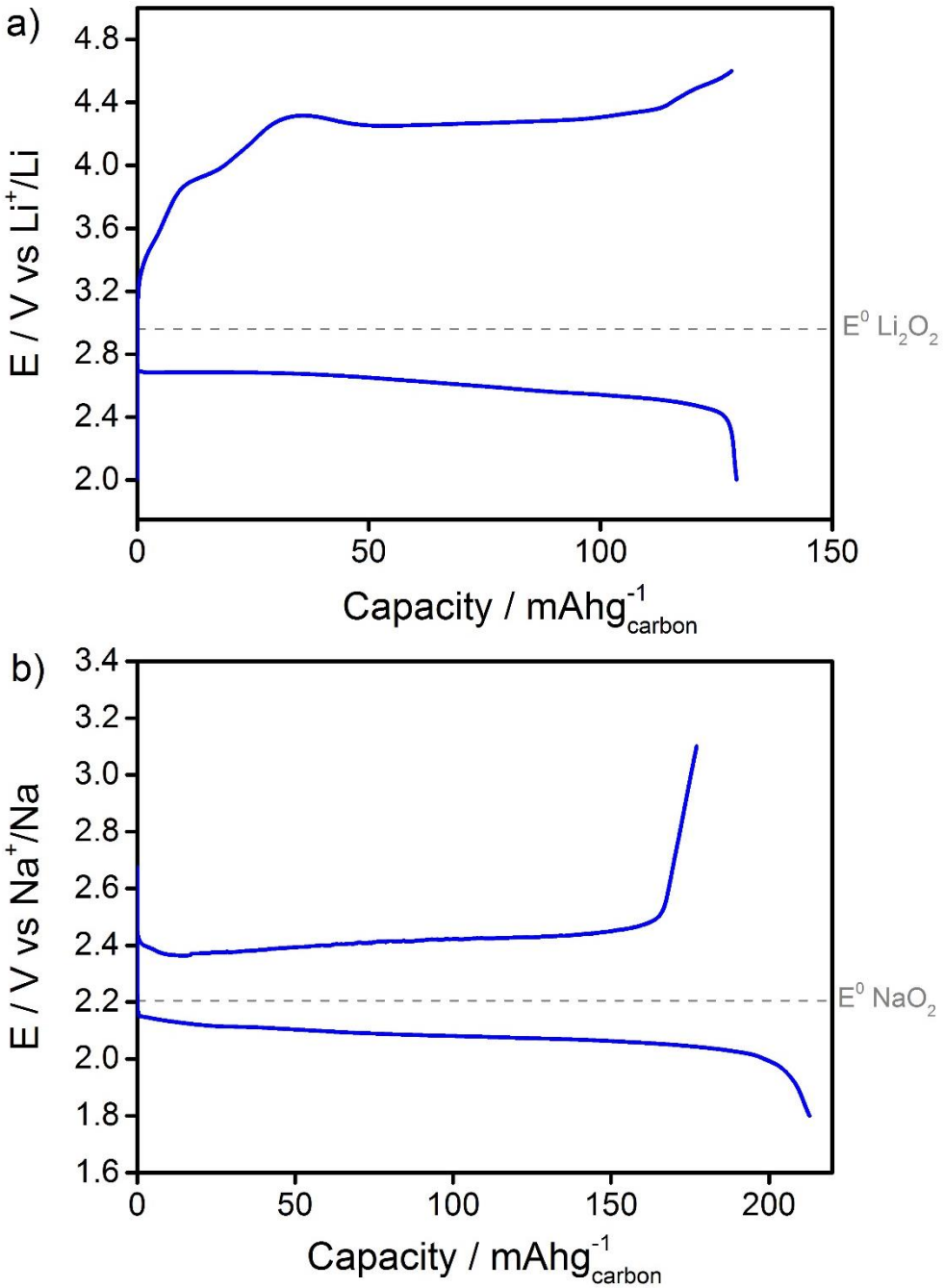

Figure A2: First galvanostatic discharge/charge cycle of analogous a) Li-O_2 and b) Na-O_2 cells using GDL H24, Freudenberg carbon cathodes. The same current density was employed in both cells: 0.12 mA cm^{-2}. Electrolytes: a) 0.5 M LiOTf in DEGDME b) 0.5 M NaOTf in DEGDME.

4.4.3 Cyclability

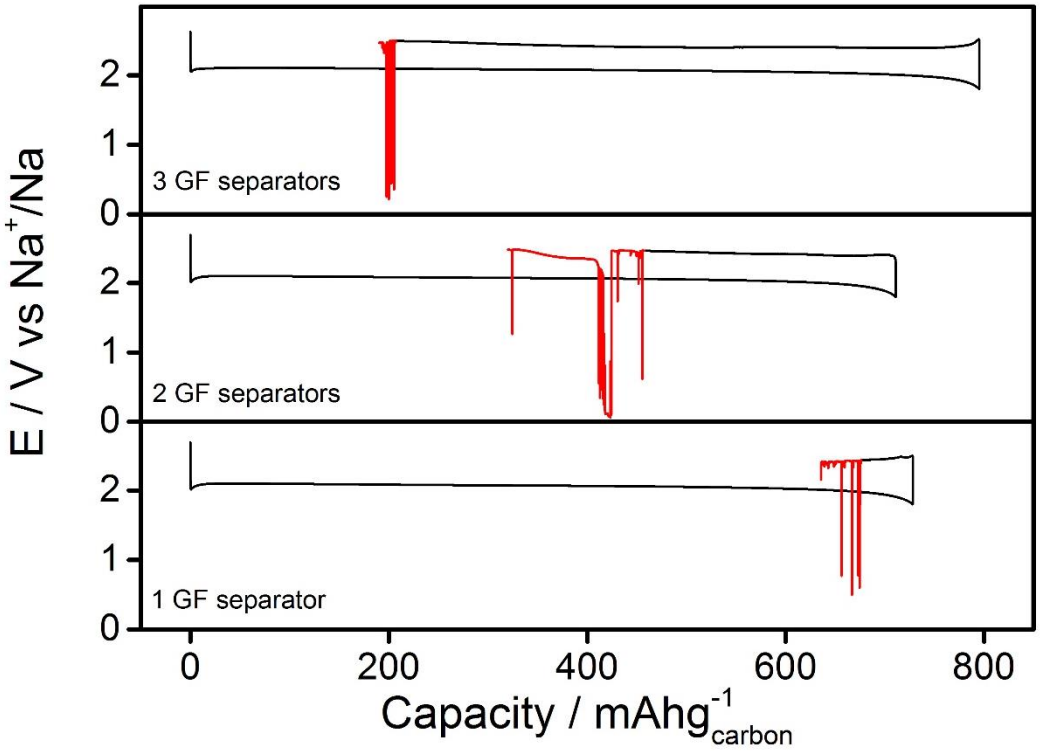

Figure A3: Effect of using multiple glass fibre separators. First galvanostatic discharge/charge cycle of the P50 Avcarb carbon fibre paper cathode in a 0.5 M NaOTf in DEGDME electrolyte at 0.12 mA cm^{-2} current rate.

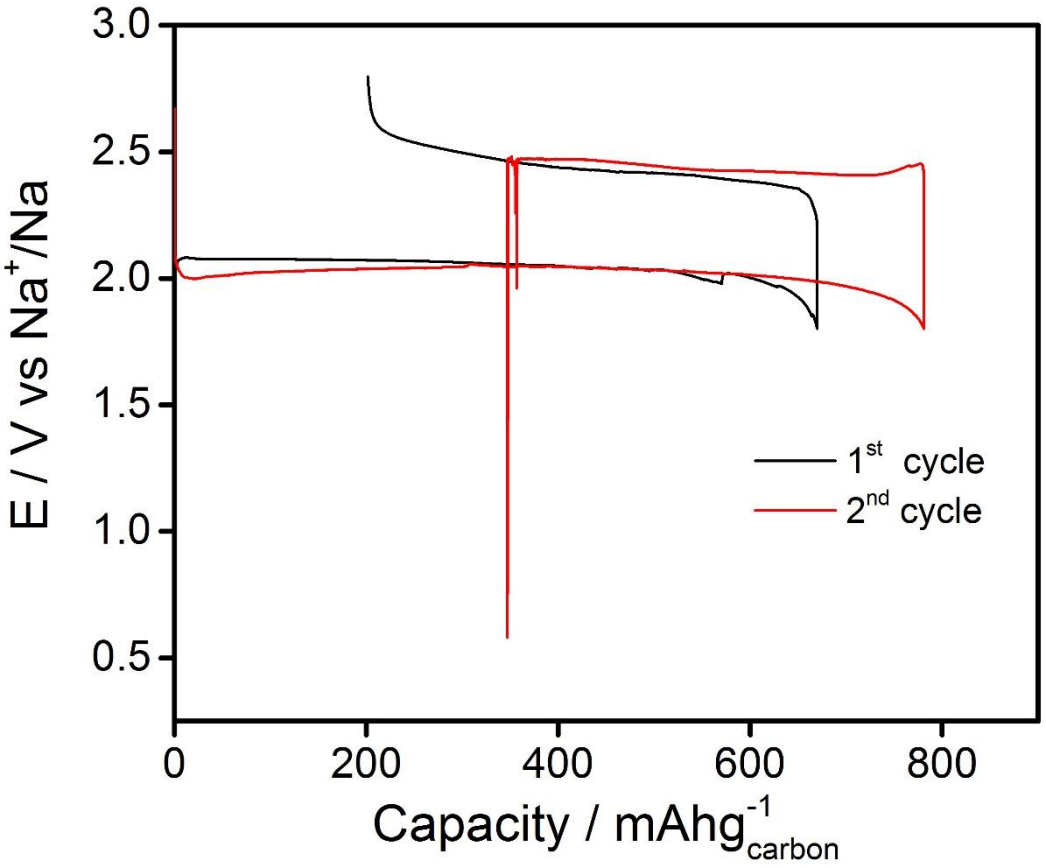

Figure A4: Effect of using ceramic separators. Two galvanostatic discharge/charge cycles of the P50 Avcarb carbon fibre paper cathode in a 0.5 M NaOTf in DEGDME electrolyte at 0.12 mA cm^{-2} current rate.

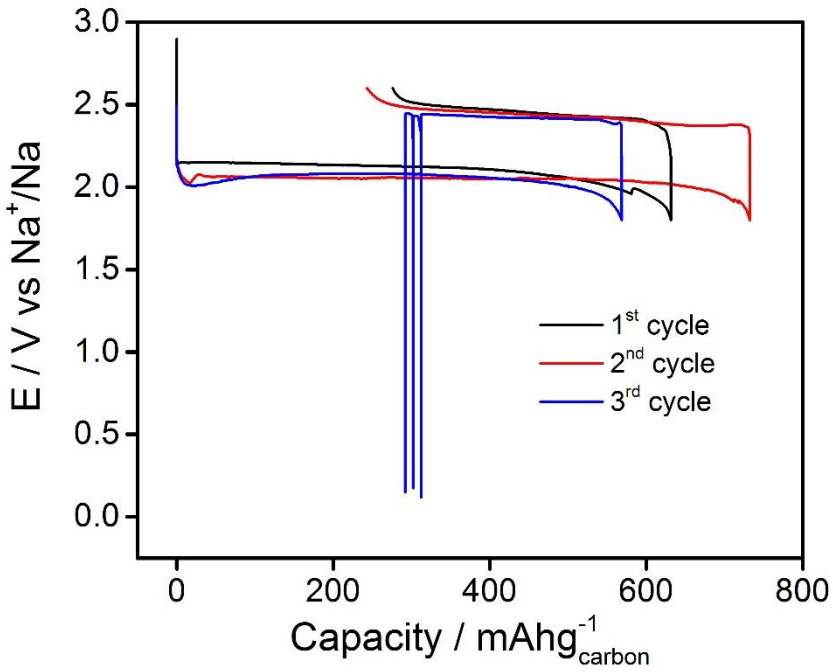

Figure A5: Effect of using bromine additives. First galvanostatic discharge/charge cycles at 0.12 mA cm^{-2} using 0.5 M $NaClO_4$ + 0.05 M $CsClO_4$ in DEGDME electrolyte and an Avcarb P50 carbon fibre paper cathode.

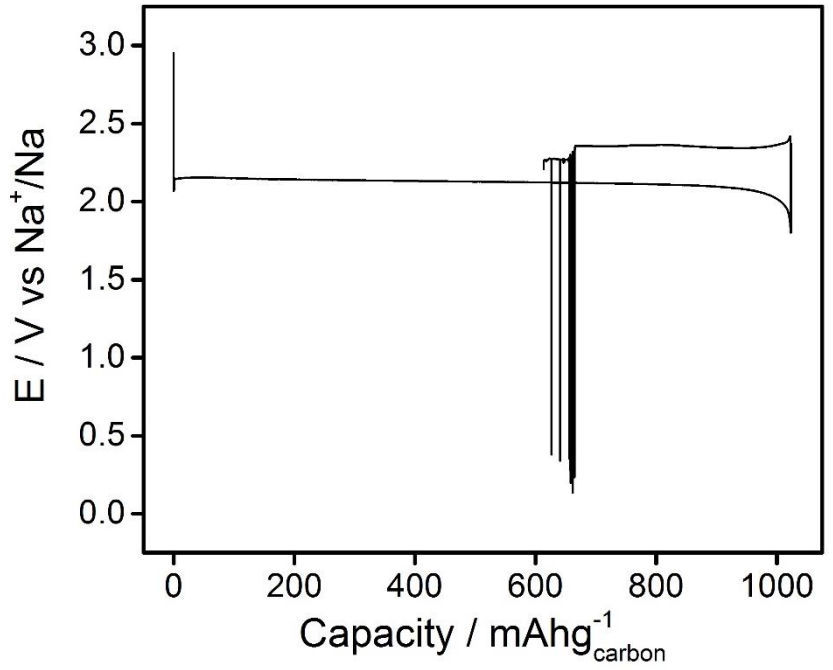

Figure A6: Effect of using bromine additives. First galvanostatic discharge/charge cycles at 0.12 mA cm^{-2} using 0.5 M NaOTf + 0.05 M $BrCH_2CH_2SO_3Na$ in DEGDME electrolyte and an Avcarb P50 carbon fibre paper cathode.

4.4.4 Effect of electrolyte solvent chain length

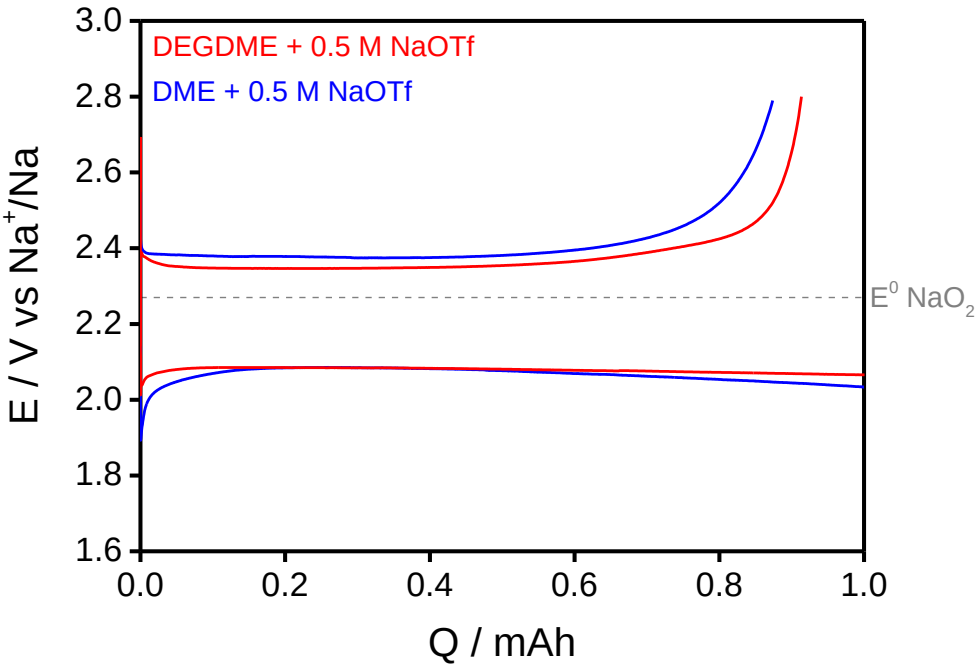

Figure A7: First galvanostatic discharge/charge cycle of the P50 Avcarb carbon cathode in a 0.5 M NaOTf in DEGDME and DME electrolyte at 0.24 mA cm^{-2} current rate with a charge limitation of 1 mAh.

4.4.5 Characterisation of NaO_2 precipitates at different states of discharge

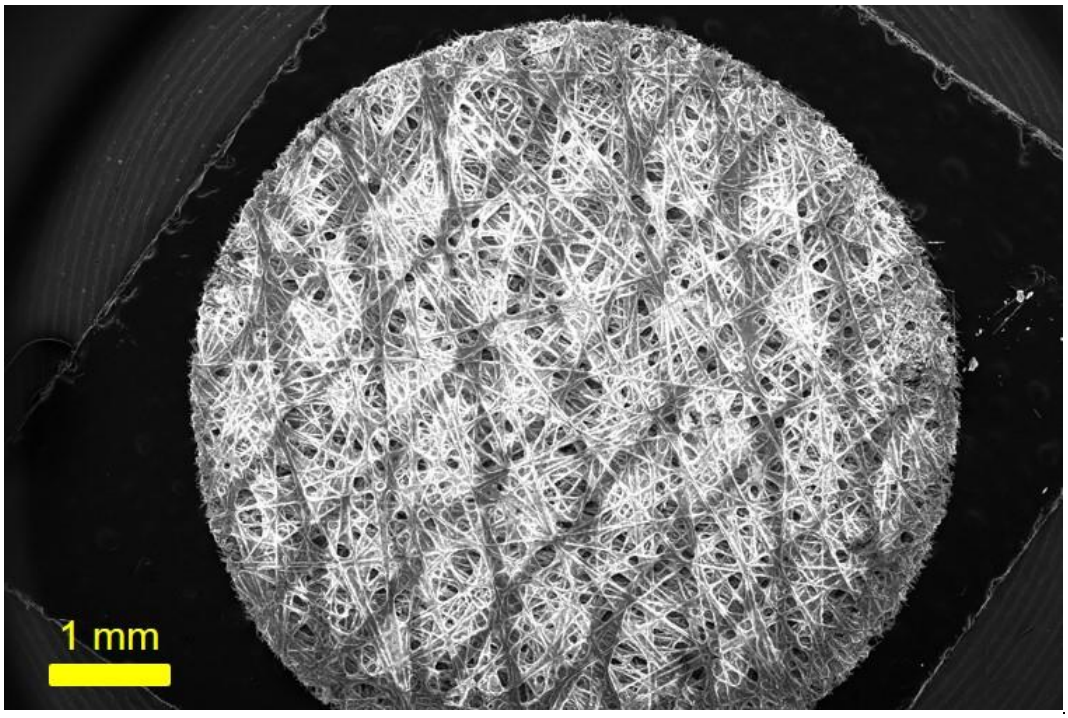

Figure A8: SEM image of a discharged Avcarb P50 carbon fibre paper cathode using 0.5 M NaOTf in DEGDME electrolyte at 0.24 mA cm^{-2} current density.

4.4.9 Effect of the polymeric binder

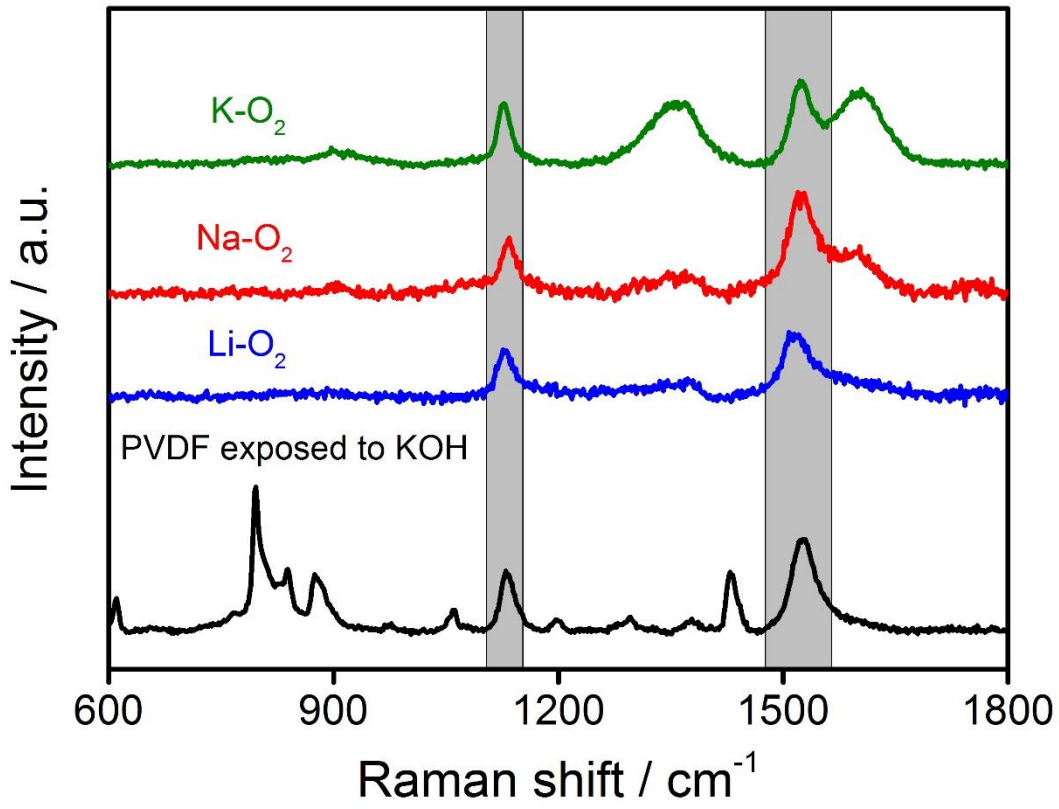

Figure A9. Raman analysis for discharged carbon black/PVDF cathodes in Li-O_2, Na-O_2 and K-O_2 cells. The same current density was employed all the cells: 0.12 mA cm^{-2}. Electrolytes: 0.5 M LiOTf in DEGDME, 0.5 M NaOTf in DEGDME and 0.25 M KPF_6 in DME.

4.4.10 Effect of the carbon air-cathode

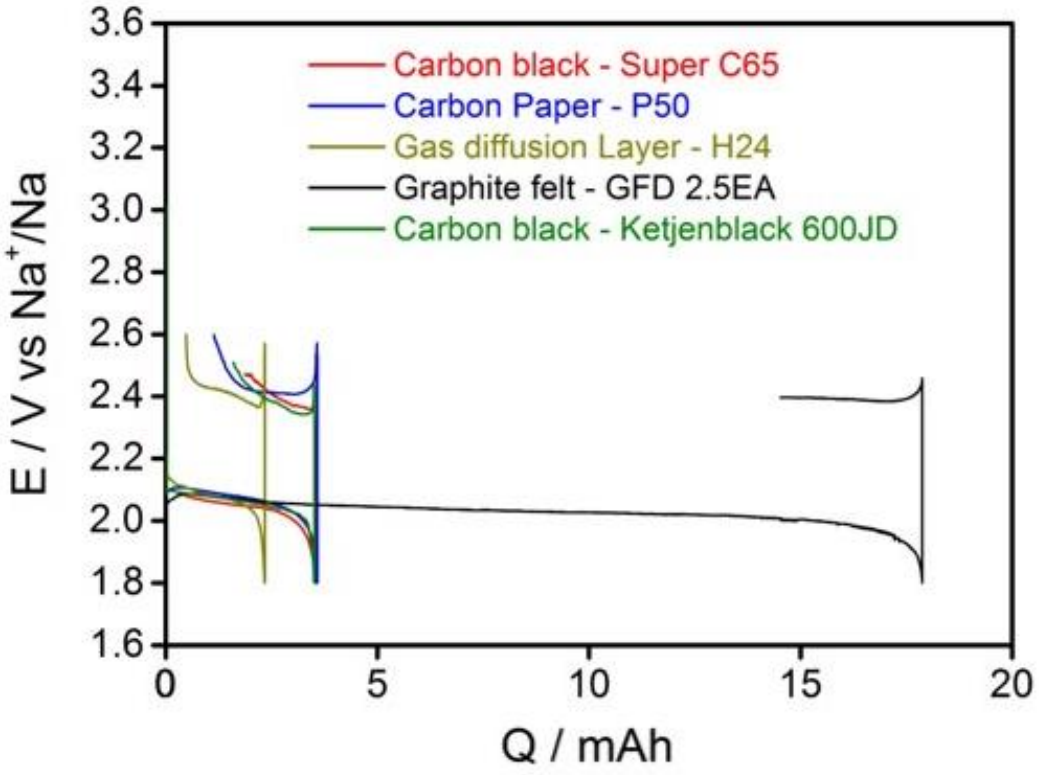

Figure A10. First galvanostatic discharge/charge absolute capacity profiles for Na-O_2 cells using different carbon cathodes with a 0.5 M NaOTf in DEGDME electrolyte at 0.12 mA cm^{-2} rate.

4.4.11 Carbon nanotube cathodes

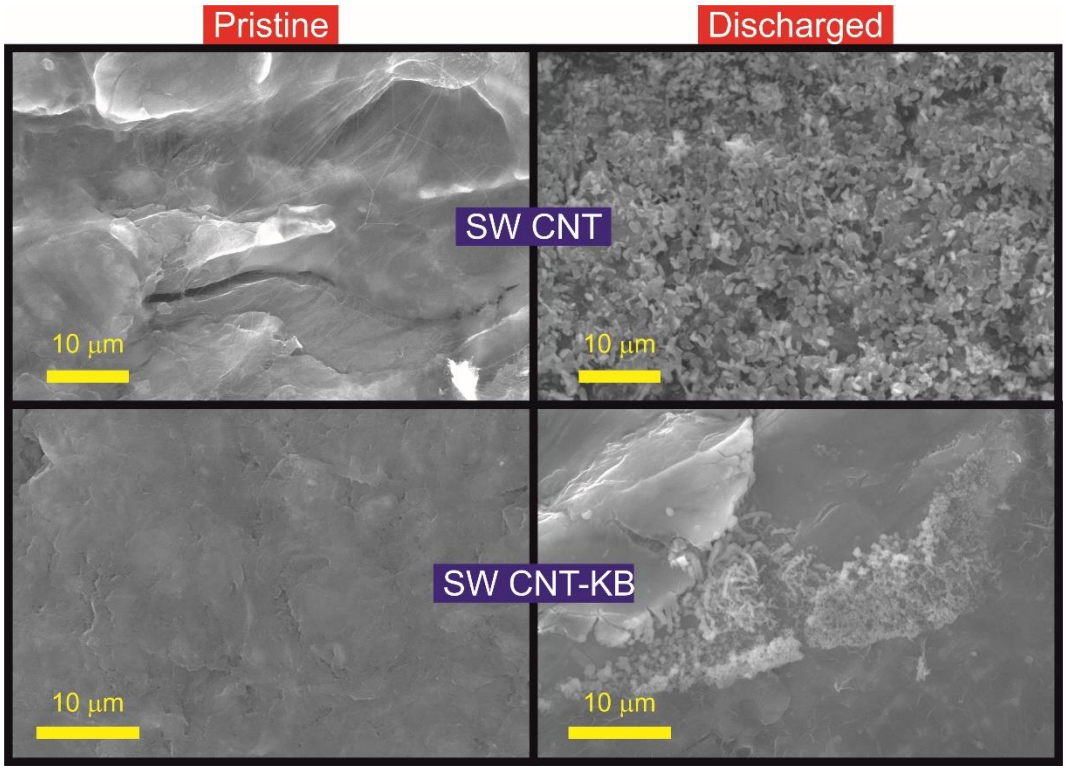

Figure A11: SEM images of pristine and discharged carbon nanotube electrodes in Na-O_2 cells using a 0.5 M NaOTf in DEGDME electrolyte.

Appendix B.

Data relating to: Chapter 5. Aprotic Potassium-Oxygen Battery Systems

5.4.1 Stability of ether-based electrolytes

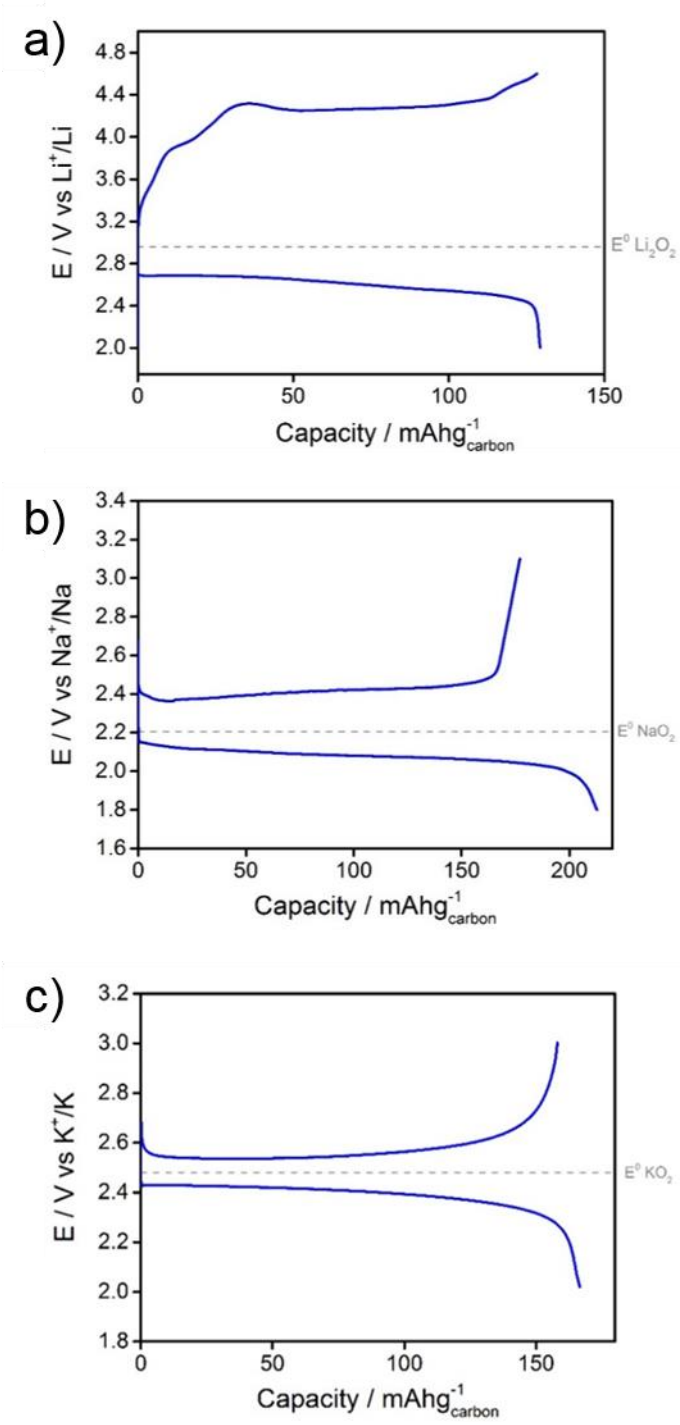

Figure B1: First galvanostatic discharge/charge cycle for a) Li-O_2, b) Na-O_2 and c) K-O_2 cells using a GDL cathode (H24, Freudenberg). The same current density was employed in all the cells: 0.12 mA cm^{-2}. Electrolytes: a) 0.5 M LiOTf in DEGDME, b) 0.5 M NaOTf in DEGDME and c) 0.25 M KPF_6 in DME.

5.4.2 Cyclability

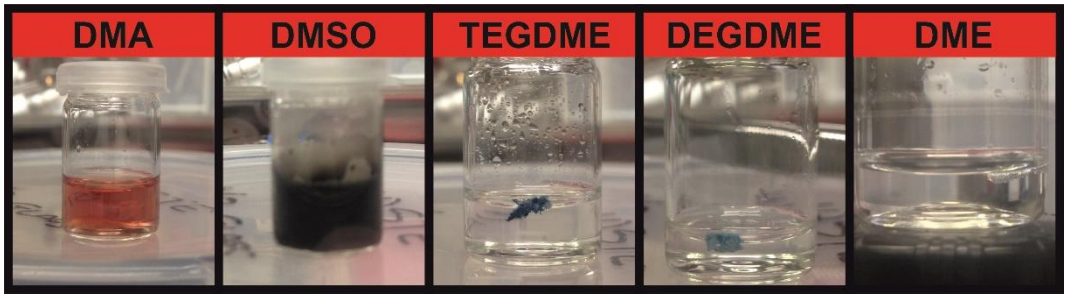

Figure B2: Chemical stability tests of the potassium metal anode against different solvents: dimethylacetamide (DMA), dimethyl sulfoxide (DMSO), tetraethylene glycol dimethyl ether (TEGDME), diethylene glycol dimethyl ether (DEGDME), 1,2 dimethoxyethane (DME).

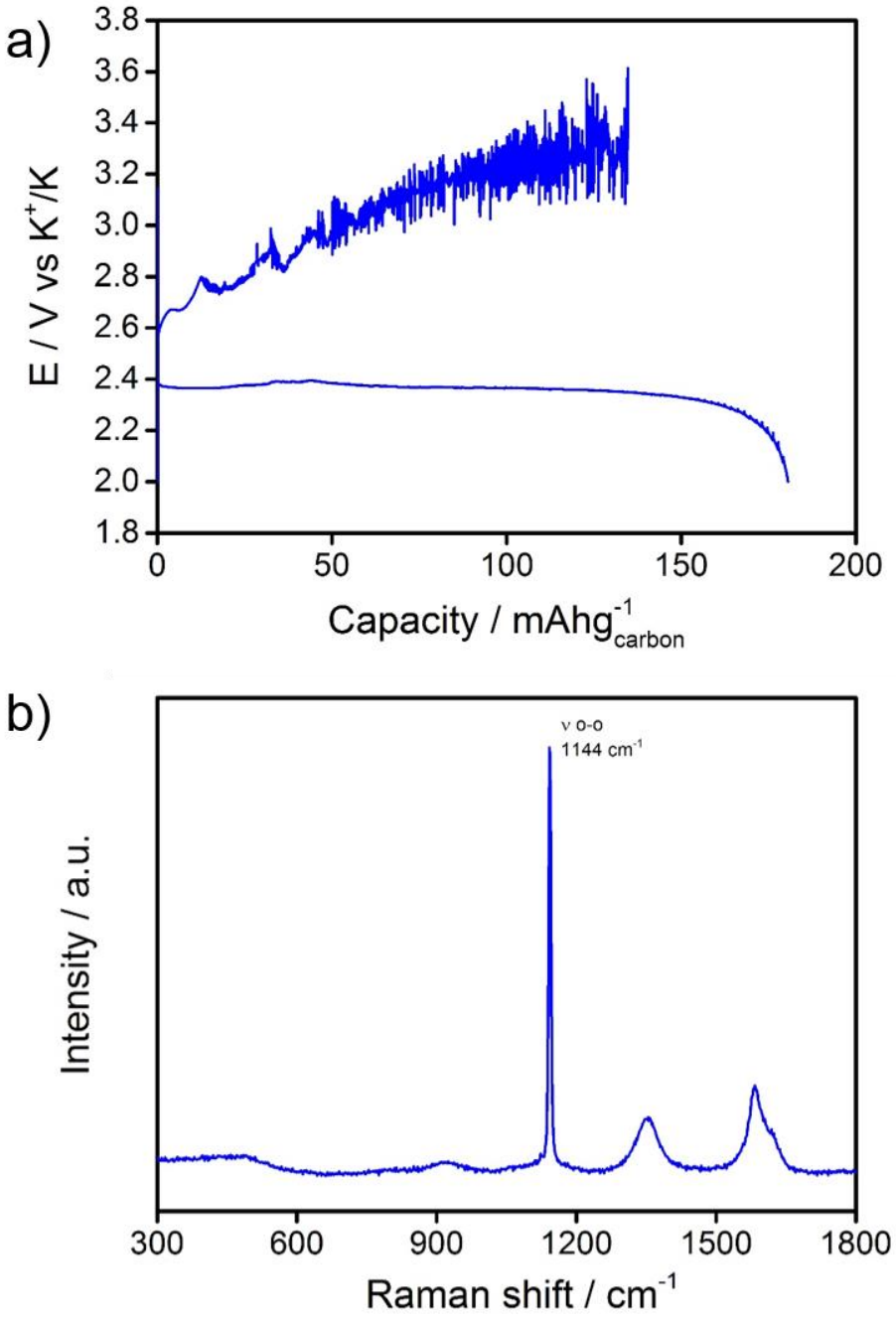

Figure B3: a) First galvanostatic discharge/charge cycle of a K-O_2 cells using a GDL (H24, Freudenberg) at 0.12 mA cm^{-2} current density b) Raman spectrum of the discharged cathode. Electrolyte: 0.25 M KPF_6 in DEGDME.

5.4.3 Effect of electrolyte salt

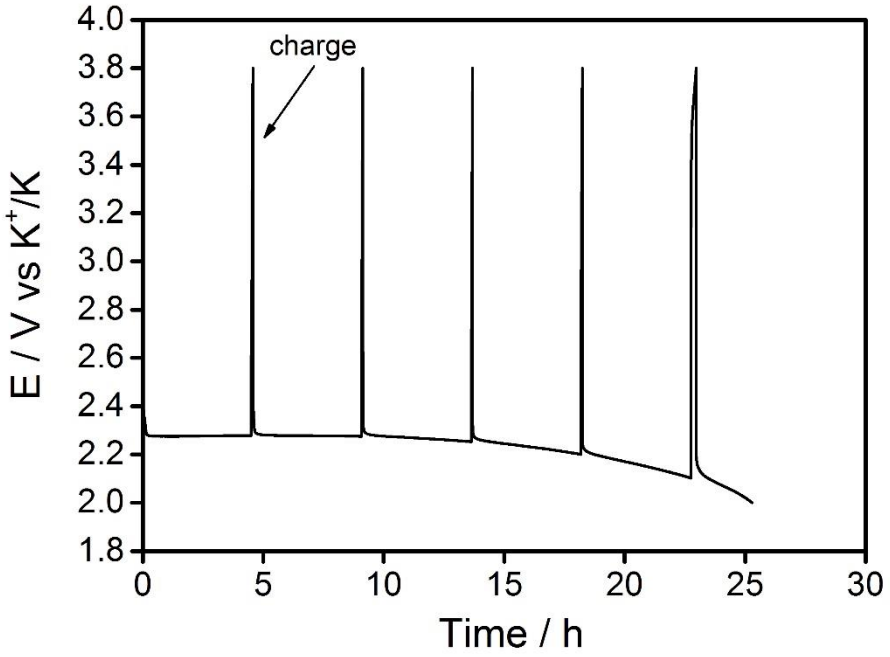

Figure B4: Galvanostatic discharge of a K-O_2 cell at 0.12 mA cm^{-2} using an Avcarb P50 carbon fibre cathode with a time limitation of 4.5 hours. Electrolyte: 0.25 M KFSI in DME.

5.4.4 KTFSI based K-O_2 cells

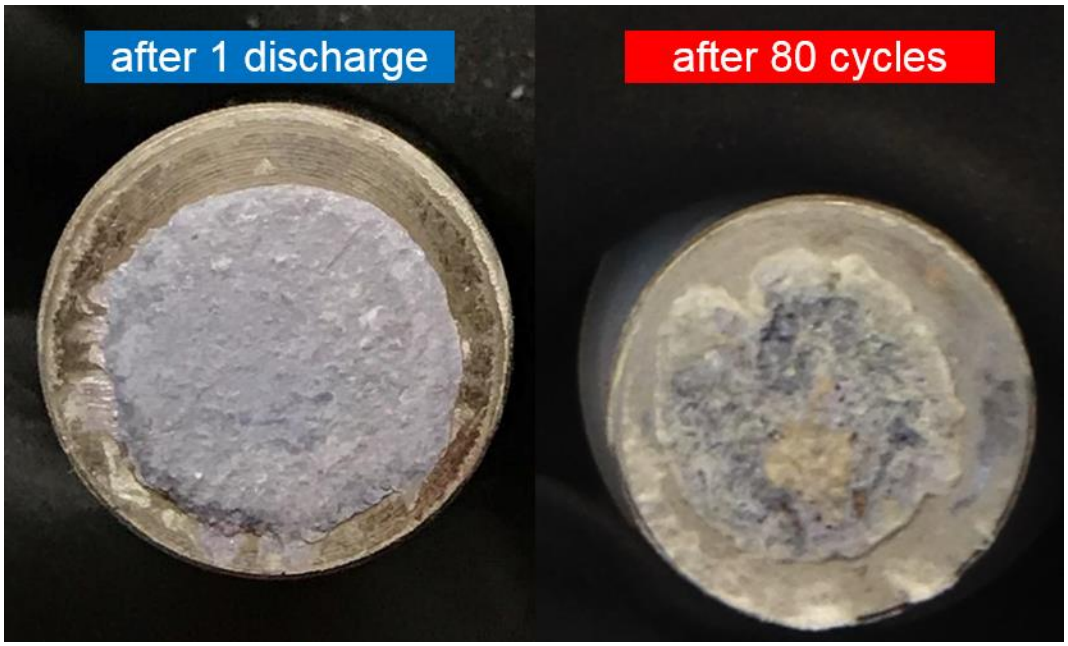

Figure B5: Images of K metal anodes after 1 discharge (left) and after 80 galvanostatic cycles (right) in a K-O_2 cell using 5 M KTFSI in DME electrolyte.

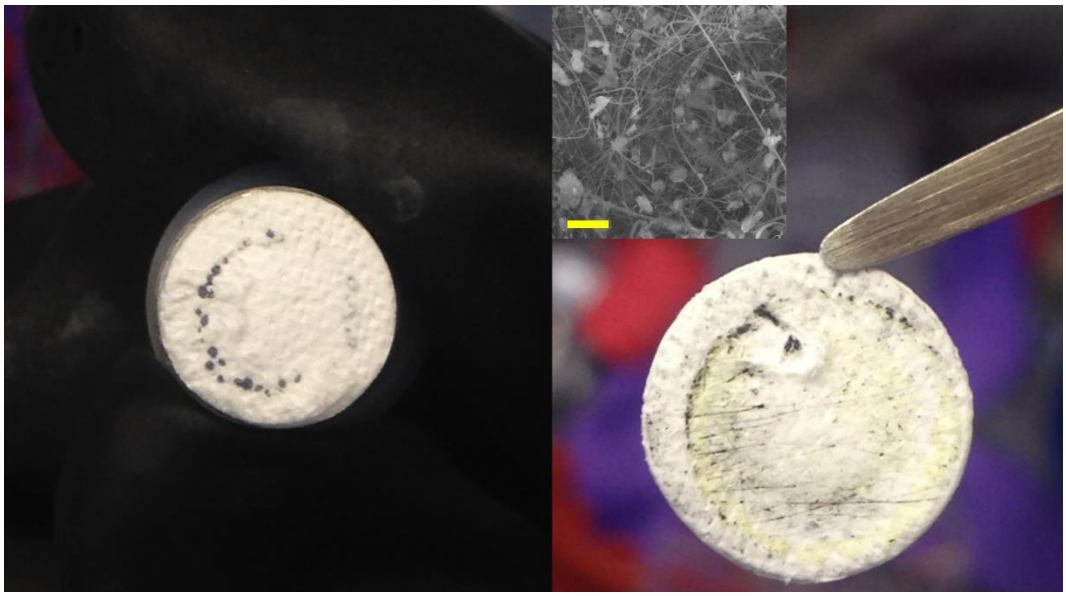

Figure B6: Images of glass fibre separator after 80 galvanostatic cycles in a K-O_2 cell using 5 M KTFSI in DME electrolyte showing dendrite growth through the fibres (left) and oxygen crossover on the fibre (right). Insert shows SEM image of KO_2 particles on the glass fibre separator (scale bar 10 μm).

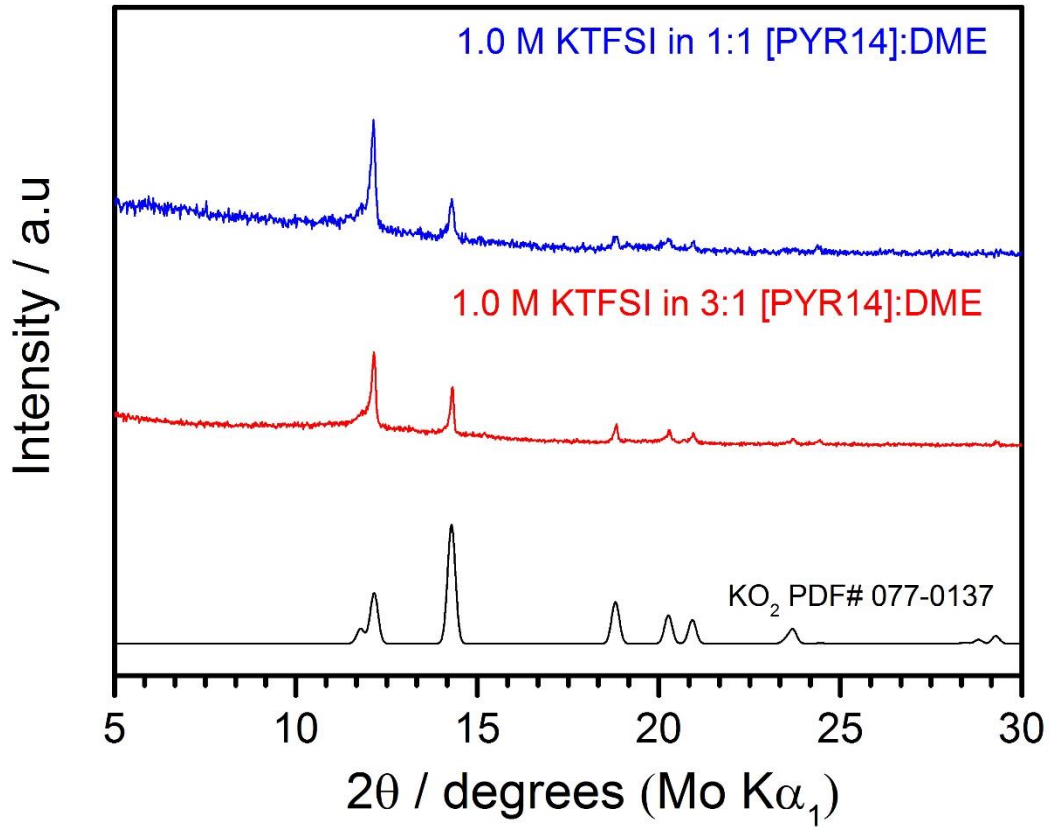

Figure B7: PXRD patterns of discharged Avcarb P50 carbon fibre cathodes at 0.12 mA cm^{-2} rate in K-O_2 cells using 1.0 M KTFSI in 1:1 DME: [PYR14][TFSI] and 1.0 M KTFSI in 3:1 DME:[PYR14][TFSI] electrolyte.

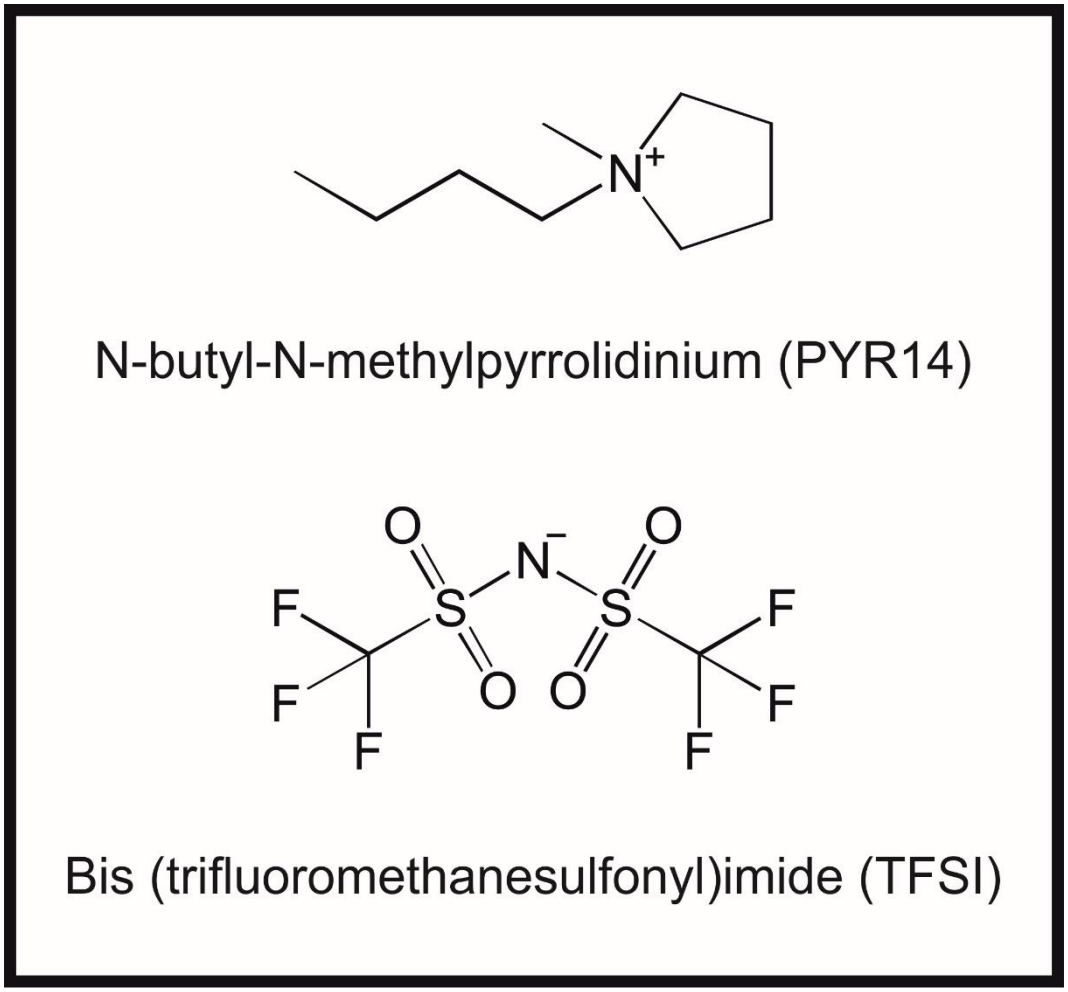

Figure B8: Chemical structure of [PYR14][TFSI] ionic liquid.

5.4.7 Effect of the polymeric binder

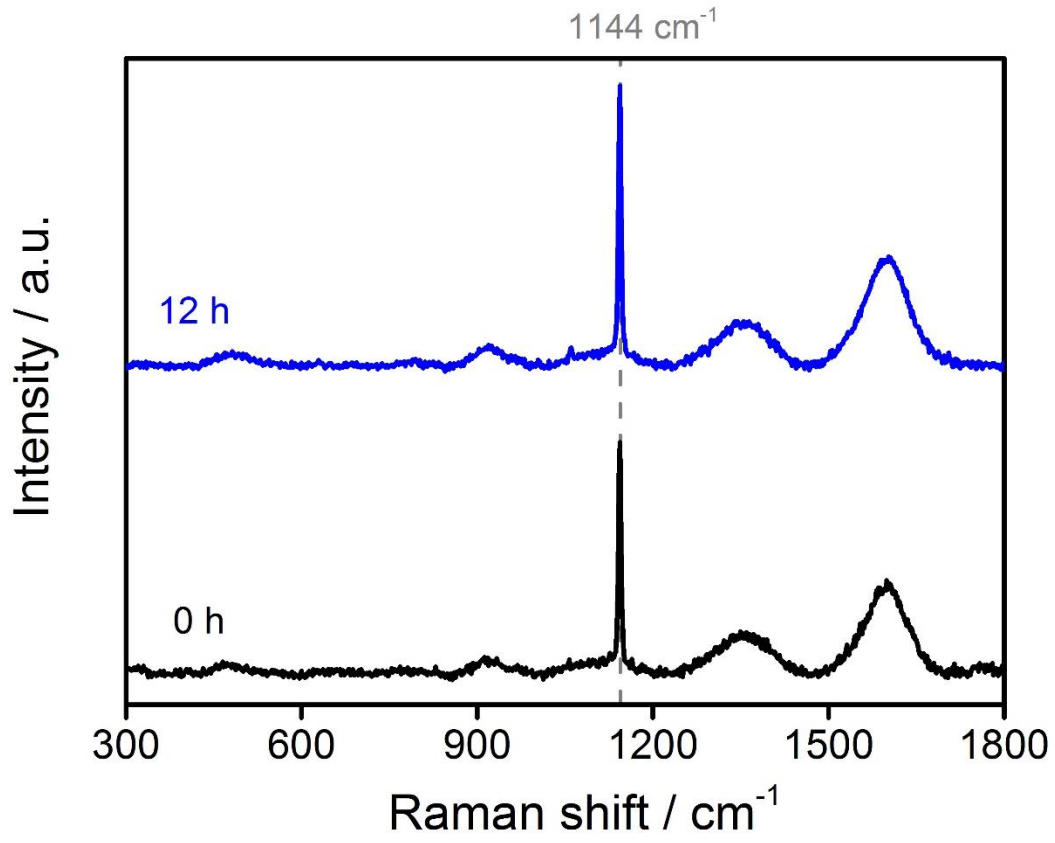

Figure B9: Raman spectroscopy analysis of the discharge product formed on K-O_2 cells using a GDL H24, Freudenberg carbon cathode in combination with a 0.25 M KPF_6 in DME electrolyte after different resting times.